REPURPOSING PETROLEUM RESERVOIRS FOR GEOTHERMAL ENERGY:
A CASE STUDY OF THE APPALACHIAN BASIN

A Dissertation
Presented to the Faculty of the Graduate School
of Cornell University
In Partial Fulfillment of the Requirements for the Degree of
Doctor of Philosophy

by
Erin Riley Camp
August 2017

REPURPOSING PETROLEUM RESERVOIRS FOR GEOTHERMAL ENERGY:
A CASE STUDY OF THE APPALACHIAN BASIN

Erin Riley Camp, Ph. D.
Cornell University 2017

ABSTRACT

Geothermal energy is a clean, renewable source of energy found in Earth's subsurface. There is inherent financial risk in the exploration and production of geothermal energy, primarily due to the high cost of drilling and the uncertainty in reservoir flow properties. Repurposing existing data from the petroleum industry has the potential to reduce uncertainty in geothermal exploration, and may lead to the identification of suitable geothermal prospects in Earth's widespread sedimentary basins. The Appalachian Basin of the eastern United States provides an opportunity for investigating the potential for low-temperature geothermal energy production, via the reanalysis of existing petroleum reservoir data. A probabilistic analysis of over 1,000 petroleum reservoirs concludes that most hydrocarbon reservoirs in the Appalachian Basin are not suitable for geothermal applications. Furthermore, a validation of these results using natural gas production data concludes that the traditional Productivity Index is not a suitable model for fractured or vuggy lithologies. However, one of the most promising plays in the region is the Trenton-Black River hydrothermal dolomite reservoirs in the Southern Tier of New York. Extensive analysis of existing datasets from a key reservoir in the play—

Quackenbush Hill—reveals a highly fractured, heterogeneous, vuggy reservoir with temperatures ~90°C, high horizontal permeability, negligible vertical permeability, and opportunities for stimulation. Assuming these reservoir features are similar for the remainder of T-BR reservoirs, this play has great promise for a petroleum-to-geothermal transition. Finally, a petrographic analysis of matrix and cements from a T-BR structural outcrop analog is conducted to determine the outcrop's diagenetic similarity to the subsurface reservoirs. The analysis suggests that the outcrop is a diagenetic analog to the subsurface reservoirs, allowing for an application of fracture knowledge from the surface outcrop to the sub-surface T-BR reservoirs. A fracture analysis of that same outcrop provides a better understanding of the fracture spacing in the subsurface, which informs a conceptual model of potential fluid flow in the T-BR reservoirs for future research to more accurately model and predict the flow of geothermal fluids through the T-BR reservoirs.

BIOGRAPHICAL SKETCH

Erin Riley Camp was born and raised in southern California, in various locations within the vast Los Angeles Basin. Her upbringing included an appreciation for science and nature (and playing outdoors with her two younger sisters), which ultimately led to her passion for earth science and climate change mitigation. At Amherst College, she studied Geology and spent a semester studying Earth Systems in New Zealand. While studying with the Kiwis, she was introduced to geothermal energy, which embodies both her passions for earth science and renewable energy. Despite her efforts to study geothermal energy for her Senior Thesis, she was assigned to a project that explored mercury concentrations in peat bogs. After graduation, Erin found her way back to hard rocks and geothermal energy via a position with the Department of Energy in the Geothermal Technologies Office. Seven months into the bureaucracy, Erin leapt at the opportunity to renew her studies in geothermal energy at Cornell, where she spent five years studying with geologists, chemical, mechanical and civil engineers, and geophysicists. After a five-year research journey guided by the amazing Teresa Jordan, Erin is [as of July 2017] living in Boston, and working as a renewable energy consultant.

Dedicated to women in science—past, present, and future.

ACKNOWLEDGMENTS

There are SO many people to thank for helping, guiding, mentoring, and supporting me during this challenging yet incredibly rewarding journey. It would certainly not have been possible alone, nor would I have wanted to do it without a loving, encouraging community by my side. In bulleted form, of course:

- My family: my parents, David Camp and Meaghan Ryan, and my sisters, Tara and Meaghan Camp. Thank you for encouraging me to be my best self, for believing in me when I felt like giving up, for loving me unconditionally, for visiting me in Ithaca from the west coast, helping me move apartments, for the bi-weekly “sister Skype” calls.
- My IGERT research group and friends: Léda Gerber, Laura Sinclair, Arna Palsdottir, Andrea Aguirre, John Mason, Koenraad Beckers, Maciek Lukawski, Calvin Whealton, and Jared Smith. Thank you to all of you for the laughs in the “morgue”, the intellectual discussions of students’ rights (e.g. office windows to the outside), fun times on IGERT field trips (e.g. Sudbury breccia), research support and idea-making, trips to CTB and Indian Buffet, and so much more.
- The Play Fairway Team: Brian Anderson, Maria Richards, Frank Horowitz, Matt Hornbach, Kelydra Welcker, Xiaoning He, Zachary Frone. Additionally, the three Cornell undergrads who assisted me with data collection: Sophie Fructer, Hannah Lang, and Tasnuva (“Ming”) Khan.
- My Ithaca friends: Jim and Jenny (and Lucy!) Bisha, Emma Silverman, Tess Pendergrast, Dave and Nicole (and Naomi!) Tedeyan, Ian Kyle, Patty Jones,

Laurel Stewart, Jansen Smith, Michael Smith, etc. Thank you for being the amazing, generous, fun, silly, adventurous people you are, and for providing me with an incredible community outside of graduate school.

- The Cornell Healthy Eating Program and SolStone. A special shout-out to my care team: Dr. A.J. Rubineau, Diane Sullivan, Bruce Brennan, and Clint Wattenberg. Thank you all for pushing me harder than I have ever been pushed before. The support you gave me made me a healthier, happier person, and you all changed my life for the better.
- My Leadership Instructors (and mentors), Erica Dawson and Werner Zorman: for giving me the tools to begin my leadership journey, which has guided me towards a more fulfilling career and life.
- My supportive, hilarious, fun, and loving partner, Yamin. Thank you for being my compass and primary support for the last 3 years, and guiding me as I begin my career.
- My committee: Terry, Jeff, and Rick. I consider myself one of the most fortunate PhD students to have had such a supportive team by my side. Though earning a PhD isn't an easy task, you all made it as simple as it could have been. Especially Terry, who I sincerely thank for caring deeply about both my research and my personal well-being. Your dedication, intellectual guidance, support, and mentorship made my experience at Cornell feel equally nurturing and rigorous. These were a wonderful five years!

TABLE OF CONTENTS

LIST OF FIGURES

LIST OF TABLES

LIST OF ABBREVIATIONS

BHT: bottom hole temperature
CL: cathodoluminescence
CNL: compensated neutron log
CV: coefficient of variation
EGS: Enhanced Geothermal Systems/Engineered Geothermal Systems
ESOGIS: Empire State Organized Geologic Information System
FPI: Fracture Productivity Index
FRPI: Fractured Reservoir Productivity Index
GIS: Geographic Information System
HTD: hydrothermal dolomite
ISIP: instantaneous shut-in pressure
J: joule
mcf: thousand cubic feet
mD: millidarcy
MPa: MegaPascal
MRCSP: Midwest Regional Carbon Sequestration Partnership
MW_{th}: megawatt thermal
NPHI: neutron porosity hydrogen index
NY: New York
Pa: Pascal
PA: Pennsylvania
PI: Productivity Index
RFC: Reservoir flow capacity
RPI: Reservoir Productivity Index
RPI_c: Reservoir Productivity Index, carbon dioxide
RPI_g: Reservoir Productivity Index, gas (methane)
RPI_w: Reservoir Productivity Index, water
sCO_2: supercritical carbon dioxide
T-BR: Trenton–Black River
TVD: Total Vertical Depth
WV: West Virginia
WVGES: West Virginia Geologic and Economic Survey

LIST OF SYMBOLS

ϕ: porosity
ϕ_N: neutron porosity
k: permeability
k_w: permeability, water as fluid
k_g: permeability, gas as fluid
ρ_{ma}: density of matrix rock
ρ_b: bulk density log reading
ρ_w: water density
ρ_r: rock density
$\mathrm{S}_{\mathrm{H,min}}$: minimum horizontal stress
$\mathrm{S}_{\mathrm{H,max}}$: maximum horizontal stress
S_{V}: vertical stress
P_f^*: injected fluid pressure for stimulation
p_f: pore-fluid pressure
σ_1: maximum principal stress
σ_3: minimum principal stress
σ_{n}^*: effective normal stress
τ: shear stress
μ: coefficient of sliding friction
$\mathrm{BHT}_{\mathrm{c}}$: corrected bottom hole temperature
$\mathrm{BHT}_{\mathrm{o}}$: measured bottom hole temperature
X_{m}: percent fraction of mud during BHT recording
d: depth of BHT recording
q_{tot}: total available heat
q_{rec}: recoverable heat
V: volume of rock
$\mathrm{C}_{\mathrm{p,w}}$: heat capacity of water
$\mathrm{C}_{\mathrm{p,r}}$: heat capacity of rock
ΔT: temperature differential
R: geothermal recovery factor
η: surface efficiency
t: time
H: reservoir thickness
D: distance between injection and production wells
b: Klinkenberg slip factor
C: conversion factor from m^3 to kg
a: fracture aperture
p: mean flowing pressure
x: percentage of open fractures
f: fracture frequency

PREFACE

Sustainable and affordable sources of clean energy are widely sought after in the United States and around the world to meet growing energy demand and increase the market for a diversified energy portfolio. Geothermal energy has been commonly suggested as a part of the solution for meeting these energy needs, as geothermal resources can provide electricity and/or heat from a spectrum of geological regimes. The spectrum ranges from convection-dominated liquid and vapor hydrothermal systems, to deep crystalline conduction-dominated Enhanced Geothermal Systems (EGS), to sedimentary or co-produced geothermal resources dominated by conduction and constrained by stratigraphy or existing oil and gas resources. Temperature, porosity, and permeability all vary across the spectrum of geothermal resources.

In the United States, geothermal energy has primarily been utilized to provide electricity (Tester, 2012), but only select places on Earth are host to the required temperatures for electricity generation at depths that allow a project to be economically viable. A sustained focus on electricity generation has limited the scope of geothermal energy to hydrothermal systems or deep crystalline EGS basement. By expanding the focus to include direct-use of hot water from the subsurface (in addition to steam), geothermal energy can play a significant near-term role as a source of energy for geographic regions that do not have the heat flow necessary for electricity generation. Additionally, when producing heat alone or coproducing heat with electricity from shallower depths, the levelized cost of energy is more competitive than that of electricity, even when EGS is employed (Beckers et al., 2014; Reber et al., 2014; Majorowicz and Minea, 2015).

Investment risk is still one of the primary factors limiting the development of geothermal energy projects, due to the high cost of drilling and uncertainty of suitable reservoirs in the subsurface. An innovative approach to reduce this risk is to target commercial oil and/or gas reservoirs in sedimentary basins, because datasets for temperature, porosity, permeability, and state of stress already exist. Furthermore, repurposing depleted conventional oil and gas fields for geothermal energy production is a promising way to harness otherwise unused heat, reuse wells or applicable data sets on reservoir quality, and collect additional data via existing wells (e.g. Deming, 1989; Barbacki, 2000; Zhang et al., 2008; Bu et al., 2012; Templeton et al., 2014; Soldo and Alimonti, 2015). The motivation of this dissertation is to characterize the geothermal reservoir opportunities available in the Appalachian Basin region of New York, Pennsylvania, and West Virginia, where drilling for oil and gas has taken place for decades, and where there is high thermal energy demand in select locations (e.g. Pittsburgh, PA; Charlestown, WV; Morgantown, WV; Elmira and Corning, NY). Improving the understanding of low-risk reservoir opportunities in this area has the potential to increase the utilization of geothermal energy for low-temperature applications in an area of the country with no geothermal energy to date.

The first chapter examines all oil and gas reservoirs from the study area, probabilistically reanalyzes existing data for geothermal energy applications, and identifies the most optimal reservoirs and plays for geothermal energy, based on permeability, reservoir thickness, and fluid viscosity. The analysis determines that a play of naturally fractured reservoirs in New York is the most outstanding choice for geothermal energy production. The second chapter dives more deeply into various

available reservoir datasets from this play—the Trenton–Black River (T-BR) gas reservoirs—and draws conclusions about its permeability, porosity, and stimulation potential. Limited available fracture data from the T-BR reservoirs leads to the work in Chapter 3, where our study of a local outcrop provides insights into fracture characteristics that may be applied to the subsurface T-BR reservoirs. Finally, Chapter 4 applies the work from previous chapters to tests a model for estimating flow through fractured reservoirs, as well as explores the role that heterogeneity plays in the T-BR reservoirs. This work is an important step forward for understanding the potential for lower-risk geothermal energy production in the Appalachian Basin, bridging the gap between modeling homogenous porous media flow and heterogeneous fracture flow, and paves a way forward for future geothermal energy production from the Trenton-Black River reservoirs.

REFERENCES

Barbacki, A., 2000, The use of abandoned oil and gas wells in Poland for recovering geothermal heat*,* Proceedings, Proceedings World Geothermal Congress, 3361-3365.

Beckers, K.F., Lukawski, M.Z., Anderson, B.J., Moore, M.C., and Tester, J.W., 2014, Levelized costs of electricity and direct-use heat from Enhanced Geothermal Systems: Journal of Renewable and Sustainable Energy, v. 6, no. 1, 013141 p.

Bu, X., Ma, W., and Li, H., 2012, Geothermal energy production utilizing abandoned oil and gas wells: Renewable energy, v. 41, p. 80-85.

Deming, D., 1989, Application of bottom-hole temperature corrections in geothermal studies: Geothermics, v. 18, no. 5, p. 775-786.

Reber, T., 2013, Evaluating Opportunities For Enhanced Geothermal System-Based District Heating In New York And Pennsylvania, A Master's Thesis, Cornell University.

Majorowicz, J., and Minea, V., 2015, Geothermal Energy Potential in Low Enthalpy Areas as a Future Energy Resource: Identifying Feasible Targets, Quebec, Canada, Study Case: Resources, v. 4, no. 3, p. 524-547.

Soldo, E., Alimonti, C., 2015, From an Oilfield to a Geothermal One: Use of a Selection Matrix to Choose Between Two Extraction Technologies*,* Proceedings, World Geothermal Congress: Melbourne, Australia.

Templeton, J.D., Ghoreishi-Madiseh, S.A., Hassani, F., and Al-Khawaja, M.J., 2014, Abandoned petroleum wells as sustainable sources of geothermal energy: Energy, v. 70, p. 366-373.

Tester, J.W., Drake, E.M., Driscoll, M.J., Golay, M.W., and Peters, W.A., 2012, Sustainable energy: Choosing among options: Cambridge, Massachusetts, MIT Press, 1019 p.

Zhang, L., Yuan, J., Liang, H., Li, K., 2008, Energy from Abandoned oil and gas reservoirs, Proceedings, SPE Asia Pacific Oil and Gas Conference and Exhibition, 10 p.

CHAPTER 1:

A PROBABILISTIC APPLICATION OF OIL AND GAS DATA FOR EXPLORATION STAGE GEOTHERMAL RESERVOIR ASSESSMENT IN THE APPALACHIAN BASIN

Abstract

Geothermal energy is a renewable, widespread, baseload energy source that has the potential to supply a large portion of the world's energy needs. High development risk, specifically high drilling costs combined with uncertainty in subsurface flow properties, have hampered growth of geothermal energy development. One option to reduce subsurface risk is to target locations where reservoir data are already available, including sedimentary basins where there has been extensive hydrocarbon production. Sedimentary basins are widespread and often have suitable geothermal gradients. This chapter presents a low-cost methodology that can be used at the pre-drilling exploration phase of a low-temperature geothermal project to accurately predict the location of low-risk reservoirs, applied to a case study of the Appalachian Basin in the eastern United States. The technique uses a Monte Carlo simulation of the Reservoir Flow Capacity and Reservoir Productivity Index (RPI) for over 1800 individual reservoirs, using water or supercritical carbon dioxide (sCO_2) as the reservoir fluid. Our results indicate that 99% of the reservoirs in the basin are of insufficient quality for geothermal heat production with water as the assumed fluid and without using stimulation technologies associated with Enhanced Geothermal Systems (EGS). In an EGS-sCO_2 system, suitable geothermal reservoir options increase from seven reservoirs to 115. When comparing the RPI results to natural gas production volumes from several selected reservoirs, the predicted RPI proves to be an accurate estimate of flow potential for porous reservoirs, but overestimates flow by a factor of three for fractured or vuggy reservoirs. A greater uncertainty ought to be utilized when applying the RPI equation to non-porous media. This methodology can be utilized in other basins that have experienced hydrocarbon exploration and production, to highlight low-risk reservoirs or geologic formations for further geothermal development.

Introduction

The uncertainty of subsurface fluid flow properties combined with high drilling costs create significant investment risk that has limited the development of geothermal energy projects worldwide. One approach that could potentially lower uncertainty is to focus exploration efforts on places in the subsurface that could be used for geothermal energy production for which data already exist, for example, in stratigraphic reservoirs in sedimentary basins that have produced hydrocarbons.

Though petroleum is not the desired commodity in the case of a geothermal system, the flow of commercial quantities of hydrocarbons through a body of rock is an important indicator of favorable permeability—a critically important factor for assessing potential geothermal energy development. Petroleum companies often give highest exploration priority to reservoirs in sedimentary formations with high porosity and high permeability zones. Therefore, the reuse of oil and gas databases and depleted reservoirs may result in an important exploration and cost-savings tool for the geothermal industry.

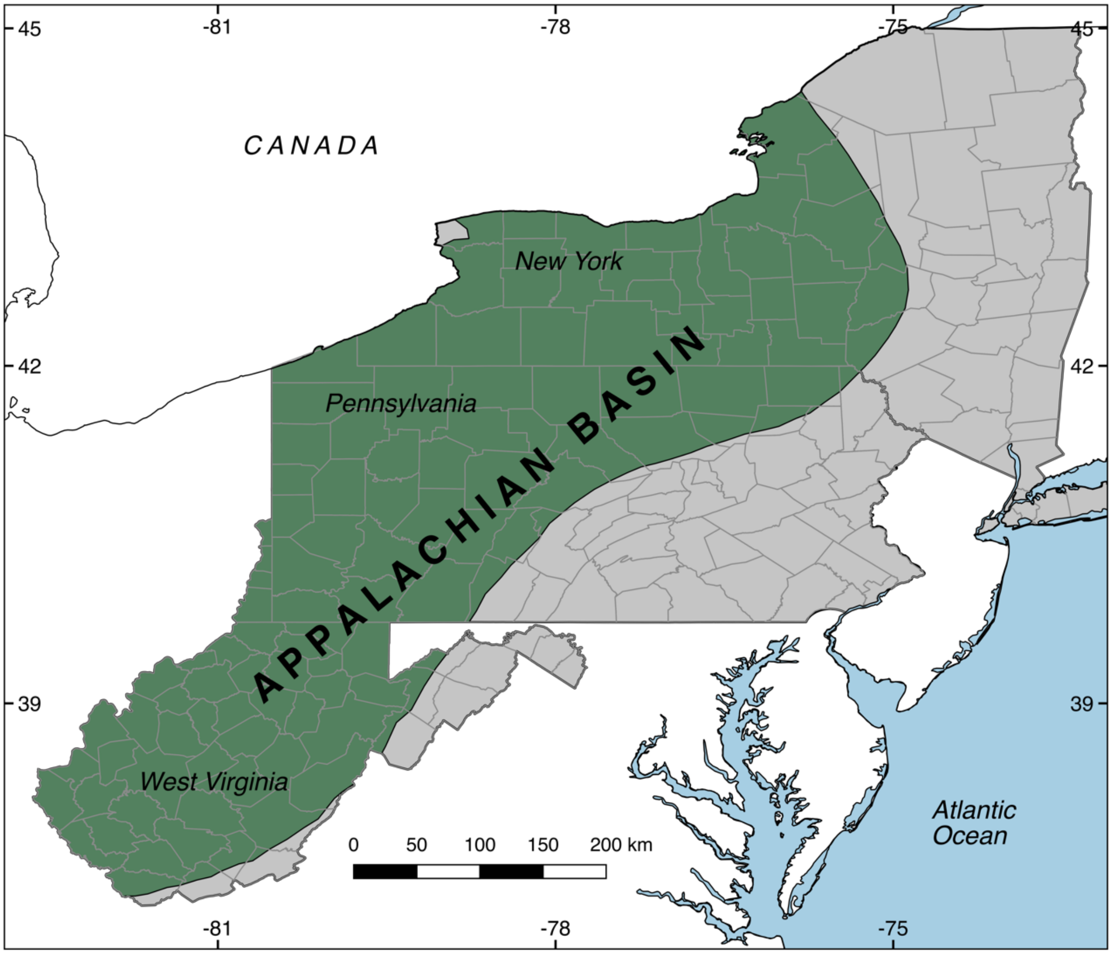

FIGURE 1.1. Study area of the Appalachian Basin within NY, PA, and WV, shown by green highlight. County boundaries are delineated by grey lines. Degrees latitude and longitude given at perimeter. Coordinate Reference System: WGS 84.

Traditional methods of locating geothermal reservoirs include costly methods such as seismic reflection surveys and slimhole drilling, which create a financial barrier to entry at the exploration stage for geothermal projects. This study presents an alternative lower-cost exploration approach that repurposes hydrocarbon industry subsurface data to identify low-risk, high-favorability reservoirs that have the potential to be repurposed as geothermal reservoirs. A case study of this methodology is applied to a three-state region in the Appalachian Basin of the eastern United States, including New York (NY), Pennsylvania (PA), and West Virginia (WV) (Figure 1). The Appalachian Basin represents an important location for geothermal resource assessment, given its large spatial coverage, high population, reliance on fossil-fuel energy sources, and geothermal resources. To date, there are no deep (> 1 km) geothermal energy systems in this region, despite the presence of cities including Buffalo, NY, Pittsburgh, PA, and Charlestown, WV. Co-location of the produced geothermal hot water with end-users of the heat is an important component for low-temperature geothermal systems.

Numerous studies have shown that the sedimentary Appalachian Basin of the eastern United States can provide low-enthalpy (<100°C) geothermal resources at economic depths (< 4 km) (e.g. Black, 1979; Hendry et al., 1982; Hodge and Fromm, 1984; Hodge, 1996; Blackwell et al., 2011; Jordan et al., 2015; Stutz et al., 2015). However, reservoir analyses of the study area have been limited to Cambrian sandstone reservoirs (541–485 mya) below New York (e.g. Pferd, 1981; Krakow and Lombard, 1983; Lynch and Castor, 1983), excluding any reservoirs beneath PA and WV, or those shallower than Cambrian formations. Pferd (1981) looked at wireline logs and bottom hole temperatures from plugged and abandoned hydrocarbon wells drilled into Cambrian formations, which he categorized as being hotter, thicker, and lower permeability than geothermal reservoirs developed in France and Canada. Both Lynch and Castor (1983) and Krakow and Lombard (1983) exclusively analyzed the Cambrian Potsdam and Galway (“Theresa”) Formations, which they concluded have satisfactory temperature, porosity, and permeability to be geothermal reservoirs. This study aims to provide a more comprehensive reservoir analysis of the Appalachian Basin, expanding into Pennsylvania and West Virginia, and the remainder of the stratigraphic column. Unconventional shale reservoirs, such as the Marcellus Shale and Utica Shale that have undergone high volume hydraulic fracturing to produce natural gas, are excluded from this study. The analysis of reservoir quality presented here is part of a more comprehensive assessment of the potential for geothermal heat extraction from the Appalachian Basin (Jordan et al., 2015), therefore this report excludes thermal quality. However, reservoir quality results similar to those presented below can be integrated with thermal quality assessments to identify high potential locations for geothermal development.

A major goal of this study is to quantify the favorability of the potential geothermal reservoirs using publicly available reservoir parameter data. In the Appalachian Basin, publicly available hydrocarbon reservoir data are low cost and have great breadth, though are not aggregated across state boundaries. Averaged reservoir data (e.g. average porosity, average thickness, average depth) are available via well logs for all known hydrocarbon reservoirs in our study area.

The metrics chosen to quantify reservoir favorability, and the associated uncertainty, are Reservoir Productivity Index (RPI) and Reservoir Flow Capacity (RFC). The RPI or well productivity index (PI) is used often by petroleum engineers and hydrologists to quantify the flow of a fluid from a reservoir. The PI is defined as the volumetric flow rate of a well divided by the pressure drop from the reservoir to the producing well:

$$RPI = PI = \frac{Q}{\Delta P} = \frac{2\pi kH}{\mu ln\frac{D}{r_w}} * C \qquad (1.1)$$

where RPI is in units of kg/MPa-s. Q is mass flow rate (kg/s), ΔP is the pressure drop from the reservoir edge to the production well (Pa), k is permeability (m^2), H is vertical reservoir thickness (m), μ is the fluid viscosity (Pa-s), D is the distance between the production well and the reservoir pressure boundary (m), and r_w is the wellbore radius (m) (e.g. Craft and Hawkins, 1959; Dietz, 1965; Gringarten, 1978). Finally, C is the conversion factor from m^3 to kg based on the fluid in the system. Equation 1.1 assumes that the reservoir is a homogeneous porous medium with horizontal intergranular flow.

PI has also been used to characterize the productivity of a well doublet for geothermal reservoirs, for both EGS reservoirs and sedimentary aquifer reservoirs, in which the PI metric is adapted by adjusting the parameter D to the distance between the geothermal injection and production wells (Gérard et al., 2006; Sanyal and Butler, 2009; Augustine, 2014; Cho et al., 2015; Hamm et al., 2016). According to Augustine (2014), the result is identical when adapting D to the distance between the injection and production well. For this study, we call this metric the Reservoir Productivity Index (RPI) and the input parameters are average reservoir values. A large pressure drop generally leads to lower flow rates and therefore a smaller RPI, unless k is a strong function of P, and requires more pumping costs to move the fluid through the reservoir. Typical RPI values for sedimentary geothermal reservoirs range between 20–300 kg/MPa-s (Sanyal and Butler, 2009).

A second favorability metric for reservoir flow capacity (RFC) considers only natural geologic qualities. This simple equation is comprised of only permeability, k in millidarcies (mD), and cumulative thickness of the permeable layers, H in meters:

$$RFC = kH \qquad (1.2)$$

The RFC, in units of mD-m (or m^3), is commonly used to describe flow in non-convective systems, like those in sedimentary aquifers with little vertical permeability. If a well in a sedimentary basin penetrates multiple sufficiently permeable layers within a formation, it can produce economic flow rates. Typical RFC values for sedimentary geothermal reservoirs range between 1,000–100,000 mD-m (or 9.9×10^{-13} to 9.9×10^{-11} m^3; Sanyal and Butler, 2009).

To quantify the uncertainty resulting from the limitations of using averaged data and/or singular values of reservoir properties, and from the inherent heterogeneity of the reservoirs, we propagate reservoir parametric inputs (i.e. permeability, thickness, fluid viscosity) within a probabilistic Monte Carlo simulation of the RPI and RFC. We input average subsurface data from the oil and gas industry and literature-derived estimates of average permeability, coupled with a user-defined uncertainty index to inform parametric distributions for individual reservoirs. Low-risk reservoirs are defined as having a high probability of high RPI or RFC and low uncertainty in terms of the coefficient of variation. The probabilistic results are displayed in a Geographic Information System (GIS) to identify locations of low-risk reservoirs. Finally, to test the assumptions used, the Monte Carlo Simulation results for four reservoirs were validated against their respective gas production volumes.

Methods

Database Compilation

Extensive reservoir data compilation was completed in the early 2000s for the purpose of carbon sequestration research through the Midwest Regional Carbon Sequestration Partnership (MRCSP; Blanco-Canqui et al., 2011). A GIS database from the MRCSP was available for use as a starting point for this project, courtesy of the West Virginia Geological and Economic Survey (WVGES). The dataset includes oil and gas reservoirs located in PA and WV, but does not include reservoirs in NY, due to NY state researchers joining MRCSP years later using a different methodology for characterizing CO2 sequestration. The MRCSP calculated potential storage volume for the reservoirs by using a volumetric analysis (porous space in the volume of rock). Therefore, the following reservoir parameters were included in the dataset: average reservoir production depth, reservoir name, formation code (geologic code for the producing formation; see Appendix A-1 for details), state, reservoir pressure, average porosity, net pay thickness, and shapefiles of the aerial extent of the reservoirs (polygons).

The reservoir information in NY was accessed through the Empire State Organized Geologic Information System (ESOGIS; New York State Museum, 2014) online database. Because the ESOGIS database does not organize their data by reservoir but rather by well, extra compilation efforts were required for reservoirs in New York. The available digital well data from ESOGIS included well total vertical depth (TVD), producing formation, field name, surface latitude, and surface longitude. To reorganize the NY well data into their respective reservoirs, well surface latitudes and longitudes were downloaded and uploaded into QGIS™ software, and grouped by reservoir using the "Field Name" option. To create GIS polygons for each reservoir similar to those in the database for PA and WV, we used the QGIS buffer zone tool to create polygons around wells that pertain to a given reservoir (Appendix A-1). Because porosity data were unavailable for reservoirs in NY, reservoirs were grouped by producing formation, and average porosity values were taken from literature that described formation quality based on wireline logs or core porosity tests (Appendix A-1). Reservoir thickness data were extracted manually from downloaded well completion reports from the ESOGIS database. For each reservoir, thicknesses from each producing well were averaged to calculate a mean thickness for the reservoir.

Neither the MRCSP nor ESOGIS database contain information about reservoir permeability, which is the most important parameter for estimating reservoir favorability. Furthermore, the ESOGIS database does not contain porosity data. To address these data limitations, reservoirs from all three states were first grouped by producing formation. For reservoirs in PA and WV, average permeability values were assigned to each reservoir using empirical relationships with reported average porosity; where empirical relationships were not available in literature, reservoirs were assigned average permeability values found in literature from core permeability tests or reservoir pumping tests, based on their producing formation. New York reservoirs did not have porosity data, so each reservoir was assigned an average permeability value from literature based on its producing formation (see Appendix A-1 for more details).

Reservoir Favorability

Reservoir favorability metrics were chosen based on the available parameter constraints: permeability, thickness (hydrocarbon pay thickness), and depth. Two metrics were ultimately chosen to estimate reservoir favorability in the Monte Carlo simulation: Reservoir Productivity Index (RPI) to quantify potential fluid production from each reservoir under conditions imposed by well-field design and management, and Reservoir Flow Capacity (RFC) to compare reservoirs based on their natural geologic qualities alone.

The RPI analysis was repeated for two types of fluid that could be used in the subsurface geothermal system. Liquid water (RPI_w) and supercritical carbon dioxide (RPI_c) were chosen as the two working fluid options for this regional study of reservoirs in the Appalachian Basin. Additionally, an RPI analysis was conducted using natural gas as the working fluid (RPI_g) on four reservoirs to enable an empirical validation of the RPI metric, described below (Page 18). Mass flow rate (kg/s) was used instead of volumetric flow rate in Equation 1, given that RPI is calculated for both an incompressible liquid (RPI_w) and a compressible gas (RPI_c) as the working fluids. The differences between the RPI_w and RPI_c are the respective inputs for fluid viscosity and average reservoir permeability. The RPI equations assume single-phase flow for both cases, neglecting residual fluids in the reservoir, which may include some combination of water, gas, and oil.

The viscosity of water varies as a function of temperature; therefore, water viscosity was assigned based on the predicted temperature at the center depth of each reservoir using the results from Smith (2015). The dynamic viscosity of water (Engineering Toolbox, 2015) was discretized into bins of ten degrees (Table 1.1). Salinity data were not available for the viscosity analysis. Pferd (1981) noted that Appalachian Basin formations have a higher concentration of dissolved solids than comparable basins with geothermal development, therefore future analyses should incorporate the effect of fluid chemistry on viscosity.

TABLE 1.1. Dynamic viscosity of water as a function of temperature. Temperatures are categorized in 10° increments (Engineering Toolbox, 2015).

Temperature (°C)	Viscosity, water (Pa-s)
10-19.99	0.00150
20–29.99	0.000900
30–39.99	0.000726
40–49.99	0.000600
50–59.99	0.000507
60–69.99	0.000436
70–79.99	0.000380
80–89.99	0.000335
90–99.99	0.000299

Note: Temperature increments stop at 99°C because mean reservoir temperatures in the basin do not exceed that temperature.

Data for dynamic viscosity of sCO_2 (Ouyang, 2011), which is a function of both temperature and pressure, are discretized into bins of ten degrees (Table 1.2). The assumed pressure of the injected sCO_2 was 15 MPa. The 438 reservoirs with a temperature lower than 40 °C were omitted from the RPI_c analysis, as the fluid cannot sustain a supercritical state below that temperature.

TABLE 1.2. Dynamic viscosity of sCO_2 as a function of temperature at a constant pressure of 15 MPa (Ouyang, 2011).

Temperature (°C)	Viscosity, CO_2 (Pa-s)
10-19.99	*n/a*
20–29.99	*n/a*
30–39.99	*n/a*
40–49.99	0.00006
50–59.99	0.00005
60–69.99	0.00004
70–79.99	0.000035
80–89.99	0.00003
90+	0.000025

Note: *Below a temperature of about 40 °C and pressure below 10 MPa, the carbon dioxide is no longer in a supercritical state; those reservoirs were omitted from the* RPI_c *simulation.*

Most core permeability measurements are measured in a laboratory using a gas (typically nitrogen) as the fluid that flows through the rock sample. Use of the gas permeability measurements (k_g) is acceptable when estimating the flow of a gas through a reservoir rock, but not when estimating the flow of liquid water through the rock, which is the typical fluid used in geothermal systems. In the case of RPI_c, the gas permeability was retained because the viscosity of sCO_2 is much like that of a gas (Brown, 2000; Pruess, 2007). However, for RPI_w the gas permeability was corrected for the difference between gas permeability and water permeability, or the Klinkenberg effect. This correction is more important for low permeability rocks than high permeability rocks (Tanikawa and Shimamoto, 2006). Because most reservoirs in the Appalachian Basin are of low permeability, this is an important step for the RPI_w calculations.

Corrections were applied to all reservoirs based on the reservoir's primary lithology. For carbonate reservoirs, the following empirical correlation from Al-Jabri et al. (2015) was applied,

$$k_w = 0.578{k_g}^{1.097} \qquad (1.3)$$

where k_w is the permeability of the rock with water, and k_g is the permeability of the rock with gas, both in units of millidarcies (mD). The constant of 0.578 carries units of mD$^{-0.097}$. The above correlation was derived from 175 permeability measurements on a fractured, vuggy limestone from cores taken from various gas reservoirs (Al-Jabri et al., 2015). Klinkenberg-corrected permeability was estimated from four measurements at different mean pressures, extrapolated to infinite mean pressure. For all other lithologies, the following empirical correlation based on the methodology Klinkenberg (1941) was used, where p is the mean flowing pressure in psi, b is the Klinkenberg slip factor for a particular gas type in a given rock in units of psi, and k_w *and* k_g have units of mD:

$$k_w = \frac{k_g}{1+\frac{b}{p}}; \qquad (1.4)$$

The Klinkenberg slip factor, *b,* has units of psi, though the equation for *b* that was used in this analysis does not directly yield units of psi. To determine *b,* Jones (1987) noted a highly correlated (R^2 of 0.90) relationship between $\frac{1}{b}$ and $\sqrt{\frac{k}{\phi}}$. That relationship is shown below, with porosity ϕ as a decimal fraction, and k_g in mD:

$$b = 15.61\left(\frac{k_g}{\phi}\right)^{-0.447} \qquad (1.5)$$

In the above equation, the constant 15.61 carries units of psi-mD$^{0.447}$.

Monte Carlo Simulation

An important piece of this project is the quantification of uncertainty in reservoir data, and its propagation into the uncertainty of the calculated RFC, RPI_c and RPI_w for each reservoir in the basin. In order to calculate the range of possible outcomes (RFC, RPI_c and RPI_w) for each reservoir, we performed a Monte Carlo simulation on all three metrics for the 1894 reservoirs in the basin.

After the compilation of the average reservoir parameter values (viscosity, permeability, and thickness), standard deviations and probability distributions (e.g. normal, log-normal, triangular) were assigned to each parameter of each reservoir. Wellbore radius and the distance between the injection and production well were held as constants in the RPI equation, at 0.1 m and 1000 m respectively.

To maintain consistency during the assignment of standard deviations, we created a simple and systematic Uncertainty Index that ranges from 0 (no uncertainty) to 5 (most uncertain). Those numbers (0, 1, …, 5) correspond to the standard deviation for reservoir thickness, permeability, and viscosity (Table 1.3). Indices were assigned to each parameter for all reservoirs in the database, but the way in which uncertainty indices were assigned differed for each parameter. The uncertainty of the mean viscosity was assigned using the standard deviation of the mean reservoir temperature (Smith, 2015), coupled with the water viscosity-temperature curve (Engineering Toolbox; Table 1.4) to determine the effect of temperature variation on fluid viscosity. Because the viscosity of water varies more at lower temperatures than at higher ones, the assignment of uncertainty differed depending on whether the mean reservoir temperature was below or above 50 °C. For example, a reservoir that has a temperature of 54 °C and a standard deviation of 6 °C is highly likely to have a temperature between 48–60 °C. That yields a one standard deviation range in viscosity of 0.00047–0.00059 Pa-s, or approximately 0.00053 ± 0.00006. That equates to a standard deviation of 11.3% from the mean, which was rounded to the nearest fifth percentage, in this case 10%. Five-percent increments were used for the viscosity Uncertainty Index, from 5% to 25%, guided by the possible variation in the temperature data.

For reservoirs in the state of New York, the population of average thickness for all producing wells in each reservoir enabled calculation of the standard deviation for each reservoir. The standard deviation was rounded to the nearest tens place to serve as increments for the thickness Uncertainty Index (i.e. 20%, 40%, 60%, 80%, or 100%). For reservoirs in Pennsylvania and West Virginia, thickness populations were not available; therefore, a moderate standard deviation of 60% of the mean thicknesses of reservoirs in New York was assigned to all reservoirs in those two states.

Because our permeability data were manually input from various sources, those standard deviation assignments were selected qualitatively based on the source and quality of the data from which the average permeability value was derived (Table 1.5). For example, permeability data that was calculated from a published empirical porosity-permeability relationship for the respective geologic formation and region was assigned an uncertainty factor of 2, equating to one standard deviation of 25% (Table 1.4). Alternatively, an average permeability value of a similar but different geologic formation was assigned an Uncertainty Index of 4, equating to one standard deviation of 100% (Table 1.4). Increments were chosen as 12.5%, 25%, 50%, 100%, and 200% based on typical variations of permeability across broad geologic formations due to heterogeneity (Murtha, 1994; Satter, 2008). This coupling of data quality and heterogeneity in the Monte Carlo addresses multiple sources of uncertainty in the estimation of reservoir permeability.

Finally, each parameter was assigned a probability distribution type for the Monte Carlo simulation (Table 1.3). Distribution types were determined based on reservoir engineering and modeling best practices and literature. More details on how the uncertainty indices were assigned can be found in the Appendix.

TABLE 1.3. Uncertainty Index reference chart for each parameter in the Monte Carlo simulation. The index numbers correspond to the amount of one standard deviation, measured in percentage of the mean value, for each parameter (i.e. a mean reservoir permeability value of 10 mD with an Uncertainty Index of 3 has a standard deviation of 50%, or 5 mD).

Uncertainty Index	**Standard Deviation**		
	Permeability	**Thickness**	**Viscosity**
	k	H	μ
0	± 0%	± 0%	± 0%
1	± 12.5%	± 20%	± 5%
2	± 25%	± 40%	± 10%
3	± 50%	± 60%	± 15%
4	± 100%	± 80%	± 20%
5	± 200%	± 100%	± 25%
Probability Distribution	log-normal	triangular	normal
References	Murtha, 1994; Satter, 2008	Peters, 2012; SPE, 2001	Based on temperature data from Smith (2015)

TABLE 1.4. Uncertainty Index assignment criteria for viscosity standard deviation data (input), which is entirely dependent on mean reservoir temperature.

Standard Deviation from mean reservoir temperature	**Viscosity Uncertainty**	**Standard Deviation**

Mean reservoir temp. < 50 °C	Mean reservoir temp. ≥ 50 °C	**Level**	
n/a	1–4.9 °C	1	5%
1–4.9 °C	5–9.9 °C	2	10%
5–9.9 °C	10–19.9 °C	3	15%
10–19.9 °C	*n/a*	4	20%
n/a	*n/a*	5	25%

TABLE 1.5. Uncertainty Index assignment criteria for permeability data.

1	Data from a published empirical porosity-permeability relationship, applicable to the respective geologic formation and reservoir.
2	Data from a published empirical porosity-permeability relationship, applicable to the respective region and formation but not the respective reservoir.
3	Data from unpublished empirical porosity-permeability relationship, applicable to the respective geologic formation but not the respective reservoir, OR Data are a published or unpublished range of values or average value for the respective geologic formation and region.
4	Data comes from unpublished empirical porosity-permeability relationship, OR Data are a published or unpublished range of values or average value for a similar geologic formation in the respective region or the same formation located in another region
5	Generic low value (≤ 1 mD) assigned due to lack of available data

The Monte Carlo Simulation was developed in MatLab and included 100,000 repetitions for all three favorability metrics (RPI_c, RPI_w, and RFC) for each of the 1894 reservoirs in the Appalachian Basin. The simulations generated an empirical probability density function for each reservoir's predicted RPI_c, RPI_w, and RFC, using the assigned uncertainty indices and parameter probability distributions in Table 1.3. From those outputs, the 10^{th}, 50^{th} (median), and 90^{th} percentile results were retained.

The uncertainty of each reservoir's RPI_w, RPI_c, and RFC is illustrated as the coefficient of variation (CV), which is the ratio of the standard deviation to the mean (Jensen et al., 2000). A small CV is more favorable than a large CV, indicating that the possible variation, or uncertainty, is low relative to the mean. Using the CV allowed us to normalize the uncertainty of each reservoir's RFC and RPI by its 50th percentile output, therefore providing a fair comparison amongst all reservoirs in the basin.

Validation

After the analysis, the RPI model was validated against volumetric natural gas production rate data for four reservoirs in New York. The selected reservoirs are the Quackenbush Hill and Wilson Hollow reservoirs in the fractured Trenton–Black River hydrothermal dolomite play, the Quinlan Reef reservoir in the Onondaga Limestone, and the Bockhahn reservoir in the Galway Sandstone.

An additional RPI model was calculated for the validation analysis. The RPI of natural gas, or RPI_g, was calculated and compared to cumulative initial gas production flow rates from all wells in the reservoir. Initial gas production data, in thousands of cubic feet per day (mcf/d), were taken from well completion reports downloaded from the ESOGIS database. We acknowledge that production volumes may be strongly influenced by the original volume of hydrocarbons in place, but believe they may be a good first-order indicator of flow potential. The cumulative initial natural gas production flow rates (mcf/day) were converted to kilograms per second (kg/s) assuming the ideal gas law applied, assuming the produced gas was pure methane, and a conversion from days to seconds under the assumption that hydrocarbons flowed out of the reservoirs continuously over the course of the day. The final mass flow rates of methane were scaled for pressure drop using a range of 3 MPa ± 1 MPa (Agemar, 2014), which accounts for up to 1 MPa of parasitic pressure losses along the injection and production wellbores.

A Monte Carlo simulation was also run on the RPI_g to predict the range of possible outcomes, using raw average permeability values and published natural gas viscosity values according to the temperature and pressure of the reservoir (Gonzalez et al., 1970; Viswanathan, 2007; Stephan, 2013). Natural gas viscosity uncertainty indices were selected using the same method as for water viscosity, in that the standard deviation of the reservoir temperature determines the standard deviation of the viscosity. Results from the gas volume productivity validation were compared to the stochastic RPI_w and RPI_g values for the same reservoirs.

Results

The P50 RPI_w and P50 RPI_c of all the reservoirs in the Appalachian Basin span more than seven orders of magnitude, from 5.0×10^{-7} to 27.0 kg/MPa/s for RPI_w, and 1.0×10^{-5} to 149.0 kg/MPa/s for RPI_c (Figure 1.2). The distributions of RPI_w and RPI_c are roughly log-normal, though values of RPI_c are greater than RPI_w by approximately ten times. Furthermore, the modal peak of the RPI_c distribution is more muted and wider than that of RPI_w, with a greater concentration of reservoirs toward higher productivity values. Because of the wide range in RPI values across many orders of magnitude, favorability thresholds were selected logarithmically from a “best case” threshold of 10 kg/MPa/s and the EGS threshold of 1 kg/MPa/s (i.e. 10, 1, 0.1, 0.01).

Agemar et al. (2014) report that pressure drawdown for sedimentary geothermal systems typically range between 1-3 MPa. If we assume the greatest pressure drop of 3 MPa, and assume that 30 kg/s is the minimum mass flow rate acceptable for the water-based system, our RPI_w threshold for the reservoir which would not require EGS stimulation is approximately 10 kg/MPa-s. Reservoir enhancement techniques can improve productivity by six to nine times (Cladouhos et al., 2014; Cho et al., 2015), so reservoirs with an RPI_w as low as 1 kg/MPa-s may be suitable with EGS. The most favorable reservoirs were selected as those having either an RPI P50 greater than 1 kg/MPa/s, thereby including reservoirs that are suitable under EGS conditions, or an RFC P50 greater than 100 mD-m, combined with a respective CV lower than 0.5.

The thresholds for RPI_c as the working fluid were determined using the thresholds for RPI_w as a baseline, which were adjusted to normalize for the heat extracted. For direct use heat applications, the difference in required mass flow rate of sCO2 instead of water should only be related to the difference in heat capacity. Per Chen and Lundqvist (2006), the heat capacity of sCO2 is about 4 kJ/kg-K, assuming the CO_2 is maintained at a constant pressure of 10 MPa and an average reservoir temperature of 60 ºC. At equivalent temperatures, the heat capacity of water is 4.2 kJ/kg-K. These values are very close; therefore, the same thresholds were applied to RPI_c.

Figures 1.3 and 1.4 map the probabilistic results of the Monte Carlo simulations of the RPI_w and RPI_c of reservoirs in the Appalachian Basin. The reservoirs whose RPI equals or exceeds 10 kg/MPa/s (dark green) are most favorable for geothermal production; the next lower class with 1–10 kg/MPa/s could be favorable with EGS (light green); the least favorable reservoirs have RPI ≤ 0.0099 kg/MPa/s (red). With water as the geothermal fluid, ten reservoirs would be suitable for geothermal energy production without EGS (Figure 1.3), with a P50 RPI_w greater than or equal to 10 kg/MPa/s. With supercritical carbon dioxide as the geothermal fluid, that number increases to 27 reservoirs (Figure 1.4). From P50 (50th percentile scenario) to P90 (most optimistic scenario), the number of suitable reservoirs increases to 17 for a water-based system, and increases to 38 reservoirs for the sCO2 system.

The probabilistic results of the RFC are shown in Figure 1.5, also using a logarithmic threshold scheme based on the distribution of results in the study area (Figure 1.2). The green reservoirs in Figure 1.5 represent the top 6% of all reservoirs in the Appalachian Basin based on the geologic properties of permeability and thickness, for a total of 112 reservoirs across nine different formations in the basin.

Permeability has the strongest influence on the calculated RPI_w and RPI_c P50, spanning over seven orders of magnitude (Figure 1.6). Reservoir thickness has the next strongest influence on RPI_w, spanning over three orders of magnitude. Viscosity has the least influence on RPI_w and RPI_c P50, spanning two orders of magnitude for RPI_w and a factor of four for RPI_c. As expected based on Equation 1.1, viscosity is inversely proportional to productivity.

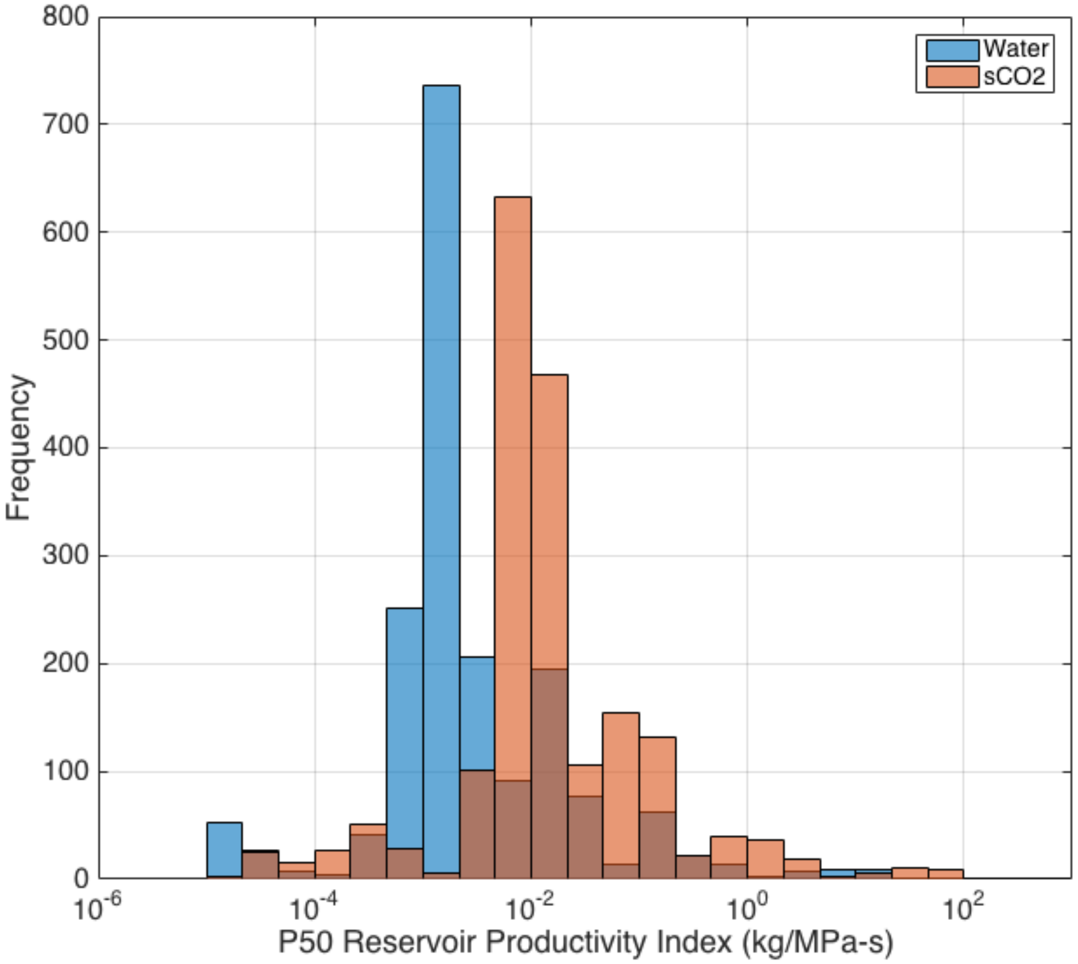

FIGURE 1.2. Histogram of P50 RPI_w (blue) and RPI_c (orange) frequencies in the Appalachian Basin; where colors overlap, they are displayed as brown. The distributions of RPI_w and RPI_c are similar in that their ranges span more than seven orders of magnitude, have one distinct peak, and are on average, very low. However, the modal peak and range of RPI_c is nearly ten times greater than that of RPI_w. Finally, the modal peak of RPI_c is more muted than that of RPI_w, shifting more reservoirs towards a higher RPI_c.

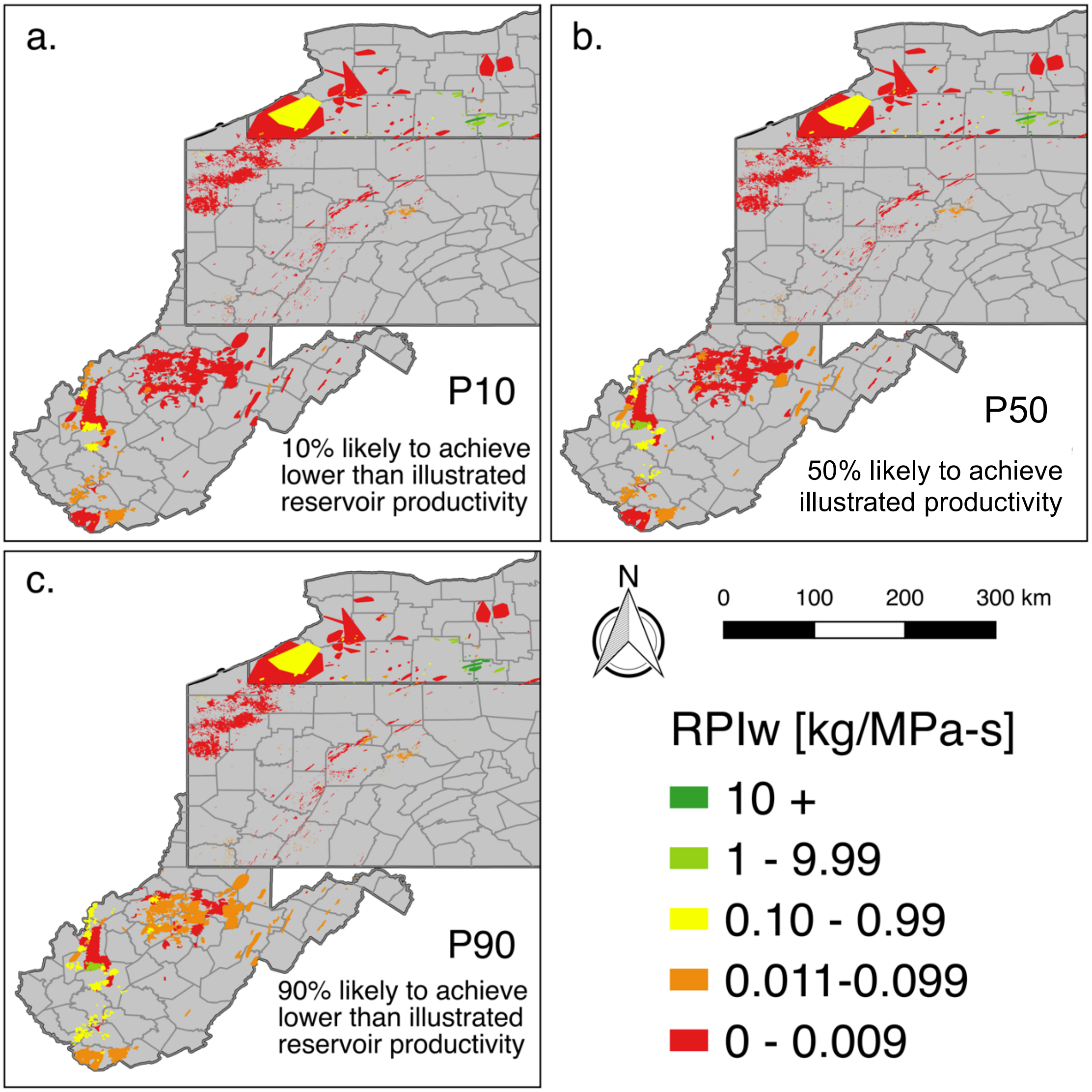

FIGURE 1.3. Probabilistic results of the Monte Carlo Simulation of the RPI_w for the case study area. The P10 (most conservative case; panel a), P50 (50th percentile; panel b), and P90 (most optimistic; panel c) expected results are shown. Reservoirs in dark green are most favorable, and red reservoirs are least favorable. In the P50 scenario, ten reservoirs (dark green in figure) are expected to be productive enough for geothermal production of hot water without EGS. From the P50 case to the P90 case, the number of suitable reservoirs increases to 17.

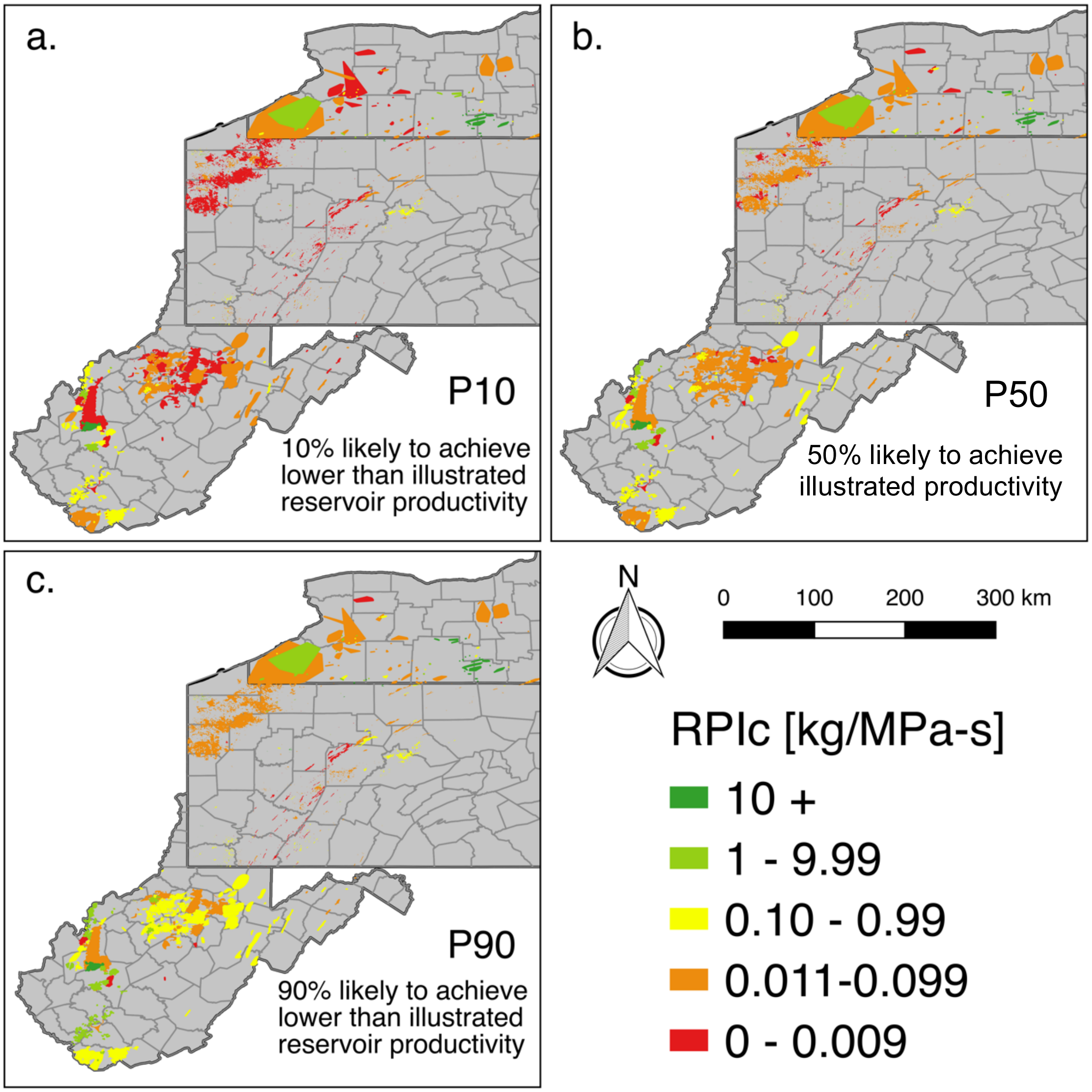

FIGURE 1.4. Probabilistic results of the Monte Carlo Simulation of the RPI$_c$ for the case study area. The P10 (most conservative case; panel a), P50 (50th percentile; panel b), and P90 (most optimistic case; panel c) expected results are shown. Reservoirs in dark green are most favorable, and red reservoirs are least favorable. In the P50 scenario, 27 reservoirs (dark green in figure) are expected to be productive enough for geothermal production without EGS. From the P50 case to the P90 case, the number of suitable reservoirs increases to 38.

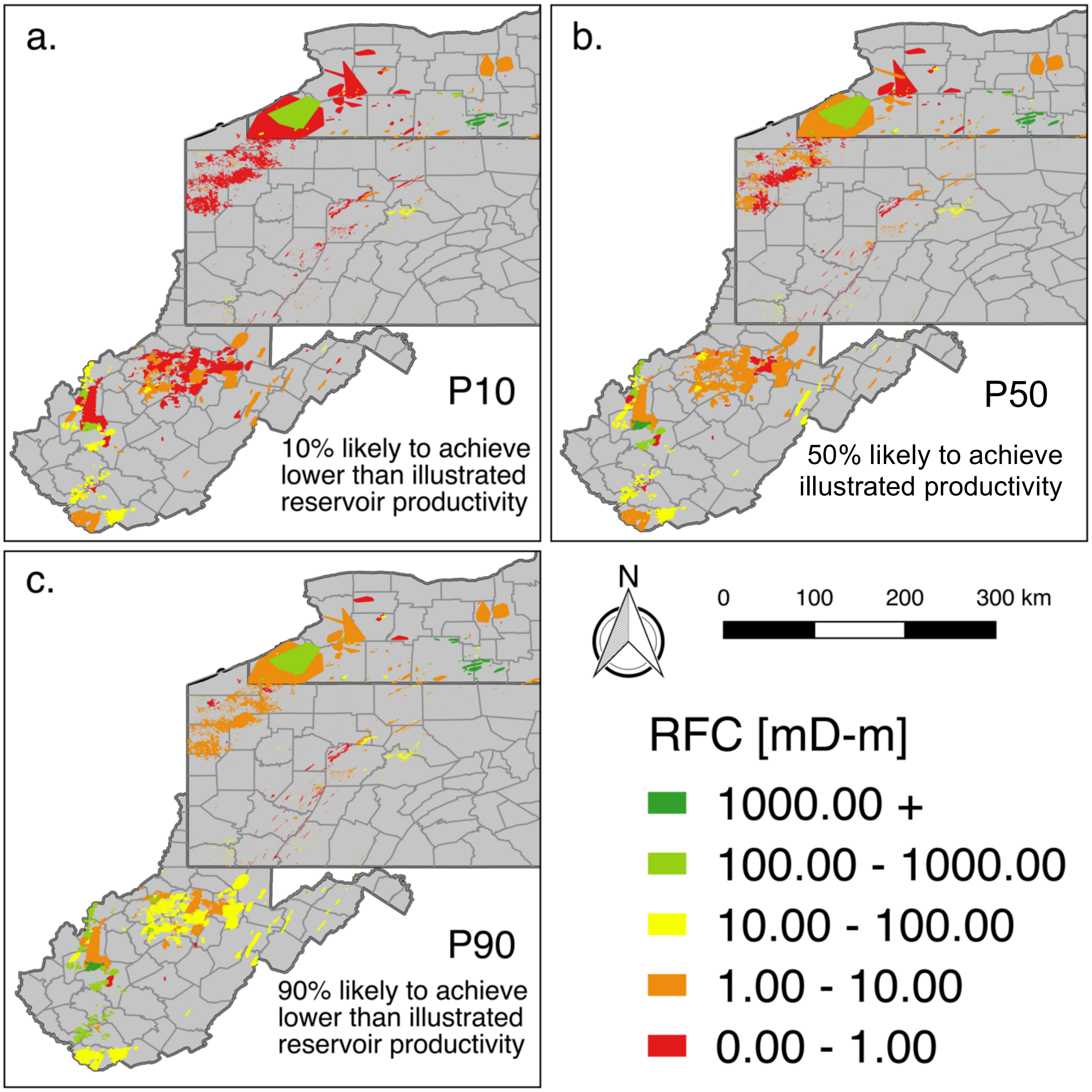

FIGURE 1.5. Probabilistic results of the Monte Carlo Simulation of the Reservoir Flow Capacity (RFC) for the case study area. The P10 (most conservative case; panel a), P50 (50th percentile; panel b), and P90 (most optimistic case; panel c) expected results are shown. Reservoirs in dark green have the most favorable geologic properties for geothermal flow, and red reservoirs have the least favorable properties. This metric compares the reservoirs based only on their geologic properties, without the influence of the chosen geothermal fluid. In the P50 case, the green and light green reservoirs represent the top 6% of reservoirs in the study area.

Figure 1.7 illustrates the uncertainty of the RPI_w, RPI_c, and RFC for each reservoir across the basin in terms of the CV. Dark red reservoirs indicate high-CV and high uncertainty relative to the P50 RPI, whereas light orange reservoirs have very low CV and low uncertainty relative to their P50 RPI. There are 821 reservoirs with a RPI_w CV lower than 0.5, 963 reservoirs with a RPI_c CV lower than 0.5, and 54 reservoirs with a RFC CV lower than 0.5. West Virginia has the highest concentration of high-CV reservoirs, whereas New York has the lowest concentration of high-CV reservoirs.

Of the reservoirs with the lowest uncertainty in the study area ($CV < 0.5$), there are a total of 28 reservoirs that meet criteria of RPI_w $P50 > 1$ kg/MPa/s, and 92 reservoirs that meet the criteria of RPI_c $P50 > 1$ kg/MPa/s (Figure 1.8; Table 1.6). These reservoirs are considered the lowest risk. Of the 92 low-risk RPI_c reservoirs, 21 are located in the Southern Tier of New York (Figure 1.8b), three are located in western West Virginia (Figure 1.8c), and 68 are located in various places in Pennsylvania (Figures 1.8b and 1.8c), though most are too small to be detected on the map scale.

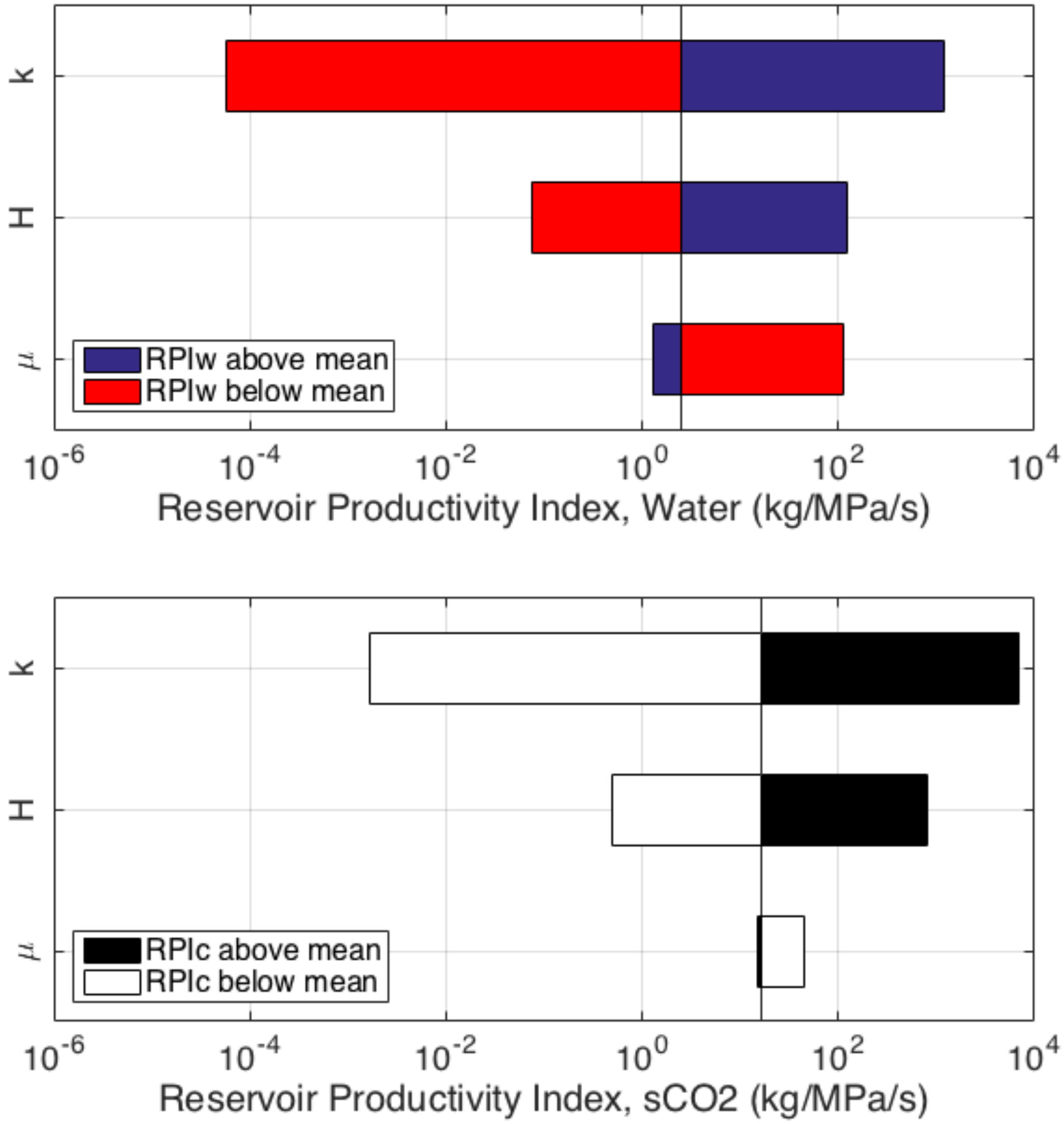

FIGURE 1.6. Tornado plot representing the sensitivity of RPI_w (above) and RPI_c (below) to the total observed ranges of the three variables, permeability, thickness, and viscosity, from the minimum to maximum value. The central line represents the mean RPI across all the reservoirs in the basin; bars to the right of the line show increases to RPI, and bars to the left show decreases to RPI. The mean RPI_c is 15.4 kg/MPa-s, 6.4 times greater than the mean RPI_w, which is 2.4 kg/MPa-s. The sensitivities of RPI_w and RPI_c to permeability and thickness are comparable; however, viscosity has a stronger impact on RPI_w than on RPI_c. As expected, viscosity is inversely proportional to RPI.

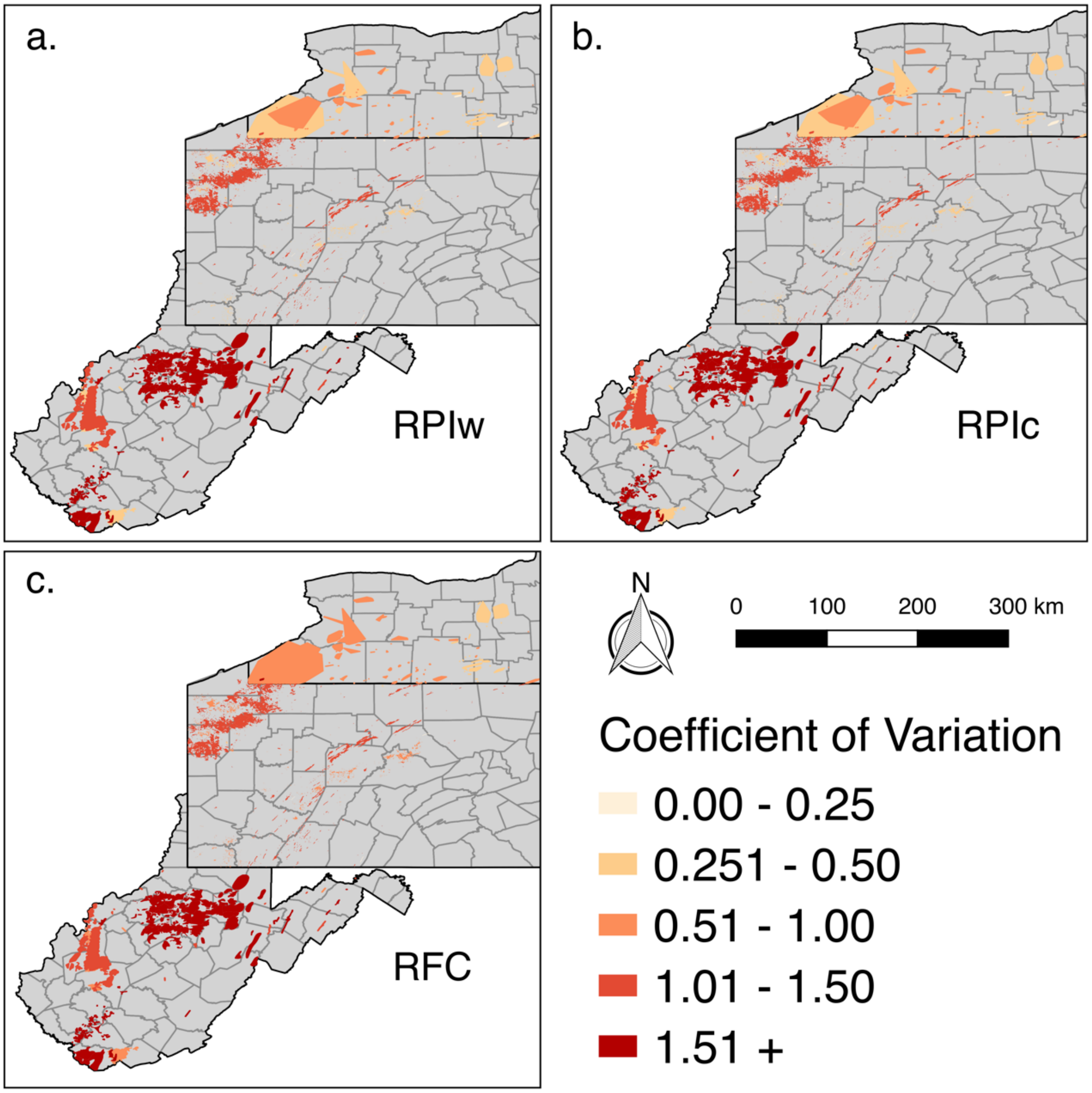

FIGURE 1.7. Maps of the coefficient of variation (CV) for RPI_w (panel a), RPI_c (panel b), and RFC (panel c). CV is the ratio of the standard deviation to the mean, used as a quantity reflecting uncertainty. Reservoirs with a lower CV are shown in light orange, and reservoirs with a higher CV are shown in red. Reservoirs with a lower CV have a lower standard deviation relative to their mean result, indicating lower uncertainty in the predicted outcome.

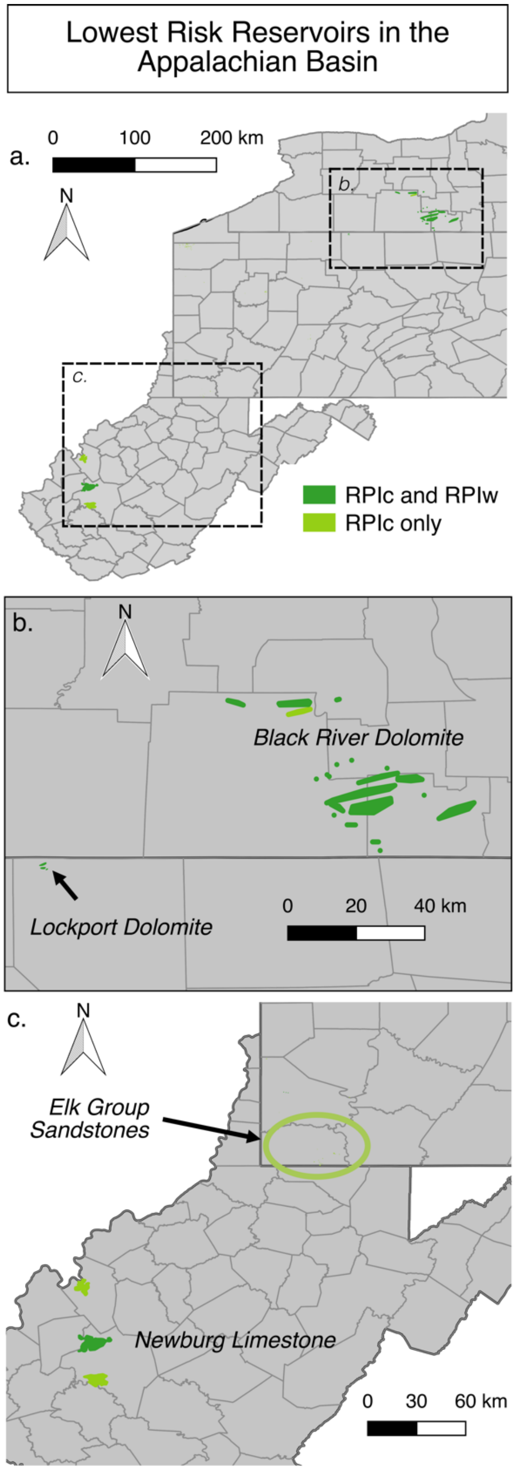

FIGURE 1.8. Reservoirs in the Appalachian Basin with an RPI greater than 1 kg/MPa/s and a CV lower than 0.5. Reservoirs for which this applies to both the RPI_w and RPI_c are shown in dark green, while reservoirs for which this applies only to RPI_c are shown in light green. The Elk Group Sandstone reservoirs shown by the lime green ellipse in panel c are too small to be detected at selected map scale. (Table 1.7)

TABLE 1.6. Low-risk reservoirs in the study area, with RPI > 1 kg/MPa-s and CV <0.5.

Note: RPI$_c$50 is the 50th percentile result of Reservoir Productivity Index for supercritical carbon dioxide, RPI$_c$CV is the unit-less Coefficient of Variation of the supercritical carbon dioxide Reservoir Productivity Index. The same applies to RPI$_w$p50 and RPI$_w$CV but for liquid water.

State	Reservoir Name	County	Latitude	Longitude	Formation Name	RPI$_c$P50 (kg/MPa-s)	RPI$_c$CV	RPI$_w$P50 (kg/MPa-s)	RPI$_w$CV
NY	Sunset Point	Yates	42.552546	-77.068452	Black River	19.69	0.45	4.10	0.48
NY	South Corning	Steuben	42.114345	-77.021775	Black River	59.93	0.37	11.43	0.37
NY	Laurel Run	Chemung	42.054748	-76.936965	Black River	76.75	0.17	14.00	0.17
NY	Pine Hill	Steuben	42.54207	-77.42663	Black River	16.46	0.45	3.42	0.48
NY	Glodes Corners Road	Steuben	42.539398	-77.220934	Black River	13.52	0.45	2.81	0.48
NY	Muck Farm	Steuben	42.509604	-77.203751	Black River	8.15	0.17	1.70	0.22
NY	Moreland	Schuyler	42.31251	-76.89656	Black River	21.65	0.29	3.95	0.29
NY	Sugar Hill	Schuyler	42.34034	-77.02043	Black River	45.36	0.29	9.26	0.29
NY	County Line	Steuben/ Chemung/ Schuyler	42.279283	-76.927766	Black River	44.95	0.29	8.57	0.29
NY	Terry Hill South	Chemung	42.275284	-76.817307	Black River	44.09	0.40	8.41	0.40
NY	Goundry Hill	Schuyler	42.325325	-77.072519	Black River	48.11	0.29	9.82	0.29
NY	McNutt Run	Steuben	42.28979	-77.10656	Black River	15.47	0.29	3.13	0.33
NY	Meads Creek	Schuyler	42.28352	-77.09912	Black River	47.77	0.29	9.75	0.29
NY	Seeley Creek	Chemung	42.02447	-76.92074	Black River	148.46	0.29	27.08	0.29
NY	Zimmer Hill	Steuben	42.27474	-77.14407	Black River	22.51	0.33	4.60	0.33
NY	Veteran Hill	Chemung	42.21804	-76.76679	Black River	42.47	0.29	8.10	0.29
NY	Wilson Hollow	Steuben/ Chemung	42.223379	-76.984964	Black River	82.48	0.29	15.72	0.29
NY	Langdon Hill	Chemung	42.16479	-76.651853	Black River	37.20	0.22	5.65	0.22

State	Reservoir Name	County	Latitude	Longitude	Formation Name	RPI$_c$P50 (kg/MPa-s)	RPI$_c$CV	RPI$_w$P50 (kg/MPa-s)	RPI$_w$CV
NY	Quackenbush Hill	Steuben/ Chemung	42.178211	-76.952613	Black River	55.68	0.29	8.46	0.29
NY	Cutler Creek	Steuben	42.176088	-77.071067	Black River	33.81	0.29	6.45	0.29
NY	Riverside	Steuben	42.14831	-77.08207	Black River	16.50	0.29	2.51	0.29
PA	HORTON	ELK	41.363235	-78.747217	Bass Islands	3.24	0.46	0.33	0.53
PA	FROGTOWN	CLARION	41.144671	-79.249301	Devonian Unconf.	6.86	0.46	0.68	0.46
PA	FROGTOWN	CLARION	41.177227	-79.250771	Devonian Unconf.	6.86	0.46	0.68	0.46
PA	FROGTOWN	CLARION	41.173708	-79.231209	Devonian Unconf.	6.86	0.46	0.68	0.46
PA	FROGTOWN	CLARION	41.191635	-79.236848	Devonian Unconf.	6.86	0.46	0.68	0.46
PA	BRADFORD	MCKEAN	41.872361	-78.617908	Galway	4.00	0.46	0.51	0.46
PA	SHARON CENTER	POTTER	41.958977	-78.087678	Lockport	82.55	0.22	14.10	0.22
PA	SHARON CENTER	POTTER	41.963183	-78.100958	Lockport	82.55	0.22	14.10	0.22
PA	SHARON CENTER	POTTER	41.97622	-78.100946	Lockport	82.55	0.22	14.10	0.22
PA	LORETTO	CAMBRIA	40.522776	-78.661957	Devonian Unconf.	1.09	0.46	0.09	0.46
PA	LORETTO	CAMBRIA	40.531123	-78.628173	Devonian Unconf.	1.09	0.46	0.13	0.46
PA	LORETTO	CAMBRIA	40.581405	-78.627885	Devonian Unconf.	1.09	0.46	0.13	0.46
PA	CANOE RIPPLE	CLARION	41.155301	-79.529924	Devonian Unconf.	7.77	0.46	0.76	0.53
PA	FIDDLERS RUN	CLARION	41.051393	-79.606397	Devonian Unconf.	6.86	0.46	0.81	0.46

State	Reservoir Name	County	Latitude	Longitude	Formation Name	RPI$_c$P50 (kg/MPa-s)	RPI$_c$CV	RPI$_w$P50 (kg/MPa-s)	RPI$_w$CV
PA	FORWARD	WASHINGTON	40.1967	-79.900858	Devonian Unconf.	8.29	0.40	0.56	0.46
PA	WOLF CREEK	MERCER	41.30597	-80.093967	Bass Islands	1.78	0.46	0.22	0.46
PA	CONNEAUT	CRAWFORD	41.816836	-80.385609	Black River	2.46	0.46	0.46	0.53
PA	CONNEAUT	CRAWFORD	41.820296	-80.427395	Black River	2.46	0.46	0.46	0.53
PA	CONNEAUT	CRAWFORD	41.789058	-80.426833	Black River	2.46	0.46	0.46	0.53
PA	CONNEAUT	CRAWFORD	41.827887	-80.440092	Black River	2.46	0.46	0.46	0.53
WV	North Ripley	JACKSON	38.880586	-81.754697	Newburg	4.60	0.40	0.50	0.46
WV	Rocky Fork	KANAWHA	38.489917	-81.687035	Newburg	17.71	0.40	1.62	0.46
WV	Kanawha Forest	BOONE	38.236778	-81.655436	Newburg	1.72	0.40	0.21	0.46
PA	MOSIER HILL	WASHINGTON	40.092517	-80.389193	Elk Group	3.29	0.46	0.35	0.46
PA	BUFFALO	WASHINGTON	40.228766	-80.326908	Devonian Unconf.	130.52	0.40	11.48	0.46
PA	BUFFALO	WASHINGTON	40.230822	-80.341131	Devonian Unconf.	130.52	0.40	11.48	0.46
PA	BUFFALO	WASHINGTON	40.233769	-80.357779	Devonian Unconf.	60.60	0.40	11.48	0.46
PA	Greeley	Greene	39.725522	-80.105102	Elk Group	2.17	0.46	0.19	0.46
PA	Grigsby	Greene	39.801828	-79.97111	Elk Group	1.84	0.46	0.16	0.46
PA	Kobys-Ertman	Crawford	41.76516	-80.265043	Galway	2.07	0.46	0.20	0.53
PA	Kobys-Ertman	Crawford	41.754158	-80.269834	Galway	2.07	0.46	0.20	0.53
PA	Kobys-Ertman	Crawford	41.833352	-80.383372	Galway	1.66	0.46	0.14	0.53
PA	Kobys-Ertman	Crawford	41.836632	-80.390903	Galway	1.66	0.46	0.17	0.53
PA	Kobys-Ertman	Crawford	41.825157	-80.38208	Galway	1.66	0.46	0.14	0.53

State	Reservoir Name	County	Latitude	Longitude	Formation Name	RPI_cP50 (kg/MPa-s)	RPI_cCV	RPI_wP50 (kg/MPa-s)	RPI_wCV
PA	Grigsby	Greene	39.804267	-79.999887	Elk Group	1.84	0.46	0.19	0.46
PA	Grigsby	Greene	39.808633	-80.008404	Elk Group	1.84	0.46	0.19	0.46
PA	Grigsby	Greene	39.799936	-80.007451	Elk Group	1.84	0.46	0.19	0.46
PA	Greeley	Greene	39.836903	-80.124344	Elk Group	2.17	0.46	0.19	0.46
PA	Greeley	Greene	39.7721	-80.086696	Elk Group	2.17	0.46	0.19	0.46
PA	Greeley	Greene	39.75974	-80.115189	Elk Group	2.17	0.46	0.19	0.46
PA	Greeley	Greene	39.738473	-80.100438	Elk Group	2.17	0.46	0.19	0.46
PA	Greeley	Greene	39.749484	-80.145671	Elk Group	2.17	0.46	0.19	0.46
PA	Kings Creek	Washington	40.464667	-80.477334	Onondaga	1.41	0.19	0.15	0.19
PA	Henlein	Mercer	41.389292	-80.350197	Galway	2.07	0.46	0.17	0.53
PA	Kobys-Ertman	Crawford	41.764909	-80.324027	Galway	2.07	0.46	0.23	0.53
PA	Kobys-Ertman	Crawford	41.77616	-80.315565	Galway	2.07	0.46	0.20	0.53
PA	Kobys-Ertman	Crawford	41.766344	-80.287745	Galway	2.07	0.46	0.20	0.53
PA	Kobys-Ertman	Crawford	41.772993	-80.276957	Galway	2.07	0.46	0.20	0.53
PA	Kobys-Ertman	Crawford	41.783785	-80.275489	Galway	2.07	0.46	0.23	0.53
PA	Kobys-Ertman	Crawford	41.792534	-80.26731	Galway	2.07	0.46	0.20	0.53
PA	Kobys-Ertman	Crawford	41.794491	-80.35202	Galway	1.66	0.46	0.20	0.53
PA	Rensma	Crawford	41.786478	-80.333216	Black River	2.46	0.46	0.63	0.53
PA	Kobys-Ertman	Crawford	41.798201	-80.332282	Galway	2.07	0.46	0.23	0.53
PA	Kobys-Ertman	Crawford	41.802587	-80.310609	Galway	2.07	0.46	0.23	0.53
PA	Kobys-Ertman	Crawford	41.792032	-80.308903	Galway	2.07	0.46	0.23	0.53
PA	Kobys-Ertman	Crawford	41.801266	-80.288495	Galway	2.07	0.46	0.20	0.53
PA	Kobys-Ertman	Crawford	41.807941	-80.28198	Galway	2.07	0.46	0.20	0.53

State	**Reservoir Name**	**County**	**Latitude**	**Longitude**	**Formation Name**	**RPI_cP50 (kg/MPa-s)**	**RPI_cCV**	**RPI_wP50 (kg/MPa-s)**	**RPI_wCV**
PA	Crossingville	Crawford	41.801642	-80.268245	Galway	2.07	0.46	0.20	0.53
PA	Kobys-Ertman	Crawford	41.813467	-80.351468	Galway	1.66	0.46	0.20	0.53
PA	Kobys-Ertman	Crawford	41.8119	-80.342613	Galway	1.66	0.46	0.20	0.53
PA	Kobys-Ertman	Crawford	41.819097	-80.33704	Galway	1.66	0.46	0.20	0.53
PA	Kobys-Ertman	Crawford	41.821489	-80.350231	Galway	2.07	0.46	0.20	0.53
PA	Kobys-Ertman	Crawford	41.825272	-80.320833	Galway	1.66	0.46	0.20	0.53
PA	Kobys-Ertman	Crawford	41.836869	-80.301674	Galway	2.07	0.46	0.20	0.53
PA	Crossingville	Crawford	41.824081	-80.252963	Galway	2.07	0.46	0.20	0.53
PA	Crossingville	Crawford	41.823067	-80.246815	Galway	2.07	0.46	0.20	0.53
PA	Crossingville	Crawford	41.830845	-80.232371	Galway	2.07	0.46	0.20	0.53
PA	Kobys-Ertman	Crawford	41.807216	-80.373126	Galway	1.66	0.46	0.17	0.53
PA	Kobys-Ertman	Crawford	41.836089	-80.331875	Galway	1.66	0.46	0.17	0.53
PA	Greeley	Greene	39.745842	-80.10948	Elk Group	2.17	0.46	0.23	0.46
PA	Greeley	Greene	39.734301	-80.089725	Elk Group	2.17	0.46	0.23	0.46

When gas production data were compared to the stochastic RPI_g and RPI_w predictions (Figure 1.9), gas volume productivity matches closely with the stochastic RPI_g result only for the Bockhahn reservoir (porous sandstone in the Galway Formation). For the Quackenbush Hill and Wilson Hollow (fractured dolostones in the Black River Formation), and the Quinlan Reef reservoir (reef limestone in the Onondaga Formation), gas volume productivity lies between the predicted RPI_w and RPI_g. For all three, RPI_g overestimates flow by about a factor of three.

Discussion

In the P50 scenario, both RPI_w and RPI_c are highly variable across the basin and, on average, below 1 kg/MP-s (Figures 1.2, 1.3, and 1.4). Among proven hydrocarbon reservoirs in the Appalachian Basin, 99.6% are of low quality (< 1 kg/MPa-s) for geothermal heat production with water as the traditional reservoir fluid. This conclusion was reached assuming a maximum of 3 MPa pressure drop and a minimum of 30 kg/s flow rate. The pressure drop could be increased to achieve higher flow rates, but higher pressures could be unstable and cause unwanted seismicity, or could result in higher parasitic losses. However, the distribution of RPI_c is about ten times greater than that of RPI_w, and there are 17 additional reservoir options available in the study area when considering the use of sCO_2 instead of water. Furthermore, assuming the implementation of EGS could increase productivity by up to an order of magnitude (RPI > 1 kg/MPa/s), 115 reservoirs are suitable for geothermal heat production using sCO_2, four times the number of reservoir options with water.

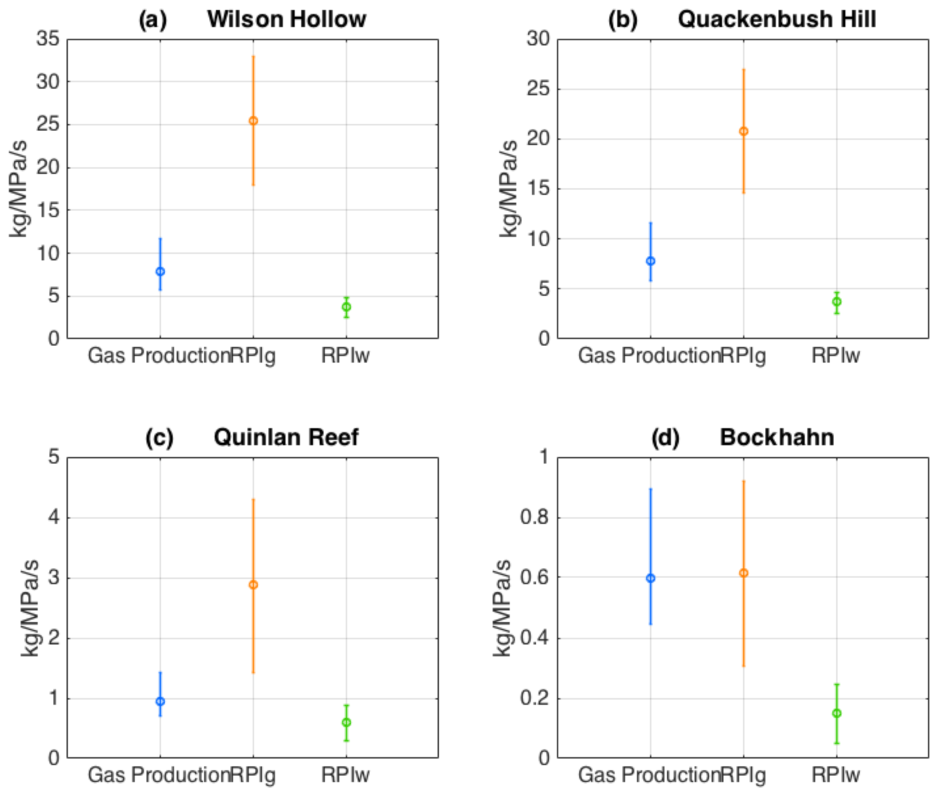

FIGURE 1.9. Results of RPI validation for the following reservoirs (a) Wilson Hollow and (b) Quackenbush Hill, which both currently produce gas from the Trenton–Black River hydrothermal dolomite; (c) Quinlan Reef, which produced gas from the Onondaga pinnacle reef limestone; and (d) Bockhahn, which currently produces gas from the Galway Sandstone Formation. In each panel, the gas production data are the blue open circle data point, which is the initial gas production (mcf/d) converted to kg/MPa/s using an average pressure drop of 3 MPa. Error bars represent drawdown of 2 and 4 MPa. The orange and green open circle data points are the results for RPI_g and RPI_w, with error bars representing one standard deviation from the Monte Carlo Simulation.

Lower uncertainty of the predicted RPI better constrains the expected or predicted productivity, thereby reducing financial risk for geothermal projects. Nearly half of the proven reservoirs in the Appalachian Basin have a low CV and therefore low uncertainty. However, low-CV reservoirs are not necessarily more ideal than high-CV reservoirs, as a reservoir with a small thickness could be very certain, while a very thick reservoir could have uncertainty. CV should therefore be coupled with absolute RPI when choosing optimal reservoirs. When high predicted productivity (greater than 1 kg/MPa-s for RPI_w or RPI_c) and low CV are combined to identify low-risk reservoirs for geothermal or EGS, 92 reservoirs are options if using sCO_2, whereas only 27 are options with water (Figure 1.8).

Lower uncertainty reservoirs are predominantly in New York, whereas higher uncertainty reservoirs are predominantly in West Virginia. This is because the data for many reservoirs in West Virginia is of lower quality than those for reservoirs in New York, and future work should address these data limitations. If better quality permeability data are collected for those high-CV reservoirs across the basin, uncertainty can be updated based on the heterogeneity of the reservoir permeability rather than on data quality.

A larger number of suitable reservoir options is advantageous for low-temperature geothermal systems that produce heat because of a higher likelihood that a suitable reservoir will be in close enough proximity to the users of heat. This implies that supercritical CO_2 is likely to be a better option for low-temperature geothermal systems where productivity is a high priority. This result is supported by work done by Atrens et al. (2010), who show mathematically that for shallow low-enthalpy geothermal systems, using sCO_2 instead of water as the reservoir fluid reduces wellbore pressure losses (while also creating a thermosiphon effect), and has only a marginal reduction in total exergy production at injection pressures under 15 MPa. Additionally, the uncertainty of RPI_c viscosity is 80% lower than the uncertainty of RPI_w (Figure 1.6) because supercritical carbon dioxide is less sensitive than water to changes in temperature it will encounter as it heats up within the reservoir. This results in less overall uncertainty of RPI when considering supercritical carbon dioxide instead of water. However, there are fluid management concerns that add complexity to the use of a supercritical fluid in the subsurface. First, supercritical CO_2 is sensitive to pressure changes in the reservoir, which were not considered in this study. Additionally, where there is still residual gas, oil, or brine left in a hydrocarbon reservoir, or in the case of phase separation of the CO_2, multiphase flow effects may decrease the potential productivity of the system. Therefore, careful management of fluids is necessary to ensure the system works in an optimal state. A nearby source of carbon dioxide, as well as surface pressurization equipment and additional energy to keep the fluid in a supercritical state are also required.

The RFC maps (Figure 1.5), which illuminate the favorable reservoirs based only on geologic properties of permeability and thickness, provide guidance for future exploration for suitable geothermal reservoirs that have not produced oil or gas. Table 1.7 summarizes the most favorable geologic formations in our study area, and the number of reservoirs that are known in each formation. These reservoirs all had a P50 RFC greater than 100 mD-m. In New York, the most geologically favorable geothermal reservoirs are those that have produced gas from the Trenton-Black River hydrothermal dolomite play. In West Virginia, the suitable geothermal reservoirs are those that produced gas from the Oriskany Sandstone and Newburg Limestone formations. The remaining suitable reservoirs are all located in Pennsylvania, but are much smaller in map view area than the previously mentioned reservoirs in NY and WV. The PA reservoirs which are most geologically favorable are located primarily in the following formations: Galway, Elk Group, and the Devonian Unconformity (Table 1.7).

TABLE 1.7. Geologic formations within which the highest geologic favorability reservoirs of the Appalachian Basin study area are located. These 112 reservoirs are those which had a P50 RFC greater than 100 mD-m.

State	Formation Name	Number of reservoirs
NY	Black River Dolomite	21
	Onondaga Limestone	11
	Galway Sandstone	2
	Bass Islands Formation	1
PA	Galway Sandstone	31
	Elk Group Sandstones	13
	Devonian Unconformity Play	10
	Black River Limestone	5
	Lockport Dolomite	3
	Onondaga Limestone	2
	Bass Islands Formation	2
WV	Oriskany Sandstone	7
	Newburg Limestone	4

Gas production volumes validate the use of the RPI metric as an estimate of productivity in porous reservoirs with intergranular flow characteristics, such as the Bockhahn sandstone (Figure 1.9). However, RPI is a poor predictor of productivity for fractured or vuggy reservoirs, such as the Black River and Onondaga Reef limestones. RPI overpredicts productivity by a factor of three for the fractured and vuggy Wilson

Hollow and Quackenbush reservoirs, and the vuggy Quinlan Reef reservoir, indicating that the productivity of all fractured and/or vuggy reservoirs in the basin have been slightly overestimated in this analysis. Furthermore, based on the validation approach utilized in this study, the use of the RPI metric is not recommended for reservoirs that do not exhibit porous, intergranular flow properties. Directly measured permeability data are often unavailable, as was the case in this study, despite being the most important variable to quantify productivity (Figure 1.6). Alternatively, high-resolution initial hydrocarbon production data can be used as a means for predicting or constraining permeability estimates in porous, non-fractured reservoirs.

The productivity and uncertainty maps display that only about 30% of the basin study area offer data with which to assess potential reservoir productivity. Two primary factors limit reservoir coverage when using hydrocarbon reservoirs as potential geothermal reservoirs. First, conventional oil and gas reservoirs are inherently not laterally extensive across a basin due to variations in porosity, sources and seals. Second, many reservoirs overlap each other in a two-dimensional GIS because they are indeed ‘stacked’ at various depths in the subsurface. Nevertheless, in a low-temperature geothermal analysis, absolute areal coverage of reservoirs in a basin is less important than the colocation of suitable reservoirs with population centers or other users of heat (Jordan et al., 2015).

A drawback to the re-utilization of data from oil and gas reservoirs in this way is that other candidate reservoirs may exist in the basin, but are ignored because they did not produce sufficient hydrocarbons, or simply have not been sufficiently explored due to an assumed lack of hydrocarbon production potential. Therefore, recommended future work includes an assessment of formations that were drilled for hydrocarbons but did not produce economic volumes of oil or gas. A second approach is the use of published geological analysis products such as paleogeographic maps, facies predictions, and tectonic analyses to target regions in which favorable formations (Table 1.7) are likely to bear similarly suitable properties and high geothermal gradients. Because the best options for geothermal reservoirs tend to be within a small set of geologic formations (Table 1.7), these results can be used to inform more widespread geothermal reservoir analysis outside the context of petroleum reservoir data. The objective of either exploration approach would be to show the geographic presence of reservoir porosity filled by formation waters instead of hydrocarbons, which could be well suited for geothermal energy production. These proposed future studies could be prioritized to address the issues of colocation with interested consumers and with favorable thermal attributes. In any region of interest, the depth and temperature at which these formations lie would strongly influence a decision to invest resources in acquisition of data needed to assess the local capacity of these reservoirs.

Conclusions

This study presents a pre-drilling analysis applicable to sedimentary basins to probabilistically identify potential geothermal reservoirs in a Geographic Information System. System properties were quantified for the Appalachian Basin to locate reservoirs that have high productivity potential and lower uncertainty, thereby reducing geothermal project risk. Based on the data analyzed, very few (0.4%) of the hydrocarbon reservoirs examined in the Appalachian Basin study area are of suitable quality for commercially attractive geothermal heat production. Seventeen additional hydrocarbon reservoirs are suitable for geothermal energy extraction when supercritical CO_2 is considered instead of water, and 88 more hydrocarbon reservoirs are suitable options if EGS is employed to improve productivity. A Reservoir Productivity Index was shown to be an accurate way to estimate productivity for only porous medium reservoirs, as validated by initial gas production data. Additionally, in the absence of permeability data, initial gas production data may be a useful tool for estimating average permeability in porous media reservoirs. However, the use of an alternate productivity prediction metric for fractured or vuggy reservoirs is recommended.

In the low-temperature Appalachian Basin, supercritical CO_2 has potential benefits over water as the subsurface geothermal fluid. First, productivity values are nearly ten times that of water, which would lead to a greater amount of heat extracted from the reservoir. Second, the variability in the viscosity of sCO_2 is one third that of water, which could further reduce the uncertainty of a geothermal project's performance. Third, the increase in number of suitable reservoir options with sCO_2 as the chosen geothermal fluid creates a higher likelihood that reservoirs will be located near enough to end-users of the heat. Finally, there is the potential to slowly sequester the CO_2 in a system that gives a secondary application for greenhouse gas mitigation. However, there are both surface and subsurface issues associated with using sCO_2 as a geothermal fluid, including multi-phase flow, leakage issues, and pressurization requirements. Though there are currently no geothermal systems utilizing sCO_2, in theory the productivity of fluid flow using sCO2 would be greater than that of water for low-temperature, low-permeability sedimentary systems.

Acknowledgements

The information, data, or work presented herein was funded in part by the Office of Energy Efficiency and Renewable Energy (EERE), U.S. Department of Energy (DOE), under Award Number DE- DE-EE0006726. In addition, the National Science Foundation IGERT Earth Energy program and the Cornell Energy Institute provided partial support for the study. The authors are grateful for the technical guidance that was provided by staff at the DOE Geothermal Technologies Office through this project. Additionally, Xiaoning He, Kelydra Welcker, Zachary Frone, Sophie Fructer, Hannah Lang, and Tasnuva "Ming" Khan are thanked for their data collection, organization, and processing efforts. In addition, Eve Sprunt, Dick Benoit, Janell Edman, technical reviewers to the DOE project, also provided valuable feedback. Koenraad Beckers, Don Fox, and Jefferson Tester of the Cornell Energy Institute provided critical technical advice as well. We thank the staffs of the state geological surveys of New York, Pennsylvania, and West Virginia for their collaboration, generous data contributions, and assistance, specifically Kristin Carter and Michelle Cooney (PA), Brian Slater (NY), and Jessica Moore (WV).

REFERENCES

Agemar, T., Weber, J., and Schulz, R., 2014, Deep geothermal energy production in Germany: Energies, v. 7, no. 7, p. 4397-4416.

Al-Jabri, R.A., Al-Maamari, R.S., and Wilson, O.B., 2015, Klinkenberg-corrected gas permeability correlation for Shuaiba carbonate formation: Journal of Petroleum Science and Engineering, v. 131, p. 172-176.

Atrens, A., Gurgenci, H., and Rudolph, V., 2010, Electricity generation using a carbon dioxide thermosiphon: Geothermics, v. 39, p. 161-169.

Augustine, C., 2014, Analysis of Sedimentary Geothermal Systems Using an Analytical Reservoir Model*, in* Proceedings, Geothermal: A Global Solution: Davis, CA, 641-647.

Barbacki, A., 2000, The use of abandoned oil and gas wells in Poland for recovering geothermal heat*,* Proceedings, Proceedings World Geothermal Congress, 3361-3365.

Black, R., 1979, Geothermal Energy and the Eastern U.S.: United States Department of Energy, 299 p.

Blackwell, D., Richards, M., Frone, Z., Ruzo, A., Dingwall, R., and Williams, M., 2011, Temperature-at-depth maps for the conterminous US and geothermal resource estimates: Geothermal Resource Council Transactions, v. 35, p. 1545-1550.

Blanco-Canqui, H., Chatterjee, A., Christopher, S.F., Eastman, C., Elder, K., Mishra, U., Mukundan, R., Stavi, I., and Swank, B., 2011, Midwest Regional Carbon Sequestration Partnership.

Bohlen, K., 2013, Pre-Exploration Geothermal Resource Assessment for the Raton Basin, Colorado – The rest of the story: GRC Transactions, v. 37, p. 933-940.

Brown, D.W., 2000, A hot dry rock geothermal energy concept utilizing supercritical CO2 instead of water Proceedings, Proceedings of the twenty-fifth workshop on geothermal reservoir engineering, Stanford University, 233-238.

Chen, Y., and Lundqvist, P., 2006, Analysis of supercritical carbon dioxide heat exchangers in cooling process, 8 p.

Cho, J., Augustine, C., Zerpa, L.E., 2015, Validation of a Numerical Reservoir Model of Sedimentary Geothermal Systems Using Analytical Models*,* Proceedings, Fortieth Workshop on Geothermal Reservoir Engineering, Stanford University, 13 p.

Cladouhos, T.T., Petty, S., Nordin, Y., Moore, M., Grasso, K., Uddenberg, M., and Swyer, M.W., 2014, Reservoir construction from the Newberry Volcano EGS Demonstration: Journal of Groundwater Science and Engineering, v. 2, no. 3, p. 1-7.

Craft, B.C., and Hawkins, M.F., 1959, Applied Petroleum Reservoir Engineering: Englewood Cliffs, NJ, Prentice Hall.

Deming, D., 1989, Application of bottom-hole temperature corrections in geothermal studies: Geothermics, v. 18, no. 5, p. 775-786.

Dietz, D.N., 1965, Determination of Average Pressure from Build-up Surveys: Journal of Petroleum Technologies, p. 955-959.

Engineering Toolbox, Water Dynamic and Kinematic Viscosity, http://www.engineeringtoolbox.com/water-dynamic-kinematic-viscosity-d_596.html (March 2015).

Gérard, A., Genter, A., Kohl, T., Lutz, P., Rose, P., and Rummel, F., 2006, The deep EGS (enhanced geothermal system) project at Soultz-sous-Forêts (Alsace, France): Geothermics, v. 35, no. 5, p. 473-483.

Gonzalez, M.H., Eakin, B.E., and Lee, A.L., 1970, Viscosity of natural gases: monograph on API Research Project 65, American Petroleum Institute, 109 p.

Gringarten, A.C., ed., 1978, Geothermics and Geothermal Energy: Springer, p. 297-308.

Hamm, V., Bouzit, M., and Lopez, S., 2016, Assessment of complex well architecture performance for geothermal exploitation of the Paris basin: A modeling and economic analysis: Geothermics, v. 64, p. 300-313.

Hendry, R., Hilfiker, K., Hodge, D., Morgan, P., Swanberg, C., and Shannon Jr, S.S., 1982, Geothermal investigations in West Virginia, Los Alamos National Laboratory, 57 p.

Hodge, D.S., 1996, Assessing geothermal energy potential in upstate New York. Final report: New York State Energy Research and Development Authority, 197 p

Hodge, D.S., and Fromm, K., 1984, Heat flow and subsurface temperature distributions in central and western New York. Final report, New York State Energy Research and Development Authority, 217 p.

Jennings, J.W., Lucia, F.J., 2003, Predicting permeability from well logs in carbonates with a link to geology for interwell permeability mapping Proceedings, SPE Annual Technical Conference and Exhibition, p. 215-226.

Jensen, J.L., Corbett, P.W., Lake, L.W., and Goggin, D.J., 2000, Statistics for petroleum engineers and geoscientists: Amsterdam, The Netherlands, Elsevier, 338 p.

Jones, S.C., 1987, Using the inertial coefficient, b, to characterize heterogeneity in reservoir rock Proceedings, SPE Annual Technical Conference and Exhibition, 10 p.

Jordan, J., Anderson, B., Richards, M., Horowitz, F., Camp, E., Whealton, C., Smith, J., Tester, J., Stedinger, J., Welcker, K., He, X., Chickering Pace, C., Hornbach, M., Frone, Z., Ferguson, C., Bolat, R., and Magnani, M.B., 2015, Low-Temperature Geothermal Play Fairway Analysis for the Appalachian Basin, Geothermal Data Repository, https://gdr.openei.org/submissions/638.

Kastner, O., Sippel, J., and Zimmermann, G., 2015, Regional-scale assessment of hydrothermal heat plant capacities fed from deep sedimentary aquifers in Berlin/Germany: Geothermics, v. 53, p. 353-367.

Klinkenberg, L.J., 1941, The permeability of porous media to liquids and gases: Proceedings, Drilling and production practice, 200.

Krakow, B., and Lombard, D., 1983, An evaluation of potential geothermal reservoirs in central and western New York state: New York Energy Research and Development Authority, 77 p.

Kristensen, L., Hjuler, M.L., Frykman, P., Olivarius, M., Weibel, R., Nielsen, L.H., and Mathiesen, A., 2016, Pre-drilling assessments of average porosity and permeability in the geothermal reservoirs of the Danish area: Geothermal Energy, v. 4, no. 1, 27 p.

Lynch, R.S., and Castor, T.R., 1983, Auburn low-temperature geothermal well. Final report: New York State Energy Research and Development Authority, 277 p.

Murtha, J.A., 1994, Incorporating Historical Data into Monte Carlo Simulation: SPE Computer Applications, v. 6, no. 02, p. 11-17.

New York State Museum, Empire State Oil and Gas Information System, www.esogis.nysm.nysed.com (August 2014).

Ouyang, L.-B., 2011, New correlations for predicting the density and viscosity of supercritical carbon dioxide under conditions expected in carbon capture and sequestration operations: Open Petroleum Engineering Journal, v. 5, no. 1, p. 13-21.

Parini, M., Riedel, K., 2000, Combining probabilistic volumetric and numerical simulation approaches to improve estimates of geothermal resource capacity*,* Proceedings, Proceedings, World Geothermal Congress, 2785-2790.

Peters, E.J., 2012, Advanced Petrophysics: Volume 1: Geology, Porosity, Absolute Permeability, Heterogeneity, and Geostatistics: Live Oak Book Company, Palo Alto, CA, 238 p.

Pferd, J.W., 1981, Geology, drill holes, and geothermal energy potential of the basal Cambrian rock units of the Appalachian Basin of New York State: New York State Energy Research and Development Authority, 76 p

Pruess, K., 2007, Enhanced Geothermal Systems (EGS) comparing water with CO2 as heat transmission fluids Proceedings, Lawrence Berkeley National Laboratory: Berkeley, California, 13 p.

Reber, T., 2013, Evaluating Opportunities For Enhanced Geothermal System-Based District Heating In New York And Pennsylvania, A Master's Thesis, Cornell

University.

Sanyal, S.K., and Butler, S.J., 2009, Geothermal Power from Wells in Non-Convective Sedimentary Formations--An Engineering Economic Analysis: Transactions Geothermal Resources Council, v. 33, p. 865-870.

Satter, A., Iqbal, G.M., and Buchwalter, J.L., 2008, Practical enhanced reservoir engineering: assisted with simulation software: Tulsa, Okla., PennWell Corp, 688 p.

Smith, J., Horowitz, F., and Whealton, C., 2015, Thermal Model Methods, in Appalachian Basin Play Fairway Analysis: Thermal Quality Analysis in Low-Temperature Geothermal Play Fairway Analysis, Geothermal Data Repository, https://gdr.openei.org/submissions/638.

Society of Petroleum Engineers, 2001, Guidelines for the evaluation of petroleum reserves and resources: A supplement to the SPE: Richardson, Texas, Society of Petroleum Engineers, 141 p.

Soldo, E., Alimonti, C., 2015, From an Oilfield to a Geothermal One: Use of a Selection Matrix to Choose Between Two Extraction Technologies, Proceedings, World Geothermal Congress: Melbourne, Australia.

Stephan, K., 2013, Viscosity of dense fluids, New York, NY: Springer Science & Business Media, 268 p.

Stutz, G.R., Shope, E., Aguirre, G.A., Batir, J., Frone, Z., Williams, M., Reber, T.J., Whealton, C.A., Smith, J.D., and Richards, M.C., 2015, Geothermal energy characterization in the Appalachian Basin of New York and Pennsylvania: Geosphere, v. 11, no. 5, p. 1291-1304.

Tanikawa, W., and Shimamoto, T., 2006, Klinkenberg effect for gas permeability and its comparison to water permeability for porous sedimentary rocks: Hydrology and Earth System Sciences Discussions, v. 3, no. 4, p. 1315-1338.

Templeton, J.D., Ghoreishi-Madiseh, S.A., Hassani, F., and Al-Khawaja, M.J., 2014, Abandoned petroleum wells as sustainable sources of geothermal energy: Energy, v. 70, p. 366-373.

Viswanathan, A., 2007, Viscosities of natural gases at high temperatures and high pressures, a Masters of Science in Petroleum Engineering, Texas A&M University, 140 p.

Zhang, L., Yuan, J., Liang, H., Li, K., 2008, Energy from Abandoned oil and gas reservoirs, Proceedings, SPE Asia Pacific Oil and Gas Conference and Exhibition, 10 p.

CHAPTER 2

FEASIBILITY STUDY OF REPURPOSING TRENTON–BLACK RIVER GAS FIELDS FOR GEOTHERMAL HEAT EXTRACTION, SOUTHERN NEW YORK

Modified slightly from version published as:

Camp and Jordan, 2016, Geosphere, v. 13, no. 1, doi:10.1130/GES01230.1

ABSTRACT

Geothermal resources have the potential to fulfill a significant portion of the low-temperature (30-100 °C) thermal energy demand in the United States. Investment risk at the exploration stage is a primary factor limiting the development of geothermal energy projects, due to the high cost of drilling and limited reservoir data. An approach to reduce this risk is to target proven, well-characterized conventional oil and gas reservoirs. We examined the suitability of the Trenton–Black River gas fields of southern New York as geothermal reservoirs. These highly productive hydrothermal dolomite fields occur within long, narrow normal–fault–bounded, en echelon grabens that are scattered with saddle dolomite-lined vugs, fractures, and breccia. The Quackenbush Hill field was analyzed using existing datasets with geothermal purposes in mind. Key geothermal reservoir characteristics examined here include rock temperature, porosity and permeability, stimulation potential, and the risk of inducing seismicity. Results indicate that the Quackenbush Hill field would produce temperatures of approximately 91 °C from a dolomite reservoir with sufficient average horizontal permeability, low vertical permeability, and significant vertical and

horizontal anisotropy. In the case that adequate flow rates cannot be achieved in practice, stimulation is a feasible option from the perspective of well-field design for optimal heat sweep; however, higher-resolution data are necessary to constrain the risk of inducing seismicity. We demonstrate the technical feasibility of transitioning conventional gas fields into geothermal heat-producing reservoirs, setting the stage for future consideration of the economics of a petroleum-to-geothermal transition.

Introduction

Sustainable and affordable sources of clean energy are widely sought after in the United States and around the world as a way to reduce dependence on fossil fuels. Geothermal energy has been commonly suggested as a part of the solution for renewable baseload electricity needs in the United States (e.g., Tester et al., 2012), but few places on Earth are host to the required temperatures for electricity generation at depths that allow a project to be economically feasible. An additional challenge faced by the geothermal industry is adequate subsurface reservoir data prior to the expensive drilling of geothermal wells. We suggest that repurposing depleted conventional oil and gas fields for low-temperature (30-100 °C) geothermal heat production is a logical, near-term solution to address the geographical and data limitations of geothermal energy. Harnessing geothermal energy for direct-use heat instead of electricity expands geographical opportunities into regions with lower geothermal gradients, significantly reducing the required depth of drilling, associated capital costs, and exploration risk. Furthermore, many sedimentary basins have already been explored and drilled extensively by the oil and gas industry and thus provide available reservoir data and infrastructure that may be reused to harness otherwise wasted heat remaining in depleted hydrocarbon reservoirs.

Heat utilized at temperatures between 30-100 °C represents over half of the total thermal energy consumption in the United States, including applications such as space and water heating, food drying, industrial processes, animal husbandry, refrigeration, or greenhouses (Lindal, 1973; Fox et al., 2011). Therefore, geothermal energy heat production is a logical choice to fill the high demand for low-temperature energy applications. In a typical closed-loop low-temperature geothermal system, relatively cool water is injected into one or more deep wells, circulated through a permeable body of hot rock and pumped to the surface from another well. The geothermally heated water is passed through a series of heat exchangers in a heating plant and reintroduced back into the reservoir to be reheated (Fig. 2.1).

We explore a gas play in the northern Appalachian Basin of the eastern United States, where hydrocarbon exploration and drilling has been ongoing for 150 years. As shown by recently published geothermal maps for the United States based on bottom hole temperature (BHT) data (Blackwell et al., 2010; Shope et al., 2012; Stutz et al., 2012), average geothermal gradients in the Appalachian Basin range from 20–25 °C/km, equating to required well depths of 1.5–5 km for direct use, depending on the application. Animation 2.1 (see Appendix B-1) shows that temperatures in the basin range between 50–150 °C at depths of 3.5 km to 4.5 km (Blackwell et al., 2011). Though hydrocarbons have been produced from the Appalachian Basin for a century and a half, most of the oil and gas plays are tight or have natural fracture systems with low permeability (Roen and Walker, 1996).

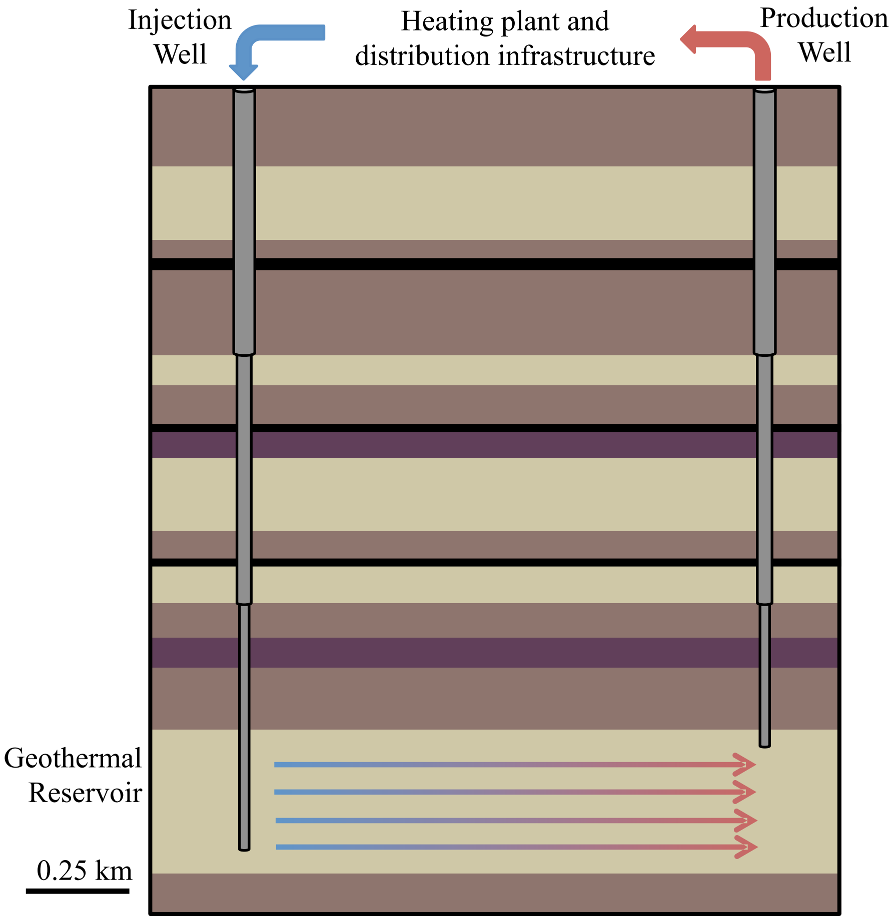

FIGURE 2.1. Schematic of a typical low-temperature closed-loop geothermal well doublet for direct-use heat. A well doublet includes one injection and one production well. In a closed loop system, water is recycled through the system, requiring little addition of water over time. The distance between the injection and production wells can range from 500-1500 meters, depending on the well field design. Suitable reservoirs and the desired application for the hot water dictate the required depth of drilling. Wellbore diameters not to scale.

Where there are exceptions with higher permeability, there is a much lower risk for geothermal energy exploitation. The Trenton–Black River (T-BR) hydrothermal dolomite (HTD) gas fields of southern New York are considered one of those exceptions.

The T-BR gas fields of southern New York (Fig. 2.2) were discovered in 1986 and have been producing large volumes of natural gas since 2000. These fields have previously been characterized as having low matrix porosity but moderate to high permeability, due to the presence of vugs (small cavities in the rock typically lined with saddle dolomite), brecciated rock, and multiple fracture sets (Smith et al., 2009). The fields vary in size but are generally long and narrow normal-fault bounded grabens, ranging from 5–20 km in length and 0.5–3 km in width. Studies have shown that these dolomite fields are hydrothermal in origin, having formed via hydrothermal alteration of limestone by hot saline magnesium-rich fluids that traveled upward along faults and concentrated below the contact between the Trenton and Black River Formations (Davies and Smith, 2006; Smith et al., 2009).

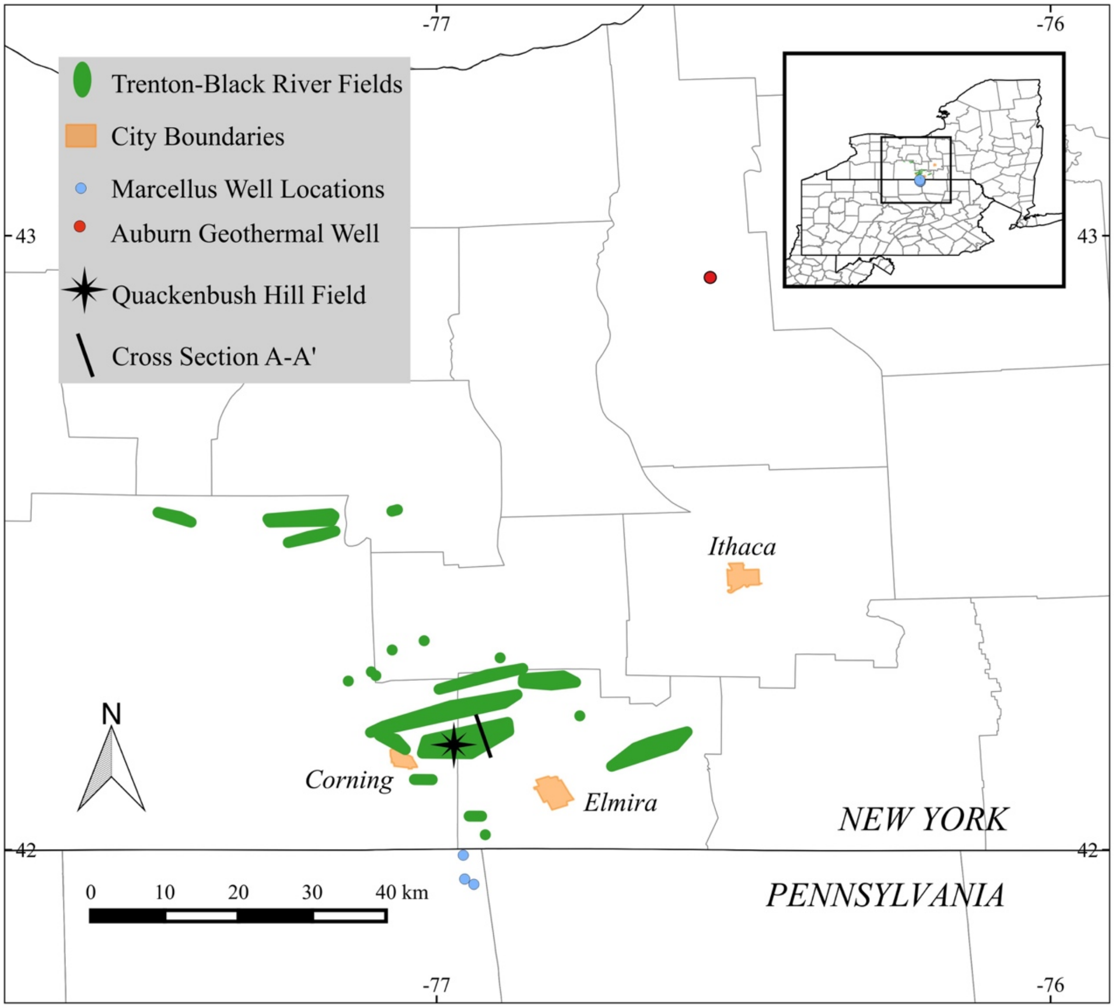

FIGURE 2.2. Location map of the Trenton-Black River gas fields of southern New York, depicted in green. This work has conducted an in-depth study of Quackenbush Hill field, denoted by the black star. This field is conveniently proximal to the towns of Corning and Elmira, New York. Stress data used for the stimulation and induced seismicity analyses were acquired from the Auburn geothermal well, shown by the red dot, and three Marcellus Shale horizontal wells in north-central Pennsylvania, shown by the blue dots.

Stratigraphic and Structural Setting

After the Grenville orogeny 1.1 billion years ago, the supercontinent in which North America was embedded experienced a long period of rifting that left an imprint of failed rift zones, extensional faults, and strike slip faults (Thomas, 1991; Van Staal, 2005). The region comprising the state of New York was part of a passive margin from the Cambrian to Late Ordovician, which allowed for the deposition of thick strata on the rifted basement. Carbonates of the Black River Formation are muddy and fine grained, including mudstone, wackestone, and packstone, indicative of deposition on a shallow tropical carbonate ramp (Smith et al., 2009). Carbonates of the Trenton Formation were deposited conformably above the Black River and include deep-water argillaceous limestone and high-energy shallow water packstone (Brett and Baird, 2002). Tectonic activity resumed when the Taconic orogeny began in the Late Ordovician, concurrent with the end of the deposition of the Black River and Trenton Formations.

Previous studies agree that the fields are negative flower structures acting as en echelon Riedel shears associated with a large-scale, northwest-trending, left-lateral transtensional basement-rooted wrench fault that experienced episodic reactivations (Hurley and Budros, 1990; Rasmussen et al., 2003; Davies and Smith, 2006; Smith et al., 2009; Slater and Smith, 2012). The timing of this deformation is not well constrained, but because the graben faults do not extend upwards past the Trenton Formation (Smith et al., 2009), deformation and hydrothermal alteration must have taken place soon after deposition of the Trenton Formation but before the Utica Shale was deposited. According to Rasmussen et al. (2003), hydrocarbon-stable, magnesium-rich paleofluids that formed in the basement by the serpentinization of peridotite contemporaneous with the Taconic orogeny, flowed upward along the wrench fault system and through the Riedel shears causing dolomitization.

Dolomitization in these reservoirs had a strong structural control and a limited stratigraphic control (Marner et al., 2008; Smith et al., 2009). As shown in Figure 2.3, dolomite is found in all facies of the Black River Formation, where it is concentrated along faults and fractures, most commonly along the hanging wall of subvertical, ENE-trending normal faults (Davies and Smith, 2006). Dolomite is occasionally found within the Trenton Formation. Outside the grabens, the unaltered limestones of the Black River and Trenton Formations are impermeable. The dolomite displays increased lateral continuity in the uppermost portion of the Black River Formation, where hydrothermal fluids are thought to have accumulated and percolated horizontally within the graben. Hydrocarbon accumulation occurred following the Late Ordovician dolomitization of the Black River limestone, all of which took place within the structural confines of the fractured grabens.

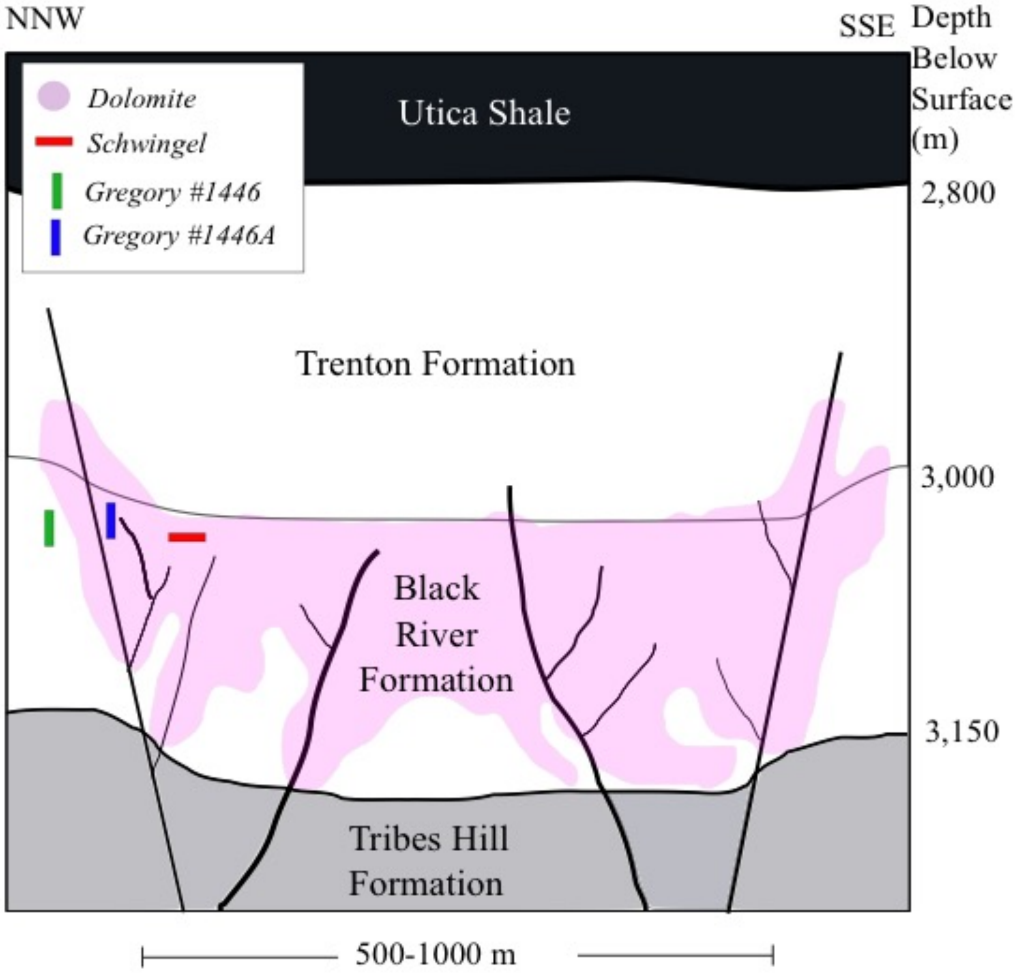

FIGURE 2.3. Generalized at-depth cross section of a typical Trenton-Black River field. Vertical scale is 3x horizontal scale. Within the Black River Formation, pink represents dolomite and white represents limestone. Dolomite is predominantly found near faults and fractures of the graben hanging wall, and gas has historically only been produced from dolomite facies of the Black River. The locations of the Schwingle and Gregory #1446 and #1446A cores are approximate.

Study Area: Quackenbush Hill Field

The Quackenbush Hill field (Figs. 2.2, 2.3, and 2.4) was chosen for a case study analysis to determine the potential to use these HTD fields as geothermal reservoirs. Quackenbush Hill field comprises two ENE-trending en echelon fault-bounded grabens, and measures approximately 13 km in length and 3 km at its widest point (Marner et al., 2008). The field consists of a total of 14 wells, including the most directional wells of any T-BR field in the state. Quackenbush Hill field is of particular interest because it is one of the highest gas-producing Trenton-Black River fields in New York, it is host to the best producing well in the play (Smith et al., 2009), and it is within 15 km from the population and business centers of Corning and Elmira, New York.

We evaluated the Quackenbush Hill field as a potential geothermal reservoir considering the following criteria: thermal availability, reservoir quality, potential for stimulation, and risk of induced seismicity. Among the necessary conditions for extracting a commercially feasible amount of heat from a rock reservoir, several relate to fluid flow through the rock. Effective heat transfer from the rock into the fluid, referred to as heat sweep, requires reservoir permeability high enough to transfer the quantity of heat to meet the project energy goals. For geothermal applications, suitable reservoir permeability is generally considered to be in the range of hundreds to thousands of millidarcies (mD) or greater. Consequently, we focused on the identification of datasets that pertain to thermal availability and permeability in the reservoir.

Much of the existing data from the Quackenbush Hill field is proprietary. Two-dimensional seismic reflection data have been collected in the past but were not available for this analysis. Two vertical cores and one horizontal core were drilled in the Quackenbush Hill field; aside from those data population statistics, the raw data are not publicly available. The first vertical core, Gregory #1446, which was drilled outside the graben wall (Fig. 2.3), sampled both the Trenton and the Black River Formations but only penetrated tight limestone. The Gregory #1446A sidetrack core (Fig. 2.3), also vertical and 64 m from the first, penetrated the interior of the graben and sampled the same stratigraphy as #1446 but its rocks are completely dolomitized, with an average porosity of 2.7% and an average permeability of 22.5 mD (Marner et al., 2008). Data from these two vertical cores exhibit a permeability range of 0.01-500 mD (Marner et al., 2008; R. Jacobi, 2014, personal commun.). The horizontal core, Schwingle 2 Hz, was bored perpendicular to the trend of the field and sampled 10 m of dolomite within the graben (Fig. 2.3). It has an average porosity of 3.2%, an average permeability of 0.11 mD, and shows numerous vugs, occasional veins with void space, horizontal and vertical stylolites (some of which are open), and multiple generations of fractures (Marner et al., 2008).

In the case that Quackenbush Hill field meets the necessary criteria to be repurposed for geothermal heat extraction, it is likely that the other T-BR fields are good candidates as well; although the fields in the T-BR play vary in size and total gas production, they are similar in origin and structure. Our results are applicable to both the geothermal and petroleum industries, in addition to municipalities and governmental bodies. Similar analyses on other conventional oil or gas fields that are ramping down production may guide future decisions about the transition from hydrocarbon production to geothermal heat production.

Methods

Reservoir Quality

Without access to field-specific permeability data, we looked outside the Quackenbush Hill field at neighboring producing fields in search of patterns in reservoir quality that could be applied to the Quackenbush analysis. The Whiteman #1 core, which sampled the Black River Formation in a nearby reservoir, was analyzed by CoreLab, Inc. for air permeability (maximum, 90° to the direction of maximum, and vertical), helium porosity, and bulk density at a confining stress of 2.7 MegaPascals (MPa; New York State Museum, 2014; see Appendix B-2). Measurements were taken at variable intervals, from 0.1–1.2 m. Because we are interested in the permeability of water through the reservoir, not air, the permeability data were corrected for the Klinkenberg effect using the power-law correlation derived for carbonates in Al-Jabri et al. (2015), where k_w is the permeability of the rock with water, and k_g is the permeability of the rock with gas, both in units of millidarcies (mD):

$$k_w = 0.578{k_g}^{1.097}. \quad (2.1)$$

Because the core permeability data are sparse but wireline log porosity data are abundant and available in a state database, we derived from core porosity and permeability data an empirical relationship to apply to well log-derived porosity from nearby gas fields, and thereby extended the reservoir analysis. We chose to apply a power law fit to the core data, based on goodness of fit and because power law fits are most realistic for carbonates (Jennings and Lucia, 2003). Porosity data were acquired from neutron porosity hydrogen index (NPHI) well logs available for download on the Empire State Oil and Gas Information System database (ESOGIS, 2014). Ten of the fourteen Quackenbush Hill wells possess NPHI logs recorded every 15 cm in the gas-producing zone of the Black River Formation, for a total of 15,760 NPHI recordings. Machine-error outliers were removed using median absolute deviation, leaving 8380 valid recordings. Dolomite was distinguished from limestone using the photoelectric factor log, in which dolomite responds as ≤ 3.14. Apparent neutron porosity was adjusted where the matrix was dolomite, using equivalence charts for the appropriate wireline logging tool, which in this case was a Schlumberger compensated neutron logging (CNL) tool for all wells in the field (Schlumberger, 2009). Where density porosity exceeded apparent neutron porosity, the gas excavation effect was corrected to true porosity using the iterative process described by Bassiouni (1994; see MatLab code in Appendix B-3). The presence of gas in a reservoir underestimates the neutron porosity reading because the CNL tool, which responds to hydrogen content in the formation, is calibrated to read porosity in a reservoir saturated with fresh water. For the remainder of the readings that were not affected by the presence of gas, true porosity was calculated using

$$\phi = \frac{(\rho_{ma} - \rho_b) + \phi_N}{\rho_{ma}}, \qquad (2.2)$$

where ϕ is true porosity, ϕ_N is apparent neutron porosity, ρ_{ma} is matrix density, and ρ_b is bulk density log reading (Bassiouni, 1994). We assumed a matrix density of 2.85 g/cm^3 for dolomite and 2.71 g/cm^3 for limestone, based on density measurements from the Whiteman #1 core (Appendix B-2).

Stimulation

If permeability is not high enough at Quackenbush to sustain high flow rates, a design option to consider is stimulation by hydraulic shearing (Mode II or III) of preexisting fractures in the reservoir (Cladouhos et al., 2014; Rinaldi et al., 2014). Mode II and III fractures experience slip parallel to the plane of the fracture, rather than outward displacement perpendicular to the plane of the fracture, which produces Mode I fractures.

Because stress field data specific to the Quackenbush Hill field do not exist, we assume stress magnitude gradients from a nearby dataset. Stress orientations were estimated by extrapolating between two nearby locations that have available data. The first data set which includes stress orientations and magnitudes, comes from the Auburn geothermal well in Auburn, New York (Fig. 2.2), approximately 90 km northeast of Quackenbush Hill field, where the top of the Black River Formation occurs approximately 1730 m shallower than in the Quackenbush Hill field. By means of mini hydraulic fracturing tests and borehole televiewer surveys, Hickman et al. (1985) determined that the minimum horizontal stress, $S_{H,min}$, increases linearly with depth and that the maximum horizontal stress, $S_{H,max}$, increases approximately linearly in an irregular fashion and is oriented approximately N83°E ±15°. Our study used a linear fit of this dataset to determine the maximum and minimum horizontal stress gradients, which were then used to calculate the horizontal stress magnitudes at a depth of 3 km, the average depth of reservoir production at Quackenbush Hill field. $S_{V,}$ the lithostatic load, was computed using an average density of 2600 kg/m^3 for sedimentary rocks through the entire sedimentary column (Manger, 1963).

Our second source of stress orientations comes from 20 km south of Quackenbush, where natural gas production relies on high pressure hydraulic fracturing of Mode I fractures to stimulate shale-gas production. Since Mode I hydraulic fractures propagate parallel to the direction of maximum horizontal stress (Hickman et al., 1985), the orientation of $S_{H,max}$ (N68°E) can be inferred from the orientation of the horizontal legs of wellbores. Stress magnitudes were not determinable at this location.

Subsequently, an approximate orientation of the principal stresses at Quackenbush Hill field was determined using a linear extrapolation of the azimuth of $S_{H,max}$ from Auburn, New York (Hickman et al., 1985) to the location of the shale gas production wells in northern Pennsylvania (Fig. 2.2). To check the accuracy of this extrapolation, we compared our result for $S_{H,min}$ with the instantaneous shut-in pressures (ISIP) recorded from Quackenbush Hill field wells (IHS U.S. Well Data, 2013) and assigned error ranges based on the deviation of the ISIP values from our estimated $S_{H,min}$.

By applying our stress field data to the principles of Mohr's circle of stress and Byerlee's law (Byerlee, 1978) we calculated the minimum pore fluid pressure required to hydroshear existing fractures, and the orientation of such fractures. The injected fluid pressure (P_f^*) required to hydroshear existing fractures is given by:

$$P_f^* = \frac{\sigma_1 + \sigma_3}{2} - \frac{(\sigma_1 - \sigma_3)(\sqrt{1+\mu^2})}{2\mu}, \qquad (2.3)$$

where σ_1 and σ_3 are the maximum and minimum horizontal stresses, respectively, in this stress regime, and μ is the sliding coefficient of fractured rock.

Induced Seismicity

Induced seismicity occurs when high-pressure injection of fluids changes the pore pressure in the subsurface and inadvertently causes slip on large faults (Talwani and Acree, 1984). At Quackenbush Hill field, the two sets of subvertical master faults that bound the grabens (5–8 km in length; Fig. 2.4) are most worrisome for reactivation given their relatively large surface areas and proximity to the aforementioned urban centers. The risk of inducing seismicity must be assessed whether or not stimulation is a feasible option. To calculate the tendency for slip along these faults, we performed a slip tendency analysis (Morris et al., 1996) by comparing the sliding friction coefficient (μ) with the ratio of the shear stress (τ) and effective normal stress (σ_n^*) on the faults. That ratio is given as

$$\frac{\tau}{\sigma_n{}^*} = \frac{\left(\frac{\sigma_1-\sigma_3}{2}\right)\sin 2\theta}{\frac{\sigma_1+\sigma_3}{2}+\left(\frac{\sigma_1-\sigma_3}{2}\right)cos2\theta-p_f}, \qquad (2.4)$$

where θ is the angle between σ_1 and the pole to the faults of interest, and p_f is the pore-fluid pressure. The faults are oriented subvertically, approximately dipping 85° (Jacobi, 2003; Rasmussen et al., 2003) and strike between N75–80°E, as estimated from map view depictions of the fields (Smith et al., 2009; Slater and Smith, 2012), well locations, and from the orientations of lineaments detected by Landsat imagery (Earth Satellite Corporation, 1997; Jacobi, 2003).

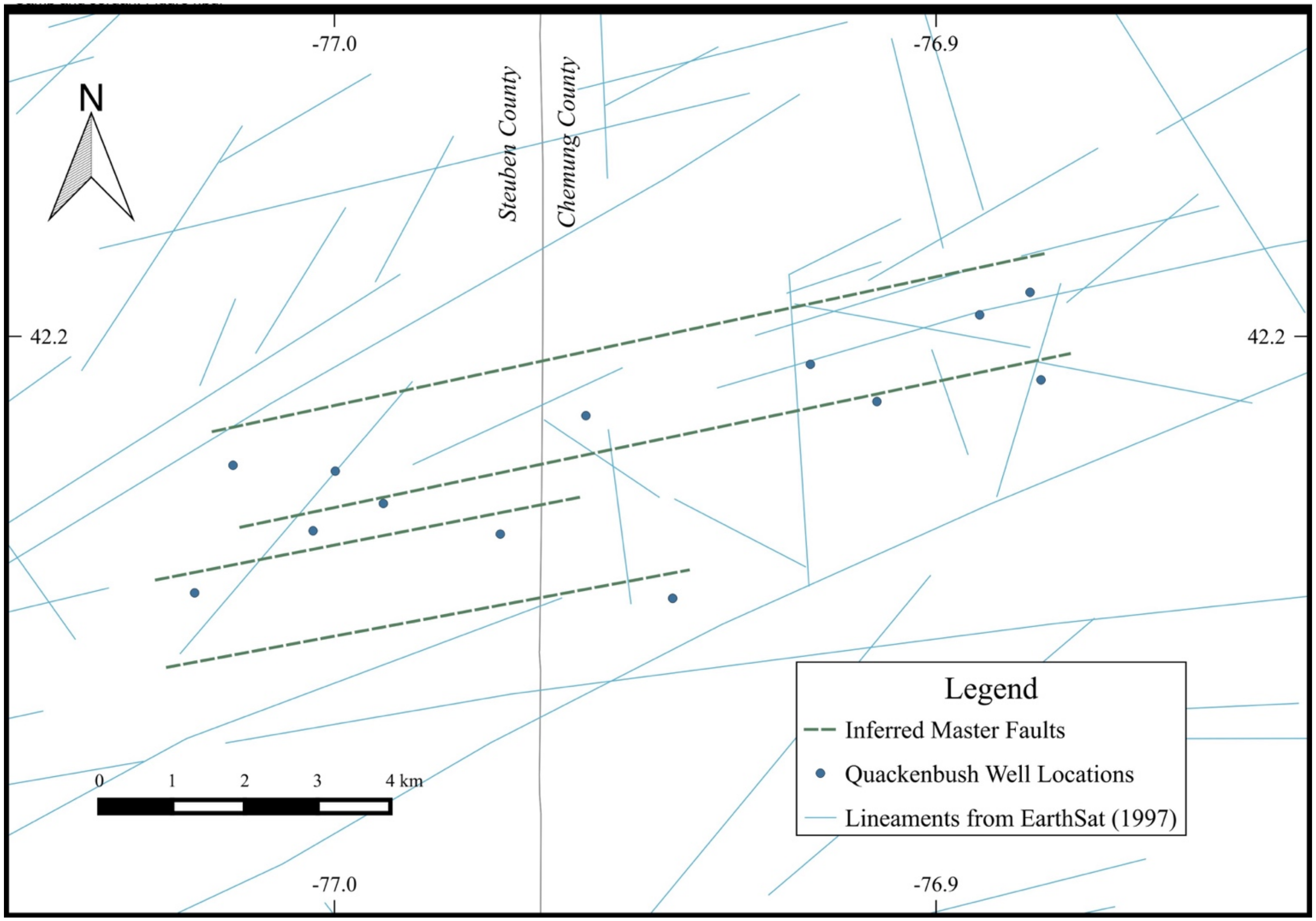

FIGURE 2.4. Map view of Quackenbush Hill field. Well locations taken from the Empire State Organized Geologic Information System (ESOGIS) database; lineaments taken from Earth Satellite Corporation (1997). Graben-bounding fault orientations are inferred from lineaments and previous reports (Smith et al., 2009).

Thermal Resource

In order to calculate the available and recoverable energy within the Quackenbush Hill field, an estimate of the reservoir temperature is needed. Eight wells targeting gas in the Quackenbush Hill field have recorded bottom hole temperatures (BHT) in the Black River Formation. BHT data often require a temperature correction to account for the influence of cooler drilling fluids interacting with the rock. Whealton et al. (2015) developed a local BHT correction that varies depending on the drilling fluid. The following correction was applied to the Quackenbush Hill field wells, which were drilled with a polymer-based fluid:

$$BHT_C = BHT_o + X_m(0.0155((1650^3 + d^3)^{0.33} - 1650)) + 15.4(1 - X_m), \quad (2.5)$$

where BHT_c is the corrected BHT in °C, BHT_o is the original BHT in °C, X_m is the percent fraction of mud or polymer in the drilling fluid (in this case, $X_m = 1$), and d is depth of the BHT recording in meters. Temperatures at the depth of the reservoir were back-calculated from the corrected BHT data using the thermal model developed by Smith et al. (2015) and the depth to the top of dolomite determined from well logs. From those eight data points, an average reservoir temperature for Quackenbush Hill field was used to calculate its total reservoir energy.

We define total reservoir energy, q_{tot}, as the maximum thermal energy in place within a certain volume of rock. The total reservoir energy in place for the Quackenbush Hill field is estimated using the relationship

$$\boldsymbol{q_{tot} = (\rho_w V \phi C_{p,w} + \rho_r V(1 - \phi) C_{p,r})\Delta T}, \quad (2.6)$$

where ρ_r and ρ_w are the densities of the rock and water in kg/m^3, V is the volume of the reservoir in m^3, $C_{p,r}$ and $C_{p,w}$ are the heat capacities of the rock and water in $\frac{kJ}{kg{\cdot}°C}$, and ΔT is the temperature differential between the reservoir and the water reinjection temperature (Tester et al., 2012). We approximate a reservoir area of 13 km by 3 km (Fig. 2.3), based on the geographic extent of the gas-producing wells and what is known of the width of the two Quackenbush grabens from seismic reflection data. The gas-producing interval of the reservoir, 33 m, was used as a conservative estimate of reservoir thickness.

All of the thermal energy in place cannot be extracted from the reservoir due to limitations of the reservoir geometry and inherent heat losses in the surface operations. What matters to the economics of the geothermal heating application is the recoverable thermal capacity of the reservoir (q_{rec}), which is estimated using the relationship:

$$\boldsymbol{q_{rec}} = \frac{\boldsymbol{q_{tot}R\eta}}{\boldsymbol{t}}. \qquad (2.7)$$

Here, t is the lifetime of the heating system in seconds, R is the recovery factor used to estimate the amount of thermal energy that can physically be extracted from the reservoir, and η is the surface efficiency, which accounts for heat loss during distribution. For this calculation we assumed a typical geothermal project lifetime of 30 years. The recovery factor largely depends on the amount of surface area available between the water and rock, which is dependent on reservoir heterogeneity and the fluid flow regime (i.e. porous media, fractures, vugs, or any combination). In this analysis we assumed a range of recovery factors, from conservative to optimistic, based on the results of the reservoir analysis, discussed below. The surface efficiency scales with distribution distance and piping insulation (0.1-1 °C/km for insulated pipes) (Ryan, 1981). Surface efficiency was approximated using the maximum distance from Quackenbush Hill field to Elmira (15 km) and an average temperature loss for insulated pipes (0.5 °C/km). Fluid losses were neglected for this calculation. The resulting value was applied to a hypothetical design of a geothermal district heating system to estimate the number of homes that could be heated.

Results

Reservoir Quality

Klinkenberg-corrected permeability data (maximum, 90°, and vertical) are presented in Figure 2.5, plotted against measured core porosity. Though the spread is very large, the maximum and 90° permeability data were fit together by a power law model with an R^2 of 0.52. That fit is:

$$k_L = 0.39\phi^{2.87}, \qquad (2.8)$$

where k_L is Klinkenberg permeability in mD, ϕ is porosity in decimal fraction, and the constant of 0.39 carries units of mD. Vertical permeability was neglected from this fit because average vertical permeability (2.6 mD) is three orders of magnitude lower than both the average 90° and average maximum permeability, and was deemed to be negligible and not of reservoir quality. Average core porosity is 7%, average maximum permeability is 4680 mD, and average 90° permeability is 2100 mD (Table 2.1).

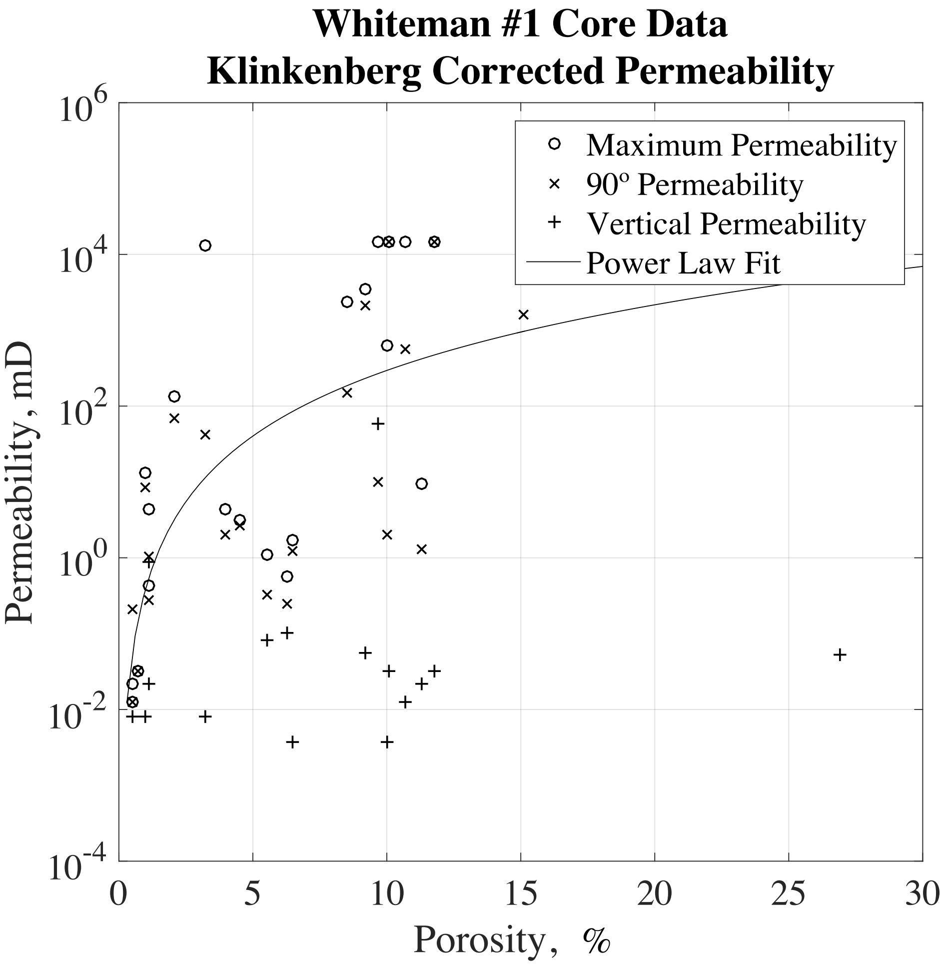

FIGURE 2.5. Log of Klinkenberg permeability versus porosity from the Whiteman #1 core (New York State Museum, 2014). Plotted are maximum horizontal permeability, 90° horizontal permeability, and vertical permeability. A power law model was applied to the maximum and 90° permeability data. Vertical permeability is negligible, and was therefore excluded from the fitting of the data.

TABLE 2.1. WHITEMAN #1 CORE DATA STATISTICS.

	Porosity	Maximum Permeability	90° Permeability	Vertical Permeability
	%	mD	mD	mD
Minimum	0.5	0.012	0.012	0
Average	7.0	4680	2100	2.6
Maximum	26.9	14,590	14,590	58.2

Note: The Whiteman #1 core dataset was corrected for the Klinkenberg effect using the correlation for carbonates determined by Al-Jabri et al. (2015). Complete dataset can be found in Appendix B-2.

Conversion Notes:
1 D = 1 Darcy = 9.869×10^{-13} m^2
1 mD = 10^{-3} Darcy = 10^{-15} m^2

When the log of maximum permeability is plotted against porosity categorized based on core features (i.e. vugs, fractures, etc.), there is a distinguishable grouping pattern (Fig. 2.6). Fractures that are either isolated or those adjacent to small vugs do not exhibit porosity exceeding 4%. Nevertheless, fracture permeability spans six orders of magnitude, and exceeds 100 mD where co-located with vugs. Porosity associated with vugs increases with vug size, reaching nearly 27% where large vugs are co-located with small and medium vugs. Permeability associated with vugs spans four orders of magnitude, from 0.5 mD to 10,240 mD.

The power law model from the core was applied to the corrected NPHI porosity data from ten wells. The maximum porosity recorded in the reservoir is 53%, and the minimum is 0.002%. Applying Equation 2.8 to the NPHI data, the average calculated permeability in Quackenbush Hill field is 120 mD. This porosity-based method predicts a maximum permeability in the reservoir of approximately 36,000 mD, which is within the same order of magnitude as the highest permeability detected in the core.

Calculated permeability from log porosity was plotted with depth (Fig. 2.7), corrected to account for the difference between measured borehole length and total vertical depth. The results show three bands of very high porosity at depths of 2850, 2950, and 3020 m; these bands show porosity up to 32%, 53%, and 19%, respectively. Additionally, the points of high porosity within these bands are recorded in both limestone and dolomite facies.

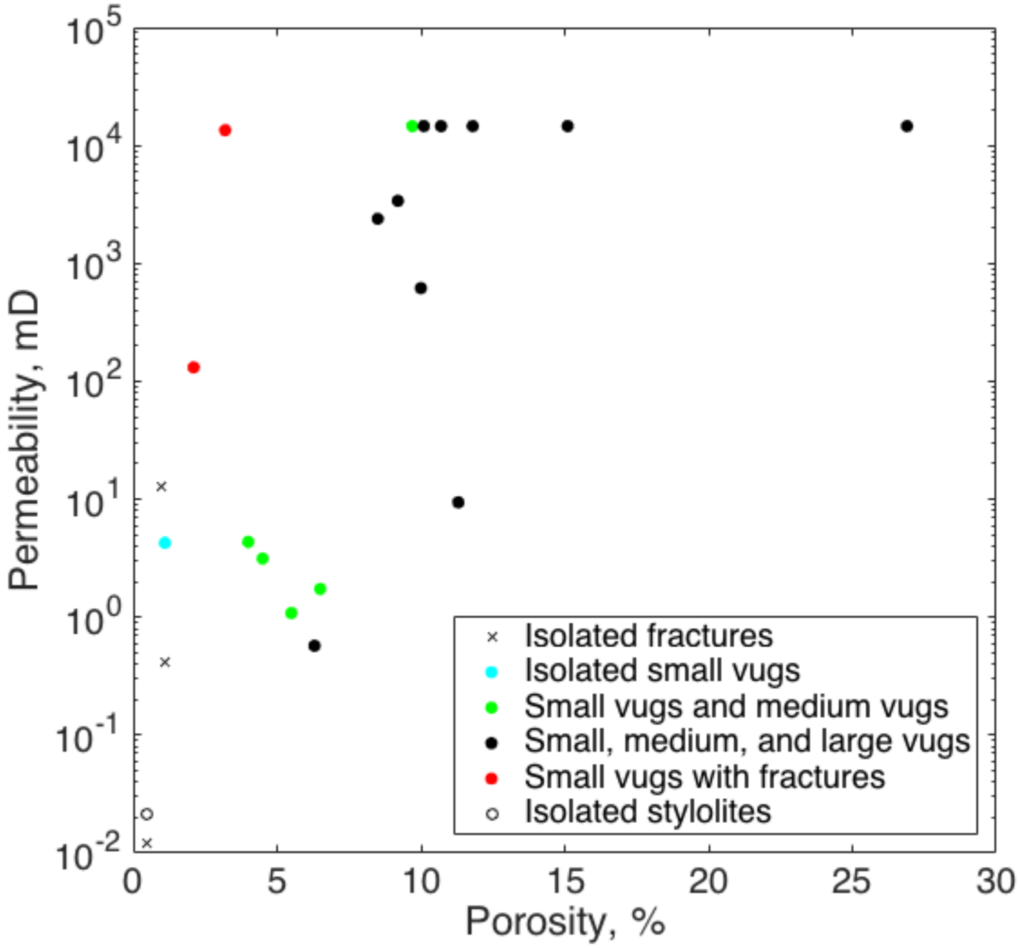

FIGURE 2.6. Log of maximum permeability versus porosity data from the Whiteman #1 core, sorted by features described at each tested interval in the core (New York State Museum, 2014). Measurements with similar core features tend to plot together. Fracture porosity does not exceed 4%, but permeability in samples containing fractures spans six orders of magnitude and is highest where the fractures are co-located with small vugs. Vuggy porosity reaches up to 27% and permeability in samples with vugs is highest (>100 mD) where there are large or medium vugs found with smaller vugs. Permeability for samples with vugs spans four orders of magnitude.

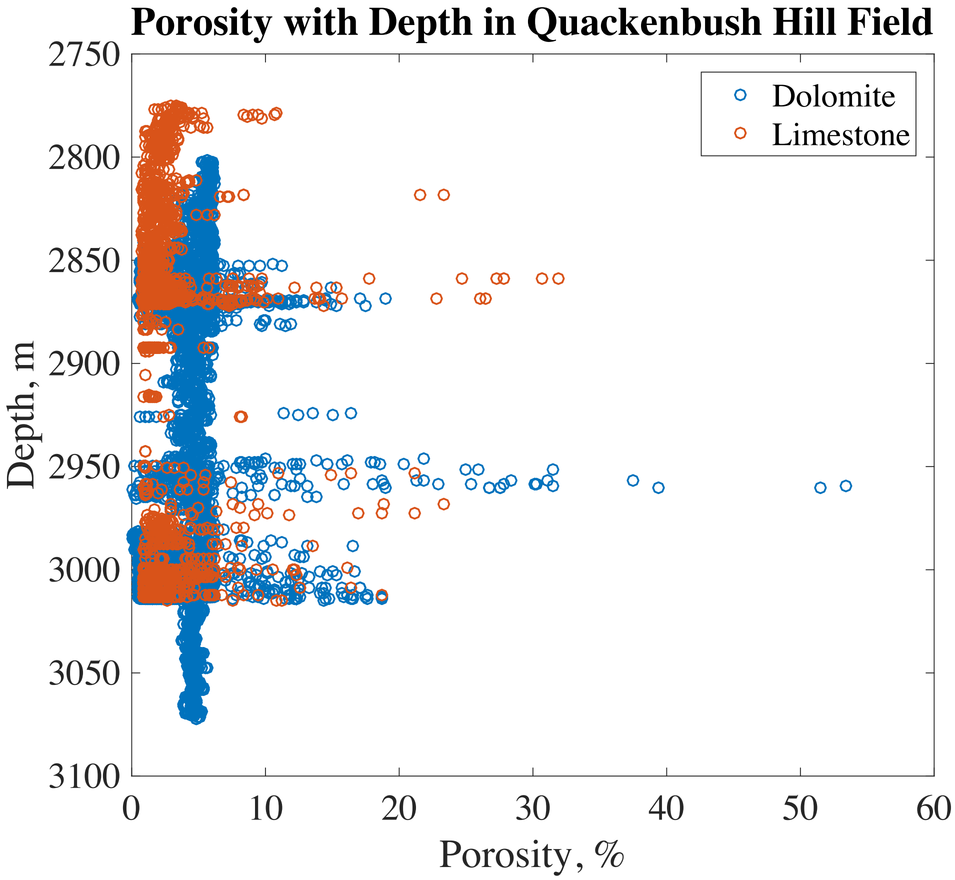

FIGURE 2.7. Adjusted neutron porosity hydrogen index (NPHI) porosity versus true vertical depth, with values sorted by lithology. Many wells in this field are horizontal; therefore, so measured positions of the data along the length of the borehole were converted to total vertical depth. Both dolomite and limestone are associated with higher porosity zones. High porosity zones are partitioned into three distinct zones, located at 2860, 2950, and 3000 m depth. These may be representative of multiple vertically partitioned zones or a single high porosity zone that dips southward with the top of the Black River Formation.

Stimulation and Induced Seismicity

A linear extrapolation of the Hickman et al. (1985) dataset to the Quackenbush Hill field predicts a $S_{H,max}$ of 85 ± 4 MPa and $S_{H,min}$ of 55 ± 3 MPa (Table 2.2). Two ISIP data points are available for Quackenbush Hill field at approximately 3 km depth, 52 and 58 MPa, which equate to 3 MPa of error on $S_{H,min}$, or about 5%. The calculated corresponding error on $S_{H,max}$ is 4 MPa.

Three wells in north central Pennsylvania were drilled directionally at N153°E, N155°E, and N167°E (Fig. 2.2; American Petroleum Institute [API] numbers 117–21426, 117–20391, and 117–20330) at depths of about 1.5 km (MarcellusGas.org, 2014). Based on the assumption that operators oriented the horizontal wells perpendicular to $S_{H,max}$, the inferred maximum horizontal stress at that location is oriented approximately N68°E. These data suggest that the stress field rotates counterclockwise from Auburn, New York (N83°E) toward north central Pennsylvania. A linear interpolation of stress orientation between Auburn and northern Pennsylvania indicates that $S_{H,max}$ at Quackenbush Hill field is approximately N71°E ± 15°. This stress vector is used for the stimulation and seismic risk calculations that follow.

Given an assumed sliding friction coefficient (μ) of 0.85 for rocks with failure planes experiencing a normal stress of less than 200 MPa (or shallower than 5 km (Byerlee, 1978)), approximately 46.8 ± 5 MPa of fluid pressure would be required to hydroshear optimally oriented preexisting fractures (Fig. 2.8). Applying the principles of slip along pre-existing planes, any fractures oriented vertically (dip of 90°) and striking approximately N045°E and N097°E ± 15° would reactivate under stimulation pressure (Fig. 2.9). As shown in Figure 2.8, the graben bounding faults would require 5.2 MPa of additional fluid pressure in order to be reactivated, assuming there is no local reorientation of the stress field. Hydrostatic gradient (~10 MPa/km) in a 3-km-deep well creates 30 MPa of hydrostatic pressure, leaving approximately 16.8 ± 5 MPa of well-head pressure required for stimulation of pre-existing fractures in the reservoir. Finally, the slip-tendency analysis (Equation 2.3) yields approximately 2.8 MPa of shear stress and 25.3 MPa of effective normal stress (assuming 30 MPa of hydrostatic pore fluid pressure, as in the previous analysis) on the two sets of graben-bounding faults, where $\theta=84°$, for a slip tendency ratio of 0.11. However, if stimulation were undertaken by adding 16.8 MPa to the in situ pore pressure, the effective normal stress would then be 8.5 MPa, which results in a slip tendency ratio of 0.33.

TABLE 2.2. CALCULATED STRESS MAGNITUDES AND ESTIMATED STRESS ORIENTATIONS FOR THE QUACKENBUSH HILL FIELD.

	Stress Magnitudes at Quackenbush (MPa)	Estimated Orientation at Quackenbush	Measured orientation at Auburn, New York	Estimated orientation at Tioga County, Pennsylvania
$S_{H,max}$ (σ_1)	85 ± 4 MPa	N71°E ±15°	N83°E ± 15°	N68°E
$S_{H,min}$ (σ_3)	55 ± 3 MPa	N161°E ±15°	N173°E ± 15°	N158°E
S_V (σ_2)	76.5 MPa	*Vertical*	*Vertical*	*Vertical*

Note: Vertical stress magnitude calculated at a depth of 3 km, assuming an average rock column density of 2600 kg/m^3. Principal horizontal stress magnitudes extrapolated from stress gradient measured by Hickman et al. (1985) in the Auburn geothermal well. Stress orientations inferred from a linear stress rotation bounded by measured orientation in the Auburn well and an estimated orientation from horizontal gas wells in northern Pennsylvania.

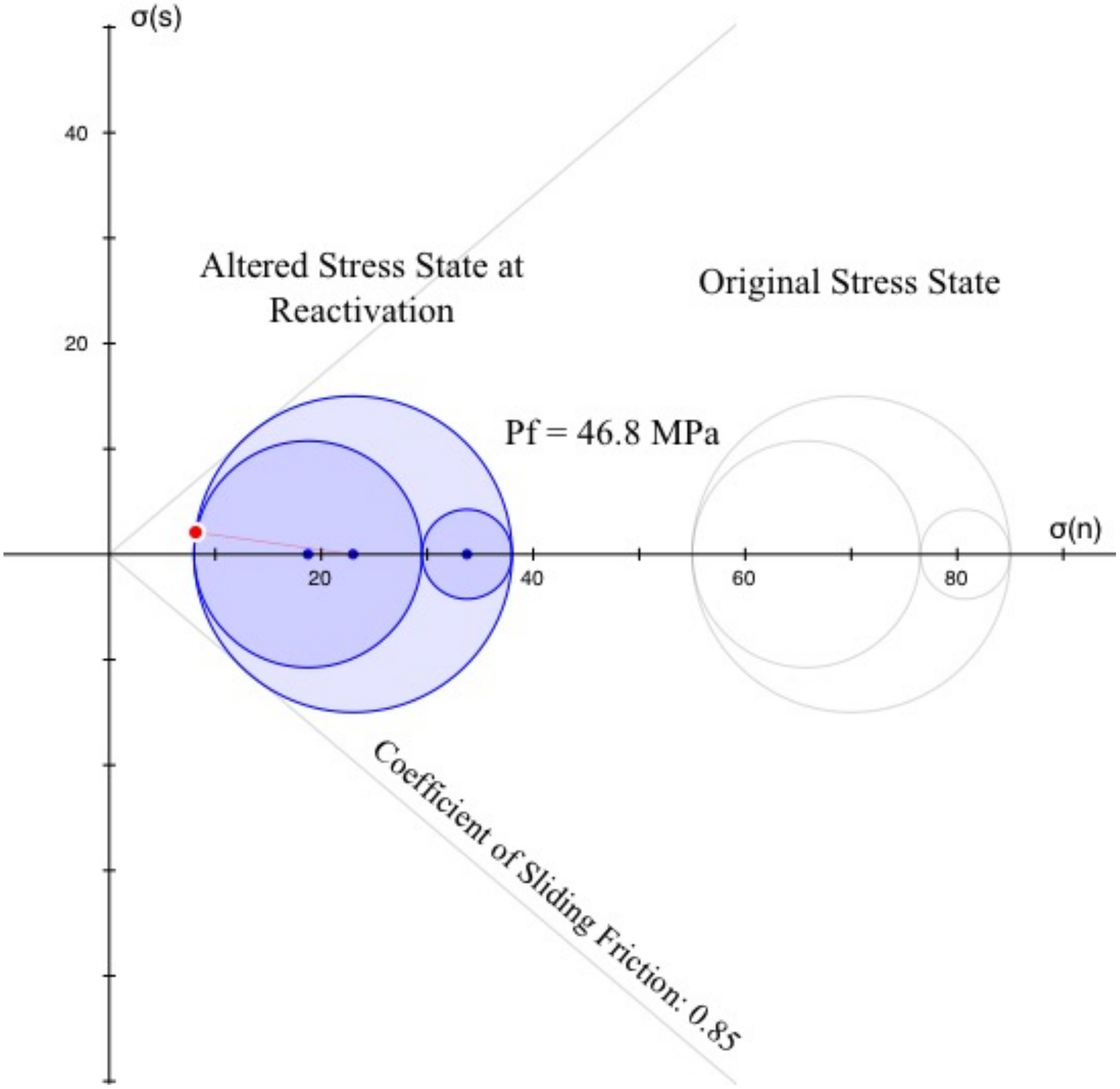

FIGURE 2.8. Mohr circle representation of stimulation by increasing pore fluid pressure within Quackenbush Hill Field, assuming a coefficient of sliding friction of 0.85 (Byerlee, 1978). Gray circles are the initial stress state, and blue circles are the stress state during stimulation. Required pore pressure to reactivate existing fractures is 46.8 MPa, which equates to 17.8 MPa of pressure at the wellhead, assuming hydrostatic pressure at the bottom of the wellbore. The angle of the graben bounding faults is shown by the red dot and line. To reactivate those faults, an additional 5.2 MPa of fluid pressure is required.

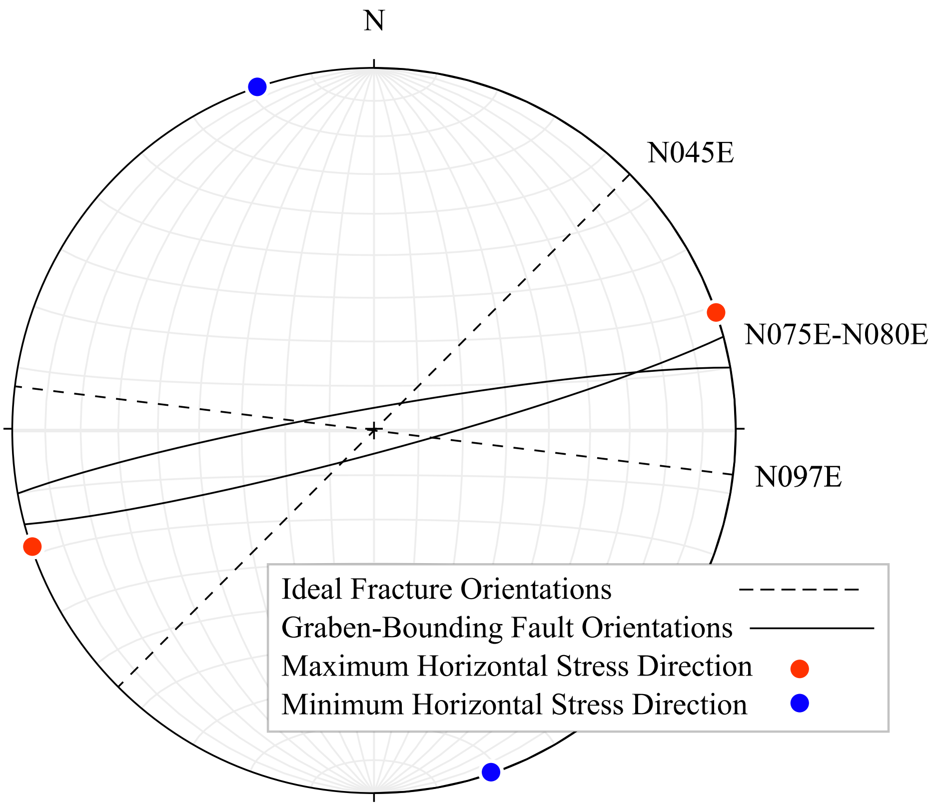

FIGURE 2.9. Equal area, lower hemisphere stereonet, with estimated propagation direction for ideally oriented hydraulically sheared vertical fractures shown by dotted lines, approximately N045°E and N097°E. Solid lines indicate the approximate orientation range of the Trenton–Black River (t-BR) field graben-bounding normal faults. Maximum horizontal stress direction shown by the red dot; minimum horizontal stress direction shown by the blue dot. Results based on stress data from the Auburn geothermal well (Hickman et al., 1985; Table 2.2).

Thermal Energy Resource

At the location of the Quackenbush Hill field, the top of the Black River Formation lies at an average depth of 3 km below the local surface elevation, where the average estimated temperature is 91 °C. Figure 2.10 illustrates the relationship between temperature and depth at the location of the dolomite in the Black River Formation among the New York T-BR fields.

Because the Trenton–Black River reservoir analysis showed both fractures and vuggy porosity, we assigned a recovery factor range that spans fractured and porous reservoir recovery, 0.05-0.25 (Williams, 2007; Williams et al., 2008). Parameters used include an approximate limestone density of 2600 kg/m^3 (Manger, 1963), limestone heat capacity of 910 J/kg/°C (Robertson, 1988), water heat capacity of 4180 J/kg/°C, reinjection temperature of 50 °C, and an average reservoir temperature of 91 °C (Fig. 2.10). Water density was approximated at 965 kg/m^3 assuming the water reaches equilibrium temperature with the rock. With those inputs, the total reservoir energy in place (Equation 2.5) for Quackenbush Hill is calculated as 1.3 x 10^{17} J. Assuming a mean recovery factor of 15% and a constant system efficiency of 90%, the estimated recoverable energy of the system is 1.7 x 10^{16} J. Our conservative (recovery factor of 5%) estimate of recoverable energy from the geothermal system (Equation 2.7) is 5.8 x 10^{15} J, and an optimistic (recovery factor of 25%) recoverable energy of 2.9 x 10^{16} J.

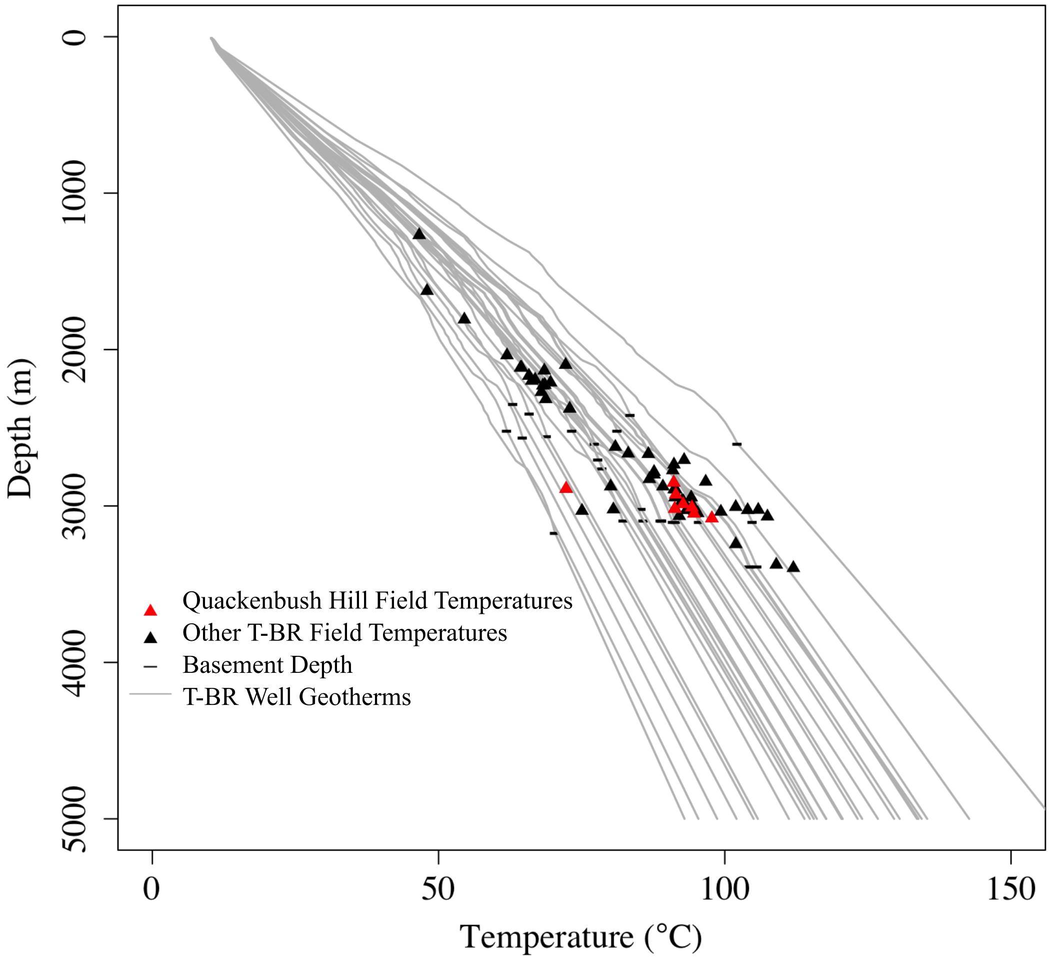

FIGURE 2.10. Temperatures at depth (triangles) and geotherms (lines) in the Trenton–Black River (T-BR) fields of southern New York. Red triangles are temperatures at the depth of the reservoir in Quackenbush Hill field. Black triangles are temperatures at depth in other Trenton-Black River fields. Reservoir depths were approximated by the top of dolomite in the Black River Formation, as indicated by the photoelectric factor wireline log. Data were taken from bottom hole temperature records of the New York State Geological Survey, corrected using local drilling-fluid dependent correction from Whealton et al. (2015). Gray lines are the geotherms of wells that drilled into the Black River Formation. Geotherm model from Smith et al. (2015).

Discussion

Reservoir Quality

The Whiteman core demonstrates that vertical permeability is not sufficient for geothermal applications; however, horizontal permeability is very good, on average. The three privately-held cores from Quackenbush Hill field (Marner et al., 2008) are reported to show permeability averages that are two to four orders of magnitude lower than from the Whiteman #1 core that was analyzed in this study. We believe this discrepancy may be a result of (1) inherent reservoir quality differences of the two fields; (2) sampling bias of the very limited number of cores from both fields due to the heterogeneity of the reservoirs, indicating that Quackenbush Hill may also have regions of higher permeability; (3) or both. In addition, little is known about the conditions under which the Quackenbush Hill cores were tested for permeability, or to what extent the data were corrected for the Klinkenberg effect. These factors may also have an effect on the apparent discrepancy.

Figure 2.6 illustrates that for the Whiteman #1 core, there is a large difference between fracture porosity and vuggy porosity, with much lower porosity for rocks containing fractures than for vuggy porosity. This suggests that the reservoir rock may be host to a dual-porosity regime, which would contribute to the apparent heterogeneity of the reservoir quality. The bimodal distribution of porosity values seen in the NPHI log (Fig. 2.11) also supports this hypothesis, where peaks are recorded at 0.5% and 8% porosity, and the mean porosity is 4%. The core data also suggest that isolated fracture permeability is not sufficient for geothermal applications, except where fractures coincide with vugs. Furthermore, isolated small vugs also do not have sufficient permeability (<100 mD), except where they coincide with medium and/or large vugs.

When Equation 2.8 was applied to the Quackenbush NPHI log data, the maximum theoretical permeability of Quackenbush Hill field is 36,000 mD, which is three times larger than the maximum recorded permeability in the Whiteman #1 core but still in the same order of magnitude. The average calculated permeability from the log data was 120 mD, though the spread is very large, spanning 13 orders of magnitude. The spread of porosity values measured by the NPHI log (0.002%-53.4%) is also wider than the range measured in the core (0.5%-26.9%). These wide spreads are expected, given the heterogeneity of the reservoir rock and the larger sample size of the logs compared to the core. When porosity is plotted with total vertical depth (Fig. 2.7), three zones of high porosity stand out at discrete depths, rather than being spread throughout the entire thickness of reservoir rock. These zones could be representative of multiple vertically partitioned high-porosity zones or a single high-porosity zone that dips southward with the top of the Black River Formation. Either way, this vertical anisotropy is consistent with the previous result that horizontal permeability dominates over vertical permeability. And because there are high concentrations of low porosity measurements within these high-porosity bands, we hypothesize that there is horizontal anisotropy as well, creating zones of high porosity that are likely concentrated in clusters, as seen in other examples of HTD reservoirs (Dewit et al., 2012).

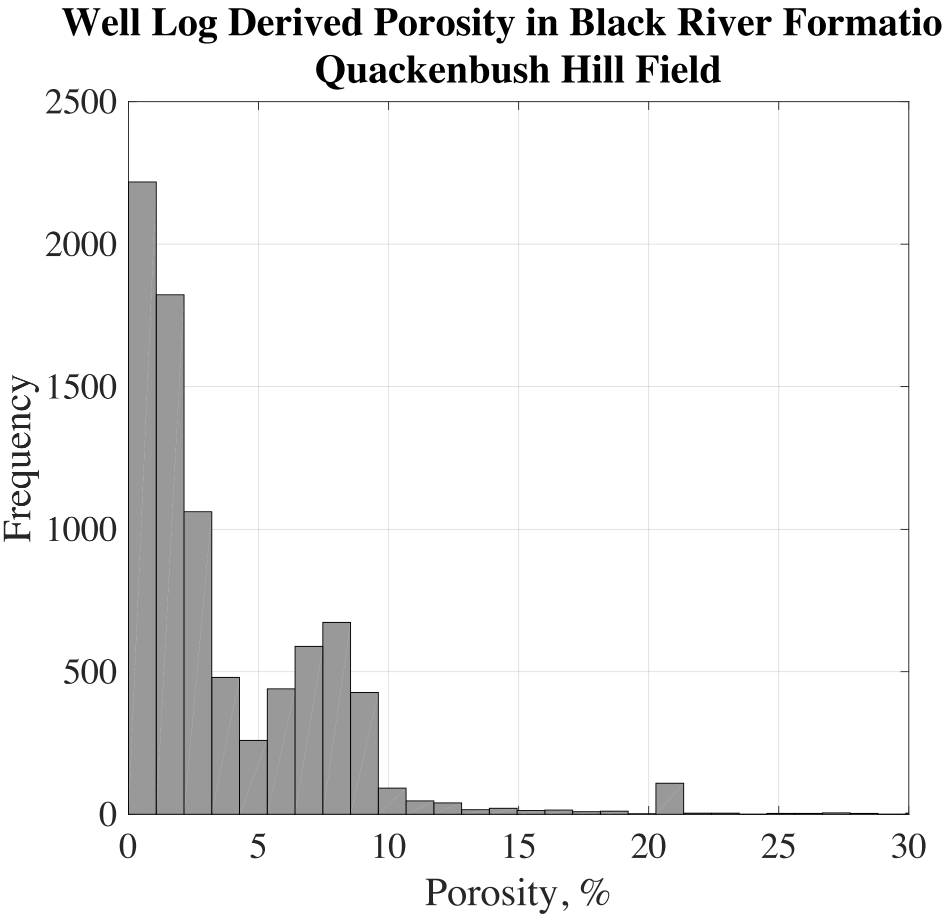

FIGURE 2.11. True porosity values corrected from neutron porosity hydrogen index (NPHI) log data collected in the producing intervals of ten wells from the Quackenbush Hill field, totaling 8380 measurements. The distribution is bimodal, with peaks at 0.5% and 8%, and a mean porosity of 4%. Data taken from Empire State Organized Geologic Information System (ESOGIS) database (ESOGIS, 2014).

Based on what is known of the origin and current reservoir quality of the Trenton-Black River HTD fields, we propose that fluid flow through an unstimulated Quackenbush Hill geothermal reservoir would most likely be controlled by fracture-connected vugs and clusters of variably sized vugs. However, the degree to which these clusters of high porosity and permeability are connected on a reservoir scale is currently unknown. A study by Philip et al. (2005) modeled fluid flow through a fractured dolostone reservoir and found that reservoirs with poorly interconnected fractures exhibit increased flow through the reservoir matrix (pore system). In a geothermal setting, this could equate to better heat sweep across a dolostone reservoir. The implementation of tracer tests at Quackenbush Hill field would help to characterize the connectivity between wells, reservoir geometry, and heat-sweep quality. Furthermore, geothermal fluid flow in these fields is likely to be confined to the dolomite regions, since tight limestone surrounds the dolomitized zones, which would conveniently prevent fluid loss and reduce pumping costs.

Stimulation

It is possible that the permeability in the Quackenbush Hill field, which was useful to the oil and gas industry, will not be suitable for geothermal heat extraction. In the case that the matrix permeability at Quackenbush Hill is too low to connect the clusters of high permeability found in vugs and fractures, then stimulation of the rock utilizing the principles of hydraulic shearing of preexisting fractures may be an option. Given the current stress regime, the first fractures to reactivate under increased pore fluid pressure would be any that are oriented vertically and strike approximately

N045°E and N097°E ± 15° at an estimated well-head pressure of 17 ± 5 MPa. Reactivation of such fractures would be favorable if the reservoir design goals included creating a network of fractures that strike obliquely to the strike of the grabens, forming serpentine pathways between the injection and production wells for increased heat sweep (Fig. 2.9). Additionally, reopening vertical fractures in the reservoir may enhance the vertical permeability, thereby optimizing heat sweep by gaining access to a greater vertical volume of rock. Stimulation may also be a feasible option for other nearby T-BR fields because their orientation (Fig. 2.2) relative to the known regional stress field is approximately the same as that of Quackenbush Hill.

Induced Seismicity

The principle of slip tendency analysis states that if the ratio of shear stress to effective normal stress on a fracture is greater than or equal to the sliding friction coefficient, slip is likely to occur (Morris et al., 1996). The slip tendency ratio for the graben-bounding normal faults under hydrostatic, non-stimulation conditions is 0.11, which is nearly seven times lower than the internal friction coefficient of 0.85 (Byerlee, 1978), indicating that the large observed faults are not close to failure in the current stress regime. Under stimulation conditions, that ratio increases to 0.33, which is still less than half of the sliding friction coefficient, indicating low risk. However, there is large uncertainty associated with the stress tensors used for this analysis. The confidence in the validity of the computed stress magnitudes is high because Quackenbush Hill field well ISIP values provided a reasonable upper and lower bound to our approximation. However, given the necessity of assuming a regional stress field at Quackenbush Hill field based on extrapolation from measurements at shallower depths in Auburn, New York and northern Pennsylvania, local stress field measurements are needed at Quackenbush Hill field. The simple slip tendency calculation on the main graben-bounding Quackenbush faults predicts that the faults are at low risk for reactivation, with or without stimulation. However, this analysis does not take into consideration any smaller sets of subsidiary faults associated with the negative flower structures, of which the orientations are unknown. To more rigorously assess the potential for reactivation of faults at Quackenbush Hill field, it would be advisable to (1) conduct geophysical surveys that could image the orientations and lateral dimensions of large faults that are not currently described by available data; (2) to better document three dimensional permeability near faults; and (3) to determine more accurately the local stress orientation with mini-frac tests. Public perception of induced seismicity, even of low magnitude (M1–M2) earthquakes that cannot damage surface infrastructure, is an important issue. Though we do not expect induced seismicity based on these preliminary results, seismic monitoring systems are highly advised if a geothermal energy production project were undertaken at Quackenbush.

Thermal Energy Utilization

An average reservoir temperature of 91 °C at an average depth of 3 km in the Quackenbush Hill field is adequate for a variety of end-use applications, including geothermal district heating, refrigeration, animal husbandry, greenhouses, swimming pool heating, and fish farming (Lindal, 1973). Residential use of the heat would increase infrastructure costs for piping and decrease efficiency because of the need to transport the heat to Elmira (15 km from center of field) or Corning (5 km from center of field). However, residential heating demand is high; according to the Energy Information Agency (2009), New York residences consumed 103 million BTU (or 1.1 x 10^{11} J) on average for space heating in the year 2009. In the case that the heat transport distance from Quackenbush Hill to either Corning or Elmira is economically feasible, the Quackenbush Hill field geothermal district heating system could provide space heating for 1,800–8,900 homes over the 30-year lifetime of the reservoir.

On-site use of the hot water would require capital costs for a new greenhouse, farm, or factory but would reduce operational costs and increase the overall efficiency of the system for the lifetime of the project. The strategy of building infrastructure at the site of the well field for on-site heat utilization would also open up the possibility of harnessing heat at T-BR fields that are farther away from population centers.

Conclusions

Our feasibility study of the Quackenbush Hill field shows promise for geothermal heating applications, given its proximity to a dense population of end users. An initial assessment suggests that this field could potentially provide between 5.8 x 10^{9}– 2.9 x 10^{10} MJ of energy to inhabitants and industries of the Elmira and Corning region for 30 years. Favorable conditions that are well understood and constrained by local data include temperature averaging 91 °C for direct-use applications at no more than 3.4 km depth and tight limestone sealing of a reservoir with suitable permeability, averaging 120 mD. Fluid flow through the entirety of the reservoir and between existing wells is less well known, though favorable stimulation conditions would optimize potential heat sweep, if needed. A preliminary analysis of the risk of inducing seismicity, using low-resolution regional stress data combined with minimal data on reservoir fault orientations, shows a low risk for inducing seismicity along major known faults. High-resolution stress and fault data are needed in future studies to reduce the uncertainty on this analysis.

These results may be applicable to the other New York T-BR hydrothermal dolomite gas fields. The T-BR gas fields that are still producing gas are nearing the end of production. If a relationship is built with the gas companies who currently own the fields, purchasing of the wells and additional data may be possible. Practical first steps to acquire higher-resolution data at Quackenbush Hill field are seismic reflection surveys, pump tests, and tracer tests to better map the field architecture and fault orientations, in addition to mini-frac tests to constrain the stress state in the reservoir.

Similar feasibility analyses can be performed on other conventional hydrocarbon fields to determine their suitability for repurposing to geothermal reservoirs. For hydrocarbon fields with sufficient permeability, heat availability, and a close proximity to potential end users of geothermal hot water, there is potential for cost savings and risk reduction for the geothermal industry in the transition from depleted hydrocarbon fields to geothermal heat production. Given the similarities in operations, infrastructure, and knowledge base between the petroleum and geothermal industries, there is also an opportunity for collaboration towards a beneficial relationship with mutual goals.

Acknowledgements

The authors are grateful to Brian Slater of the New York State Museum for his help in navigating the ESOGIS website and for kindly sharing his knowledge and data from the T-BR fields. We would also like to thank Dr. Robert Jacobi for sharing his detailed posters and knowledge from previous work on the T-BR fields, Professor Katie Keranen for her expertise on induced seismicity, Professor Richard Allmendinger for his insights and for the use of his MohrPlotter and Stereonet software, and Don Fox for his reservoir engineering wisdom. We appreciate the generosity of Petra IHS for providing free software licensing for university research. A special acknowledgment is warranted for the anonymous reviewers, the associate editor, and named reviewer Maria Richards, whose critiques of a previous manuscript led to significant improvements. Support for Erin Camp was provided by the National Science Foundation's Integrative Graduate Education and Research Training program (IGERT) through an award to Cornell University (DGE-0966045).

REFERENCES

Al-Jabri, R.A., Al-Maamari, R.S., and Wilson, O.B., 2015, Klinkenberg-corrected gas permeability correlation for Shuaiba carbonate formation: Journal of Petroleum Science and Engineering, v. 131, p. 172-176.

Bassiouni, Z., 1994, Theory, measurement, and interpretation of well logs: Richardson, TX, Henry L. Doherty Memorial Fund of AIME, Society of Petroleum Engineers.

Blackwell, D., Richards, M., Frone, Z., Ruzo, A., Dingwall, R., and Williams, M., 2011, Temperature-at-depth maps for the conterminous US and geothermal resource estimates: Geothermal Resource Council Transactions, v. 35, p. 1545-1550.

Blackwell, D.D., Richards, M., Batir, J., Frone, Z., and Park, J., 2010, New geothermal resource map of the northeastern US and technique for mapping temperature at depth: Geothermal Resources Council Transactions, v. 34, p. 313-318.

Brett, C.E., and Baird, G.C., 2002, Revised stratigraphy of the Trenton Group in its type area, central New York State: Sedimentology and tectonics of a Middle Ordovician shelf-to-basin succession: Physics and Chemistry of the Earth, Parts A/B/C, v. 27, no. 1, p. 231-263.

Byerlee, J., 1978, Friction of rocks: Pure and applied geophysics, v. 116, no. 4-5, p. 615-626.

Cladouhos, T.T., Petty, S., Nordin, Y., Moore, M., Grasso, K., Uddenberg, M., and Swyer, M.W., 2014, Reservoir construction from the Newberry Volcano EGS Demonstration: Journal of Groundwater Science and Engineering, v. 2, no. 3, 7 p.

Davies, G.R., and Smith, L.B., 2006, Structurally controlled hydrothermal dolomite reservoir facies: An overview: American Association of Petroleum Geologists Bulletin, v. 90, no. 11, p. 1641-1690.

Dewit, J., Huysmans, M., Muchez, P., Hunt, D.W., Thurmond, J.B., Vergés, J., Saura, E., Fernández, N., Romaire, I., and Esestime, P., 2012, Reservoir characteristics of fault-controlled hydrothermal dolomite bodies: Ramales Platform case study: Geological Society, London, Special Publications, v. 370, no. 1, p. 83-109.

Earth Satellite Corporation, 1997, Remote sensing and fracture analysis for petroleum exploration of Ordovician to Devonian fractured reservoirs in New York State: Rockville, Maryland, New York State Energy Research and Development Authority: http://www.earthsat.com/HTML/naturalvue/.

Energy Information Agency, 2009, Household Energy Use in New York: http://www.eia.gov/consumption/residential/reports/2009/state_briefs/pdf/NY.pdf.

Empire State Organized Geologic Information System (ESOGIS), New York State Museum, www.esogis.nysm.nysed.com (August 2014)

Fox, D.B., Sutter, D., and Tester, J.W., 2011, The thermal spectrum of low-temperature energy use in the United States: Energy & Environmental Science, v. 4, no. 10, p. 3731-3740.

Hickman, S.H., Healy, J.H., and Zoback, M.D., 1985, In situ stress, natural fracture distribution, and borehole elongation in the Auburn geothermal well, Auburn, New York: Journal of Geophysical Research: Solid Earth, v. 90, no. B7, p. 5497-5512.

Hurley, N.F., and Budros, R., 1990, Albion-Scipio and Stoney Point Fields-USA, Michigan Basin, *in* Foster, N., and Beaumont, E., eds., Stratigraphic Traps I: Treatise of Petroleum Geology Atlas of Oil and Gas Fields: Tulsa, Oklahoma, American Association of Petroleum Geologists, p. 1-37.

IHS U.S. Well Data, 2013, https://www.ihs.com/products/us-well-data.html (August 2014).

Jacobi, R., June 2014, pers. comm.

Jacobi, R., 2003, Definition of Trenton/Black River Prospects in the Finger Lakes Region, New York State, New York State Energy Research and Development Authority, Agreement NO. 4877-ERTER-ER-99, p. 1-42.

Jennings Jr, J.W., Lucia, F.J., 2003, Predicting permeability from well logs in carbonates with a link to geology for interwell permeability mapping, *in* Proceedings, Society of Petroleum Engineering (SPE) Annual Technical Conference and Exhibition: New Orleans, Louisiana, p. 215-225.

Lindal, B., 1973, Industrial and other applications of geothermal energy , *in* Armstead, C., ed., Geothermal Energy: Review of Research and Development, UNESCO, p. 135-148.

Manger, G.E., 1963, Porosity and bulk density of sedimentary rocks: U.S. Geological Survey Bulletin 1143–E, 55 p.

MarcellusGas.org, www.marcellusgas.org (June 2014).

Marner, P., Packard, J., Coulter, S., Jacobi, R., Agle, P., 2008, Cores from the Trenton-Black River (Ordovician) HTD Play in the Quackenbush Hill Field, Chemung County, New York: Calgary, Alberta, Canada, Canadian Society of Petroleum Geologists (CSPG) 2008 C3Geo Convention, Core Conference Abstracts, p. 35-53.

Morris, A., Ferrill, D.A., and Henderson, D.B., 1996, Slip-tendency analysis and fault reactivation: Geology, v. 24, no. 3, p. 275-278.

New York State Museum, 2014, FEI_Whiteman_core_analysis_030120.xls, Sep. 2014.

Philip, Z.G., Jennings, J.W., Olson, J.E., Laubach, S.E., and Holder, J., 2005, Modeling coupled fracture-matrix fluid flow in geomechanically simulated fracture networks: Society of Petroleum Engineers (SPE) Reservoir Evaluation & Engineering, v. 8, no. 4, p. 300-309.

Rasmussen, J.C., Keith, S.B., Swan, M.M., Laux, D.P., and Caprara, J., 2003, Strike-slip faulting and reservoir development in New York State: Albany, New York, New York State Energy Research and Development Authority, Agreement no. 6894, 161 p.

Rinaldi, A.P., Rutqvist, J., Sonnenthal, E.L., and Cladouhos, T.T., 2014, Coupled THM modeling of hydroshearing stimulation in tight fractured volcanic rock: Transport in Porous Media, v. 108, no. 1, p. 131-150.

Robertson, E.C., 1988, Thermal properties of rocks, U.S. Geological Survey Open File Report 88-441: Reston, Virginia, 106 p.

Roen, J.B., and Walker, B.J., 1996, The atlas of major Appalachian gas plays, West Virginia Geological and Economic Survey, Publication V-25, 201 p.

Ryan, G.P., 1981, Equipment used in direct heat projects: Geothermal Resources Council Transactions, v. 5, p. 233-241.

Schlumberger, 2009, Schlumberger Log Interpretation Charts: Sugar Land, Texas, Report 09-FE-0058, 293 p.

Shope, E.N., Reber, T.J., Stutz, G.R., Aguirre, G.A., Jordan, T.E., Tester, J.W., 2012, Geothermal resource assessment: A detailed approach to low-grade resources in the states of New York and Pennsylvania*:* Stanford, California, Stanford University, Proceedings of the 37th Workshop on Geothermal Reservoir Engineering, 9 p.

Slater, B.E., and Smith, L.B., 2012, Outcrop analog for Trenton-Black River hydrothermal dolomite reservoirs, Mohawk Valley, New York: American Association of Petroleum Geologists Bulletin, v. 96, no. 7, p. 1369-1388.

Smith, J., Horowitz, F., and Whealton, C., 2015, Thermal Model Methods, in Appalachian Basin Play Fairway Analysis: Thermal Quality Analysis in Low-Temperature Geothermal Play Fairway Analysis, Geothermal Data Repository, https://gdr.openei.org/submissions/638.

Smith, L., Nyahay, R., and Slater, B., 2009, Origin, distribution and reservoir characteristics of hydrothermal dolomite in lower Paleozoic carbonates in New York State: Albany, New York, New York State Energy Research and Development Authority, Contract no. 6605, p. 1691-1718.

Stutz, G.R., Williams, M., Frone, Z., Reber, T.J., Blackwell, D., Jordan, Tester, J.W., 2012, A well by well method for estimating surface heat flow for regional geothermal resource assessment: Stanford, California, Stanford University, Proceedings, 37th Workshop on Geothermal Reservoir Engineering, 16 p.

Talwani, P., and Acree, S., 1984, Pore pressure diffusion and the mechanism of reservoir-induced seismicity: Pure and Applied Geophysics, v. 122, no. 6, p. 947-965.

Tester, J.W., Drake, E.M., Driscoll, M.J., Golay, M.W., and Peters, W.A., 2012, Sustainable energy: Choosing among options: Cambridge, Massachusetts, MIT Press, 1019 p.

Thomas, W.A., 1991, The Appalachian-Ouachita rifted margin of southeastern North America: Geological Society of America Bulletin, v. 103, no. 3, p. 415-431.

van Staal, C.R., 2005, The Northern Appalachians, *in* Selley, R.C., and Plimer, I.R., eds., Encyclopedia of Geology: Amsterdam, Elsevier Academic, p. 81-91.

Whealton, C., Stedinger, J., and Horowitz, F., 2015, Thermal Quality Analysis BHT Corrections, in Appalachian Basin Play Fairway Analysis: Thermal Quality Analysis in Low-Temperature Geothermal Play Fairway Analysis, Geothermal Data Repository, https://gdr.openei.org/submissions/638.

Williams, C.F., 2007, Updated methods for estimating recovery factors for geothermal resources: Stanford, California, Stanford University, Proceedings, 32nd Workshop on Geothermal Reservoir Engineering, 7 p.

Williams, C.F., Reed, M.J., and Mariner, R.H., 2008, A review of methods applied by the U.S. Geological Survey in the assessment of identified geothermal resources: U.S. Geological Survey Open-File Report 2008–1296, 27 p.

CHAPTER 3

PREDICTING FRACTURE FREQUENCIES IN THE TRENTON-BLACK RIVER GAS FIELDS USING A DIAGENETIC ANALOG IN OUTCROP: AN APPLICATION TO GEOTHERMAL ENERGY EXTRACTION IN SEDIMENTARY RESERVOIRS

Abstract

The Trenton–Black River (T-BR) gas reservoirs of New York have been shown as promising candidates to repurpose for geothermal energy extraction (Chapters 1 and 2). Whereas these gas reservoirs are widely understood to be fracture-dominated systems, the architecture of fracture populations, including apertures and frequencies, is completely unknown. Characterizing the fracture architecture of these reservoirs is an important step before attempting to model their performance as geothermal reservoirs. Given that fractures are difficult to record in wireline logs (low resolution) and cores do not record a representative sample of large fractures, this study turns to an outcrop near Utica, New York that has been proven as a structural analog to subsurface T-BR hydrothermal dolomite reservoirs. Cathodoluminescence microscopy of samples from the outcrop suggest that the outcrop shares a similar diagenetic history to the subsurface gas reservoirs, despite differences in the original parent material at each location. A pilot fracture study of three transects at the outcrop indicated that a power law relationship exists between aperture and frequency in two of the three transects, though there is high uncertainty given the limited number of data points. Collecting fracture data from additional data transects is recommended in

future work to better constrain the relationship between fracture aperture and frequency in the subsurface T-BR reservoirs, which may serve as good candidates for future geothermal energy production.

Introduction

The Trenton–Black River (T-BR) hydrothermal dolomite grabens of New York formed during the late Ordovician shortly after their deposition, when transtensional tectonics led to the creation of highly fractured, negative flower structures that later became dolomitized by many stages of hydrothermal fluids (Hurley and Budros, 1990; Rasmussen et al., 2003; Davies and Smith, 2006; Patchen et al., 2006; Smith, 2006; Slater and Smith, 2012). When compared to other hydrocarbon reservoirs in the Appalachian Basin for potential geothermal fluid productivity (Chapter 1) and when analyzed individually for multicomponent geothermal feasibility (Chapter 2), the T-BR reservoirs show promising potential for sedimentary geothermal energy extraction. However, the understanding of the fracture architecture still needs improvement before conducting reservoir modeling to predict the performance of these gas fields as geothermal reservoirs. In this study, the term fracture architecture includes fracture apertures, orientations, and frequencies in the reservoir.

There are three primary reasons why the fracture architecture in these reservoirs is still poorly characterized. First, their reservoir quality is notoriously heterogeneous and laterally discontinuous (Smith, 2006; Smith et al., 2009; Slater and Smith, 2012), making it difficult to characterize the reservoirs with a simple model. As noted in Chapter 2, porosity in these reservoirs is found in both fractures and vugs, but not all vugs and fractures are still open (Smith et al., 2004; Marner, 2008). Work has not been done to quantify the heterogeneity and secondary fracture apertures (post-diagenesis), a step that is critical for a conceptual model of geothermal fluid flow. Open and partially sealed fractures and vugs, with sufficient permeability, are of interest to geothermal systems, as fluids can freely flow through them to be heated and pumped to Earth's surface for utilization.

Second, fracture frequencies and apertures are difficult to quantify or predict on the kilometer scale using cores and wireline image logs on the meter scale, which are currently the only data types available. Wide aperture fractures, which are of greatest interest, typically have low frequencies and may not be encountered by boreholes (Narr, 1991). When they are encountered by boreholes, it can be difficult to measure accurately their apertures if the fracture is not still intact. And third, these reservoirs have undergone multiple reactivations and fluid flow events since their original formation, creating new cements and fracture fills that have partially overprinted the original fracture porosity. Smith (2006) created a simple paragenetic timeline for these hydrothermal fields, in which a primary episode of fluid flow dolomitized the rock matrix, a secondary episode of fluid flow precipitated saddle dolomite cement in vugs and fractures, and a later fluid flow episode precipitated quartz and calcite. The exact timing of vug development relative to these fluid flow events is unknown (Smith, 2006). This study attempts to better understand the diagenetic history, cement growth patterns, and fracture architecture of the subsurface T-BR fields using an outcrop hydrothermal dolomite analog.

Slater and Smith (2012) studied a fully-exposed 55 m horizontal outcrop of a

Tribes Hill Formation hydrothermal dolomite body located within a quarry in Palatine Bridge, NY. At the end of the study, Slater and Smith (2012) concluded that the outcrop is a suitable match as a small-scale structural analog for the subsurface T-BR reservoirs. This study reports on a comparison of the hydrothermal dolomite bodies of the Palatine Bridge quarry rocks and those in a core from the County Line T-BR field. Cathodoluminescence microscopy (CL) is a key tool used to compare the outcrop and core samples. Thereafter, fracture sets in the outcrop hydrothermal dolomite system are studied and aperture-frequency relationships are quantified, and applied to the T-BR subsurface system.

Background

Fractures, Pore Space, and Dolomite

In rocks there exists void space, or porosity, which expresses itself in the form of fractures or pores, some of which are smaller and some of which are larger (vugs). The intention of this study is to predict the occurrence of fractures and vugs, both of which allow fluid flow through rocks.

The prevalence of dolomite in a rock that originated as a limestone is evidence of post-depositional chemical and mineralogical change, or diagenesis. The diagenetic process of a limestone becoming a dolomite is called dolomitization. During the process of dolomitization, pore space is preserved as relict porosity from the time of deposition. A compilation analysis of dolostone porosity by Lucia (2004) conclusively shows that dolomitized limestones inherit their porosity and fabric from the parent limestone without the creation of additional porosity. Over time, some or all of these pores can be filled via precipitation of new minerals (e.g. dolomite, quartz, calcite) during periods of hydrothermal fluid flow, becoming paleo-pores. When those pores are later filled with dolomite, that process is termed “over-dolomitization”. Henceforth, paleo-vugs are used to describe vugs that have been completed sealed, while vugs are those that have open pore space remaining. This applies to paleo-fractures and fractures as well.

A modern outcropping of a rock unit that is found elsewhere as a deep subsurface reservoir is not likely to possess the same pore space or diagenetic texture as a deep subsurface reservoir, even if the two reservoirs formed under identical conditions. This is because 1) diagenesis continues through time, inclusive of the time spent during uplift and exposure of the modern outcrop, and 2) because the two locations have experienced different paleo- and modern stress states, especially for the exposed outcrop rock unit which likely has an additional set of fractures created via the exhumation process.

The purpose of this study is to determine whether the deep subsurface reservoir and the outcrop analog had a similar history of pore space creation and diagenetic pore-reduction, after which their histories diverged. If their diagenetic histories are in fact similar, the primary hypothesis of this work is that a study of the outcrop will shed light on the pore space creation and destruction that took place before the geologic divergence of the outcrop and the subsurface reservoir. Prior studies of dolomite and dolomitization provide an understanding of how to recognize and characterize different types of dolomite and their crystal growth textures, which are distinct from primary sedimentary matrix material. In the remainder of this chapter, the term matrix refers to the bulk rock, while the term cement refers to crystals precipitated in fractures and vugs during late-stage diagenesis.

For example, saddle dolomite is a large-crystal dolomite precipitated during late-stage hydrothermal diagenesis. It is characterized by an opaque white color, curving or saddle-shaped crystal faces, and undulose extinction (Radke and Mathis, 1980). Furthermore, euhedral dolomite textures are composed of rhombohedral angular crystals; subhedral dolomite textures are composed of crystals with straight boundaries but not all rhombic; nonplanar dolomite textures are composed of closely packed crystals with curved boundaries (Sibley and Gregg, 1987). Saddle dolomite is considered a nonplanar dolomite texture.

Palatine Bridge Outcrop

In the Palatine Bridge outcrop, dolomite is localized in two en echelon fault-bounded segments with lengths of 17 and 33 m, both of which are oriented approximately NW-SE (Figure 3.1). Slater and Smith (2012) constructed a detailed fracture map of the outcrop, ran a 3D ground-penetrating radar survey, drilled six 5-cm diameter cores ranging from 12-20 meters in length (Holes 1–6; Figure 3.1), and drilled plugs incrementally along a lengthwise (L) transect, which starts at the southeast end of the exposure and continues northwestward through the dolomite bodies. The authors report the presence of vugs lined with quartz, calcite, and saddle dolomite throughout the dolomite bodies. Brecciation occurs throughout the dolomite, though it is most common at the tips of the dolomite bodies. Slater and Smith (2012) reported that the maximum fracture length is 30.48 m. Furthermore, there is a sharp contrast at the fault surfaces, separating tight limestone from the dolomitized rock bodies. The GPR survey indicates that the two en echelon segments are connected at depth. Slater and Smith (2012) tested calcite and dolomite cements in the outcrop for fluid inclusion homogenization temperatures and salinities, stable isotopes (δ^{18}O and δ^{13}C), and Strontium isotope ratios, and compared the results to those of cores from producing fields reported by Smith (2006). Their Strontium and fluid inclusion results plot within the same ranges as those from the producing fields. Furthermore, the authors conclusively demonstrated that the outcrop is of hydrothermal origin, like the subsurface reservoirs studied by Smith (2006).

However, the authors did not compare the trace elements and their impact on the growth texture of late-stage pore- and fracture-filling saddle dolomite. Furthermore, the authors did not determine the extent to which the differing original formations (Tribes Hill Limestone versus Black River Limestone) impacted the pre-diagenetic porosity and permeability of the respective reservoirs, and therefore the modern porosity, permeability, and texture of matrix dolomitization. For example, the Black River Formation is a muddy, fine-grained limestone that was deposited on a shallow tropical carbonate ramp (Smith et al., 2009), while the Tribes Hill Formation is characterized as a well-bedded, subtidal carbonate deposit with the presence of ooids and intraclasts (Braun and Friedman, 1969). Because of its larger grain size, the Tribes Hill limestone likely had a higher original porosity than the Trenton-Black River limestone, and therefore may have different characteristics of matrix diagenesis, including matrix cement quantity and growth textures. These two aspects of reservoir diagenesis, the dolomite growth textures and the impact of original lithology, are important to assess before adopting the outcrop as a diagenetic analog to the subsurface T-BR reservoirs. This relationship is important in determining the extent to which porosity has been reduced in the subsurface reservoirs, including the post-diagenetic fracture aperture reduction, which is important for geothermal applications.

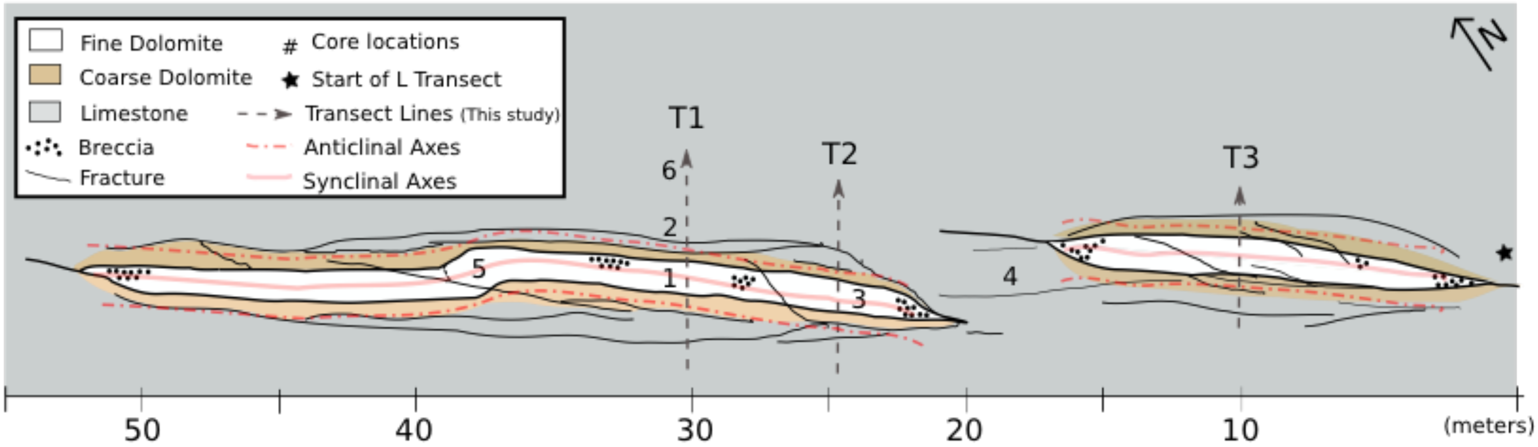

FIGURE 3.1. Schematic of the Palatine Bridge outcrop hydrothermal dolomite floor exposure, studied by Slater and Smith (2012) and in this work. The exposure is approximately 55 m in length, separated into two discrete dolomite bodies, one about 17 m in length, the other about 33 m in length. The dolomite bodies are composed of fine dolomite and flanked by fine-grained dolomite. The center of the dolomite bodies forms a syncline between a set of two anticlines that flanks the northeastern and southwestern sides of the dolomite bodies. Breccia (shown by black dots) is present at the tips of the two dolomite bodies. Fractures (indicated by solid black lines) are primarily oriented parallel to the orientation of the dolomite bodies, with a separate fracture set trending diagonally across the bodies, NW-SE. The core locations (Slater and Smith, 2012) are shown by the numbers 1–6, and the starting location of Slater and Smith's (2012) L transect is shown by the black star. The scale bar starts from the right side of the image to align with the directionality of the L transect. The locations of the three transects for this study's fracture analysis are shown by the gray dashed line arrows. The length of the arrows does not represent the true length of the transects, though each transect crosses the complete width of the dolomite body. Transect #1 is 7.6 m long; Transect #2 is 6.7 m long, and transect #3 is 5.3 m long.

Cathodoluminescence and Cement Stratigraphy

CL is a process by which a sample is bombarded with an electron beam until its contents luminesce. CL can be used as a qualitative tool to interpret details of carbonate diagenesis that traditional optical microscopy cannot detect (Boggs and Krinsley, 2006). Carbonates luminesce along different spectral peaks depending on the relative concentrations of Mn^{2+} and Fe^{2+} (Machel and Burton, 1991; Machel, 2000; Boggs and Krinsley, 2006). Manganese is the most common activator of luminescence in carbonates, whereas iron is the most common quencher of luminescence. CL can be used to determine different generations of fluid flow during diagenesis using relative luminescence and cement stratigraphy (Yoo et al., 2000; Boggs and Krinsley, 2006), porosity evolution during subsequent generations of fluid flow using crystal texture and zoning analysis (Mclimans, 1991; Machel, 2000), and sometimes even paleo-fluid flow direction (Machel, 2000; Yoo et al., 2000). In this study, CL was utilized in two ways: cement stratigraphy of saddle dolomite cements in vugs and fractures, and a fabric analysis of matrix dolomite textures.

Cement stratigraphy is a process by which one compares the textures, luminescence, and thicknesses of diagenetic minerals (that line and occlude paleo-pores and paleo-fractures) within a single thin section, across many samples from a core, or across samples from different locations to determine diagenetic similarity (Machel, 2000; Boggs and Krinsley, 2006). Cement stratigraphy via CL was utilized in this study as a tool to qualitatively determine the diagenetic similarity (number of CL bands, zoning style) of porosity-reducing saddle dolomite between the gas reservoir core and the outcrop samples. The Whiteman #1 core from the County Line gas reservoir in New York was utilized for this study. Smith (2006) conducted a petrographic analysis of the core, noting that more than 95% of the core is medium to coarse (50–400 µm) matrix replacement dolomite, with negligible porosity.

Fracture Architecture

Fracture intensity measurements, including spacing and apertures, were recorded at the Palatine Bridge outcrop. The ability to scale up and apply a fracture aperture-frequency relationship from a small outcrop analog to a much larger (up to 200x) hydrothermal dolomite reservoirs is valuable where fracture data from the subsurface are unavailable. Therefore, we apply the scale-independent fracture intensity analysis used by Ortega et al. (2006), which allows for fracture frequency relationships to be scaled up after being normalized by the length of the exposure measured. This method also addresses the borehole fracture sampling problem mentioned above, which is a fundamental challenge to subsurface fracture characterization. We expect an inverse relationship between fracture aperture and cumulative frequency: smaller aperture fractures should have higher frequencies, and larger aperture fractures should have lower frequencies.

Methods

Petrographic Comparison

Forty-two samples were selected from the Fortuna Whiteman #1 core (Whiteman) and the Palatine Bridge outcrop L transect plugs and cores, all of which are currently housed at the New York State Museum warehouse in Rotterdam, NY

(Table 3.1). All the samples were made into standard microscopy thin sections by Mann Petrographics. To help differentiate between dolomite and calcite, all the thin sections were half-stained with an Alizarin Red-hydrochloric acid mixture by Wagner Petrographics. Because calcite is more reactive to weak acid than dolomite, calcite retains the red stain, while dolomite does not.

Saddle dolomite composition, texture, and luminescence were characterized in thin section using a Technosyn cold-cathodoluminescence (CL) stage unit attached to an Olympus SZX-10 stereomicroscope equipped with an Olympus DP72 12.8MP digital color camera. Operating conditions were controlled with a Reliotron console, typically at 7–8 kV beam voltage and 0.6–0.8 mA beam current, with a chamber pressure between 80–90 mTorr. This machine is located at St. Lawrence University, in the carbonate laboratory of Professor Antun Husinec. All interesting examples of void-filling saddle dolomite were photographed in plane light and under CL conditions.

Petrography was applied to the reservoir rock matrix to assist in determining the effect of original lithology on matrix dolomitization, and therefore on diagenesis in the reservoirs. For example, the differences in dolomite crystal size and boundary shape, such as crystal faces that are planar (euhedral or subhedral) or instead anhedral, were noted.

TABLE 3.1. Catalog of samples examined during CL and petrographic analysis. Note: Core locations are depths, while plug locations are distance along the L transect.

Sample	**Formation**	**Sample Type**	**Location**	**Location Units**
H2D1.5	Tribes Hill	Core	1.5	Inches (in)
H2D7.2	Tribes Hill	Core	7.2	in
H3D39	Tribes Hill	Core	39	in
H3D31	Tribes Hill	Core	31	in
H3D1	Tribes Hill	Core	1	in
H3D17	Tribes Hill	Core	17	in
H3D41.5	Tribes Hill	Core	41.5	in
H4D1	Tribes Hill	Core	1	in
H5D31.2	Tribes Hill	Core	1.2	in
H5D11	Tribes Hill	Core	11	in
H5D25	Tribes Hill	Core	25	in
H6D31.5	Tribes Hill	Core	31.5	in
H6D37	Tribes Hill	Core	37	in
H6D19	Tribes Hill	Core	19	in
L6	Tribes Hill	Plug	6	in
L18	Tribes Hill	Plug	18	in
L28	Tribes Hill	Plug	28	in
L54	Tribes Hill	Plug	54	in
L62	Tribes Hill	Plug	62	in
L78	Tribes Hill	Plug	78	in
L96	Tribes Hill	Plug	96	in
L106	Tribes Hill	Plug	106	in
L110	Tribes Hill	Plug	110	in
L114	Tribes Hill	Plug	114	in
L132	Tribes Hill	Plug	132	in
9529.5	Black River	Core	9529.5	Feet (ft)
9530.5	Black River	Core	9530.5	ft
9531	Black River	Core	9531	ft
9532	Black River	Core	9532	ft
9532.6	Black River	Core	9532.6	ft
9533.2	Black River	Core	9533.2	ft
9534	Black River	Core	9534	ft
9535	Black River	Core	9535	ft
9535.5	Black River	Core	9535.5	ft
9537.3	Black River	Core	9537.3	ft

Sample	**Formation**	**Sample Type**	**Location**	**Location Units**
9538	Black River	Core	9538	ft
9538.5	Black River	Core	9538.5	ft
9549	Black River	Core	9549	ft
9549.5	Black River	Core	9549.5	ft
9550	Black River	Core	9550	ft
9553.3	Black River	Core	9553.3	ft
9555.2	Black River	Core	9555.2	ft

Outcrop Fracture Measurements

The outcrop was in poor condition compared to when the Slater and Smith (2012) study was conducted, as the entire dolomite body was covered in four years' worth of dust, silt, and vegetation. Three transects were cleaned of dust and silt particles using brooms, a leaf blower, water, and brushes. After cleaning, the transects were better exposed but small sections along the central region of the dolomite bodies retained a silt cover.

The transects at the outcrop are oriented approximately NNE—perpendicular to the orientation of the dolomite bodies and to many fracture sets associated with the dolomite bodies. The start of each transect began approximately two to three meters southwest of the dolomite bodies in the fractures limestone (on the southern flank of the southern anticline), crossed the entire width of the dolomite, and ended two to three meters northeast of the dolomite bodies (on the northern flank of the northern anticline). Along each transect, all discernable paleo-fractures (those that existed during the time of hydrothermal diagenesis) were recorded for aperture, distance from transect origin, strike, and dip. Measurable fractures were located in the limestone surrounding the dolomite bodies, as well as in the coarse and fine dolomite portions of the bodies (Figure 3.1). However, due to the silt cover remaining in the central syncline of the dolomite bodies, very few fractures were measurable there.

To prevent the recording of modern fractures that originated from recent explosive blasting, only mineralized veins and paleo-fractures with some degree of mineralization were recorded. Though non-mineralized subsurface fractures are of interest for this study, the assumption is that the frequencies of partially to completely mineralized outcrop fractures are indicative of the frequencies of partially to completely mineralized subsurface fractures in the Trenton-Black River reservoirs. Furthermore, the work in Chapter 4 addresses the issue of the degree of fracture mineralization.

Each paleo-fracture's aperture was measured using a calibrated logarithmic comparator and a hand lens, the distance from the transect origin was measured using a measuring tape, and strike and dip were measured using either a Brunton compass or an iPhone compass app. Measuring paleo-fractures with a logarithmic comparator groups fracture into logarithmically graduated 'aperture groups' (e.g. 0.5, 0.62, 0.75, 0.95 mm). For example, a paleo-fracture measured in outcrop that is approximately 0.52 mm would be grouped in the 0.5 mm aperture group.

Paleo-Fracture Analysis and Scaling

Paleo-fracture data were analyzed using the cumulative process described by Ortega et al. (2012). All fractures were ordered by aperture from largest to smallest, and assigned increasing numbers, starting at one. Next, the cumulative numbers were normalized by the length of the transect. The resulting aperture data were plotted against cumulative fracture frequency, and a least squares regression was performed to detect a trend in the data.

Results

Petrography

The Whiteman core includes original limestone matrix-replacement dolomite, saddle dolomite lining vugs and paleo-fractures, paleo-vugs now sealed completely by saddle dolomite, and quartz and calcite cement completely sealing paleo-vugs and paleo-fractures. Two distinct types of original limestone matrix-replacement dolomite occur: Type 1, a dull to non-luminescent, nonplanar to subhedral dolomite matrix (5-400 µm; Figure 3.2), and Type 2 a dull orange luminescent subhedral dolomite matrix (100-500 µm; Figure 3.3). Euhedral dolomite crystals ranging in size from 50-250 µm are present in the Type 1 matrix, occurring in distinct bands (Figure 3.7). These crystals do not luminesce under CL, and contain dark inclusion-rich cores. In the Type 2, the luminescent matrix replacement dolomite is present only in a 3-foot section of the core between 2908.2–2909.2 m depth (Table 3.1), which includes brightly luminescent sealed microfracture sets, open vugs, bitumen, and a wispy texture only detectable under CL (Figure. 3.4).

Saddle dolomite is present as a porosity-reducing fill in paleo-fractures and paleo-pores throughout the core. The first generation of saddle dolomite (nearest to the wall of paleo-fractures and paleo-pores) does not luminesce; however, a later generation that precipitated on top of the older generation is concentrically zoned, alternating non-luminescent and bright orange luminescent, with up to five discrete CL bands (Figure 3.5). There are both open vugs (filled slightly by saddle dolomite but still contain some pore space) and sealed paleo-vugs (which have no remaining pore space) present in the Whiteman core, with open vugs up to 6 mm in width. Vugs are elongate to circular in shape, often lined with saddle dolomite, and often connected to a fracture (Figure 3.6). Some paleo-vugs contain quartz and calcite cements that post-date the saddle dolomite. Dissolution surfaces of luminescent saddle dolomite are noted at depths of 2909.1 (Figure 3.4), 2912.6, and 2912.8 m in the core (Table 3.1). Brightly luminescent calcite-mineralized fractures, which post-date the saddle dolomite, often found in parallel sets, are noted throughout the core (Figures 3.3 and 3.4).

In the Palatine Bridge outcrop, there are four distinct matrix fabrics observed in thin section. These range from Type 3 which displays only a small degree of dolomitization of the primary depositional calcite, to categories that are fully dolomitized. Type 3 occurs in two of the surface transect plugs, where the original calcite matrix is preserved and contains occasional euhedral dolomite crystals and fossil remnants (Figure 3.8). These two plugs were drilled at 54 and 62 feet from the eastern tip of the outcrop, which is situated between the two dolomite bodies. Calcite is identified by the preservation of the red alizarin stain. In the half of the calcite thin sections that did not receive the stain, the original calcite luminesces a red-orange color. Where the calcite is stained, the calcite luminescence is dampened. The euhedral crystals found in the calcite matrix have dull red-orange concentric zoned luminescence, with up to five zones, and have been partially dissolved post-emplacement. Dissolution appears to post-date all five luminescence zones. The crystals are situated in a linear fashion, in line with the narrow zone of non-luminescence in the un-stained half of the thin section (Figure 3.8).

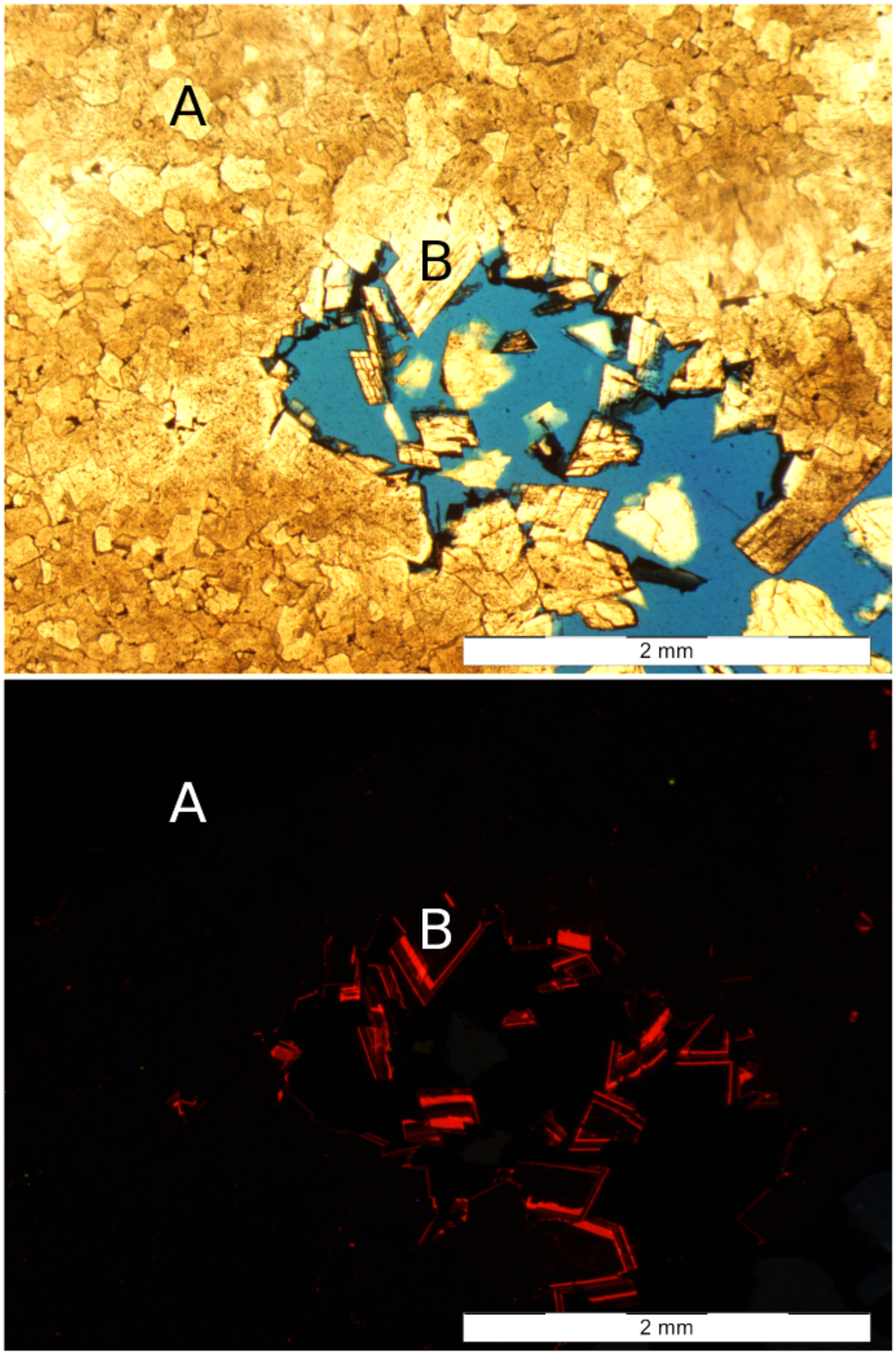

FIGURE 3.2. Fortuna Whiteman #1 thin section images from 2907.4 m depth, plane light (above) and CL (below). Two dolomite textures are present: (A) WM Type 1 non-planar to subhedral matrix replacement dolomite that does not luminesce under CL, and (B) saddle dolomite cement, which has a concentric zoning under CL, lining the open vug. The blue area in the plane light image is an open vug. Scale bar is 2 mm.

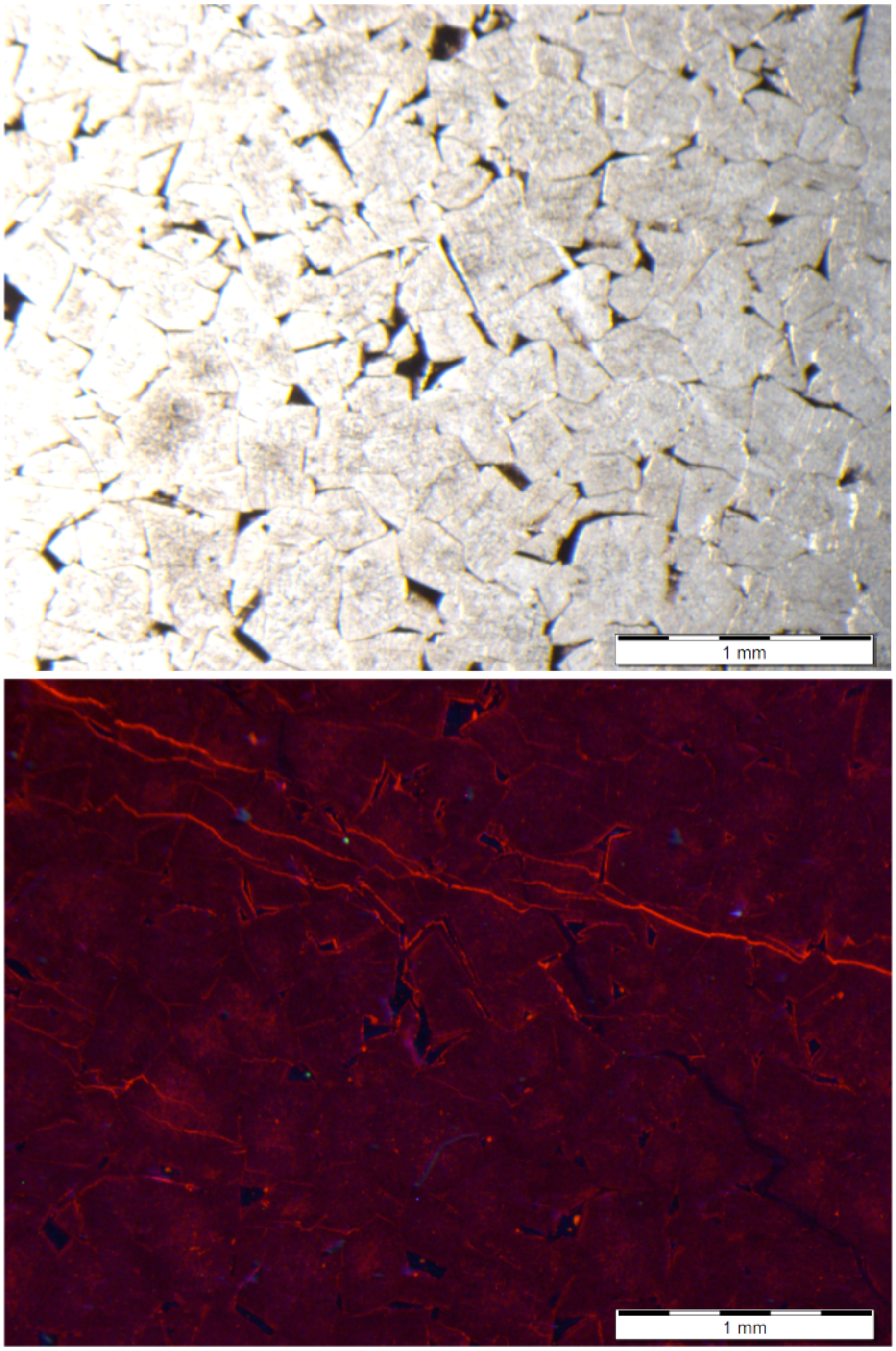

FIGURE 3.3. Fortuna Whiteman #1 thin section images from 2909.2 m depth, plane light (above) and CL (below). The images show WM Type 2 matrix fabric, a subhedral to nonplanar matrix dolomite texture that has dull to moderate luminescence. Bitumen is in the pore spaces. The bright luminescent parallel lines interpreted as mineralized calcite microfractures. Scale bar is 1 mm.

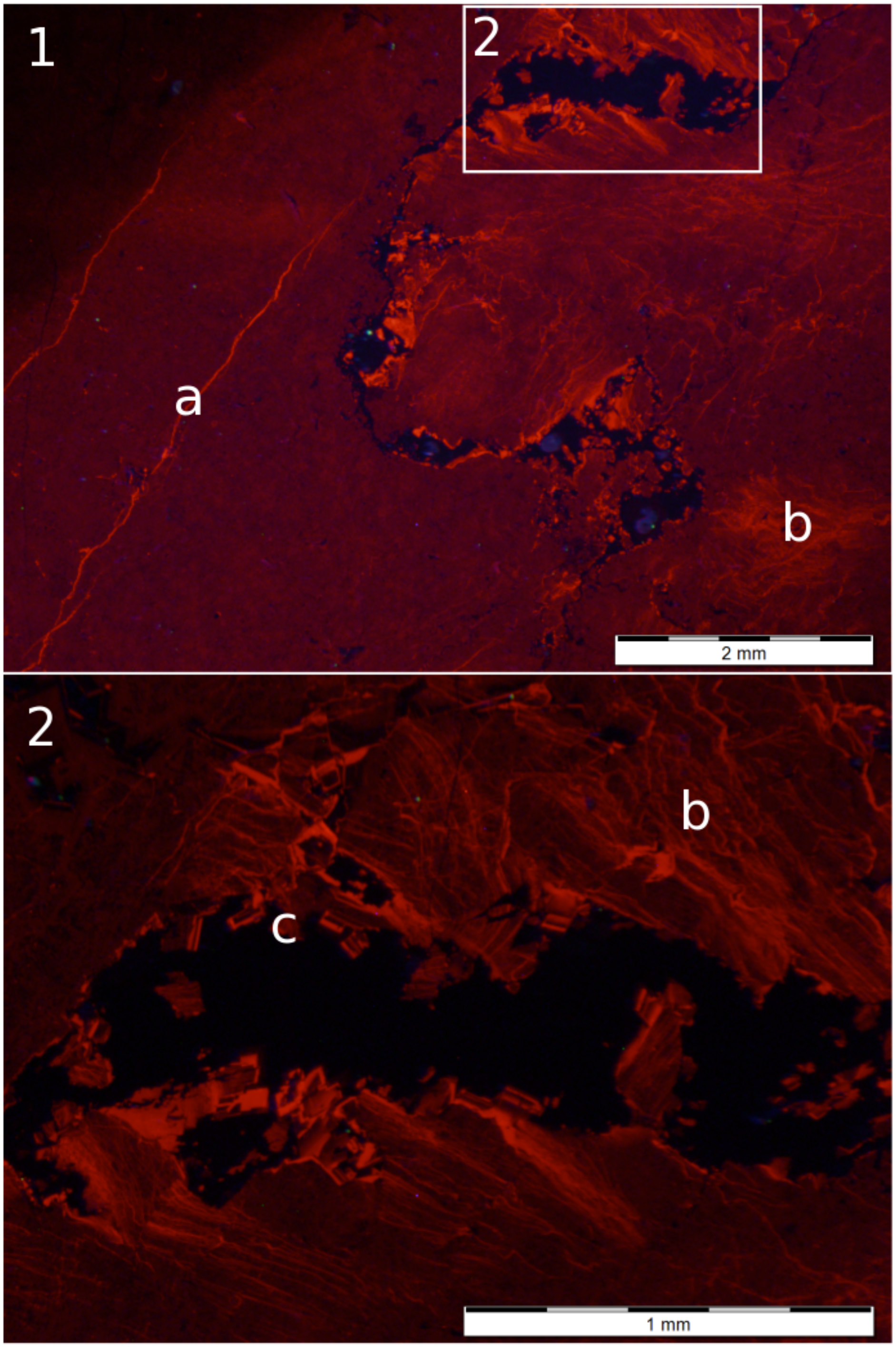

FIGURE 3.4. Fortuna Whiteman #1 thin section CL images from 2909.1 m depth. Panel 1 above shows an open vug system, a set of sealed brightly luminescent paleo-fractures (a), moderately luminescent matrix dolomite, and wispy vein-like patterns of luminescence in the matrix (b). The white rectangle inset is enlarged below in Panel 2, where small crystals of zoned saddle dolomite are present along the walls of the vug (c), but appear to have been altered post-emplacement, likely by a fracturing and additional fluid flow event. Scale bar above is 2 mm and below is 1 mm.

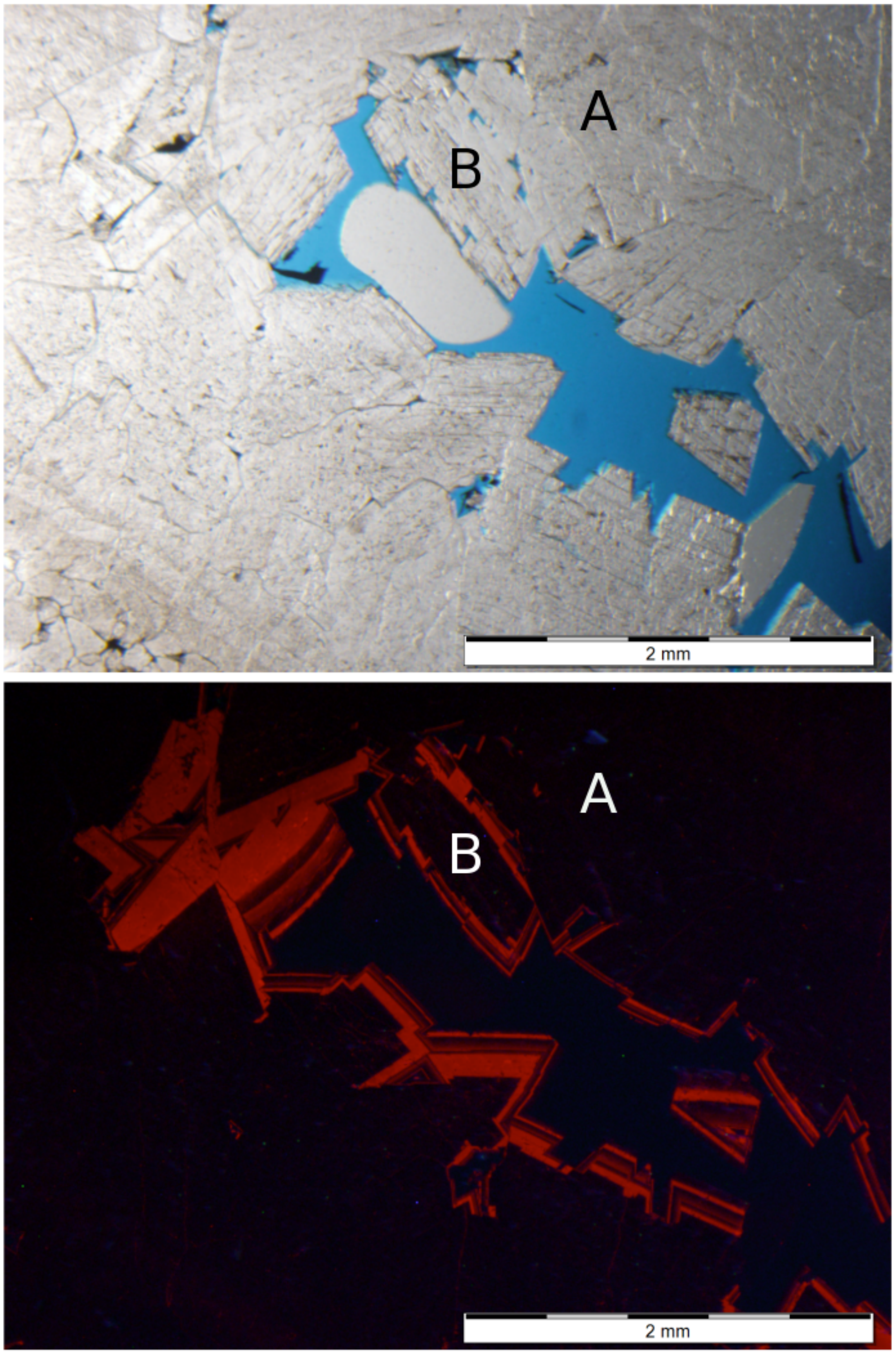

FIGURE 3.5. Fortuna Whiteman #1 thin section images from 2908.2 m depth, plane light (above) and CL (below). The images show an elongate open vug approximately 1 mm in width and 4 mm in length. The vug is lined with saddle dolomite, first by a non-luminescent generation (A) and later by a concentrically zoned luminescent generation (B). The blue area in the plane light image is pore space, which includes a white bubble in blue epoxy. Scale bar is 2 mm.

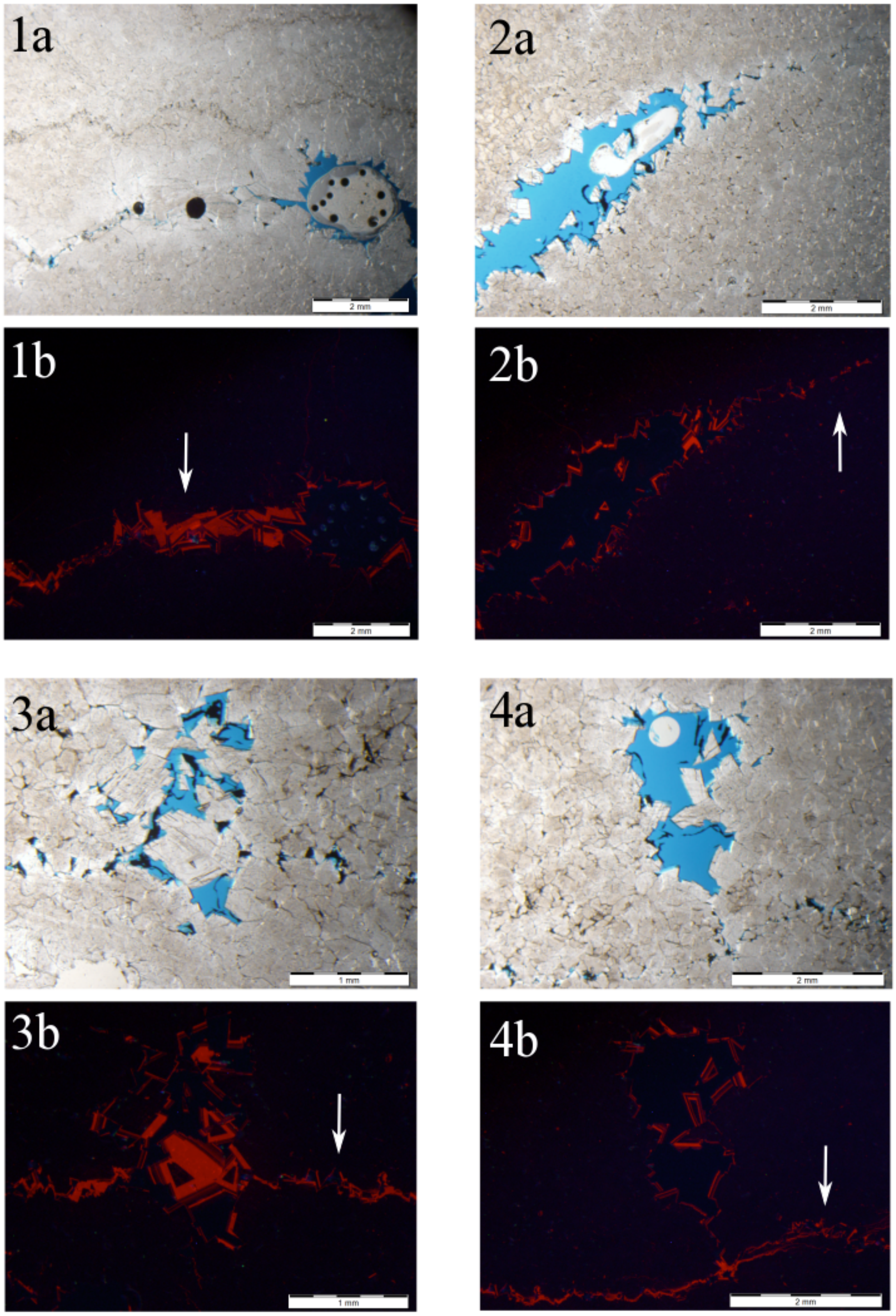

FIGURE 3.6. Fortuna Whiteman #1 thin section images under plane light (1a, 2a, 3a, and 4a) and CL (1b, 2b, 3b, 4b), depicting open vugs associated with fractures (shown by white arrows). Vugs can have a circular shape (1a, 1b), elongate shape aligned with the fracture (2a, 2b), or elongate and perpendicular to the trend of the fracture (3a, 3b, 4a, 4b). Images 1a and 1b are from 2906.5 m depth; images 2a and 2b are from 2907.4 m depth; images 3a-4b are from 2907.9 m depth. The blue areas in the plane light images are pore spaces, occasionally filled with bitumen and air pockets.

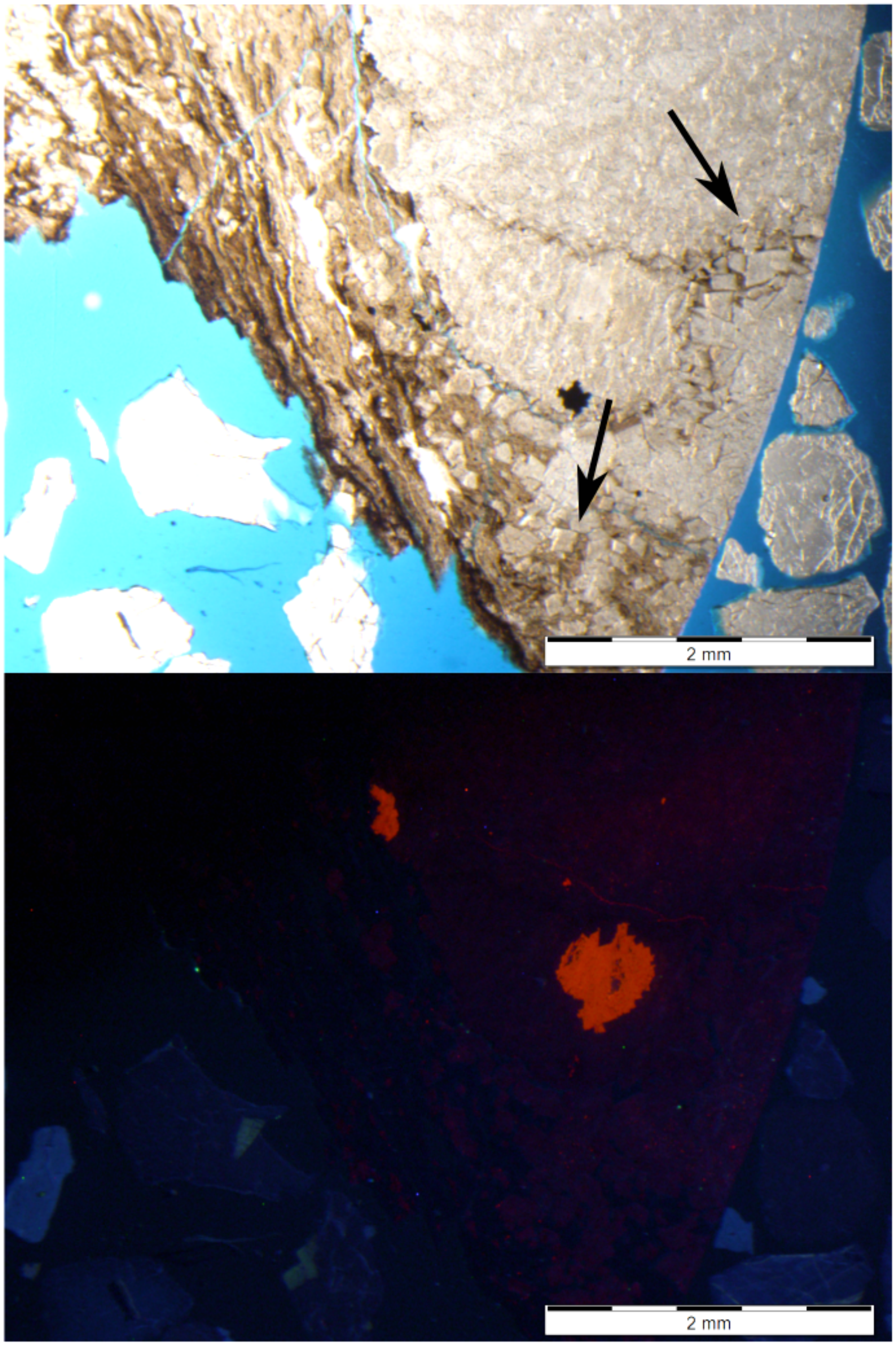

FIGURE 3.7. Fortuna Whiteman #1 thin section images from 2912.8 m, plane light (above) and CL (below). Black arrows indicate euhedral dolomite crystals, which range from 50–250 µm. In the lower CL image, those dolomite crystals do not luminesce. The bright orange luminescent patches are calcite, precipitated post-saddle dolomite. The scale bar in all images is 2 mm.

TABLE 3.2. Cathodoluminescence results for Whiteman #1 core samples.
Notes: the numbers in square brackets refers to the quantity of vugs or fractures identified in the sample.

Depth (m)	Vugs [#]	Fractures [#]	Matrix #	Saddle Dolomite	Other
2906.50	[3] 2 mm open vugs lined with saddle dolomite	[1] 1 mm semi-open fracture; vugs lie along fracture	1	2 generations: (1) non-luminescent, (2) Concentric zoning, 4 bands	Non-luminescent generation is older
2906.80	[1] 4 mm open vug lined with saddle dolomite	none	1	2 generations: (1) non-luminescent, (2) Concentric zoning, 4 bands	See above; dissolution present
2906.96	[1] 1 mm open vug, lined with saddle dolomite; [2] sealed vugs (<1mm)	[1] vein (< 1 mm), only detectable in CL	1	2 generations: (1) non-luminescent, (2) Concentric zoning, 4 bands	Non-luminescent generation is older
2907.26	none	[1] 1 mm vein, filled with saddle dolomite	1	Semi-dissolved luminescent crystals	Dissolution present
2907.44	[1] 2-6 mm open vug lined with saddle dolomite	Vug pinches out to a fracture	1	2 generations: (1) non-luminescent, (2) Concentric zoning, 4 bands	Non-luminescent generation is older
2907.63	[1] 2 mm open vug lined with saddle dolomite	none	1	2 generations: (1) non-luminescent, (2) Concentric zoning, 4 bands	See above; dissolution present
2907.87	[1] 2.5 mm open vug lined with saddle dolomite; [1] 2 mm open vug lined with saddle dolomite	[1] Semi-filled fracture, lined with zoned saddle dolomite.	1	2 generations: (1) non-luminescent, (2) Concentric zoning, 4-6 bands	Fewer zones in fracture than in vug. Vug sits perpendicular to fracture, connected by small fracture.
2908.33	[1] 3 mm open vug and [1] part of a 6 mm open vug	[5] calcite veins, luminescent bright orange. All < 1 mm.	1	2 generations: (1) non-luminescent, (2) Concentric zoning, 4-6 bands	Dissolution present

Depth (m)	Vugs [#]	Fractures [#]	Matrix Type	Saddle Dolomite	Other
2908.88	[1] 5 mm open vug lined with saddle dolomite	[9] calcite veins, luminescent bright orange. All < 1 mm.	1	2 generations: (1) non-luminescent, (2) Concentric zoning, 4-5 bands	Bright fractures are in two distinct sets, ~120° from each other. Dissolution present
2909.09	[2] curved connected vugs, lined with saddle dolomite	[2] parallel, luminescent calcite veins.	2	2 generations: (1) non-luminescent, (2) Concentric zoning, 4 bands	One fracture intersects open 2mm vug; dissolution present
2909.24	none	[4] en echelon calcite veins filled with bright orange luminescence.	2	none	Euhedral dolomite crystals have faint zoning
2912.60	none	[1] 3 mm vein, now filled by dolomite, saddle dolomite, and calcite	1	none	Remnants of zoned crystals that have been dissolved
2912.60	[1] open 2 mm vug (cut off by edge of thin section), lined with saddle dolomite	none	1	2 generations: (1) non-luminescent, (2) Concentric zoning, 5 bands	Very thick zones in saddle dolomite, up to .75 mm thick
2912.75	[1] sealed 8 mm vug, with saddle dolomite and calcite cement	none	1	2 generations: (1) non-luminescent, (2) Concentric zoning, 5 bands	
2912.75	[1] sealed 6 mm vug, lined with saddle dolomite and calcite	[1] luminescent fracture adjacent to vug	1	2 generations: (1) non-luminescent, (2) Concentric zoning, 5 bands	Dissolution present
2913.76	[1] 2 mm sealed vug with saddle dolomite and calcite	[3] parallel (<1 mm) luminescent calcite veins	1	2 generations: (1) non-luminescent, (2) Concentric zoning, 3 bands	Zoned bands are very thin; calcite dominates
2914.28	[1] 0.5 mm vug sealed by saddle dolomite and calcite	[2] parallel luminescent thin calcite veins	1	none	Calcite dominates

Fabric Type #4 is most common, and contains anhedral blue-luminescent replacement-dolomite crystals (< 50 μm) scattered with orange luminescent euhedral to subhedral dolomite cement crystals that show evidence of dissolution. This fabric type is found across the entirety of the L transect, except for the non-dolomitized section between the two dolomite bodies. This fabric is also found in core holes #3, 5, and 6, between the depths of 0.3–9.5 m (Table 3.2).

Type 5 is a dolomite matrix that has preserved the original ooid-shaped grainstone fabric of the rock. The ooid-dominated rock luminesces deep red-orange, and is composed of crystals ranging from 100–250 μm in diameter (Figure. 3.10). This fabric type is located in holes 5 and 6 at depths of 0.8 m. Type 6 dolomite fabric is very fine-grained (<100 μm), contains dolomitized intraclasts and does not luminesce (Figure 3.11). This fabric is observed in holes #2, 3 and 4, at depths of 0.04 m, 0.2 m, and 1 m.

The CL images of types #3, and 4 display a blue speckled-luminescence (Figures 3.8 and 3.9), most likely due to contributions of Mg^{2+} or Fe^{2+} from accessory siliciclastic grains (Major, 1991) originally deposited in the Tribes Hill that have since been dissolved.

Saddle dolomite is present as the lining in vugs and fractures throughout the outcrop. The first generation of saddle dolomite (closest to the wall of the vugs and fractures) is non-luminescent, followed by concentrically-zoned saddle dolomite, which alternates from non-luminescent to bright orange (Figure 3.12).

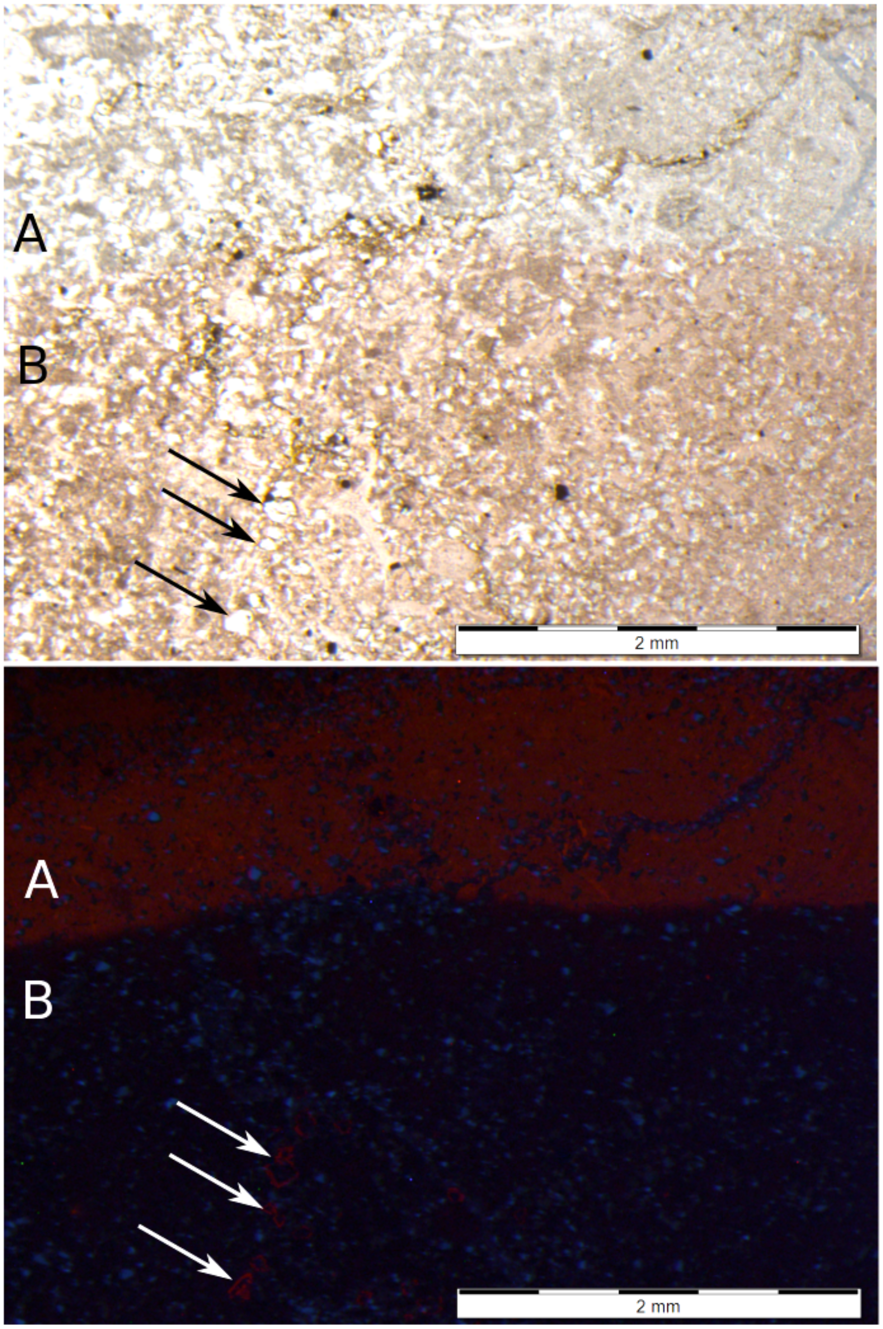

FIGURE 3.8. Palatine Bridge outcrop thin section images of the original depositional limestone Type 3 matrix, plane light above and CL below. Sample taken from a plug located 18.9 m from the start of the surface transect. In both images, the Alizarin Red-stained area of the thin section is identified by the letter B, and the unstained area by the letter A. When stained, the calcite-dominated matrix does not luminesce, and where unstained, luminesces a dark red-orange color. Occasional small luminescent euhedral dolomite grains are found in this matrix type, shown in both images by the arrows, which are touching the crystals. The scale bar in both images is 2 mm.

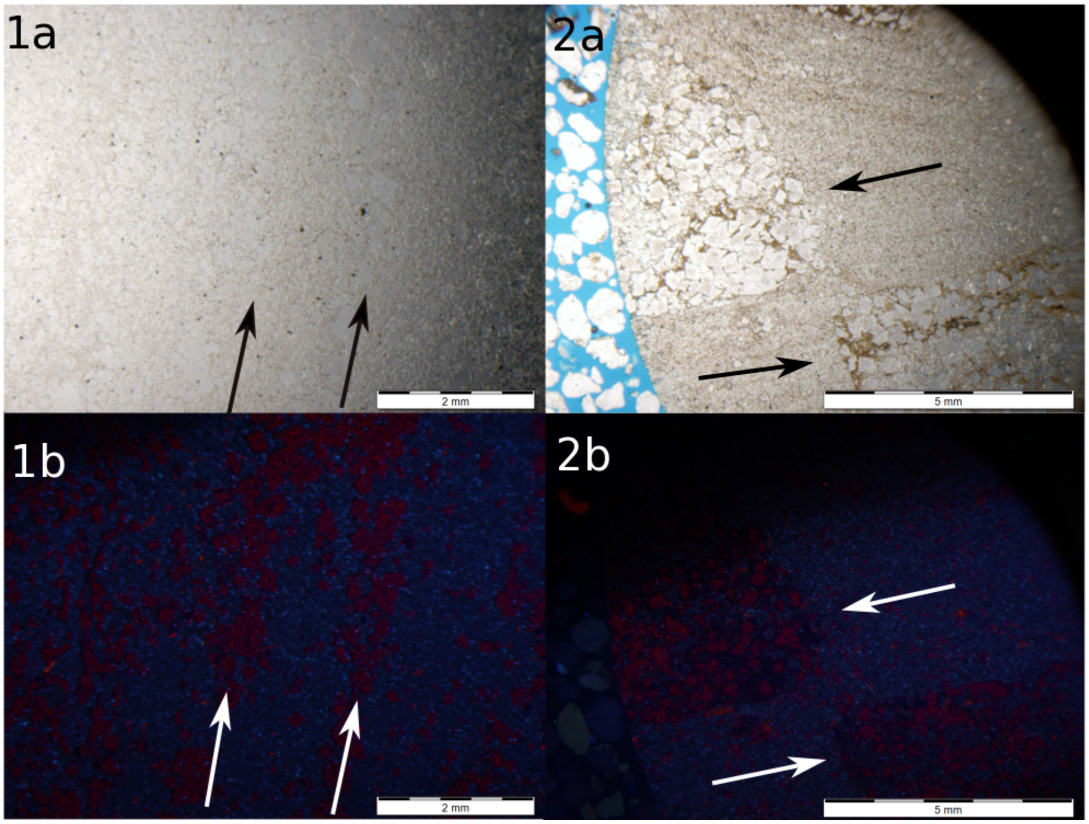

FIGURE 3.9. Palatine Bridge outcrop thin section images of Type 4 matrix fabric, plane light above and CL below. Samples taken from plugs at 32.3 m (1a and 1b), and 34.8 m (2a and 2b) along the L surface transect. In these images, the fine-grained blue-luminescent dolomite matrix is scattered with distinct ‘bands’ of larger dull orange luminescent euhedral dolomite cement crystals (arrows oriented parallel to bands). The scale bar in 1a and 1b is 2 mm and in 2a and 2b is 5 mm.

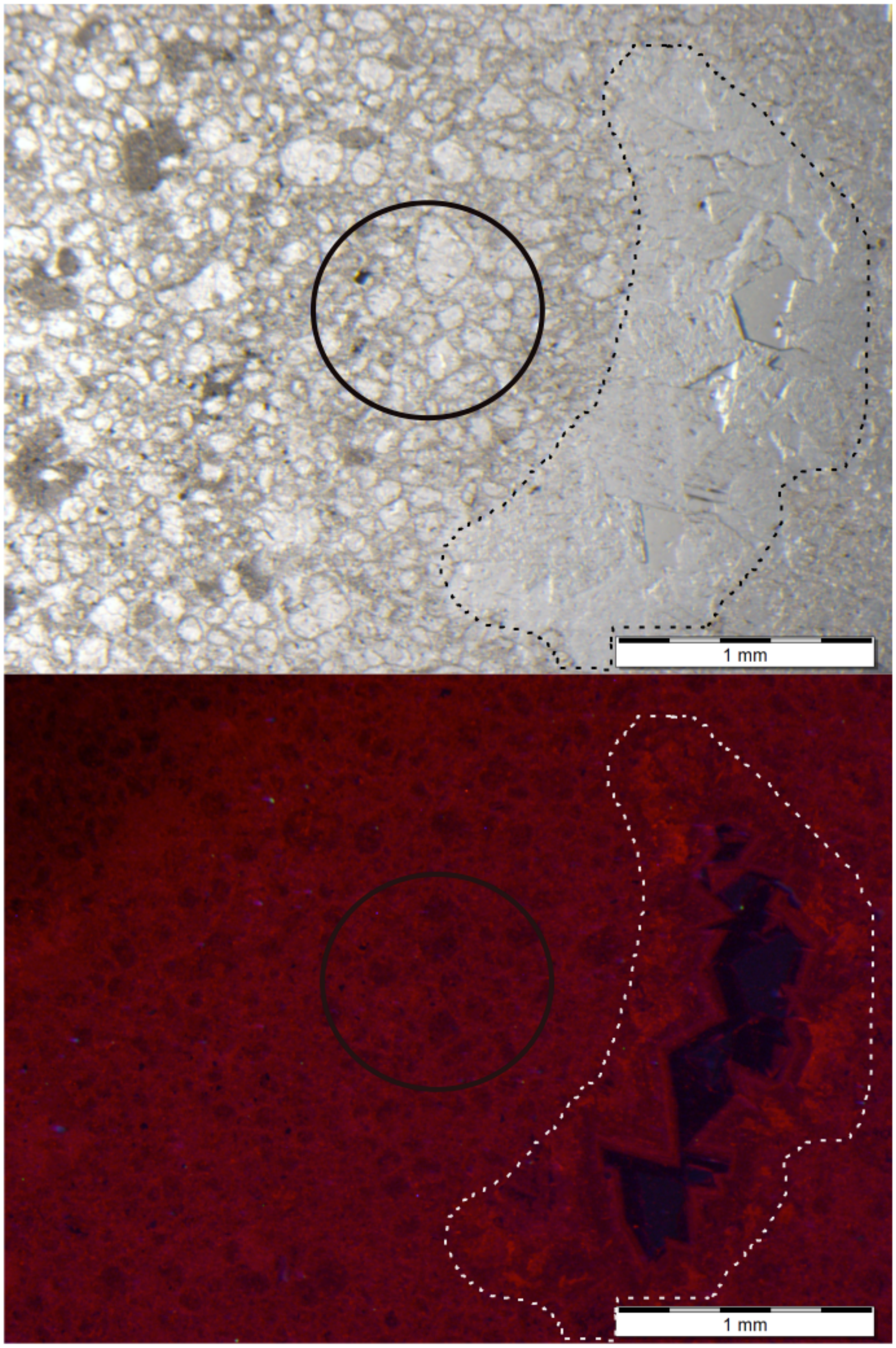

FIGURE 3.10. Palatine Bridge outcrop thin section images of Type 5 matrix replacement dolomite, plane light above and CL below. Sample taken from Hole 5, at a depth of 0.8 m. Type 5 is a dolomite matrix that has preserved the original high-porosity grainstone fabric of the rock. The ooid-dominated matrix (shown in black circles) luminesces dark red-orange, and is composed of grains ranging from 100–250 µm in diameter. In this thin section, a 1 mm by 2 mm vug is apparent, shown by a black or white dashed line, and sealed by zoned saddle dolomite. Scale bar is 1 mm.

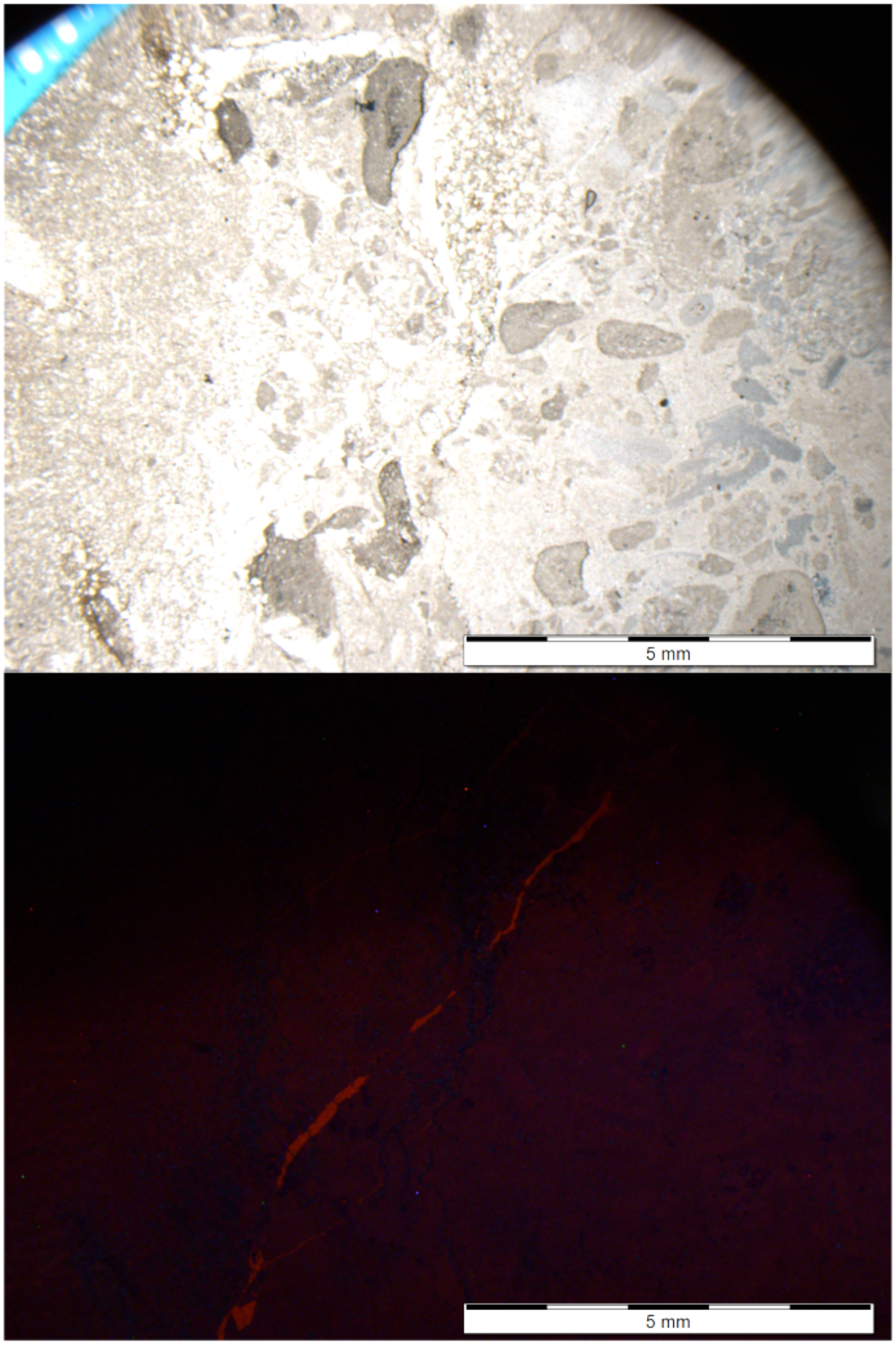

FIGURE 3.11. Palatine Bridge outcrop thin section images of Type 6 matrix replacement dolomite, plane light above and CL below. Sample taken from Hole 2, at a depth of 0.04 m. Type 6 fabric contains dolomitized allochems in what was originally a carbonate sandstone. This fabric has very faint to dull luminesce. Through the middle of the image, there is a small (< 1 mm) fracture sealed with a bright orange luminescent dolomite fill. There is no visible porosity in this sample. The scale bar is 5 mm.

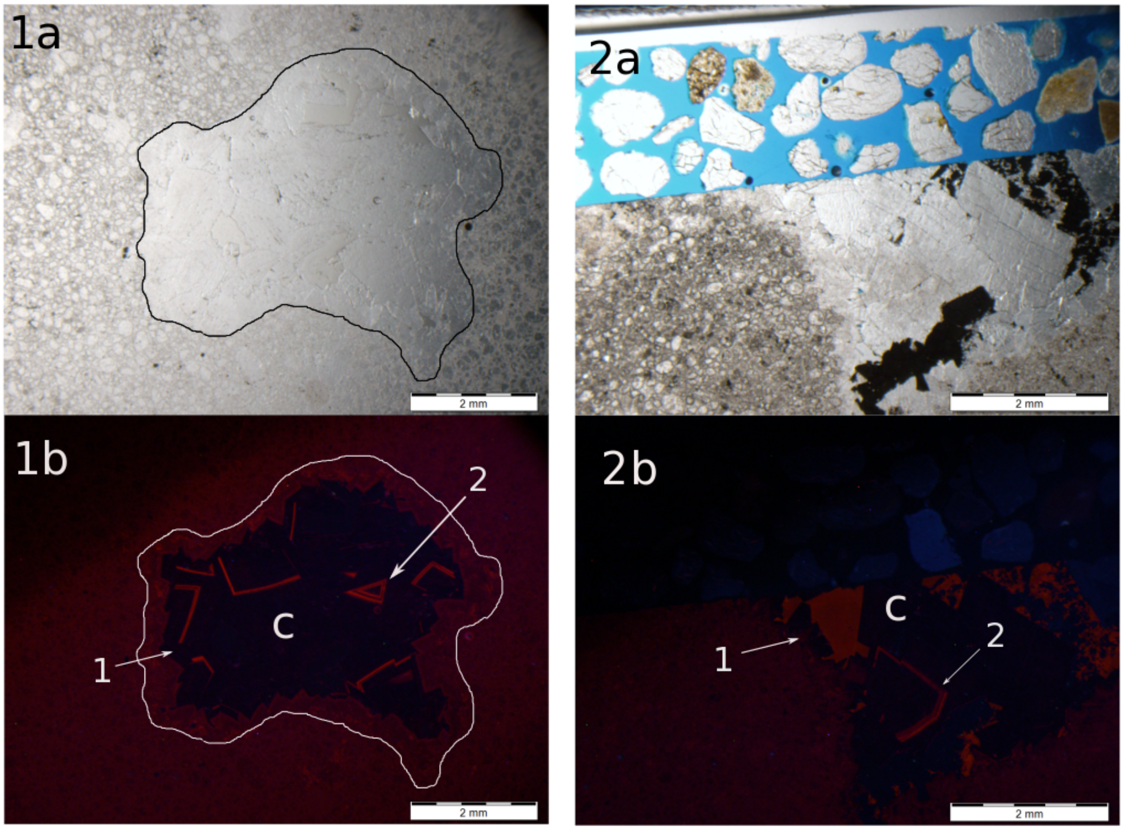

FIGURE 3.12. Saddle dolomite in paleo-vugs found in samples taken from Holes 5 (1a and 1b) and Hole 6 (2a and 2b) at the Palatine Bridge outcrop, both at a depth of 0.8 m. Both paleo-vugs are completely sealed by saddle dolomite and calcite (c). Both paleo-vugs contain non-luminescent (1), and concentrically zoned (2) saddle dolomite. Bitumen is also present in the paleo-vug in images 2a and 2b. In image 1a, the edge of the paleo-vug is outlined by a black line. In image 1b, the outline of the paleo-vug is in white, and the CL texture of the dolomite penetrates the original extent of the paleo-vug.

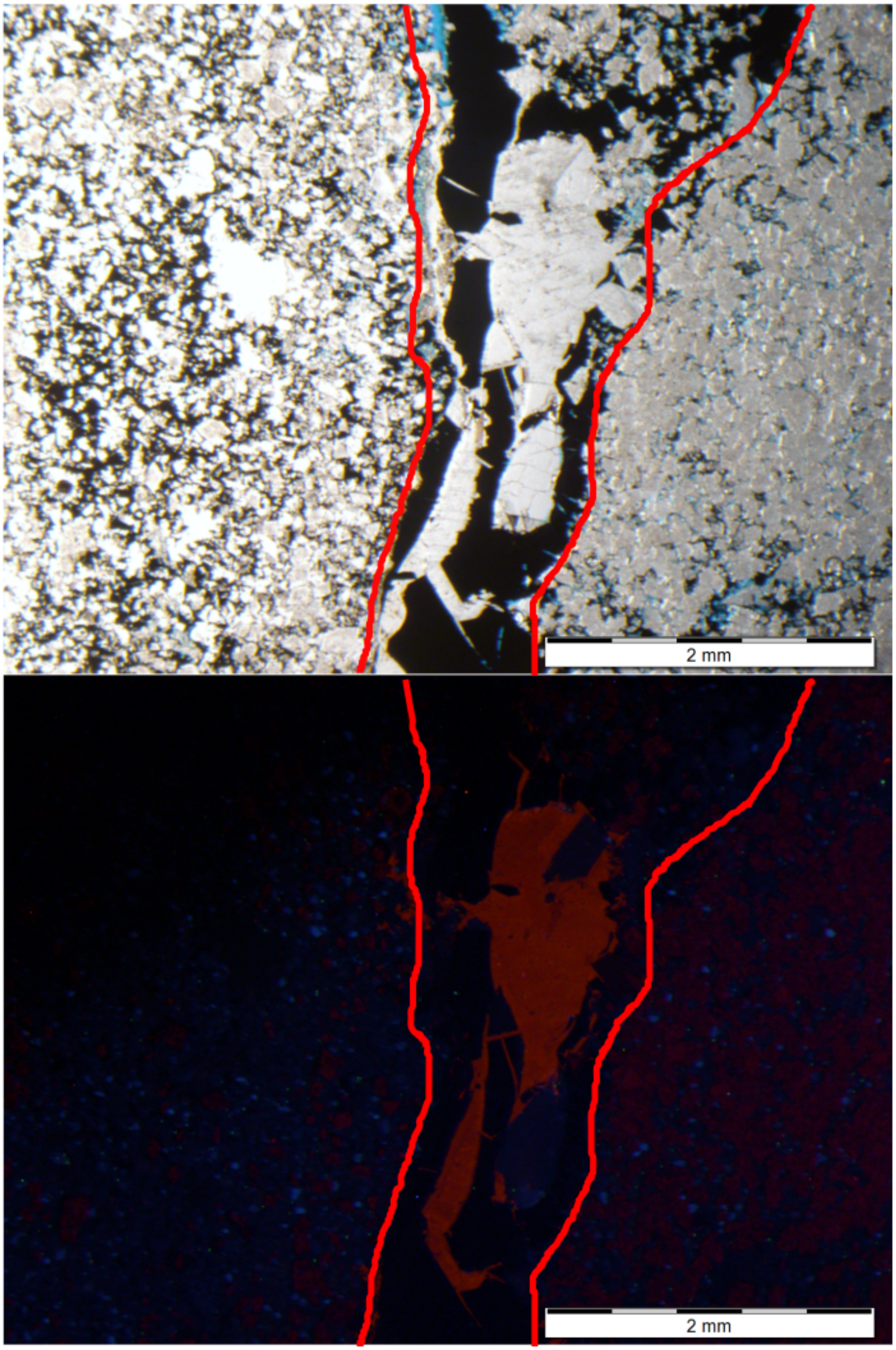

FIGURE 3.13. Example of a semi-open 1–2 mm fracture, delineated with red lines, in the Palatine Bridge outcrop, at a depth of 0.8 m in Hole 3. The fracture is filled with bitumen and calcite. Scale bar is 2 mm.

TABLE 3.3 Cathodoluminescence results from Palatine Bridge outcrop core samples.

Depth (in)	Depth (cm)	Hole #	Vugs [#-quantity]	Fractures [#-quantity]	Matrix Type	Saddle Dolomite	Other
1	2.54	4	[0]	[0]	4	none	original fabric still noticeable
1	2.54	3	[0]	[0]	4	none	Dissolution of euhedral crystals apparent in CL
1.5	3.81	2	[0]	[1] <1mm sealed fracture	6	None	Bright luminescent calcite in fracture
7.2	18.29	2	[1] 5mm sealed vug lined with saddle dolomite, sealed by calcite	[0]	6	Non-luminescent saddle dolomite lines vugs, then one band of orange luminescence	Calcite has bright orange luminescence
11	27.94	5	[1] 6mm sealed vug lined with saddle dolomite	[0]	4	Non-luminescent saddle dolomite lines vugs, then one band of orange luminescence	Calcite has bright orange luminescence
17	43.18	3	[0]	[0]	4	none	Dissolution of euhedral crystals apparent in CL
19	48.26	6	[1] 2 mm sealed vug, with zoned euhedral crystals	[1] 1.5 mm fracture sealed by saddle dolomite, and some discrete zoned crystals	4	Saddle dolomite in fracture has gradational banded luminescence	

Depth (in)	Depth (cm)	Hole #	Vugs [#-quantity]	Fractures [#-quantity]	Matrix Type	Saddle Dolomite	Other
25	63.5	5	[0]	[0]	4	none	Euhedral dolomite crystals have 3-4 CL bands
31	78.74	3	[0]	[1] 1-2mm semi-sealed fracture filled with saddle dolomite, calcite, quartz, and bitumen	4	Saddle dolomite in fracture has gradational banded luminescence	*Only fracture not completely sealed
31.2	79.25	5	[3] 0.5mm sealed elongate vugs lined with saddle dolomite; [1] 5mm sealed vug	[0]	5	3-4 CL bands in saddle dolomite, following a non-luminescent saddle dolomite generation	*Matrix dolomitization extends into first lining of vug
31.5	80.01	6	[1] 4mm sealed vug filled with saddle dolomite, calcite and bitumen	[0]	5	3-4 CL bands in saddle dolomite, following a non-luminescent saddle dolomite generation	
39	99.06	3	[0]	[1] 1mm, completely sealed	6	Saddle dolomite in fracture has gradational banded luminescence	
41.5	105.41	3	[0]	[1] 0.5-1mm completely sealed	6	Saddle dolomite in fracture has gradational banded luminescence	SD is darker in center of fracture

TABLE 3.4. Cathodoluminescence results from Palatine Bridge outcrop L transect samples.
Note: No saddle dolomite present in these samples.

Dist. (ft)	Dist. (m)	Vugs [#]	Fractures [#]	Matrix Type	Other
6	1.83	[0]	[0]	4	Dissolution of euhedral crystals apparent in CL
18	5.49	[0]	[0]	4	Dissolution of euhedral crystals apparent in CL
28	8.54	[0]	[0]	4	Euhedral crystals organized into bands; Dissolution of euhedral crystals apparent in CL
54	16.47	[0]	[0]	3	The calcite matrix luminesces where it is not stained, but not where it is stained; dissolution of euhedral crystals apparent in CL
62	18.91	[0]	[0]	3	See above
78	23.79	[0]	[1] 1 mm modern fracture? No mineralization	4	Euhedral crystals organized into bands; Dissolution of euhedral crystals apparent in CL
96	29.28	[0]	[1] 1 mm modern fracture? No mineralization	4	Euhedral crystals organized into bands; Dissolution of euhedral crystals apparent in CL
106	32.33	[0]	[0]	4	Displacement within the band of euhedral dolomite crystals (offset fracture?); Dissolution of euhedral crystals apparent in CL
110	33.55	[2] sealed vugs, 1 mm and 2 mm, lined by saddle dolomite	[0]	4	Euhedral crystals organized into bands; Dissolution of euhedral crystals apparent in CL
114	34.77	[0]	[0]	4	Euhedral crystals organized into bands; Dissolution of euhedral crystals apparent in CL
132	40.26	[0]	[0]	4	Dissolution of euhedral crystals apparent in CL

0

All paleo-vugs in the Palatine Bridge thin sections are completely mineralized, circular to elongate in shape, and range in size from 0.5–6 mm in diameter (Figures 3.10 and 3.12). They are observed in holes #2, 4, 5, and 6, at depths ranging from 0.2–0.8 m depth. Only two paleo-vugs are observed in thin section from the surface L transect plugs (1 and 2 mm diameter; Table 3.4). The CL texture surrounding the paleo-vugs located in the ooid-dominated fabric penetrates the vug by 0.5–1 mm, before the saddle dolomite CL texture begins. (Figure 3.12, 1a and 1b).

Paleo-fractures are observed in the cores at depths between 0.4–1 m depth, are mostly commonly mineralized, and the mineralized paleo-fractures range in aperture from 0.05 mm to 2 mm. The only fracture observed in thin section that is not completely mineralized is located at a depth of 0.8 m in Hole 3 (Figure 3.13).

Fracture Analysis

Seventy-two paleo-fractures (partially or completely mineralized) were measured at the Palatine Bridge outcrop, across three transects (Table 3.5). Most fractures strike WNW-ESE, approximately perpendicular to the strike of the transects, which was about N030E (Figure 3.14). The fractures are located in the fine and coarse dolomite portions of the dolomite bodies, and in the limestone surrounding the dolomite bodies. The majority of measured fractures (approx. 70%) were located in surrounding limestone due to the difficultly of measuring fractures in the silt-covered central syncline of the dolomite bodies (Figure 3.1). Apparent fracture apertures were adjusted for dip, though there is low confidence in the dip measurements because they were often measured on a two-dimensional surface, on which fracture dip is difficult to measure precisely (Figures 3.15b, 3.16b, and 3.17b). The apertures of recorded fractures range from 0.062–9.5 mm; 0.062 mm was the smallest aperture measurable by eye with the comparator and a hand lens. Transect #1 is 7.6 m long, is located 30 m from the eastern tip of the exposure, and contains 15 detectable fractures. Transect #2 is 6.7 m long, is located 25 m from the eastern tip of the exposure, and contains 45 detectable fractures. Transect 3 is 5.3 m long, is located 10 m from the east tip of the exposure, and has 13 fractures.

Relationships between aperture and cumulative frequency were plotted for both the raw aperture data and the dip-corrected aperture data. All datasets show an inverse relationship between fracture aperture, *x* in mm, and cumulative frequency, *y* in m^{-1}. Regressions of the fracture data from transects #2 and #3 have the strongest fit (highest R^2) when regressed using a power law. Fractures in transect #2 follow a primary power law fit with an R^2 of 0.97 across one order of magnitude, from apertures of 0.215 mm to 2.15 mm, as follows:

$$y = 1.7x^{-0.8\pm0.02}. \tag{3.1}$$

Below 0.215 mm and above 2.15 mm, the tails of the data deviate from the power law trend. Interestingly, the tails also seem to follow power law trends (Figure 3.15a). The dip-corrected data in Transect 2 plot in a similar fashion to the raw data, with minimal change in the coefficient and no change in the exponent (Figure 3.15b).

Fractures in transect #3 follow a power law fit with an R^2 of 0.96 across five aperture groups, from 2.15 mm to 7.5 mm, as follows:

$$y = 3.3x^{-1.0\pm0.11}. \tag{3.2}$$

Below 2.15 mm, the tails of the data deviate downward away from the power law trend (Figure 3.16a). The dip-corrected data of Transect 3 plot in a similar fashion to the raw data, with minimal change in the coefficient and the exponent (Figure 3.16b).

The fracture data from transect #1 do not show a power law fit. However, the data plot in two discrete linear trends, which can be fit with power law relationships similar to the tails of Transects 2 and 3 (Figure 3.17). The first spans apertures from 0.095 to 2.65 mm with an R^2 of 0.97, as follows:

$$y = 1.3x^{-0.11} \tag{3.3}$$

The second spans apertures from 2.65 to 9.5 mm with an R^2 of 0.94, as follows:

$$y = 7.7x^{-1.9} \tag{3.4}$$

The dip-corrected data of Transect 1 plot nearly identically to the raw data, due to the recorded dips being primarily about 90° (Figure 3.17b).

TABLE 3.5. Raw fracture data from the Palatine Bridge, NY outcrop.

Note: All dip measurements are recorded using right-hand rule, and not all fractures could be measured for dip.

Fracture Number	Transect	Distance from start of transect (cm)	Aperture (mm)	Strike (°)	Dip (°, RHR)
1	1	31	0.62	313	90
2	1	227	5	267	90
3	1	230	5	277	90
4	1	258.5	3.3	76	90
5	1	262	0.095	262	90
6	1	543.56	4	143	90
7	1	561.34	9.5	125	90
8	1	565.15	1.75	106	90
9	1	605.028	4	121	90
10	1	606.552	3.3	117	90
11	1	610.235	3.3	116	n/a
12	1	613.41	2.65	296	60
13	1	744.855	0.265	122	n/a
14	1	426.72	5	120	n/a
15	1	424.18	4	139	n/a
16	2	25.908	0.4	330	65
17	2	59.436	0.062	302	76
18	2	64.008	0.215	296	55
19	2	67.056	0.095	304	66
20	2	74.676	0.095	134	56
21	2	92.964	0.62	75	70
22	2	85.344	0.115	122	76
23	2	85.9536	0.115	122	76
24	2	79.248	0.095	128	65
25	2	132.588	0.075	124	76
26	2	134.112	0.075	124	76
27	2	140.208	0.4	133	53
28	2	155.448	0.95	197	61
29	2	231.648	3.3	130	79
30	2	259.08	0.62	127	70
31	2	257.556	0.175	120	65
32	2	262.128	0.4	124	74
33	2	283.464	0.265	150	57
34	2	286.512	0.265	150	57
35	2	280.416	0.295	150	57
36	2	288.036	0.295	150	57
37	2	277.368	0.295	150	57

Fracture Number	Transect	Distance from start of transect (cm)	Aperture (mm)	Strike (°)	Dip (°, RHR)
38	2	274.32	0.295	150	57
39	2	294.132	0.295	150	57
40	2	298.704	0.295	150	57
41	2	329.184	1.4	127	45
42	2	313.944	0.75	122	50
43	2	315.468	0.75	122	50
44	2	307.848	0.62	117	76
45	2	318.516	0.62	119	78
46	2	350.52	0.62	295	50
47	2	329.184	0.62	118	42
48	2	370.332	0.33	102	75
49	2	411.48	1.75	296	52
50	2	423.672	2.65	296	52
51	2	425.196	0.5	116	52
52	2	429.768	0.75	119	52
53	2	490.728	5	126	75
54	2	518.16	2.15	117	54
55	2	521.208	2.15	121	48
56	2	524.256	1.4	122	45
57	2	522.732	2.56	122	45
58	2	515.112	0.33	303	50
59	2	667.512	1.75	135	60
60	3	134.112	3.3	297	55
61	3	201.168	2.15	126	66
62	3	202.692	0.62	136	66
63	3	207.264	1.4	130	66
64	3	219.456	5	126	46
65	3	445.008	5	115	65
66	3	448.056	2.65	107	65
67	3	451.104	2.15	110	65
68	3	452.628	0.95	113	65
69	3	505.968	2.65	287	51
70	3	509.016	9.5	295	70
71	3	512.064	7.5	295	70
72	3	530.352	2.15	296	60

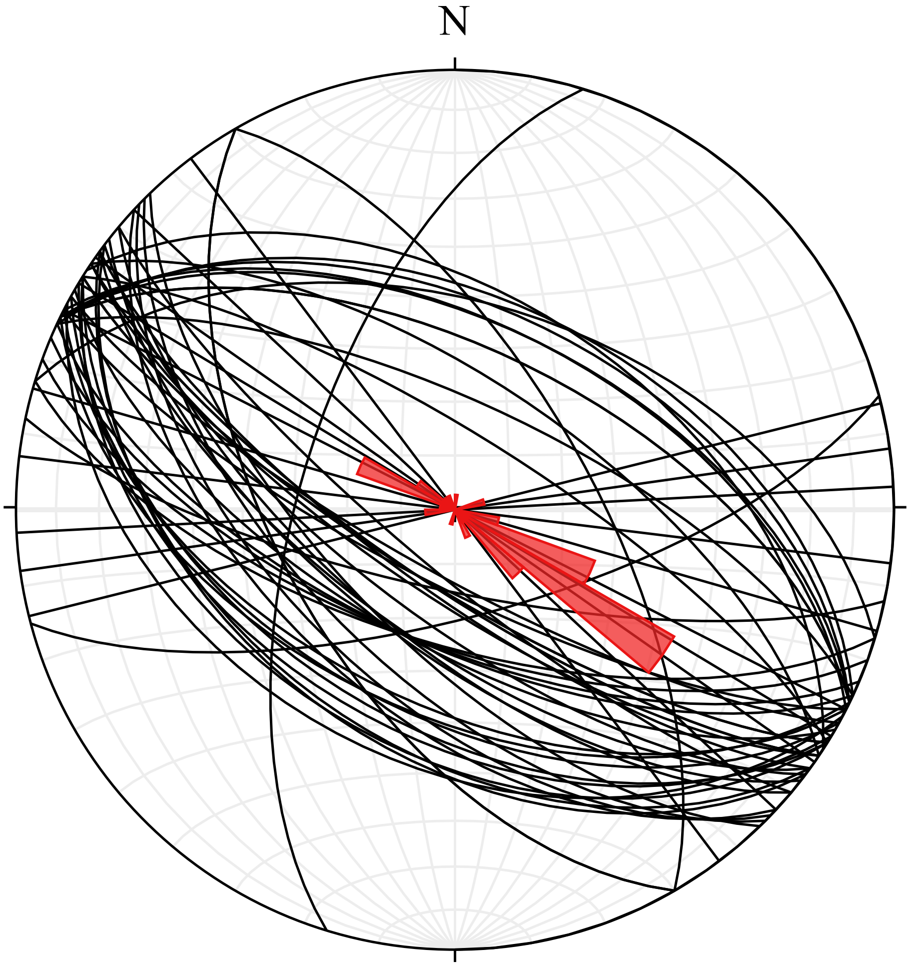

FIGURE 3.14. Dips of fractures measured at the Palatine Bridge outcrop, plotted on an equal area stereonet. The red polygon in the center of the stereonet is a rose diagram of the fracture sample set.

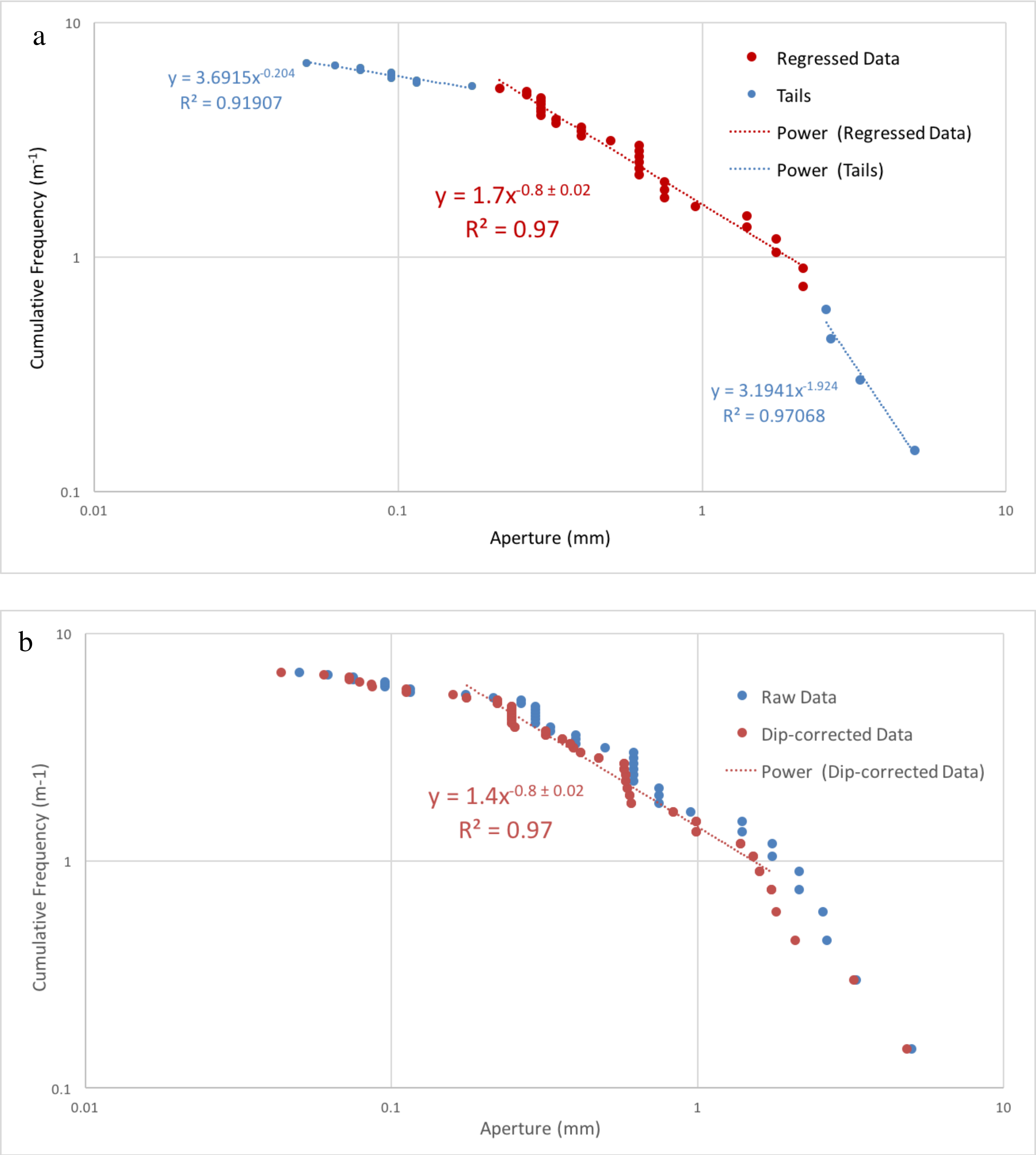

FIGURE 3.15. Fracture aperture and cumulative frequency data from transect #2 plotted on a log-log graph (N=45). All cumulative frequency data are normalized by the length of the transect. In graph (a), red dots are those which were regressed for the power law fit, and the remaining blue dots are data points in the tails. The dotted red line illustrates the power law fit with respect to the regressed data. The dotted blue lines illustrate the power law fits in the upper and lower tails. The power law relationship and R^2 are shown in red text. In graph (b), the raw data (blue) are plotted next to the dip-corrected data (red), with the red dotted line showing the regression of the dip-corrected data.

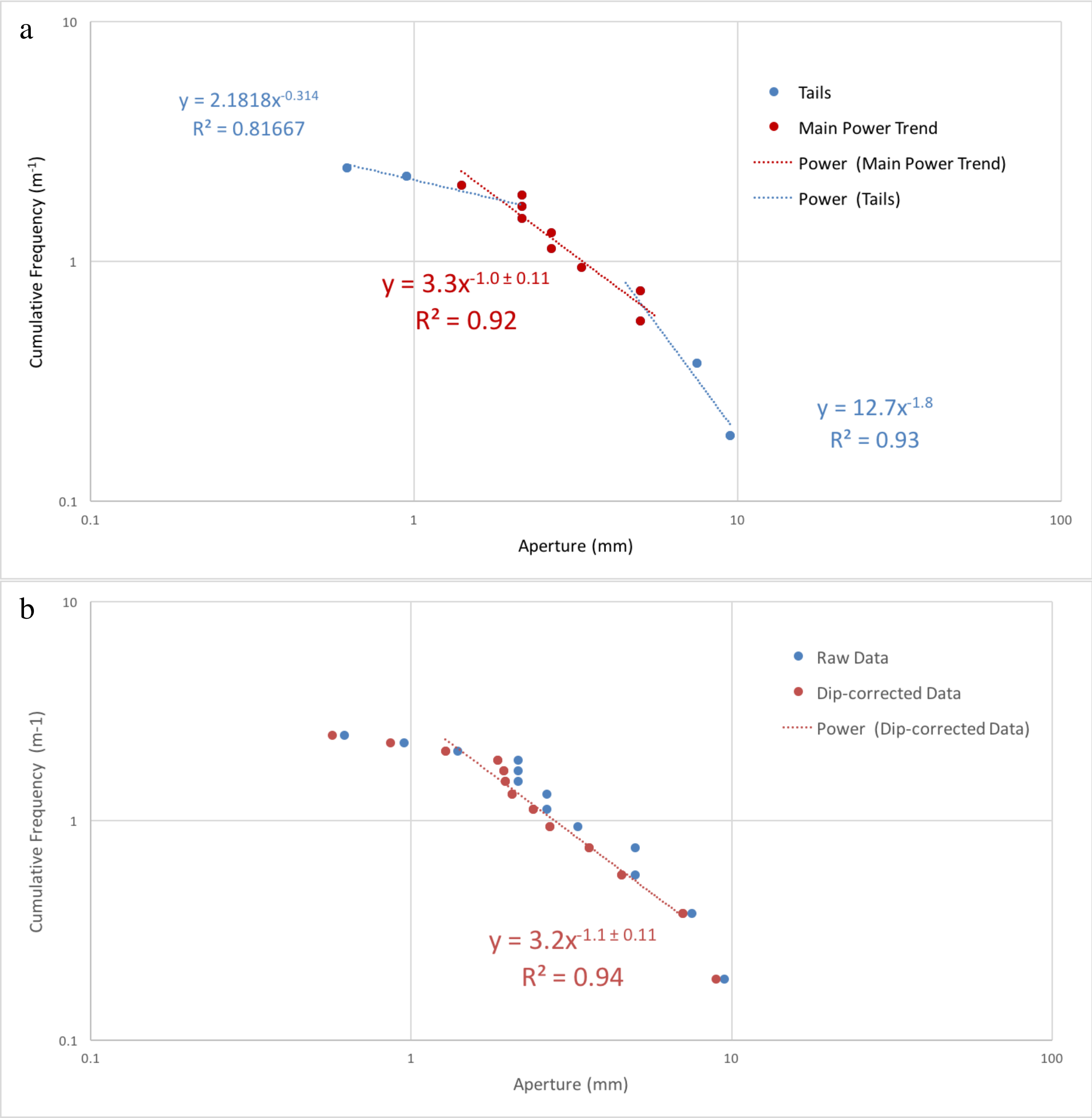

FIGURE 3.16. Fracture aperture and cumulative frequency data from transect #3 plotted on a log-log graph (N=13). All cumulative frequency data are normalized by the length of the transect. In graph (a), red dots are those which were regressed for the power law fit, and the remaining blue dots are data points in the tails. The dotted red line illustrates the power law fit with respect to the regressed data. The dotted blue lines illustrate the power law fits in the tails. The power law relationship and R^2 are shown in red text. In graph (b), the raw data (blue) are plotted next to the dip-corrected data (red), with the red dotted line showing the regression of the dip-corrected data.

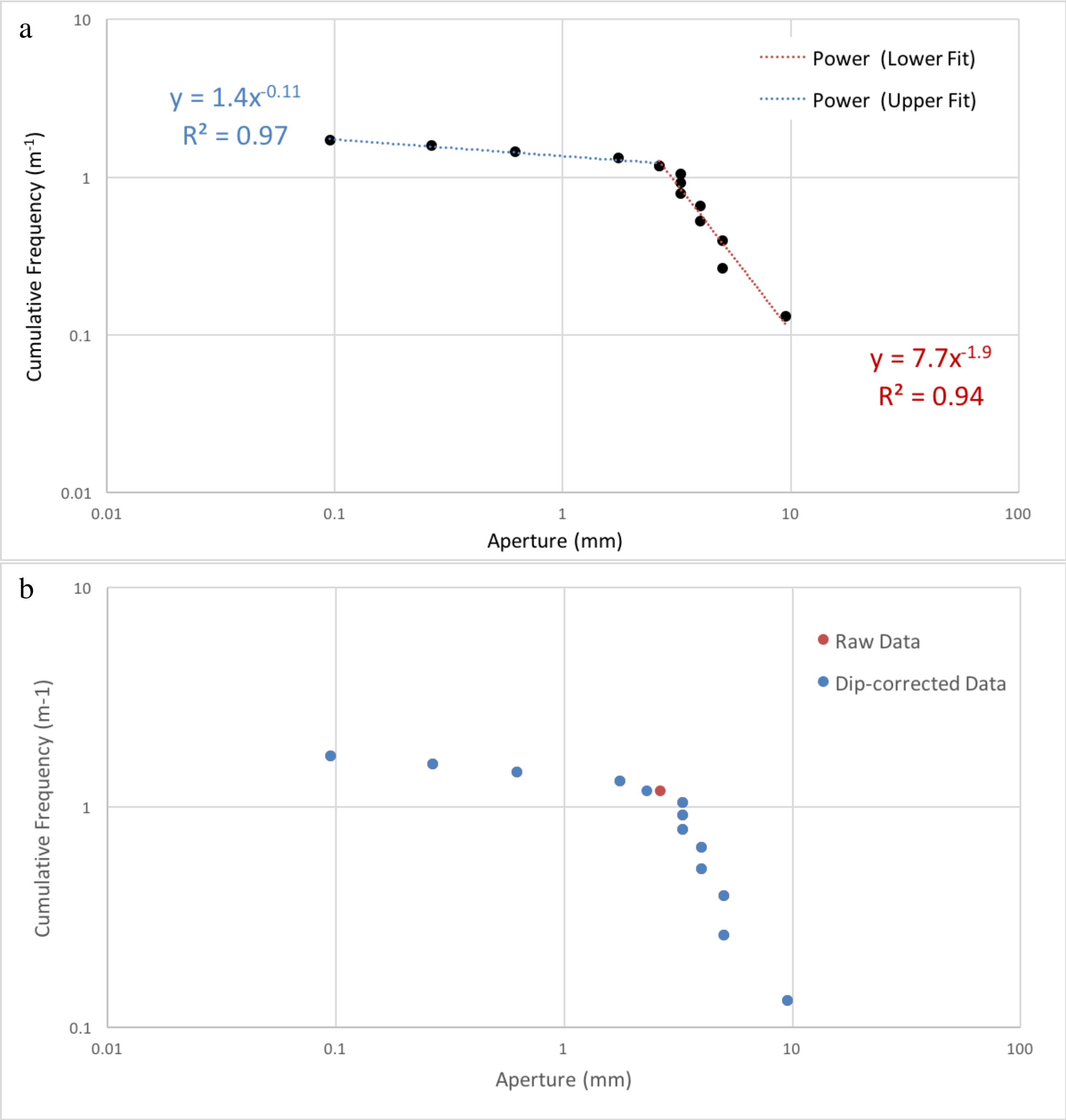

Figure 3.17. Fracture aperture and cumulative frequency data from transect #1 plotted on a log-log graph (N=15). All cumulative frequency data are normalized by the length of the transect. In graph (a), all data points are shown as black dots. Two power law trends are observed in the data, shown by blue and red dotted lines. The two power law relationships and their respective R^2 values are shown in red and blue text. In graph (b), the raw data (blue) are plotted next to the dip-corrected data (red), with the red dotted line showing the regression of the dip-corrected data.

Discussion

Petrography

A comparison of the petrographic features in the Whiteman core and Palatine Bridge outcrop is presented in the context of the paragenetic sequence within which the reservoirs were created (Smith, 2006; Slater and Smith, 2012). In both the outcrop and core samples, there appear to be three main phases of dolomite diagenesis caused by hydrothermal fluid flow, the third of which is directly linked to the present state of fractures, vugs and paleo-vugs in the outcrop and reservoir.

After deposition and early compaction of the Tribes Hill and the Black River limestones, the first stage of dolomite diagenesis was triggered by fracturing, allowing hydrothermal fluids to travel up to the limestone formations (Smith, 2006). This stage of diagenesis involved pervasive dolomitization of the Tribes Hill and Black River limestones. Samples from the Whiteman #1 core and the Palatine Bridge outcrop display different matrix (bulk rock) dolomite fabrics, both in quantity and luminescence. In the Whiteman #1 core samples, there are two types of dolomite matrix fabrics, while at the Palatine Bridge outcrop, there are three dolomite matrix fabrics (Table 3.6). Of these five dolomite matrix types, each one is distinct and there is no similarity in either texture or luminescence between the Whiteman and Palatine Bridge samples. The majority of samples from the Palatine Bridge outcrop display a blue luminescent matrix, a CL color typically uncommon in carbonate rocks. At the end of this stage of dolomite diagenesis, porosity is present in the dolomite in the form of both fractures and vugs. According to Smith (2006), it is uncertain whether vugs were created before or after the pervasive matrix dolomitization, but this work proves that vugs were present in the limestone prior to the stage of matrix dolomitization.

Cathodoluminescence of the Palatine Bridge samples sheds light on the timing of vug development in the paragenetic history of these hydrothermal dolomite bodies. In samples with a luminescent matrix, the crystal growth texture of the matrix in the Palatine Bridge outcrop samples, as identified by CL microscopy, penetrates the inner-most dolomite lining of the paleo-vug (Figure 3.12). This feature is not detectable in the Whiteman samples, because the matrix does not luminesce. Therefore, CL microscopy of the luminescent Palatine Bridge samples shows that the development of paleo-vugs and vugs must have taken place before matrix dolomitization, likely via a stage of limestone leaching. Vugs and paleo-vugs observed in thin section from both the Whiteman core and the Palatine Bridge outcrop are often located adjacent or connected to a fracture or paleo-fracture. However, exceptions located within the Palatine Bridge ooid fabric are not clearly associated with a fracture or paleo-fracture. There is no apparent relationship between vug size and degree of vug mineralization (sealed or not) in either set of samples. However, in four Whiteman samples below 2912.8 m only paleo-vugs are observed. Because the core ends at 2914.3 m, it is unclear whether this is an anomaly or a cluster of paleo-vugs.

After the limestone became completely dolomitized, the hydrothermal fluids began to over-dolomitize the rock, by filling in available pore space. This second stage of fluid flow emplaced the pore-filling euhedral matrix cement. The pore-filling euhedral dolomite crystals observed in the Whiteman #1 and Palatine Bridge samples both tend to occur in discretely organized bands (Figure 3.9), implying that the precipitation of these cement crystals may have been influenced by the original bedding, and perhaps porosity, of the parent rock. These pore-filling crystals are more commonly found in the Palatine Bridge samples than the Whiteman samples. Because dolomitized limestones inherit their porosity and fabric from the parent limestone (Lucia, 2004), it is highly likely that the parent Tribes Hill limestone had higher original porosity than the parent Black River limestone. After the dolomitization, the higher porosity would have allowed for precipitation of a greater concentration of euhedral dolomite crystal cements in the Tribes Hill formation. Photomicrographs of the luminescent Palatine Bridge calcite samples show narrow zones of non-luminescent dolomite coincident with the linear cluster of zoned euhedral dolomite crystals (Figure 3.8). This suggests that whatever fluid precipitated the euhedral dolomite crystals also dolomitized calcite grains in its path, and that these two phases of diagenesis may have occurred simultaneously. Because dolomite crystals are present outside the fault boundary of the dolomite bodies at the Palatine Bridge outcrop, a small volume of fluid must have been able to travel outside the structural confines of the fault system, but not enough to completely dolomitize the limestone.

TABLE 3.6. Complete list of matrix (bulk rock) fabrics and saddle dolomite types found in the Palatine Bridge cores and the Whiteman #1 core.

Type	Textural Attributes	CL color/pattern	Sample/Location
Type 1	Anhedral to subhedral dolomite crystals; crystals < 5-400 μm; Euhedral dolomite crystals (50-250 μm) occur in distinct bands	Dull to non-luminescent	Whiteman core
Type 2	Subhedral dolomite crystals < 100-500 μm	Dull orange luminescent	Whiteman core; occurs only 2908.2–2909.2 m
Type 3	Isolated euhedral dolomite crystals embedded in original calcite; dolomite crystals < 50 μm; crystals partly dissolved	Blue luminescence in bulk rock; bright red concentric zone luminescence in euhedral dolomite crystals	Palatine Bridge; found only in surface samples
Type 4	euhedral to subhedral crystals; crystals < 50 μm; some crystals partially dissolved	Blue luminescence in bulk rock; bright red concentric zone luminescence in euhedral dolomite crystals	Palatine Bridge; widespread
Type 5	Ooid grainstone texture preserved, expressed by sub-circular forms 100-250 μm diameter	Deep red-orange	Palatine Bridge
Type 6	Intraclast packstone or grainstone texture preserved, anhedral dolomite crystals < 50 μm	Does not luminesce	Palatine Bridge
Early saddle dolomite	Occurs in earliest (innermost) layer of paleo-vugs, vugs, paleo-fractures, and fractures	Does not luminesce	Whiteman and Palatine Bridge
Late saddle dolomite	Concentrically zoned; occurs in outermost layer of paleo-vugs, vugs, paleo-fractures, and fractures	Alternating non-luminescent and bright orange luminescent	Whiteman and Palatine Bridge

Though the organization of the euhedral dolomite crystals is similar across both sample sets, their luminescence is different. In the Palatine Bridge outcrop samples, the dolomite crystals have a concentrically-zoned luminescence (non-luminescent to bright orange), while those in the Whiteman #1 samples are non-luminescent. Because the degree of luminescence is controlled by the ratio of Manganese (Mn^{2+}) to Iron (Fe^{2+}) (Machel et al., 1991; Boggs and Krinsley, 2006), two scenarios could have led to the difference in luminescence: (1) the fluids that precipitated the euhedral crystals had different original trace element compositions, or (2) the differences in original trace element composition of the parent Tribes Hill and Black River limestones impacted the dolomitization, and therefore the luminescence, of these pore-filling cement dolomite crystals. Though Smith (2006) and Slater and Smith (2012) did not compare trace element compositions of matrix dolomite samples from the Palatine Bridge and Whiteman samples, the isotopic and geochemical analyses of the matrix and cement material pointed to a strong similarity in fluid origin and temperature between the two samples. Therefore, it is more likely that the dolomitizing fluids had comparable trace element compositions, and the matrix replacement dolomite crystals in the Palatine Bridge outcrop may be luminescent due to fluid interaction with the bright orange luminescent Tribes Hill limestone (Figure 3.8). Under this hypothesis, Mn^{2+} and Fe^{2+} in the parent material would have been dissolved into the fluid, transported by the dolomitizing fluids, and later reprecipitated in the form of the euhedral crystals.

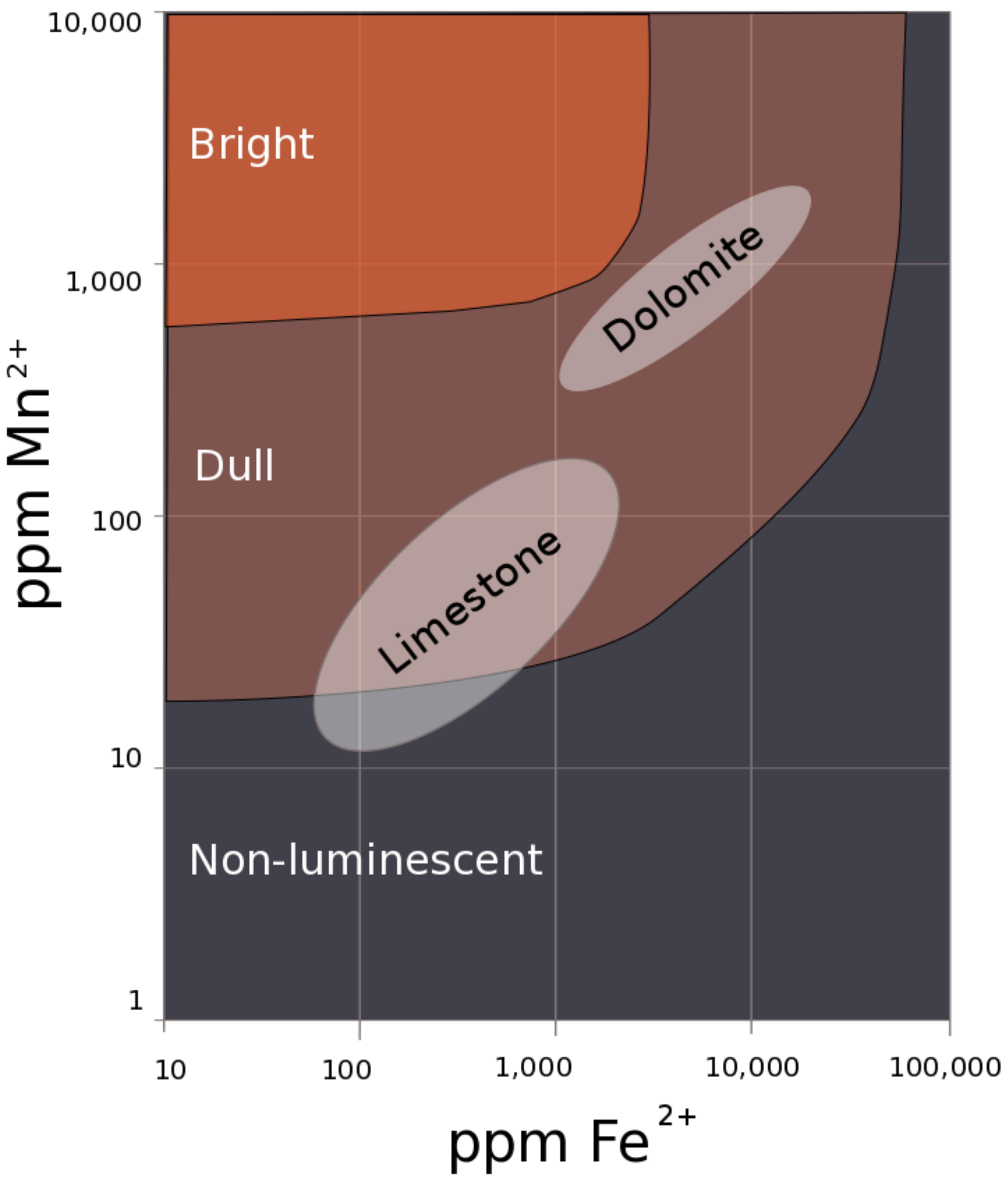

FIGURE 3.18. Whiteman #1 core samples and other T-BR field samples (limestone and dolomite) plotted on a luminescence graph developed by and adapted from Machel et al. (1991). Both limestone and dolomite samples have Mn^{2+} and Fe^{2+} concentrations that suggest the original limestone facies of the Black River Formation would not luminesce under CL conditions. Limestone and dolomite regions on this graph are taken from trace element analyses data collected by Smith (2006).

In the case of the Palatine Bridge outcrop, those crystals luminesce brightly like the Tribes Hill calcite. In the case of the Whiteman reservoir, those crystals do not luminesce, though lacking thin sections of the original limestone facies we do not have direct evidence for this property in the neighboring calcite. Nevertheless, trace element analyses done by Smith (2006) on the limestone facies of the Black River Formation can be plotted on a Mn^{2+}-Fe^{2+} luminescence graph developed by Machel et al. (1991) to predict the luminescence of unaltered Black River limestone. Both dolomite and limestone from the Whiteman samples and other gas-producing fields contain ratios of Mn^{2+} to Fe^{2+} that plot in the "dull" luminescence zone (Figure 3.18), which is in partial agreement with the non-luminescent dolomite matrix observed in Whiteman samples. This hypothesis could be further tested by use of Scanning Electron Microscopy with CL capability (SEM-CL) to compare the compositions of the euhedral dolomite crystals with their associated original limestone facies.

After the conversion of calcite to dolomite and the growth of dispersed euhedral crystals where enabled by original porosity, an episode (or episodes) of faulting and fracturing took place, creating additional pore space in the reservoir (Smith, 2006; Slater and Smith, 2012). This led to the third and final stage of hydrothermal fluid flow and dolomite diagenesis: the precipitation of saddle dolomite cements in the vugs and fractures. Cement stratigraphy of saddle dolomite in the Whiteman #1 and Palatine Bridge samples shows similar characteristics of luminescence, suggesting similar diagenetic fluids and growth history. In both sets of samples, an early generation of non-luminescent saddle dolomite nucleated on the margins of fractures and vugs, partially or completely occluding the pore space. A younger generation of saddle dolomite grew attached to the first generation, and displays a concentrically-zoned luminescence with between four to six CL bands in the Whiteman sample, and up to four bands in the Palatine Bridge samples. Slater and Smith (2012) confirmed similarities in saddle dolomite $\partial^{18}O$, Strontium ratios, and fluid inclusions salinities and temperatures between the two sample sets; therefore, the discrepancy in band quantity is unlikely to be due to a difference in fluid source. Instead, fewer episodes of change in trace element content (Mn^{2+} and Fe^{2+}) of the fluids could contribute to differences in luminescent band thickness and frequency. Trace elements were not measured quantitatively by Slater and Smith (2012) or in this study. However, the CL color and brightness qualitatively suggest a similarity of the saddle dolomite trace element (Mn^{2+} and Fe^{2+}) chemistry, while the style of concentric ("banded") growth zones and the order of the luminescent bands suggest a similarity in saddle dolomite diagenesis between the outcrop and the subsurface reservoir.

The differences in luminescence of the matrix dolomites in the Palatine Bridge outcrop and the Whiteman #1 core are interpreted to be largely related to differences in the original parent rock material. Furthermore, the luminescence of the cement fills in the Palatine Bridge outcrop and the Whiteman #1 core are nearly identical. The concentric zonation characteristic, order of CL zonation bands, and quantity of saddle dolomite generations, as well as the euhedral dolomite crystals embedded in the host rock material, is consistent between the two locations. Diagenesis of cement fill in fractures and vugs is therefore interpreted to be comparable, which provides confirmation that the outcrop can be used as not only a structural analog (Slater and Smith, 2012), but also a diagenetic analog, to the subsurface Trenton-Black River hydrothermal fields. This sets the stage for the fracture analysis work done in the following section. At some unknown point following the stages of fracturing, vug development, and hydrothermal alteration in the subsurface T-BR reservoir and the Palatine Bridge outcrop, their geologic histories diverged. This divergence led to the exhumation of the Palatine Bridge outcrop.

Fractures in Outcrop

The total number of recorded mineralized fractures at the outcrop is low, primarily due to poor exposure except where the outcrop was cleaned. Additionally, the number of fractures recorded is conservatively low, due to the exclusion of open fractures. Though this decision ensured the exclusion of fractures created by quarry blasts, it may have also led to an omission of ancient fractures with relict or secondary porosity. The total range of apertures measured spans 0.062–9.5 mm, which is just over two orders of magnitude. A criterion for recognition that a line fit to the data can be treated as a good approximation of a fractal data set is that the fit should span at least one order of magnitude (Bonnet et al., 2001).

There is large variation in the number of fractures recorded in each of the three transects. Transect 2 has three times the number of recorded fractures in transect 1. Transects 1 and 3 have a similar number of fractures, but Transect 1 is 1.4 times longer than Transect 3 thus there are fewer data points in each aperture bin in Transect 1. There is no detectable relationship between transect length and fracture quantity, as the longest transect (1) at 7.6 meters has a comparable number of fractures as the shortest transect (3) at 5.3 meters length. We propose three potential explanations for the large difference in fracture quantity between the three transects: (1) incomplete identification of fractures due to low visibility and exclusion of open fractures; (2) the location of transect 2, near the tip of the longest dolomite body, may influence its concentration of fractures; and/or (3) one-dimensional sampling bias of long, large-aperture fractures.

Fracture data in transects 2 and 3 follow an inverse power law relationship with a high level of fit ($R^2 > 0.95$). The power law trend in Transect 2 covers a full order of magnitude, while that of Transect 3 covers half an order of magnitude. Because transect 2 has a larger number of fractures in the regression and a wider span of the regression across more aperture bins than Transect 3, the fit in Transect 2 is stronger than that in transect 3. Both transect datasets show sampling artifacts, i.e. have ‘drooping tails’ at both ends of the primary power law relationships. Given the low number of data points in this study, the nature of the 1-dimensional transects on a 2-dimensional surface, and the quality of the exposure, these tails were expected (Cowie et al., 1996; Marrett et al., 1999; Bonnet et al., 2001). An insufficient sampling of small aperture fractures—also known as resolution bias—is a likely contributor towards the deviation from the power law trend at smaller aperture bins. The tails at the large-aperture end of the datasets can most likely be explained by sampling truncation bias, in which large faults are not sampled by the 1D transect due to their lower frequency in the exposure, or their tips of smaller apertures are recorded instead. The low-aperture tails in Transects 2 and 3 can be fit well ($R^2 > 0.99$) with power-law trends. These trends have similar coefficients and exponents: $y_2 = 3.7x^{-0.2}$ and $y_3 =$

$2.2x^{-0.21}$. This suggests a strong similarity in sampling artifacts of small aperture fractures in at least two transects at this outcrop.

Given that Transect 1 was only five meters from Transect 2 and sampled the same section of the dolomite body and the surrounding limestone, it was expected that Transects 1 and 2 would have a similar fracture aperture-frequency relationship. However, the data in transect 1 do not follow a distinct power law relationship between expected 'tails', as was observed in the data from transects 2 and 3. Instead, the data in transect 1 plot in two discrete trends as opposed to three trends seen in transects 2 and 3. The exponent and coefficient of the small-aperture power law trend in Transect 1 match closely with the small-aperture tails in Transects 2 and 3: $y_1 = 1.3x^{-0.11}$. Despite the high goodness-of-fit ($R^2 = 0.97$) of the small-aperture power law trend in Transect 1, it is unlikely to represent the primary relationship between fracture aperture and frequency, and more likely to be a result of sampling artifacts. Similarly, the larger-aperture trend in Transect 1 has a similar exponent to that of the large-aperture tail in Transect 2: $y_1 = 7.7x^{-1.9}$ and $y_2 = 3.2x^{-1.9}$. Therefore, both high-R^2 power law trends from Transect 1 were likely affected by similar sampling artifacts to those of the upper and lower tails of Transect 2. Furthermore, Transect 1 has the lowest number of recorded fractures per transect length of all three transects, and has very few data points in each aperture bin in the lower tail of the data. Possible explanations for sampling bias during the recording of fractures in Transect 1 include: (1) the quality of fracture measurement may have been poor for Transect 1, as there was a learning curve for the use of the logarithmic comparator on the first transect recording; (2) Transect 1 was cleaned and analyzed on an earlier date before the leaf blower was available, which could have resulted in a lower quality of cleaning compared to the other two transects; or (3) the data recorded in Transect 1 are more heavily influenced by the 1-dimensional sampling of a two-dimensional exposure than the other two transects. This sampling artifact occurs because large aperture fractures have a greater likelihood of being sampled than small aperture fractures. Because the data from transect 1 were more strongly affected by various sampling biases than were Transects 2 and 3, the data from Transect 1 were omitted for the remainder of the analysis.

When the fracture aperture data were corrected for true aperture using the dip measurements, there was minimal change in the relationship between aperture and cumulative frequency. The coefficients and exponents in the power law regressions of the dip-corrected data were very similar to the regressions of the raw data. Given this similarity and the low confidence in the dip measurements, the raw data regressions were used for the remainder of the analysis.

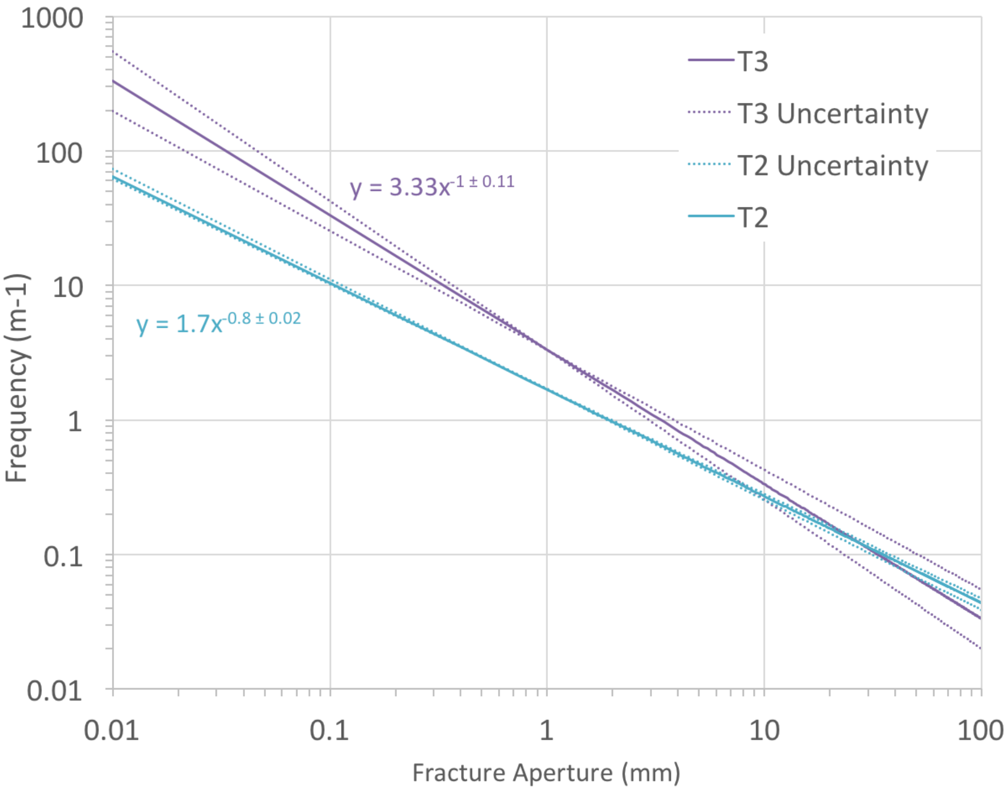

FIGURE 3.19. Power regressions from transects 2 (blue) and 3 (purple), shown on a log-log plot of fracture aperture (mm) versus frequency (m^{-1}). The area between the two indicates the area of discrepancy between the two regressions. The discrepancy gets smaller as fractures get larger, and the two regressions' uncertainty zone converge near 7 mm.

The primary power law regressions from Transects 2 and 3 (Figure 3.19) were applied to predict the frequency of fractures in a hypothetical Trenton-Black River geothermal reservoir (Table 3.6). The predicted fracture frequencies for four aperture bins from Transect 2 and 3 were compared. For fractures smaller than 0.01 mm, the frequency discrepancy is just over a factor of five. Fractures larger than 1 mm have a lower discrepancy in predicted frequency, reduced to a factor of two. The uncertainty bands of the original regressions from transects 2 and 3 converge at apertures of above approximately 7 mm (Figure 3.19). The discrepancy between the two regressions is largely due to the difference in exponents. Because the slope of the line is controlled exponentially, an exponential factor of 0.2 makes a large difference in predicted frequency. The differences in the regressions could be due to sampling biases, or due to inherent differences in the relationship between fracture aperture and frequency in the outcrop, given that transect 2 crosses the main dolomite body while transect 3 crosses the smaller dolomite body. This would imply that lateral variation, or heterogeneity, in these structures impacts fracture frequencies. Additional data is necessary to determine the cause of the differences in the two power law regressions, and to better constrain the uncertainty in the relationship between fracture aperture and frequency.

TABLE 3.6. Example of predicted vein frequencies based on aperture, derived from Equations 3.1 and 3.2.

Aperture (mm)	Cumulative Frequency (m^{-1}) From Transect 2	Cumulative Frequency (m^{-1}) From Transect 3
0.01	64	339
0.1	10	34
1	2	3

Furthermore, future studies of this topic ought to dig deeper into the exposure for a clean surface that is free of silt and fractures associated with the explosive blasts. Removing the upper layers of the exposure for a clean surface of the dolomite bodies would allow for the measurement of open fractures in addition to mineralized fracture, and would expose a second dimension of the fractures to better measure their dips. If available, a similar analysis ought to be conducted on a Black River outcrop analog to test the similarity in fracture aperture and spacing between the Tribes Hill outcrop and a Black River outcrop. Subsequently, with one or several vetted fracture aperture relationships for the analog to the T-BR reservoirs, a general architecture of open fractures in the T-BR reservoirs can be approximated for reservoir modeling purposes. Chapter 4 investigates this concept more deeply by testing the results from this chapter with a standard fracture flow equation.

Implications

This study began with limited knowledge of the nature of fractures in the Trenton-Black River gas reservoirs in New York State. Though fractures have been reported in the Quackenbush Hill field (e.g. Marner et al., 2008), apertures and frequencies of those fractures have not previously been described. From the microscopy work, this study confirms that semi-open fractures, mineralized by over 90% from their original aperture, exist in at least one subsurface T-BR reservoir, and given the similarities across the T-BR fields described by Smith (2006), likely in others as well. These fractures also tend to be associated with open vugs. This discovery is a step forward, given that much of the literature on the Trenton-Black

River fields does not indicate open fractures were encountered in cores (Jacobi, pers. Comm., Jacobi

Cathodoluminescence (CL) microscopy provides confirmation that the Palatine Bridge outcrop can be used as not only a structural analog, but also a diagenetic analog, to the Trenton-Black River reservoirs. Following a first round of fracture data collection and analysis, it is hypothesized that most large fractures associated with the T-BR dolomite bodies run parallel to the bodies, lie outside the central dolomitized zone, and dip both toward and away from the center of the dolomite bodies. However, the majority of fractures measured are located in the surrounding limestone, which may exhibit different frequency tendencies than fractures measured in the dolomite bodies. Fluid flow associated with geothermal energy extraction from the T-BR reservoirs would, on average, need to be oriented parallel to the trend of the reservoirs, while also moving toward or away from the center of the dolomite bodies due to the dip of the fractures. However, accessing open fractures at one end of the dolomite structure with a vertical well may be difficult given the sub-vertical nature of the fractures and the heterogeneity of the system. Two horizontal wells at each end of the dolomite-filled graben, serving as one injector and one producer, with the horizontal legs oriented perpendicular to the trend of the dolomite structure, would increase the likelihood of encountering an open fracture system (Figure 3.20).

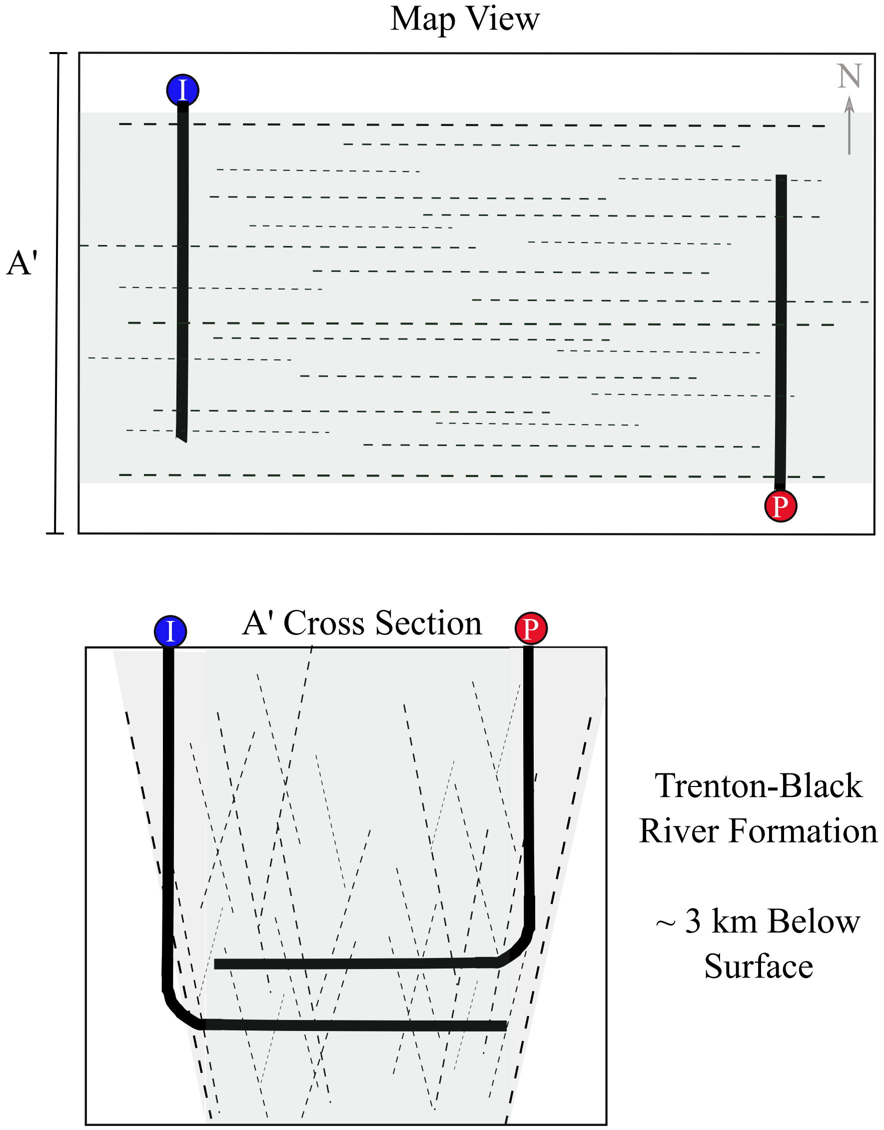

FIGURE 3.20. Two-dimensional schematic of a possible Trenton-Black River wellfield design. The upper figure is the map view of the wellfield, shaded in gray, with the vertical leg of injection well labeled by a blue "I" and the vertical leg of the production well labeled by a red "P". The horizontal legs of both wells are shown by a thick black line. Fractures in the reservoir are marked by dashed black lines. The lower image is a cross section of the 3 km-deep T-BR geothermal reservoir, shaded in gray, at the A' location in the upper image (perpendicular to long edge of reservoir). The horizontal leg of the production well is shallower than that of the injection well, as buoyancy will likely cause the warming water to rise in the reservoir.

This study, in combination with the results from Chapter 2, aids in the understanding of what constitutes heterogeneity in the T-BR reservoirs, and how that heterogeneity in the T-BR reservoirs would impact future geothermal fluid flow, either positively (increased flow) or negatively (restricted flow). A deeper quantitative understanding of any of the following reservoir aspects would reduce the uncertainty of geothermal fluid flow in the T-BR reservoirs:

- The distribution of open vugs adjacent and connected to fracture surfaces, which may increase variability in flow paths in the reservoir (where vugs are interconnected with other vugs or fractures; see Chapter 2), and therefore heat sweep,
- The variation in and degree of mineralization of fractures in the reservoirs, which may impact effective permeability and flow direction in the reservoirs,
- Intersections of open fractures parallel to the dolomite structure, which could increase the flow path variability in the reservoir and therefore heat sweep.

Conclusions

Cathodoluminescence (CL) sheds additional light on the diagenetic similarities between the Palatine Bridge Outcrop and the subsurface Trenton-Black River hydrothermal dolomite reservoirs. Similarities exist for the saddle dolomites that partially or completely occlude early vugs and fractures: both rock units experienced two dominant generations of saddle dolomite crystallization, and the fluid properties were similar at the two locations. This work provides confirmation that the outcrop can be used as not only a structural analog, but also a diagenetic analog, to Trenton-Black River reservoirs.

Fracture frequency work conducted at the Palatine Bridge outcrop produced a low overall quantity of recorded fractures due to the poor condition of the exposure. Thus, this analysis serves as a proof of concept but does not provide a fully developed analysis. Two transects yielded power law relationships between fracture aperture and cumulative frequency, which have strong R^2 values, similar coefficients and moderately similar exponents. Transect 1 did not yield a suitable power law relationship. All three datasets were likely affected by resolution, truncation, and dimensional biases, due to the low number of total fractures collected for this work. The power-law regressions from the two high-quality transects can be used as high-uncertainty preliminary bounds on the relationship between fracture aperture and frequency in subsurface T-BR reservoirs.

Additional field work needs to be conducted to better constrain the fracture architecture relationships in these hydrothermal dolomite reservoirs. Future work should include more preparatory cleaning of the exposure, more fracture data recorded in additional transects, and analysis of fractures that are not completely sealed. With more data, this method can lower the uncertainties on the power law relationships, aid in the prediction of aperture-based fracture frequencies in the subsurface, and determine which fracture apertures in the subsurface are most likely to allow for modern geothermal fluid flow.

REFERENCES

Boggs, S., and Krinsley, D., 2006, Application of cathodoluminescence imaging to the study of sedimentary rocks, Cambridge University Press, 165 p.

Bonnet, E., Bour, O., Odling, N.E., Davy, P., Main, I., Cowie, P., and Berkowitz, B., 2001, Scaling of fracture systems in geological media: Reviews of Geophysics, v. 39, no. 3, p. 347-383.

Braun, M., and Friedman, G.M., 1969, Carbonate lithofacies and environments of the Tribes Hill Formation (Lower Ordovician) of the Mohawk Valley, New York: Journal of Sedimentary Research, v. 39, no. 1.

Cowie, P.A., Knipe, R.J., and Main, I.G., 1996, Scaling laws for fault and fracture populations: Analyses and Applications, Special Issue of J. Structural Geology, v. 18, no. 2, p. 135-383.

Davies, G.R., and Smith, L.B., 2006, Structurally controlled hydrothermal dolomite reservoir facies: An overview: AAPG Bulletin, v. 90, no. 11, p. 1641-1690.

Hurley, N.F., and Budros, R., 1990, Albion-Scipio And Stoney Point Fields-USA, Michigan Basin, *in* Foster, N., and Beaumont, E., eds., Stratigraphic Traps I: Treatise of Petroleum Geology Atlas of Oil and Gas Fields, American Association of Petroleum Geologists, p. 1-37.

Lucia, F.J., 2004, Origin and petrophysics of dolostone pore space: Geological Society, London, Special Publications, v. 235, no. 1, p. 141-155.

Machel, H.G., Mason, R.A., Mariano, A.N., and Mucci, A., 1991, Causes and emission of luminescence in calcite and dolomite, *in* K Barker, C.E., and Kopp, O.C., eds., Luminescence microscopy and spectroscopy: Qualitative and quantitative applications, Special Publications of SEPM, p. 9-26.

Machel, H.G., and Burton, E.A., 1991, Factors governing cathodoluminescence in calcite and dolomite, and their implications for studies of carbonate diagenesis, *in* Barker, C.E., and Kopp, O.C., eds., Luminescence microscopy and spectroscopy: Qualitative and quantitative applications, Special Publications of SEPM, p. 37-57.

Machel, H.G., 2000, Application of cathodoluminescence to carbonate diagenesis, *in* Pagel, M., Barbin, V., Blanc, P., and Ohnenstetter, D., eds., Cathodoluminescence in geosciences, Springer, p. 271-301.

Major, R.P., 1991, Cathodoluminescence in post-Miocene carbonates, *in* Barker, C.E., and Kopp, O.C., eds., Luminescence Microscopy and Spectroscopy: Qualitative and Quantitative Applications, Special Publications of SEPM, p. 149-154.

Marrett, R., Ortega, O.J., and Kelsey, C.M., 1999, Extent of power-law scaling for natural fractures in rock: Geology, v. 27, no. 9, p. 799-802.

Mclimans, R.K., 1991, Studies of reservoir diagenesis, burial history, and petroleum migration using luminescence microscopy, *in* Barker, C.E., and Kopp, O.C., eds., Luminescence microscopy and spectroscopy: Qualitative and quantitative applications, Special Publications of SEPM, p. 97-106.

Narr, W., 1991, Fracture Density in the Deep Subsurface: Techniques with Application to Point Arguello Oil Field (1): AAPG bulletin, v. 75, no. 8, p. 1300-1323.

Ortega, O.J., Marrett, R.A., and Laubach, S.E., 2006, A scale-independent approach to fracture intensity and average spacing measurement: AAPG bulletin, v. 90, no. 2, p. 193-208.

Patchen, D.G., Hickman, J.B., Harris, D.C., Drahovzal, J.A., Lake, P.D., Smith, L.B., Nyahay, R., Schulze, R., Riley, R.A., and Baranoski, M.T., 2006, A geologic play book for Trenton-Black River Appalachian basin exploration: U.S. Department of Energy Report: Morgantown, West Virginia, U.S. Department of Energy.

Radke, B.M., and Mathis, R.L., 1980, On the formation and occurrence of saddle dolomite: Journal of Sedimentary Research, v. 50, no. 4.

Rasmussen, J.C., Keith, S.B., Swan, M.M., Laux, D.P., and Caprara, J., 2003, Strike-slip faulting and reservoir development in New York State: Albany, New York, New York State Energy Research and Development Authority.

Sibley, D.F., and Gregg, J.M., 1987, Classification of dolomite rock textures: Journal of Sedimentary Research, v. 57, no. 6, p. 967-975.

Slater, B.E., and Smith, L.B., 2012, Outcrop analog for Trenton-Black River hydrothermal dolomite reservoirs, Mohawk Valley, New York: AAPG bulletin, v. 96, no. 7, p. 1369-1388.

Smith Jr, L.B., 2006, Origin and reservoir characteristics of Upper Ordovician Trenton--Black River hydrothermal dolomite reservoirs in New York: AAPG bulletin, v. 90, no. 11, p. 1691-1718.

Smith, L., Nyahay, R., and Slater, B., 2009, Origin, distribution and reservoir characteristics of hydrothermal dolomite in lower Paleozoic carbonates in New York State: Albany, New York, New York State Energy Research and

Development Authority.

Yoo, C.M., Gregg, J.M., and Shelton, K.L., 2000, Dolomitization and dolomite neomorphism: Trenton and Black River limestones (middle Ordovician) northern Indiana, USA: Journal of Sedimentary Research, v. 70, no. 1.

CHAPTER 4

FUTURE GEOTHERMAL ENERGY IN THE APPALACHIAN BASIN: THE TRENTON-BLACK RIVER DOLOMITE FIELDS

Abstract

This chapter integrates the conclusions drawn in Chapters 1–3, with a focus on geothermal prospects in the Appalachian Basin and the heterogeneity of the Trenton-Black River hydrothermal dolomite play. Assessments of the gaps in knowledge and future research needs and opportunities are discussed. The thematic sections provide an example of brownfield exploration using knowledge developed in Chapters 1 and 2, apply fracture data presented in Chapter 3 to a critical analysis of the productivity of the reservoirs, and conclude with a conceptual fluid flow model for geothermal applications in the Trenton–Black River reservoirs.

Sedimentary Geothermal Energy Potential in the Appalachian Basin

Whereas many reservoirs in the Appalachian Basin have sufficient permeability to produce commercial quantities of hydrocarbons, Chapter 1 showed through calculation of Reservoir Productivity Index (RPI) that very few (0.05%) of those same natural reservoirs have sufficient permeability for geothermal applications. The realization that emerges is that thick stratigraphic aquifers with high permeability and a wide lateral extent, like those successfully utilized in the Paris Basin and the German Basin (Agemar et al., 2014; Hamm et al., 2016), are not known to exist in the Appalachian Basin. The likely reason for this distinction lies in the differing geological histories of these sedimentary basins: the Paleozoic Appalachian Basin suffered more impacts of mountain building events, burial, erosion and groundwater flow, all of which contributed to diagenesis of the sedimentary formations. Numerous examples of diagenesis and deformation (e.g., compaction, cementation, dissolution, hydrothermal circulation, cement precipitation, fracturing) contributed to lower permeability in Appalachian Basin formations. Unfortunately, most of the high-rank RPI reservoirs in the region are not located near major urban centers, like Buffalo, NY and Pittsburgh, PA. Consequently, if the natural sedimentary aquifers of the Appalachian Basin are to be harnessed for geothermal heat, the end-users of heat are likely to include more favorably located small to mid-sized towns, industries, and universities.

Trenton-Black River Play as a Future Geothermal Prospect

T-BR in Tompkins County, NY

Chapter 1 examined oil and gas reservoirs in the Appalachian Basin that are already known and characterized, also known as ‘brownfield’ reservoirs, and determined their suitability to be repurposed as low-enthalpy geothermal reservoirs. Unexplored locations, or ‘greenfield’ reservoirs, were not examined in this body of work. In Chapter 1, future analyses of data from wells that did not produce hydrocarbons, but may still have sufficient porosity and permeability, were suggested. This approach is illustrated based on the wells drilled into the Black River Formation underneath Tompkins County, NY, home to the town of Ithaca, Ithaca College, and Cornell University (Figure 4.1).

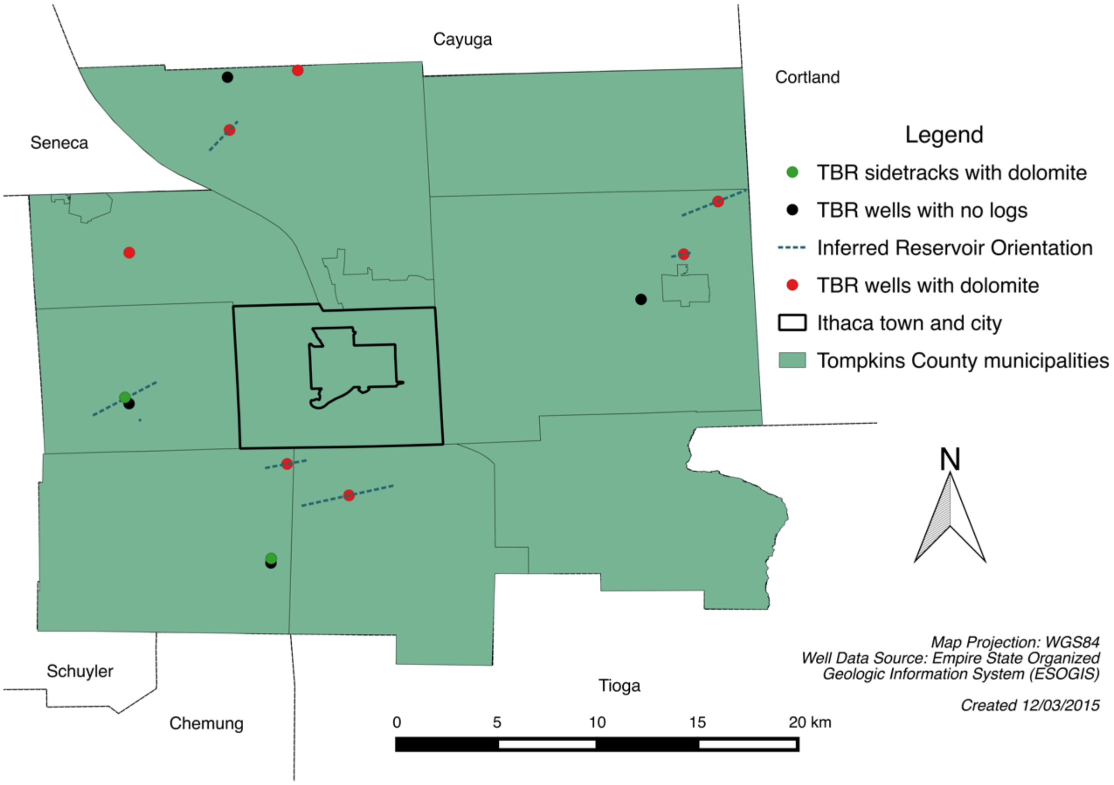

FIGURE 4.1. Map of Tompkins County, NY, and locations of wells (circles) that targeted gas in the Black River Formation. The color of the circles denotes well type and the presence of dolomite, an indicator of secondary porosity and permeability. The dotted lines indicate the inferred orientation of potential (unknown) reservoirs associated with the drilled wells. Those dotted lines are approximated by the direction from the vertical well to sidetrack locations, assuming that direction is parallel to the long direction of the reservoirs. Well locations taken from the New York State Museum, ESOGIS Database (2015).

Petroleum companies drilled thirteen wells in Tompkins County in search of gas in narrow linear grabens within the Black River Formation, like those found in nearby Steuben, Yates, and Chemung Counties. None of the Tompkins wells produced natural gas. Yet nine of those wells penetrated dolomite in the Black River Formation (Figure 4.1). In a study of the wells outside of Tompkins County that produced natural gas from the Trenton–Black River (T-BR) Formation, Smith (2006) had found that all the productive wells had dolomite in the upper half of the Black River Formation. Given the assumptions that permeability is a requirement for natural gas production and that there is a documented correlation between porosity and permeability in this play (Chapter 2), it can be inferred that the porosity and permeability of T-BR dolomite are likely to be higher than that of undolomitized T-BR limestone.

Two wells in Tompkins County that penetrated dolomite lie within 10 km of the town of Ithaca, just south of the town border (Figure 4.1). If either of these wells is associated with a hydrothermal dolomite reservoir approximately the size of Quackenbush Hill (Chapter 2), Ithaca could be supplied residential heat for 1,800–8,900 homes. Alternatively, Cornell could be supplied with hot water district heating of school buildings and greenhouses at a temperature of about 85-90°C from a depth of about 2.8–3 km. Because these wells did not produce large volumes of gas or oil, the associated reservoirs may be better candidates for a water-based EGS system than reservoirs that produced large volumes of gas or oil, because there would be less risk of dual-phase flow effects. Permeability data are not available for these wells; however, the nine wells that penetrate dolomite have wireline log data that may be analyzed in future work to characterize porosity with similar methods used in Chapter

2. After processing available wireline log data of these wells, their porosity distributions can be compared to those of wells drilled into the Quackenbush Hill reservoir (Chapter 2). While being aware that porosity is weakly correlated with permeability in the Black River dolomite, a finding of similar porosity to that of Quackenbush Hill may be indicative of satisfactory T-BR geothermal reservoir conditions in Tompkins County. This type of exercise can be applied to nonproducing wells associated with other promising Appalachian Basin hydrocarbon plays that were highlighted in Chapter 1 (e.g. Elk Group Sandstones, Lockport Dolomite, Newburg Sandstone), to determine if dry reservoirs are candidates for geothermal heat extraction.

Reservoir Considerations

Permeability

Prior to the work done in this dissertation, the former average reservoir permeability value cited for the T-BR reservoirs (Chapter 1) was guided by a Department of Energy brine disposal report conducted by Smith et al. (2004). That report regressed the Whiteman #1 core horizontal permeability data using an *exponential* fit, a technique that is commonly used to correlate porosity and permeability, as follows:

$$k = 1.8716e^{0.4967\phi}, \tag{4.1}$$

where k is in mD, ϕ is in porosity percent, and the constant 1.8716 has units of mD. That regression was applied to the average porosity value from the core, resulting in a calculated average permeability of 60 mD. Core permeability is measured with a gas rather than a liquid, so the values were corrected for the Klinkenberg effect. These values were corrected for the Klinkenberg effect using a correlation for carbonates (Al-Jabri, 2015), resulting in a permeability value of 52 mD. However, Equation 4.1 yields unrealistic permeability values for empirically realistic porosity values. For example, an empirical core porosity measurement of 25% yields a permeability of 462,500 mD, which is 45 times greater than the largest permeability value recorded in the Whiteman #1 core (approximately 10,200 mD).

As mentioned in Chapter 2, Jennings and Lucia (2003) have found that power law fits are more accurate for porosity–permeability relationships in carbonates. This led to the power law regression in Equation 2.8 of Chapter 2,

$$k_L = 0.39\phi^{2.87}, \tag{4.2}$$

which calculates a more realistic permeability of 4,000 mD for a Trenton-Black River sample with 25% porosity (Figure 4.2), based on empirical measurements from the core. Therefore, the average permeability value derived from the application of the power law regression to adjusted NPHI porosity recordings was applied to the Monte Carlo simulation in Chapter 1, instead of the average permeability value derived from the exponential fit in Equation 4.1. Table 1 illustrates that this decision results in a factor of 2.3 difference in calculated average reservoir permeability from the NPHI porosity logs for the Trenton-Black River reservoirs. Further analysis of NPHI wireline logs from additional reservoirs (excluding Quackenbush Hill) and additional collection and measurement of cores from other producing fields (excluding County Line) ought to provide greater precision on the average permeability value for this gas play. Nevertheless, the average permeability value calculated in Camp and Jordan

(2016; Chapter 2) is treated as an improved approximation of average permeability in the Trenton-Black River reservoirs, despite the limitations of a reservoir analysis based on an empirical relationship from one core.

TABLE 4.1. Comparison of Klinkenberg-corrected average permeability values available for the Whiteman #1 core.

	Smith et al. (2004)	**Camp and Jordan (2016)**
Average *k* (mD)	52 (Eq. 4.1)	120
Source	Exponential regression of Whiteman core data to average Whiteman core porosity	Applying power law regression of Whiteman core data to average porosity from NPHI logs recorded in Quackenbush Hill reservoir

EGS and Phase Effects

Based on the results from Chapter 1, even those reservoirs with the highest-ranked RPI in the region are likely to require reservoir stimulation techniques via Enhanced Geothermal Systems (EGS). This is especially true in the case of water-based geothermal systems, which would yield an RPI six times less than the same system using supercritical carbon dioxide (sCO_2) (Table 1).

Dual-phase flow effects were not considered in Chapter 1 due to time and data constraints, but they are important for assessing the degree to which residual oil, gas, water, or some combination may hinder geothermal productivity and heat sweep. These effects are a concern for both water-based and CO_2-based systems in repurposed, depleted hydrocarbon reservoirs. The challenges of utilizing supercritical CO_2 include the additional pressure and energy required to keep the CO_2 in a supercritical state, especially as the temperature and density change along the wellbore, as well as additional costs of procuring pure CO_2.

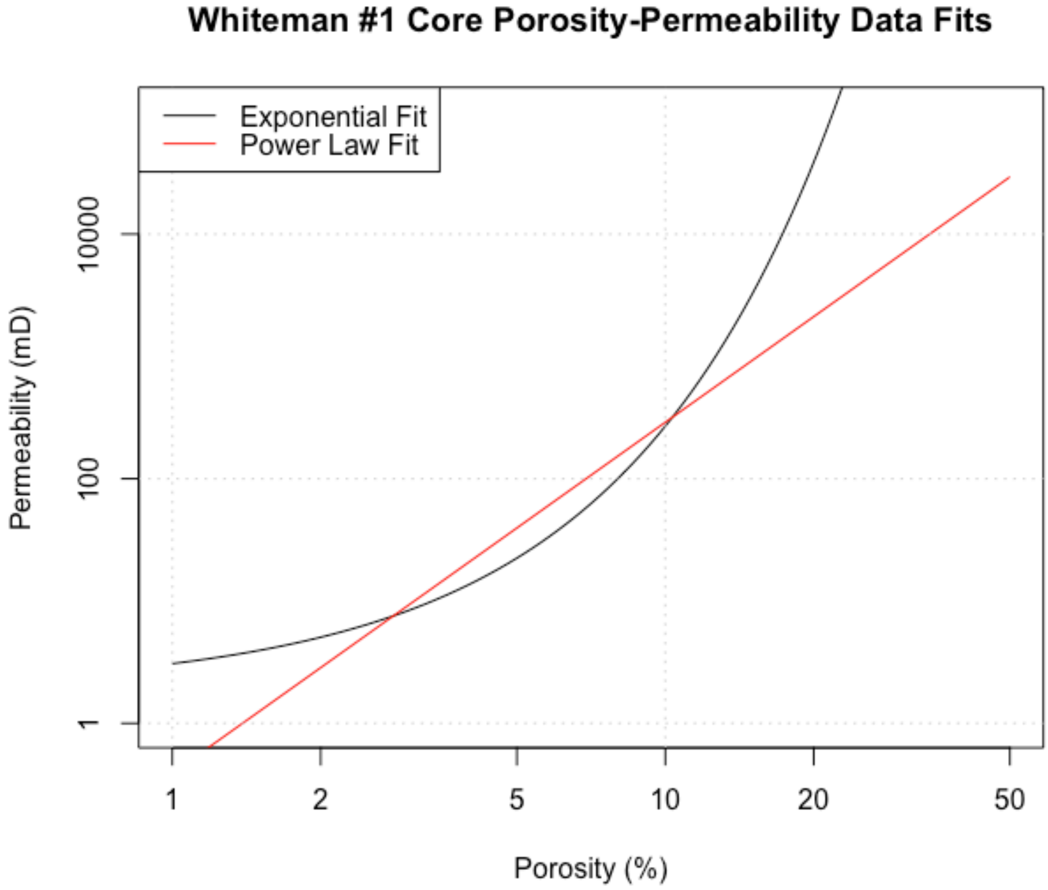

FIGURE 4.2. Comparison of the exponential (black line) and power law (red line) fits of the Whiteman #1 core porosity and permeability data. Note that both axes use a logarithmic scale. The power law fit predicts a higher permeability than the exponential fit for porosity values between 3-10%. The exponential fit predicts a much higher and unrealistic permeability for a porosity over 10% than the power law fit does.

If residual gas and water data are available for future work, they may help determine the best geothermal fluid choice for the reservoirs. For example, if residual water is very high in a reservoir, a water-based system may be a wise option. In contrast, if residual gas is very high, a CO_2-based system may be the best option.

TABLE 4.2. Comparison of RPI P50 results for Trenton–Black River reservoirs. The differing variables in these two systems are fluid viscosity and permeability, due to the slight Klinkenberg correction.

	Water-based System	**CO_2-based system**
Minimum RPI (kg/MPa-s)	1.7	8.1
Maximum RPI (kg/MPa-s)	27.8	148.5

Flow through Fractures versus Intergranular Flow

Because the databases mined for data across the Appalachian Basin lack information about fracture frequency, Chapter 1 develops an estimate of reservoir productivity potential based only on the principles of intergranular flow. The results from Chapter 1 show that the intergranular flow RPI predictions match closely with initial gas production data from a homogeneous sandstone formation, the Bockhahn Sandstone. However, the RPI predictions overestimate the gas production from two Trenton-Black River reservoirs, Wilson Hollow and Quackenbush Hill, which are classified as highly fractured reservoirs with negligible intergranular porosity or permeability (Smith, 2006). In the evaluation of this result, the uncertainties that derive from several assumptions within the validation model (Chapter 1) must be acknowledged: averaged reservoir parameters, pressure drive during initial gas production (3 ± 1 MPa), and the composition of produced natural gas (pure methane) among others. Nevertheless, the results indicate that the intergranular flow RPI approximation does not produce accurate results for the T-BR reservoirs, and perhaps for fractured reservoirs in general.

As an alternative to estimating RPI due to intergranular flow, an analogous function more appropriate to fracture flow was investigated. An approximation of a fractured reservoir productivity index was created based on the cubic law for flow in a single horizontal fracture (Tsang and Witherspoon, 1981; National Research Council, 1996), in the hopes that it could be applied in the Monte Carlo simulation for reservoirs like the Trenton-Black River. The radial flow model from Tsang and Witherspoon (1981) was modified using the relationship between fracture aperture and permeability (Zimmerman and Bovarsson, 1996), where k is the permeability in m^2 and a is the fracture aperture in meters:

$$k = \frac{a^2}{12}. \tag{4.3}$$

The resulting fracture productivity index (FPI) for radial flow through a single horizontal fracture is:

$$FPI = \frac{Q}{\Delta P} = C\,\frac{\pi(12k)^{\frac{3}{2}}}{6\mu\ln\left(\frac{D}{r_w}\right)}. \tag{4.4}$$

In the above equation, FPI is in kg/MPa-s, k is the permeability in m^2, D is the distance between the wellbores in m (held constant at 1000 m), r_w is the wellbore radius in m, μ is the fluid viscosity in Pa-s, and C is the constant for conversion from m^3 to kg (Tsang and Witherspoon, 1981). Despite the absence of reservoir thickness in Equation 4.4, its units are the same as that of Equation 1.1: flow rate per pressure drop.

The calculated productivity from Equations 1.1 (intergranular flow RPI) and 4.4 (FPI) were compared across a range in permeability up to 9.0 x 10^{-8} m^2 (i.e. fracture aperture of about 1 mm) in a reservoir with a thickness of 100 m (Figure 4.3). For the FPI, a range of fracture intensities, or the number of fractures per unit of length (Ortega et al., 2006), was modeled in Equation 4.2: one fracture in the entire reservoir, one fracture per meter, ten fractures per meter, 100 fractures per meter, and 1,000 fractures per meter. For example, for the model of 1,000 fractures per meter, the FPI of one fracture was multiplied by 1,000.

The RPI of a 100-m thick porous medium is nearly six orders of magnitude greater than the productivity of a 100-m thick rock body with a single fracture (Figure 4.3a). As the fracture intensity increases in the reservoir, the FPI approaches the value of RPI for an equivalent permeability or fracture aperture. FPI exceeds that of RPI when there are at least 1,000 1-mm fractures per meter present in the reservoir, which is the point at which all rock space has been consumed by fractures. The productivity displayed in Figures 4.3a and 4.3b expresses only fluid flow, not heat transfer, which is the practical objective. Though a reservoir with 100 small fractures (< 0.01 mm apertures) per meter (Figure 4.3b) is going to have a lower fluid productivity than a reservoir with one large fracture (~1 mm aperture) per meter (Figure 4.3a), the set of smaller fractures is going to provide more surface area to the fluid for higher heat transfer than the single fracture.

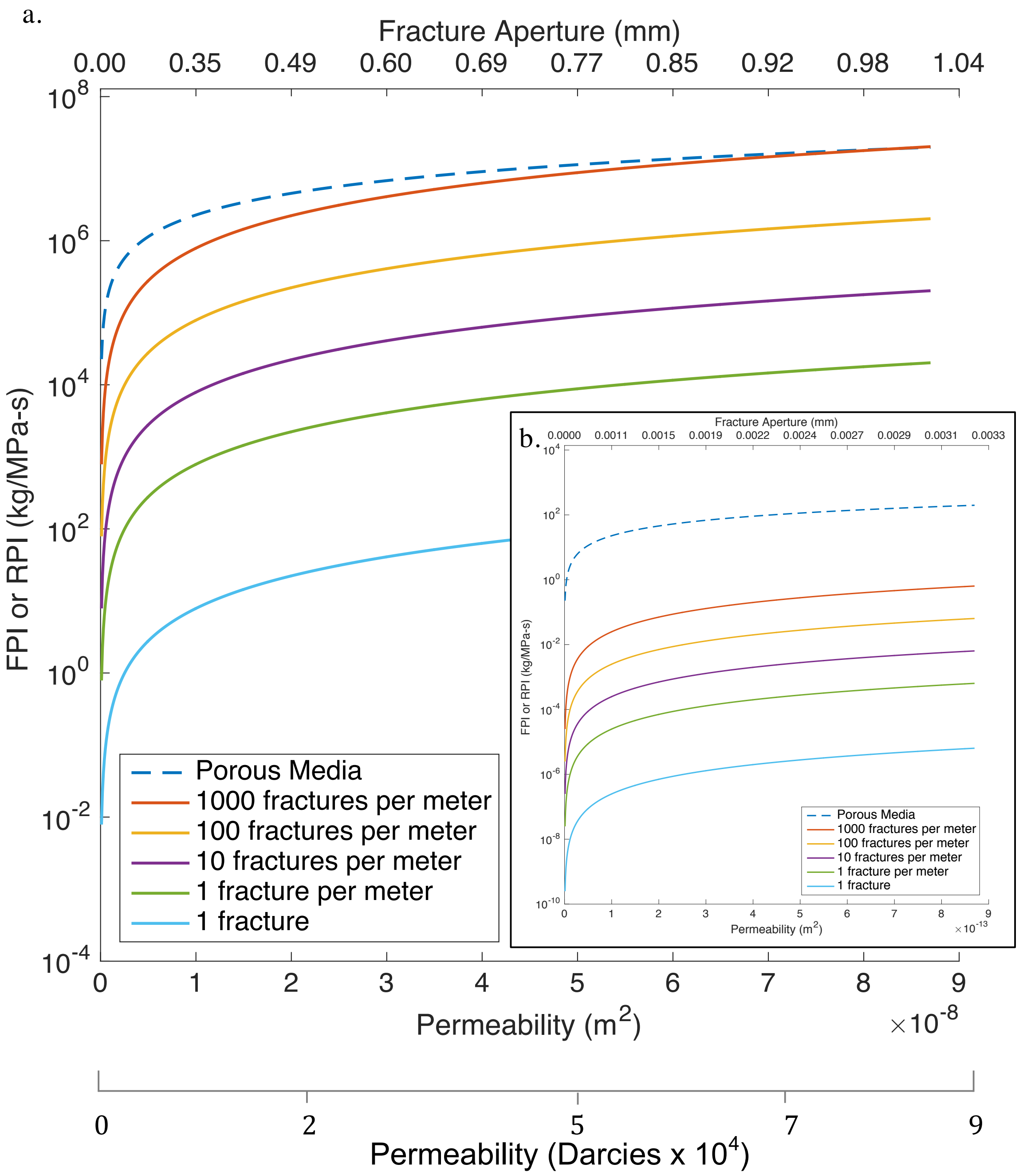

FIGURE 4.3. Response of Reservoir Productivity Index (Eq. 1.1; or Fractured Productivity Index, Eq. 4.4) to changes in permeability, for porous media and fractured media. In figure (a), FPI meets that of porous media when there are 1,000 1-mm fractures per meter present in the reservoir, which is the point at which all rock space has been consumed by fractures. The permeability range extends to 9 x 10^{-8} m^2, or 90,000 Darcies. In inset (b), the FPI with 1,000 fractures per meter is four orders of magnitude lower than the porous media RPI. Here, the permeability range extends to 9×10^{-13} m^2, or 900 mD.

When designing a geothermal energy system, fluid flow productivity and heat productivity must be considered in tandem. The fluid productivity needs to be high enough to produce economically acceptable heat productivity, which involves a tradeoff between achieving a sufficiently high energy extraction rate and preventing premature depletion of the reservoir. To satisfy this tradeoff, the fluid must sweep through a large volume of the reservoir, along rock surfaces within the permeable zones of the reservoir defined in part by the injection and production well separation. Noting that the thermal energy production rate is linearly proportional to the mass flow rate and the temperature difference between injection and production, there is an incentive to increase mass flow rate. However, the maximum pressure within the reservoir must not exceed the confining strength of the rock to prevent uncontrolled growth or reactivation of fractures and faults. This ultimately constrains the flow rate of the system even if the swept area of the reservoir is very large. For example, for the Quackenbush Hill reservoir, the calculated RPI from Chapter 1 is 4 ± 1 kg/MPa-s. From Chapter 2, the Quackenbush reservoir can sustain a wellhead injection pressure up to 20 ± 5 MPa without reactivating the large graben-bounding faults. As a result, the maximum fluid flow productivity that can be sustained within the reservoir without reactivating the large faults is 80 ± 28 kg/s. However, if the economically acceptable flow productivity needed to sustain heat production for the lifetime of the project (approx. 10-20 years) was estimated as 40 ± 10 kg/s, then there is a range of 40 ± 29 kg/s in which sustainable heat production is feasible. A more detailed treatment of heat transfer considerations specific to fractures (e.g. Fox et al., 2013) in the Quackenbush Hill reservoir is not addressed in this scope of work.

However, the FPI applies only to a single horizontal fracture (or a single set of fracture frequencies, as shown in Figure 4.3) in a reservoir of any thickness, rather than all fractures of many different apertures and frequencies present in a reservoir with a defined thickness. Summing the FPI across multiple fractures of varying aperture sizes can theoretically be used to approximate the productivity contributions from all fractures. To do this, the reservoir thickness and the cumulative fracture intensity or spacing are needed to approximate the resulting Fractured Reservoir Productivity Index (FRPI),

$$FRPI = x\sum_{i=1}^{n} Hf_i[FPI]_i \ . \qquad (4.5)$$

In the FRPI equation, i is the fracture aperture class, where the aperture classes 1, 2, 3, …, n correspond to an aperture of 0.05, 0.62, 0.75, …, 5.0 mm. H is the reservoir thickness, f is the frequency of fractures (m^{-1}) at the i^{th} aperture class, FPI_i is the fracture productivity index for a fracture of aperture class i, and x is the percentage of all fractures in the reservoir that are open and allow for fluid flow.

Although fracture frequency or aperture are not available in most data sets for the Appalachian Basin reservoirs (Chapter 1), the core and field data appropriate to the Trenton-Black River plays of central New York (Chapter 3) enable a more thorough comparison to RPI and FPI metrics. New approximate fracture aperture–frequency relationships (Chapter 3) for the Quackenbush Hill T-BR reservoir serve as input to the FPI equation, and the result can be compared with the gas data-validated RPI value (Chapter 1). Aperture–frequency relationships from Chapter 3 (transects two and three) can be used in conjunction with Equation 4.5 at various fracture aperture intervals to predict a FPI for fractures within Quackenbush Hill reservoir, which has an average thickness of 33 m. Fracture intervals in the Quackenbush Hill reservoir were selected using the same logarithmic intervals as the fracture analysis in Chapter 3.

TABLE 4.3. Pre- and post-mineralization fracture apertures in thin sections of the Whiteman #1 core. Measurements recorded using image processing software.

Sample #	9529.5-1	9529.5-2	9534-2	9534-1
Fracture Aperture, pre-mineralization (mm)	4.0	3.0	1.24	1.0
Fracture Aperture, post-mineralization (mm)	0.18	0.03	0.05	0.08
	0.17	0.07	0.05	0.02
	0.06	0.14	0.06	0.09
	0.05	0.11	0.03	0.07
	0.06	0.2	0.06	0.06
	0.09	0.14	0.03	0.05
	0.09	0.2	0.09	0.06
	0.12	0.13	0.06	0.05
	0.17	0.09	0.04	0.03
	0.04	0.05	0.08	0.03
Median aperture (mm)	0.09	0.12	0.055	0.055
% Aperture Reduction	98%	96%	96%	95%

Whereas the aperture-frequency relationships of Chapter 3 describe mineralized and partially mineralized paleo-fractures in an outcrop, the objective is to apply them to a subsurface situation in which it is hypothesized that similar fractures would contain less mineral fill. Consequently, the vein aperture data were adjusted using the petrographic images from the Whiteman core (Chapter 3). In the Whiteman #1 core thin sections, partially mineralized fracture apertures are approximately 96% smaller than their original pre-mineralized fracture, due to various stages of mineralization (Table 4.3). Therefore, as an example, the predicted total productivity of a 0.03-mm *open* fracture in the subsurface was applied to the predicted frequency of 0.75-mm mineralized fractures in the outcrop. The FPI values from each fracture aperture interval within a 33 m thick unit were then summed to create a total FRPI. These final products can be compared to the predicted and validated RPI P50 of Quackenbush Hill from Chapter 1.

Table 4.4 shows that during the comparison of FRPI and RPI for Quackenbush Hill, total FRPI overestimates productivity by a factor of 33. Of the veins observed in the Whiteman #1 core samples in Chapter 3, four of 28 observable veins were partially open, resulting in a 14% open rate. If the total FRPI were reduced by 86% to reflect the reduction in flow due to fractures which were sealed completely, 14% FRPI is still five to six times greater than the natural gas productivity. There are several assumptions built into this model which may help explain that discrepancy. First, the FRPI assumes that each of the fractures is isolated and does not interfere with the others, which would affect the FRPI. Second, it also assumes that each fracture is essentially two parallel plates separated by a constant distance. This assumption ignores the effect of surface roughness, or asperities, on the ideal radial flow, and therefore overestimates the predicted productivity. Additionally, the model assumes radial flow, whereas fluid flow in a two-well geothermal system would likely be dipole flow from an injection well to a production well. But with an increasing number of wells in the geothermal wellfield (e.g. five-spot well pattern), fluid flow would deviate from dipole flow towards radial flow. The FRPI equation assumes horizontal flow in horizontal fractures, but the majority of fractures in the T-BR reservoirs are nearly vertical. However, horizontal permeability in the T-BR reservoirs is significantly higher than vertical permeability. Therefore, the horizontal fracture model is likely a close approximation of horizontal flow through vertical fractures in the T-BR reservoirs. And finally, this model does not incorporate the effects of buoyancy, which are important to consider when there is a large temperature differential between the injected water and the reservoir, and when designing a system with horizontal wells. It is likely that, of the above assumptions listed, the effect of asperities and surface roughness along the fractures would have the greatest impact on the productivity estimate.

TABLE 4.4. Comparison of Fractured Reservoir Productivity Index (FRPI) and natural gas productivity of Quackenbush Hill reservoir (33 m thick).

Outcrop Vein Aperture (mm)	Assumed Subsurface Fracture Aperture (mm)	T2 Fracture Frequency (m^{-1}), Eq. 3.1	# Fractures in Quackenbush (T2)	T3 Fracture Frequency (m^{-1}), Eq. 3.2	# Fractures in Quackenbush (T3)	T2 FRPI (kg/MPa-s)	T3 FRPI (kg/MPa-s)
0.05	2.00E-03	18.07	596	66	2178	9.04E-04	3.30E-03
0.062	2.48E-03	15.24	502	53.23	1756	1.45E-03	0.01
0.075	3.00E-03	13.1	432	44	1452	2.21E-03	0.01
0.095	3.80E-03	10.86	358	34.74	1146	3.73E-03	0.01
0.115	4.60E-03	9.34	308	28.7	947	0.01	0.02
0.14	0.01	7.99	263	23.57	777	0.01	0.03
0.175	0.01	6.69	220	18.86	622	0.01	0.04
0.215	0.01	5.68	187	15.35	506	0.02	0.06
0.265	0.01	4.82	159	12.45	410	0.04	0.09
0.33	0.01	4.05	133	10	330	0.06	0.14
0.4	0.02	3.47	114	8.25	272	0.09	0.21
0.5	0.02	2.91	96	6.6	217	0.15	0.33
0.62	0.02	2.45	80	5.32	175	0.23	0.51
0.75	0.03	2.11	69	4.4	145	0.36	0.74
0.95	0.04	1.75	57	3.47	114	0.6	1.19
1.15	0.05	1.5	49	2.87	94	0.92	1.75
1.4	0.06	1.29	42	2.36	77	1.41	2.59
1.75	0.07	1.08	35	1.89	62	2.31	4.04
2.15	0.09	0.92	30	1.53	50	3.64	6.11
2.65	0.11	0.78	25	1.25	41	5.78	9.27
3.3	0.13	0.65	21	1	33	9.37	14.38
4	0.16	0.56	18	0.83	27	14.33	21.13
5	0.2	0.47	15	0.66	21	23.45	33.02
6.2	0.25	0.4	13	0.53	17	37.71	50.77
7.5	0.3	0.34	11	0.44	14	57.39	74.29
9.5	0.38	0.28	9	0.35	11	96.7	119.19
	Total FRPI					254.60	339.94
	14% FRPI					35.64	47.59
	Natural Gas Productivity (kg/MPa-s)					**7.79 [5.9–11.5]**	

In Chapter 1, the intergranular flow RPI overestimated gas productivity by approximately three times. Therefore, at present, RPI is a closer approximation of flow through the fractured Trenton-Black River reservoirs than the FRPI approximation. Before the fracture flow model can be accurately utilized to predict productivity in the T-BR reservoirs, two components ought to be studied further: the effect of asperities (fracture roughness) and fracture interconnections on productivity in the T-BR. Additional work is also needed to quantify the effect of fracture fill heterogeneity on the productivity of these reservoirs. Furthermore, work is needed to reduce uncertainty on the fracture aperture–frequency relationships, by measuring fractures along three to five additional transects at the Palatine Bridge outcrop.

Two hypotheses are presented to explain why RPI more accurately reflects the flow of fluids through the Trenton-Black River reservoirs. First, there may be error in either the outcrop vein aperture measurements (Chapter 3), or in the conversion of vein aperture to open subsurface apertures (Chapter 4), either of which may lead to a poor FRPI approximation. Second, fractures coupled with vugs in the T-BR may cause the reservoirs to deviate from fracture flow behavior towards that of a porous medium. This theory is supported by the observation of a brightly luminescent matrix dolomite section of the Whiteman core, surrounded above and below by non-luminescent matrix dolomite (Chapter 3). Not only does this imply there is vertical anisotropy in the dolomite section, but it also implies that some portion of the Black River dolomitization was controlled by intergranular flow. Furthermore, in Chapter 1, the RPI prediction of the highly porous and vuggy pinnacle reef Onondaga Limestone was also overestimated by about a factor of three, similar to the T-BR results. This suggests that the presence of vugs may play a more dominant role than fractures in the fluid flow within the T-BR reservoirs.

Conceptual Model of Fluid Flow in T-BR Reservoirs

Dolomitization transformed the upper section of the fractured Black River limestone into a porous, heterogeneous, and horizontally permeable dolomite reservoir. The vertical thickness of the dolomite delineates the permeable thickness of the T-BR reservoirs, as the limestone below and flanking the dolomite grabens have very low permeability (Smith, 2006; Smith et al., 2009; Slater et al., 2012). The dolomite thickness throughout the reservoirs is known to be heterogeneous, based on recorded dolomite thicknesses from producing wells (Smith et al., 2009), and is therefore difficult to constrain between wells.

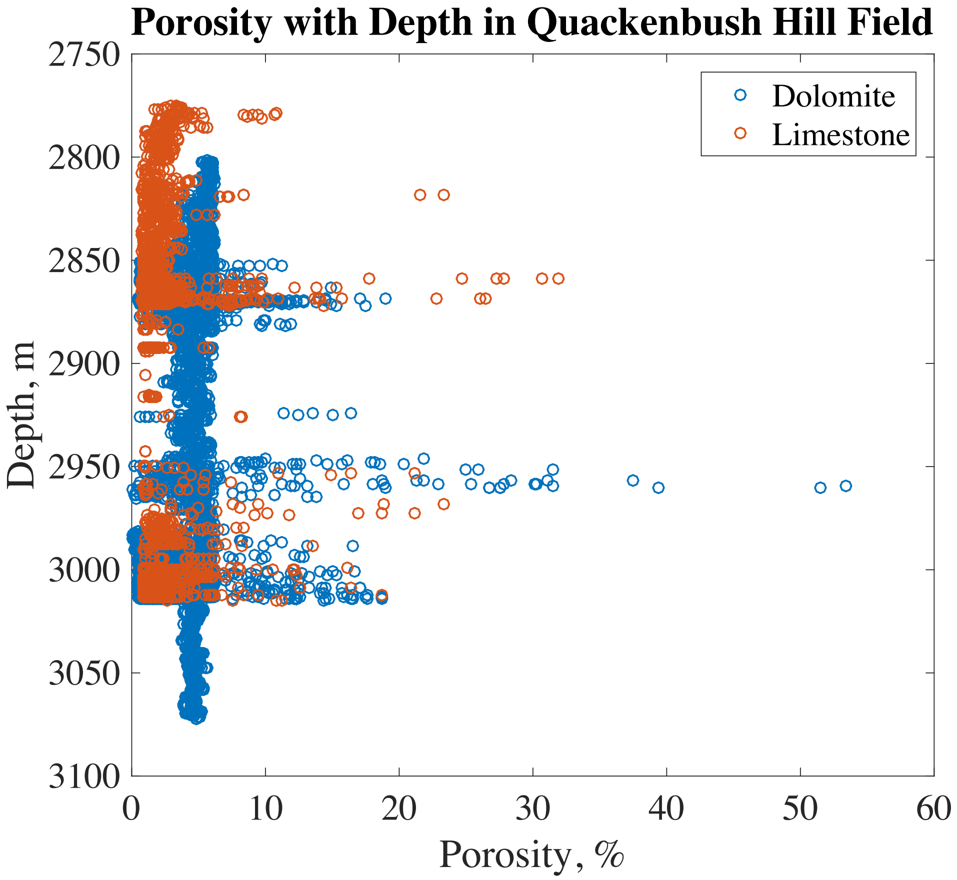

FIGURE 4.4. (Also Figure 2.7) Adjusted neutron porosity hydrogen index (NPHI) porosity versus true vertical depth, with values sorted by lithology. Many wells in this field are horizontal; therefore, measured depth locations along the length of the borehole were converted to total vertical depth. Both dolomite and limestone are associated with higher porosity zones. High porosity zones are partitioned into three distinct zones, located at 2860, 2950, and 3000 m depth. These may be representative of multiple vertically partitioned zones or a single high porosity zone that dips southward with the top of the Black River Formation.

Fluid flow through the Black River is likely to be approximately horizontal, confined by a single zone of high porosity and permeability dolomite, dominated by vugs and perhaps less so by fractures. Though Chapter 2 discussed the possibility of multiple horizontal zones of high porosity within the dolomite section of the Black River Formation (2850–2875 m, 2940-2960 m, and 3000–3025 m; Figure 4.4 or Figure 2.7), a more likely hypothesis is that there is only one zone of high porosity in the dolomite section that dips 3° southward. This conclusion is drawn because the northern wells in the field penetrate the Black River Formation at a shallower depth than the southern wells in the field. For example, Gregory 1446-A, the northernmost well in the Quackenbush Hill well-field, penetrates the Black River Formation at a depth of 2861 m (9388 ft; New York State Museum, 2017), while Andrews 1, the southernmost well in the well-field, penetrates the Black River Formation at a depth of 3011 m (9879 ft; New York State Museum, 2017). Wells between the two penetrate the Black River Formation between 2861 and 3011 m.

In several of the T-BR fields, there exist multiple parallel, en echelon grabens through which geothermal fluids could flow. The Quackenbush Hill reservoir is an example of such fields, comprised of two fault-bounded, parallel, en echelon grabens that overlap by at least 4 km (Chapter 2). At the Palatine Bridge outcrop, there are three dolomite grabens (‘bodies’), two of which are connected at the surface. At depth, all three dolomite bodies of the quarry are at least partially connected to each other (Slater and Smith, 2012). If the dolomitized sections of the two Quackenbush grabens are connected to each other, fluid flow could theoretically be sustained between the two grabens. However, if those dolomitized sections are not connected, separate well pairs would be needed to access both grabens, or EGS would be required to artificially connect them. Chapter 2 shows calculations that the first fracture sets to reactivate are oriented vertically and oblique to the strike of the fields, which is an ideal orientation for connecting the two grabens.

A suggested well-field design for the Trenton-Black River reservoirs is one that harnesses horizontal flow through permeable fractures and vugs, given that vertical permeability in these fields is negligible (Chapter 2). Horizontal wells were extremely successful in producing high volumes of gas from the Quackenbush Hill reservoir (Smith, 2006), therefore horizontal injectors and producers may also be a successful approach for a T-BR geothermal system design. Though heterogeneity of permeability is difficult to predict, a starting point for further exploration could begin with locations nearby to wells that produced the largest volumes of gas and had high initial production rates (Figure 4.5). These wells may be indicators of high permeability regions in the reservoir.

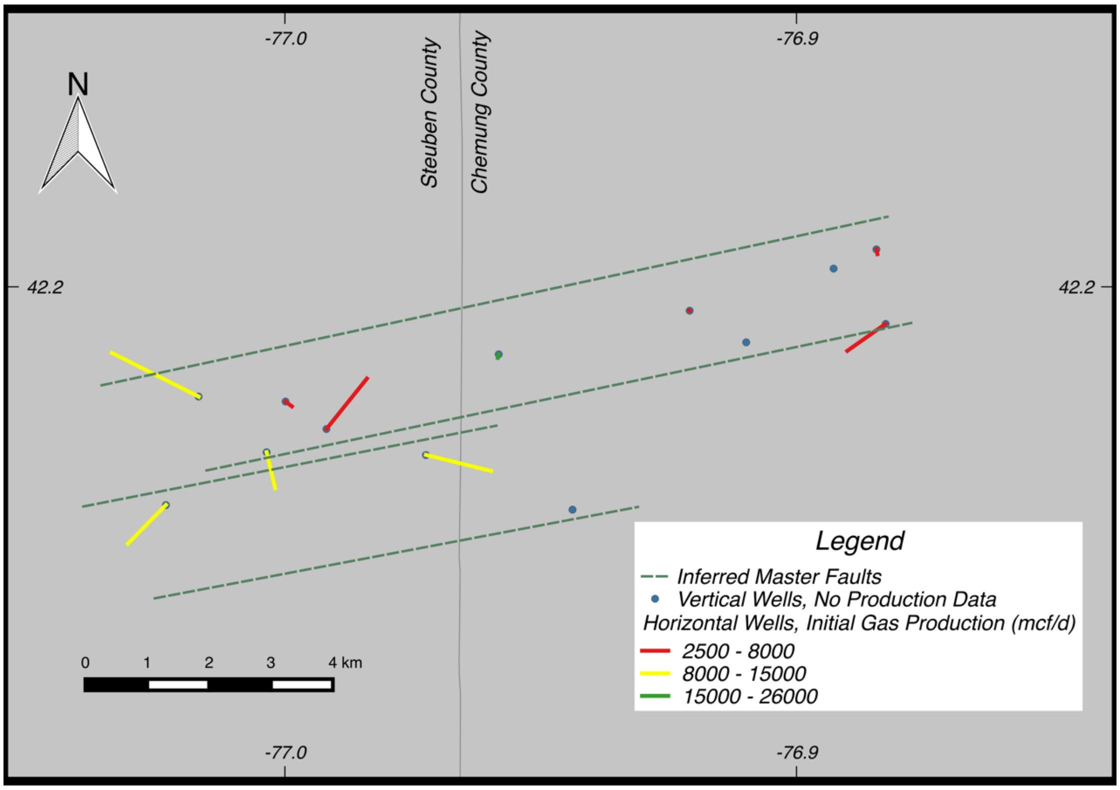

FIGURE 4.5. Map view of the Quackenbush Hill well-field, showing vertical (blue) and horizontal wells orientations and lengths (green, yellow, and red). The dashed green lines indicate the inferred master fault locations and orientations. The well with the highest gas production rates, Lovell, is located at the center of the north graben, shown by a green dot due to its short horizontal leg. A map of this sort can be used as a baseline to describe lateral heterogeneity in the reservoir.

Conclusions

The Trenton-Black River reservoirs of New York are unequivocally the best sedimentary aquifer candidates for geothermal energy production in the Appalachian Basin region of NY, PA, and WV, based on predicted fluid productivity from an analysis of available data in Chapters 1–3. An important characteristic of this hydrocarbon play in the Appalachian Basin is the domination by secondary porosity (post-depositional alteration), rather than by factors controlling primary porosity. In other sedimentary basins with long geologic histories like the Appalachian Basin, geothermal reservoir exploration and characterization should include formations with secondary, porosity-enhancing alteration (like dolomitization).

While both the porous media approximation and the fractured reservoir approximation overestimate natural gas production rates, at this time the porous media approximation provides a closer estimate of productivity in the T-BR reservoirs. This may be related to the coincidence of both fractures and permeable vugs in the reservoirs, or error in assumptions or fracture data collection.

In the exploration and modeling phase of a future T-BR geothermal project, a first-order reservoir simulation can be conducted to determine the feasibility of the project before drilling even begins. More complex reservoir models of the T-BR fields can incorporate the results of this body of research, including:

- The dual porosity model: 0.5% and 8% (fractures and vugs; Chapter 2),
- The dip of the reservoir: 3° (Chapter 4), coupled with the N075E-N085E orientation of the fields,
- The statistical distribution of variable reservoir thickness (Chapter 1),

- The statistical distribution of variable reservoir permeability and porosity (Chapters 1 and 2),
- Detailed fracture aperture–frequency predictions (such as those from Chapter 3).

Reservoir modeling of the T-BR reservoirs can also be guided by the conceptual fluid-flow model developed in this chapter, with the addition of flow orientation, approximate location and orientation of major faults, and amount of fracture mineralization. Following reservoir modeling, additional raw subsurface data are needed to better understand the heterogeneity within these reservoirs. Additional cores, geophysical surveys, pressure tests and tracer tests between existing wells are recommended as the next stage of data collection. If additional data analysis of the Trenton–Black River reservoirs continues to prove them as promising options to repurpose as geothermal reservoirs, they have the potential to provide a clean, reliable source of heat to homes, businesses, industries, and municipalities of southern New York.

REFERENCES

Agemar, T., Weber, J., and Schulz, R., 2014, Deep geothermal energy production in Germany: Energies, v. 7, no. 7, p. 4397-4416.

Al-Jabri, R.A., Al-Maamari, R.S., and Wilson, O.B., 2015, Klinkenberg-corrected gas permeability correlation for Shuaiba carbonate formation: Journal of Petroleum Science and Engineering, v. 131, p. 172-176.

Camp, E., and Jordan, T., 2016, Feasibility study of repurposing Trenton--Black River gas fields for geothermal heat extraction, southern New York: Geosphere, v. 13, no. 1, 14 p.

Fox, D.B., Sutter, D., Beckers, K.F., Lukawski, M.Z., Koch, D.L., Anderson, B.J., and Tester, J.W., 2013, Sustainable heat farming: modeling extraction and recovery in discretely fractured geothermal reservoirs: Geothermics, v. 46, p. 42-54.

Hamm, V., Bouzit, M., and Lopez, S., 2016, Assessment of complex well architecture performance for geothermal exploitation of the Paris basin: A modeling and economic analysis: Geothermics, v. 64, p. 300-313.

Jennings, J.W., Lucia, F.J., 2003, Predicting permeability from well logs in carbonates with a link to geology for interwell permeability mapping Proceedings, SPE Annual Technical Conference and Exhibition, p. 215-226.

National Research Council, 1996, Rock fractures and fluid flow: contemporary understanding and applications: Washington, D.C., National Academies Press.

New York State Museum, Empire State Oil and Gas Information System, www.esogis.nysm.nysed.com (Accessed August 2015).

New York State Museum, Empire State Oil and Gas Information System, www.esogis.nysm.nysed.com (Accessed January 2017).

Ortega, O.J., Marrett, R.A., and Laubach, S.E., 2006, A scale-independent approach to fracture intensity and average spacing measurement: AAPG bulletin, v. 90, no. 2, p. 193-208.

Slater, B.E., and Smith, L.B., 2012, Outcrop analog for Trenton-Black River hydrothermal dolomite reservoirs, Mohawk Valley, New York: AAPG bulletin, v. 96, no. 7, p. 1369-1388.

Smith, L., Lugert, C., Bauer, S., Ehgartner, B., and Nyahay, R., 2004, Systematic Technical Innovations Initiative Brine Disposal in the Northeast, Department of Energy National Energy Technology Laboratory, 269 p.

Smith, L.B., 2006, Origin and reservoir characteristics of Upper Ordovician Trenton--Black River hydrothermal dolomite reservoirs in New York: AAPG bulletin, v. 90, no. 11, p. 1691-1718.

Smith, L., Nyahay, R., and Slater, B., 2009, Origin, distribution and reservoir characteristics of hydrothermal dolomite in lower Paleozoic carbonates in New York State: Albany, New York, New York State Energy Research and Development Authority, 88 p.

Tsang, Y.W., and Witherspoon, P.A., 1981, Hydromechanical behavior of a deformable rock fracture subject to normal stress: Journal of Geophysical Research, v. 86, no. B10, p. 9287-9298.

Zimmerman, R.W., and Bodvarsson, G.S., 1996, Hydraulic conductivity of rock fractures: Transport in porous media, v. 23, no. 1, p. 1-30.

APPENDIX A-1

This appendix is intended to augment Chapter 1 of this dissertation, by providing additional details about the original databases and modified inputs for the Appalachian Basin Geothermal Play Fairway Analysis project. All research and literature that affected decisions for the reservoir data inputs are recorded here, including data for geologic formations in the Appalachian Basin.

Database Integration

Two disparate databases were integrated for this project: 1) the Empire State Organized Geologic Information System (ESOGIS; data for reservoirs in New York), and 2) the Midwest Regional Carbon Sequestration Partnership (MRCSP; data for reservoirs in Pennsylvania and West Virginia). When the two databases were merged, there were discrepancies between the available data and the terminology used in each database.

1. Geologic Formation Name: The following formation codes were listed in the MRCSP database. The decrypted formation name for each is listed next to the code. Very often, the name of a formation in Pennsylvania and West Virginia is different than the given name of the same formation in New York. For those formations, the New York formation name was used. If a reservoir is listed as having produced from a smaller unit within a larger formation, the formation name was used. Any formation name changes are listed in parentheses next to the original formation name, shown below.
    a. BLDG: Bald Eagle

   b. BILDF: Bass Islands Formation
   c. BKMN: Beekmantown
   d. BNSN: Benson
   e. BERE: Berea
   f. BRRL: Brallier (Elk Group)
   g. CHZY: Chazy (Black River)
   h. CLNN: Clinton (Medina)
   i. DVSHL: Devonian Shale
   j. DVNNU: Devonian Unconformity Play
   k. ELKG: Elk Group
   l. GBRG: Gatesburg (Rose Run)
   m. GRDN: Gordon
   n. HDBG: Helderberg
   o. HRVL: Huntersville
   p. HVOK: Huntersville/Oriskany
   q. KEFR: Keefer
   r. LCKP: Lockport
   s. MDIN: Medina
   t. MLTI: “Multi”
   u. NWBG: Newburg
   v. ONDG: Onondaga
   w. ORSK: Oriskany
   x. RSRN: Rose Run
   y. SCHR: Scherr (Elk Group)
   z. SDCI: Silurian Devonian Carbonate Interval (Lockport)
   aa. TRNN: Trenton
   bb. TLLY: Tully
   cc. TCRR: Tuscarora
   dd. WEIR: Weir

2. Average Reservoir Depth

The MRCSP database holds values for each reservoir’s “Average Production Depth”, which is interpreted as the top of the reservoir production zone. The ESOGIS database does not have production depth data reported; therefore, reservoir depth was extracted manually from well completion reports downloaded from the ESOGIS website. To calculate an average production depth for the NY reservoirs, the reported reservoir tops from each well in a given reservoir were averaged.

3. New York Reservoir Polygons

The MRCSP database includes shapefiles of the reservoir polygons, which is an estimate of the aerial extent of each reservoir. The ESOGIS database does not contain shapefiles, so they were created manually in a GIS. The buffer distance around producing wells in each reservoir in NY was chosen as 900 meters. This choice was made by comparing the only available polygons for NY reservoirs, which were the Trenton-Black River reservoirs (Patchen et al., 2006). Inputting those shapefiles into a GIS and comparing them to the locations of the wells showed that an average distance of 900 meters around all wells in a reservoir would create polygons compatible with Patchen et al.'s approach (Figure A-1).

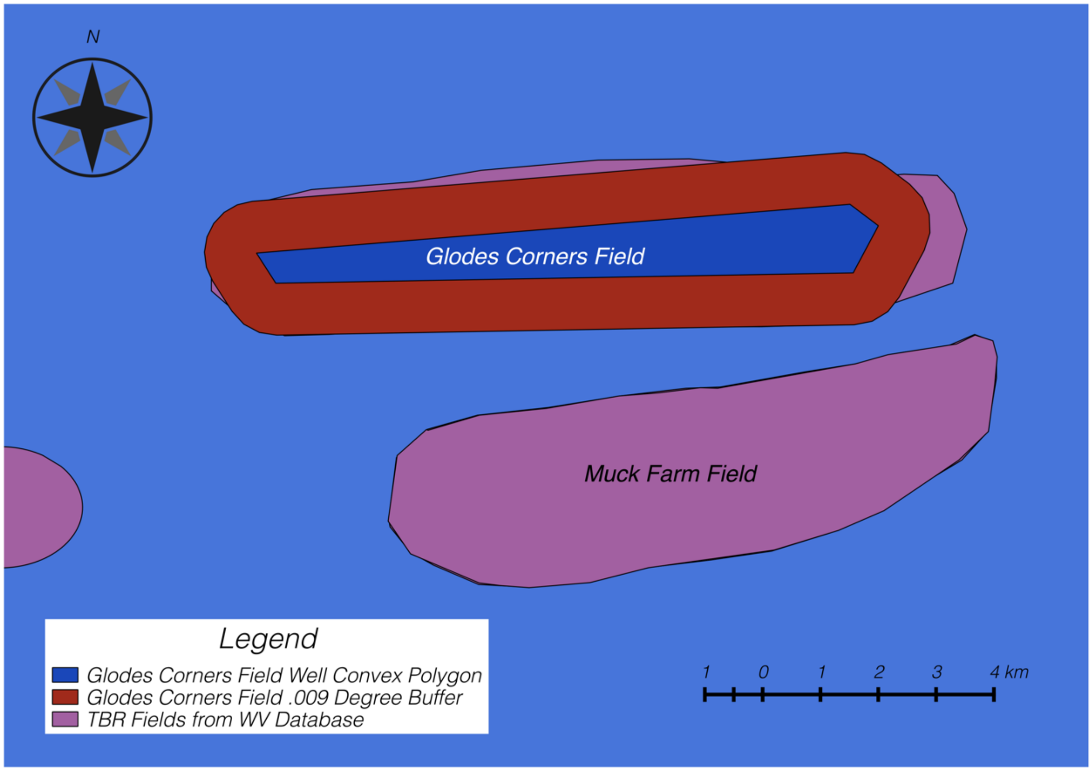

Figure A-1. Example of Trenton-Black River polygons in GIS, which aided in creating a systematic buffer zone for NY reservoirs. 0.009 degrees is equivalent to 900 meters. The West Virginia Database comes from Patchen et al. (2006).

4. Porosity and Permeability

Porosity and permeability values were assigned based on the producing geologic formation in which the reservoir is located. New York reservoirs derivation required derivation of both porosity and permeability values from sources other than ESOGIS. The MRCSP database provided porosity data for reservoirs in Pennsylvania and West Virginia, so only permeability had to be input based on other sources. For all three states, empirical porosity-permeability relationships (if available) were applied to the porosity values for each formation. Otherwise, average permeability values were applied to all reservoirs of a given geologic formation.

If empirical relationships were used, the calculated permeability values are not reported below because the data vary from reservoir to reservoir. However, if an average permeability value was applied to all reservoirs of a given formation, that value is listed below. The first section describes formations that are host to reservoirs in New York, and therefore require porosity inputs; however, these formations may also be host to reservoirs in Pennsylvania and West Virginia. In such cases, any differences in average values across the three states are noted below. The last section describes formations that are host to reservoirs only in Pennsylvania and West Virginia, and therefore only require permeability inputs.

Formations located in New York:

a. Queenston: Data chosen for the Queenston were taken from Lugert et al. (2006). Eighty-three samples from the Delany Core were analyzed by H.J. Gruy and Associates, which gave the following results:
    - i. Average porosity of core: 10.8%
    - ii. Porosity-permeability fit from core data, where k is permeability in units of mD and ϕ is porosity in porosity units (p.u.): $k = 0.0005\exp(0.5478\phi)$
    - iii. Average permeability for a porosity of 10.8% is 0.185 mD
    - iv. Lithology: Sandstone

b. Black River: Data chosen for the Black River Formation (also known as the Trenton-Black River in New York State) were taken from Lugert et al. (2006). Samples from the Whiteman #1 Core were analyzed by CoreLab, Inc.
    - i. Average porosity of core: 7%
    - ii. Porosity-permeability fit from core data, where k is permeability in units of mD and ϕ is porosity in porosity units (p.u.):

$$k_L = 0.39\phi^{2.87}$$

    - iii. Applying above equation to NPHI data from Black River reservoirs (see Chapter 2) is 120 mD.
    - iv. Lithology: Limestone/Dolomite

c. Galway/Theresa/Rose Run:

i. New York: The Galway Formation has long been called the Theresa Sandstone play in the subsurface, but that name is inaccurate when compared to the outcrop stratigraphy. Smith et al. (2010) show that the Galway Formation is Upper Cambrian in age and occurs above the Potsdam Sandstone (earliest Upper Cambrian in age) and below the Little Falls Formation (uppermost Cambrian in age). The Theresa is Ordovician in age and is actually younger than even the Tribes Hill Formation. The Theresa can only be found in northernmost New York in the Ottawa Graben. The producing formation in Western New York is the Galway Formation. Smith et al. (2010) confirm that Bockhahn, Cascade Brook, and Northwoods fields all produced from the Rose Run, in the Galway Formation. Those are 3 of the 10 Galway fields in the New York database, and those 10 fields are all in the same region. It is believed that the Rose Run is the unit within the Galway which produced gas (B. Slater, pers. comm.). The following porosity and permeability core data are from the Hooker Chemical #1 Well, which include measurements from the Potsdam Sandstone. For this work, the Potsdam data were removed, as they are not stratigraphically part of the Galway Formation.

        1. Average porosity: 6.5% for the Galway/Theresa/Rose Run reservoirs. (Smith et al., 2010)
        2. Porosity perm relationship fit from core data, where *k* is permeability in units of mD and ϕ is porosity in porosity units (p.u.):

$$k = 0.6621\phi - 1.7261$$

        3. Average permeability is 2.6 mD for a porosity of 6.5%, according to the above equation
    ii. Galway in Pennsylvania and West Virginia: Data taken from reports of producing fields in Pennsylvania and West Virginia, in Roen and Walker (1996).
        1. Porosity ranges from 2-25% and averages 10%.
        2. Permeability ranges from 0.01 to 198 mD and averages 5 mD.
        3. The MRCSP database reports porosities between 8-10 for the Galway/Rose Run fields, so an average of 5 mD was applied for all the PA and WV Rose Run reservoirs.
    iii. Lithology: Sandstone
d. Medina: Data chosen for the Medina were taken from Lugert et al. (2006). No core data were available, so average values from a high-volume producing field–the Lakeshore Field–were applied. The following values were applied to Medina reservoirs in all three states.

    i. Average porosity: The report states that porosity ranges between 6-8%, so an average porosity of 7% was chosen.
    ii. Average permeability: 0.1 mD.
    iii. Lithology: Sandstone

e. Onondaga: Data for Onondaga reservoirs come from Roen and Walker (1996). Average porosity and permeability values were derived from plugs taken from a productive Onondaga field in Steuben County, NY. The following values were used for reservoirs in all three states, due to a lack of permeability data available for Onondaga reservoirs in Pennsylvania and West Virginia. Because reported porosity values from Onondaga reservoirs in Pennsylvania and West Virginia were similar to the average porosity of Onondaga reservoirs in New York, the average permeability value from Onondaga reservoirs in New York was applied to those in Pennsylvania and West Virginia as well.
    i. Average porosity: 5.2%.
    ii. Average permeability: 22.4 mD.
    iii. Lithology: Limestone

f. Oriskany: Data for the Oriskany reservoirs come from Appendix D of Riley et al. (2010). All the data presented there come from cores in Pennsylvania and Ohio, but were applied to reservoirs in New York and West Virginia as well.
    i. Average porosity: 5%.
    ii. Average permeability: 1 mD

        iii. Lithology: Sandstone

g. Helderberg: There is one producing field from the Helderberg Formation in the database: the Stagecoach field. According to Lugert et al. (2006), geologists reclassified the producing formation of the Stagecoach to the Oriskany Formation (page 23).
h. Bass Islands: There is no available porosity or permeability data for the Bass Islands Formation in the Appalachian Basin; however, there are data from the Bass Islands Formation in the Michigan Basin (Harrison III et al., 2009). The following value were used for Bass Islands reservoirs in all three states.
    i. Average porosity: 12.5%. This value from Harrison et al. (2009) agrees with the range of porosity values listed for Bass Islands reservoirs in the PA/WV database, which is 10–14% porosity.
    ii. Average permeability: 22.4 mD
    iii. Lithology: Dolomite

Formations found only in Pennsylvania and/or West Virginia regions of the Basin:

i. Lockport: Data for the Lockport reservoirs come from Appendix A of Riley et al. (2010).
    i. Porosity-permeability relationship fit from core data, where k is permeability in units of mD and ϕ is porosity in porosity units (p.u.):

$$k = 3.0 \times 10^{-5} \exp(1.1716\phi)$$

    ii. Lithology: Dolomite

j. Elk Group: For simplicity, the Brallier, Gordon, and Benson were combined into the Elk Group, based on formation grouping. Data for the Elk Group were taken from Roen and Walker (1996).
    i. Porosity of the Elk Group ranges from 5–10%
    ii. Permeability ranges from 0.1–2.0 mD.
    iii. Validation: The MRCSP database reports an average porosity of 11% for all the Elk Group reservoirs; therefore, the upper end of average permeability (2 mD) was used.
    iv. Lithology: Sandstone; clay-rich turbidite slope apron deposit (Roen and Walker, 1996).
k. Lockhaven: Lockhaven was given the same permeability values as Elk Group, but not renamed.
    i. Lithology: Mudstone
l. Bald Eagle: There is only one Bald Eagle reservoir in the MRCSP database: the Grugan field, located in Pennsylvania.
    i. Permeability: 0.07 mD was reported in Roen and Walker (1996). Most permeability is from fractures.
    ii. Lithology: Sandstone
m. Beekmantown: Lugert et al. (2006) state that there are no major distinctions between the reservoir properties of the Queenston and the Beekmantown, so they were not evaluated separately.

    i. Permeability: 0.185 mD
    ii. Lithology: Limestone/Dolomite

n. Berea:
    i. Porosity: 12% (Roen and Walker, 1996)
    ii. Permeability: 3.84 mD (Roen and Walker, 1996)
    iii. Validation: The Berea reservoirs in the MRCSP database report 10% porosity, which is consistent with the Roen and Walker (1996).
    iv. Lithology: Sandstone

o. Chazy: According to Walcott (1896), the Chazy is another term for the Black River limestone. These fields are listed as having porosity of 8% in the MRCSP database. Their formation name was therefore changed to Black River, and the empirical porosity-permeability relationship from the Black River reservoirs in New York was applied. This results in a permeability of 99.5 mD for all four reservoirs in Pennsylvania.

p. Helderberg: According to Lewis et al. (2009), the permeability of the Helderberg Formation is very low, approximately 0.001 mD.
    i. Lithology: Limestone

q. Huntersville and Huntersville/Oriskany play: Riley et al. (2010) provides a maximum permeability of 0.003 mD for the Huntersville/Oriskany play. This value was used for the Huntersville reservoirs as well, due to a lack of data unique to the Huntersville.
    i. Lithology: Chert and Sandstone

r. Loysburg: Applied values from Beekmantown Dolomite. No other data available.

s. Newburg: The accompanying database to Roen and Walker (1996) contains two sets of core porosity and permeability data points. Because the other fields without permeability data had very similar porosity values, those data were fit to get an exponential relationship where permeability is in mD and porosity is in porosity units:

$$k = 2.1591\exp{(0.1699\phi)}$$

   i. Lithology: Limestone

t. Weir: There are two Weir reservoirs with porosity data in the MRCSP database, and one of those reservoirs is listed in Roen and Walker (1996) and has average porosity and permeability values. Because the porosity values aligned with what was already reported in the MRCSP database, the following permeability value was applied to both reservoirs.

   i. Permeability: 8 mD
   ii. Lithology: Sandstone

u. Keefer:

   i. Permeability: Roen and Walker (1996) report an average permeability for the Keefer Formation of 7.06 mD. That value was applied to the single Keefer reservoir in the MRCSP database.
   ii. Lithology: Sandstone

v. Devonian Unconformity Play:
    i. Permeability: Roen and Walker (1996) report an average permeability of 15.3 mD for this formation.
    ii. Lithology: Limestone

Formations with Very Limited Data:

w. Tuscarora: Roen and Walker (1996) report one Tuscarora field with permeability ranging from 0 to 10.7 mD. Many reports note similarities between Tuscarora, Medina, and Clinton. Due to a lack of specific data, a value of 0.1 mD was used for the Tuscarora, consistent with the Medina Formation.
    i. Lithology: Sandstone
x. “Multi”: These are reservoirs that produced hydrocarbons from a wide variety of undetermined formations. With no data to use, a high uncertainty and low permeability value of 0.1 mD was used.
y. Trenton: This play is found only in West Virginia, where permeability is associated primarily with fractures. Just like similar play types, a permeability of 0.1 mD was applied because more precise data cannot be found.
    i. Lithology: Limestone
z. Tully: There is only one Tully reservoir in the MRCSP database. There is no permeability data available, so it was assigned a low permeability value of 0.1 mD with a high uncertainty.
    i. Lithology: Limestone

aa. Mahantango: There is only one Mahantango reservoir in the MRCSP database. There are no permeability data available, so it was assigned a low permeability value of 0.1 mD with a high uncertainty.

    i. Lithology: Mudstone

REFERENCES

Harrison III, W.B., Grammer, G.M., and Barnes, D.A., 2009, Reservoir characteristics of the Bass Islands dolomite in Otsego County, Michigan: Results for a saline reservoir CO2 sequestration demonstration: Environmental Geosciences, v. 16, no. 3, p. 139-151.

Lewis, J.E., McDowell, R.R., Avary, K.L., and Carter, K.M., 2009, Characterization of the Helderberg Group as a geologic seal for CO2 sequestration: Environmental Geosciences, v. 16, no. 4, p. 201-210.

Lugert, C., Smith, L., Nyahay, R., Bauer, S., and Ehgartner, B., 2006, Systematic Technical Innovations Initiative Brine Disposal in the Northeast: Albany, NY, New York State Energy Research and Development Authority.

Patchen, D.G., Hickman, J.B., Harris, D.C., Drahovzal, J.A., Lake, P.D., Smith, L.B., Nyahay, R., Schulze, R., Riley, R.A., and Baranoski, M.T., 2006, A geologic play book for Trenton-Black River Appalachian basin exploration: U.S. Department of Energy Report: Morgantown, West Virginia, U.S. Department of Energy.

Riley, R., Harper, J., Harrison III, W., Barnes, D., Nuttall, B., Avary, K.L., Wahr, A., Baranoski, M., Slater, B., and Harris, D., 2010, Evaluation of CO2-Enhanced

Oil Recovery and Sequestration Opportunities in Oil and Gas Fields in the MRCSP Region MRCSP Phase II Topical Report October 2005 October 2010. DOE Cooperative Agreement No.

Roen, J.B., and Walker, B.J., 1996, The atlas of major Appalachian gas plays, West Virginia Geological and Economic Survey, Publication V-25.

Slater, B., March 2015, pers. comm.

Smith, L., Nyahay, R., and Slater, B., 2010, Integrated Reservoir Characterization of the Subsurface Cambrian and Lower Ordovician Potsdam, Galway and Theresa Formations in New York: Albany, NY, New York State Energy Research and Development Authority.

Walcott, C., 1896, Cambrian Rock of Pennsylvania, United States Geological Survey, http://pubs.usgs.gov/bul/0134/report.pdf.

APPENDIX B-1

The original publication contained a .gif animation. Because of the printed nature of this dissertation, the five individual images from the original electronic animation are shown below.

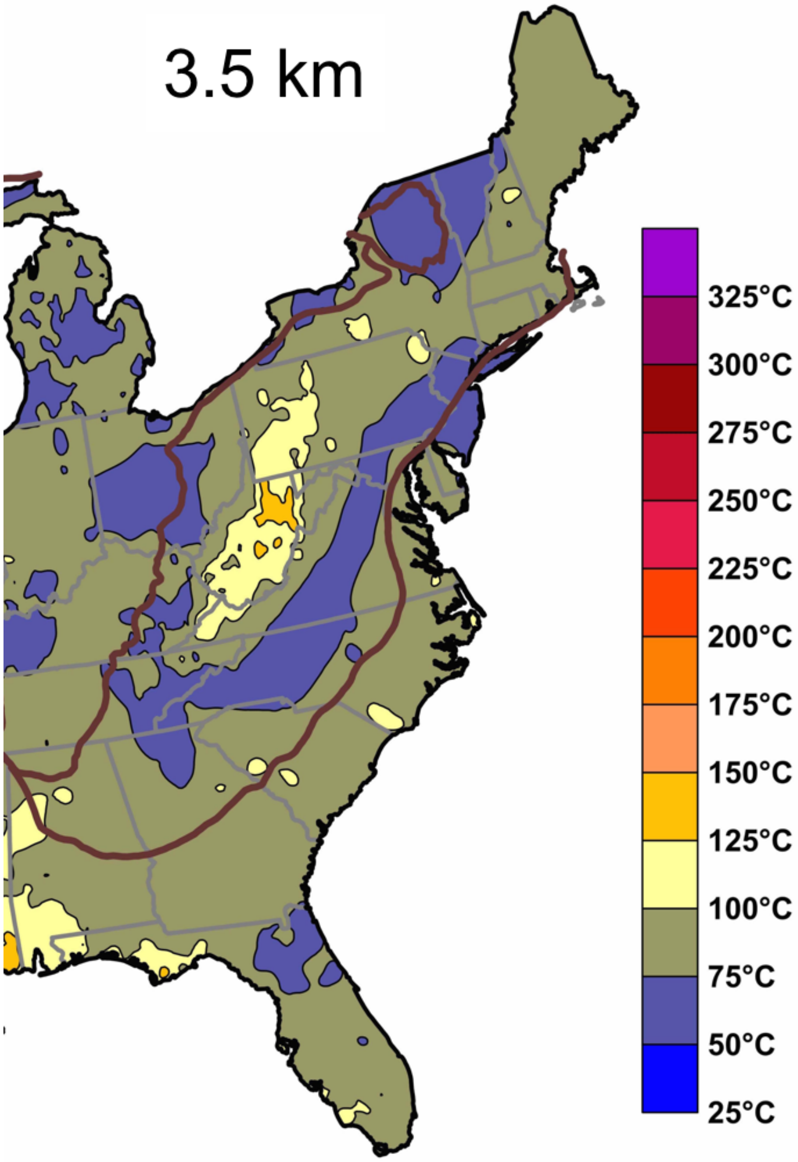

Animation 1, Image 1. Animation of temperatures at depth for the eastern sector of the United States. Temperatures in this image are shown at 3.5 km depth. (Adapted with permission from Southern Methodist University's Geothermal Laboratory)

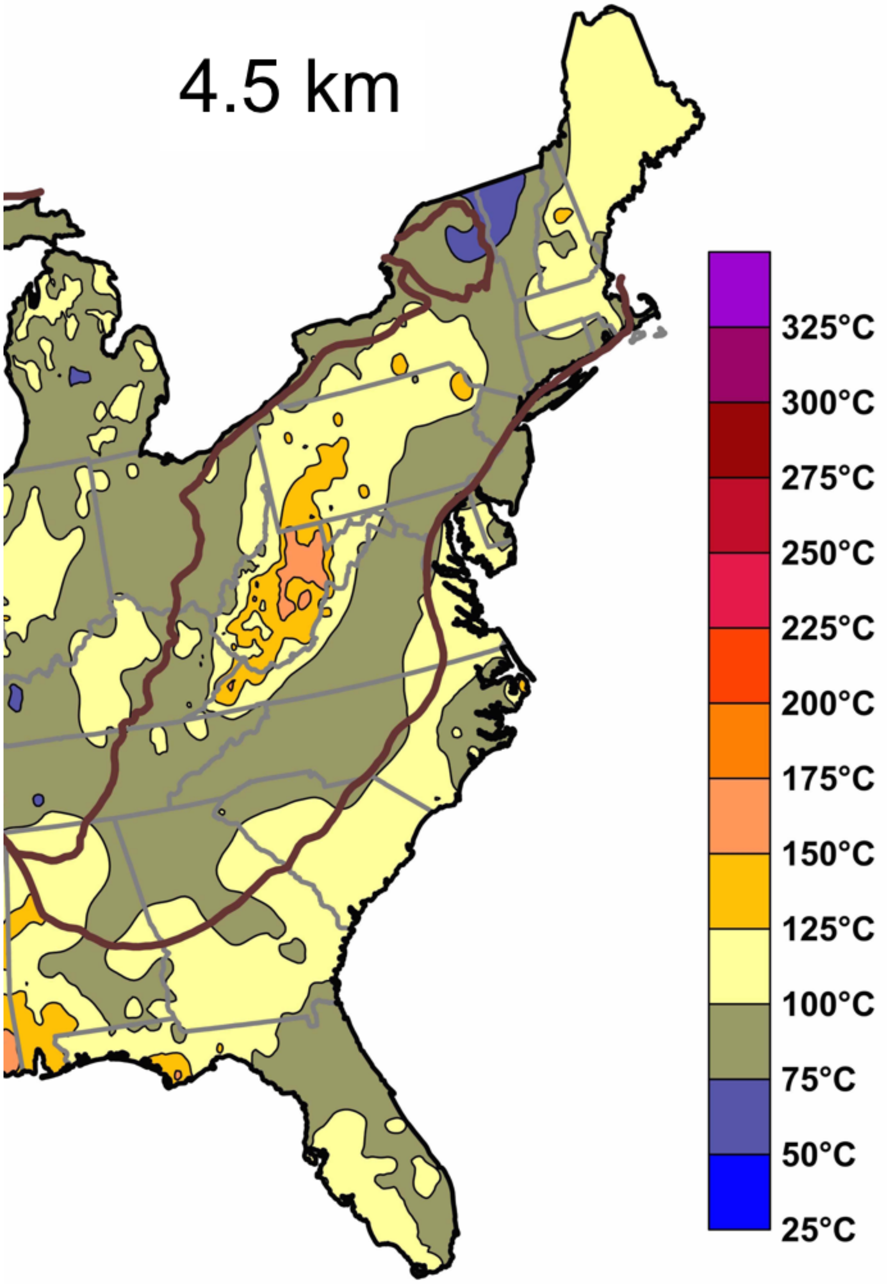

Animation 1, Image 2. Animation of temperatures at depth for the eastern sector of the United States. Temperatures in this image are shown at 4.5 km depth. (Adapted with permission from Southern Methodist University's Geothermal Laboratory)

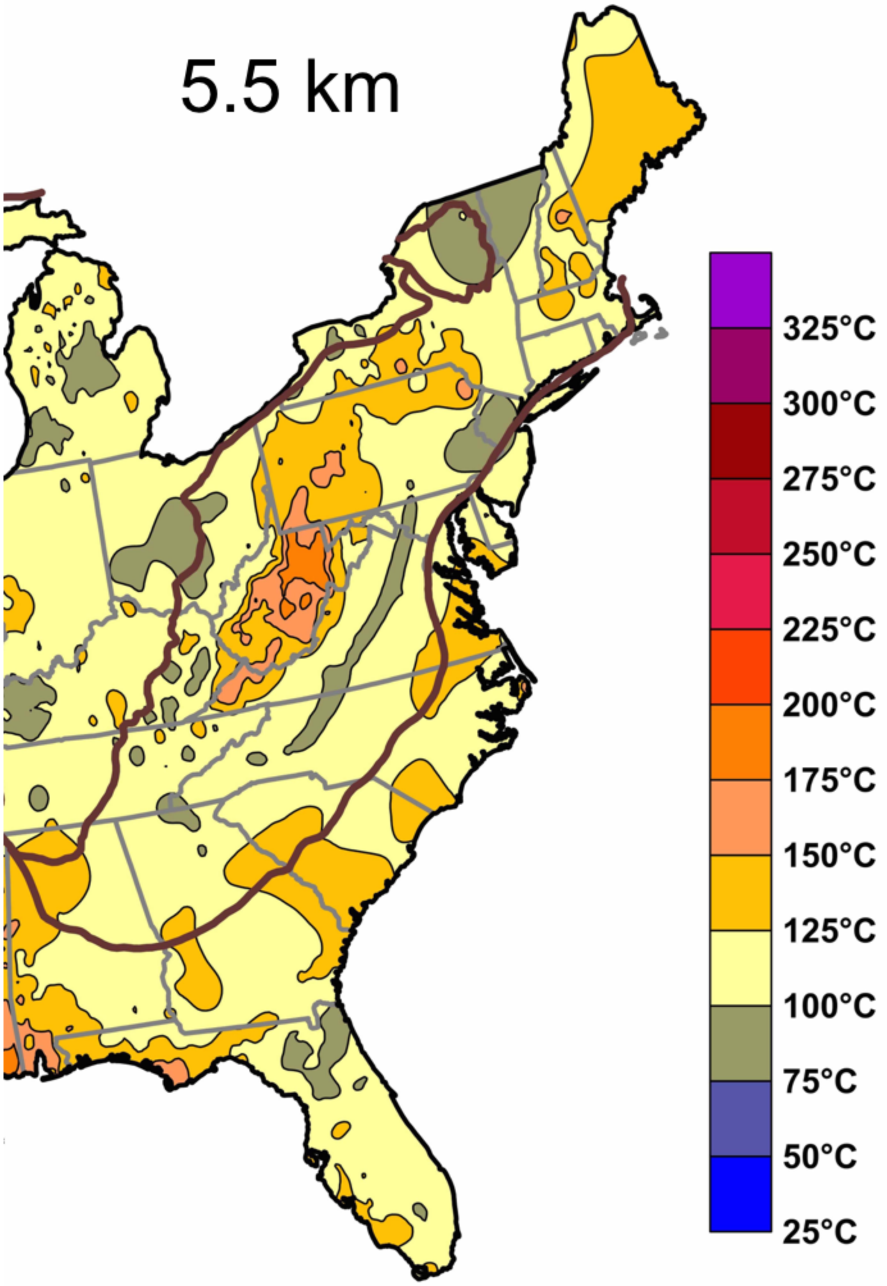

Animation 1, Image 3. Animation of temperatures at depth for the eastern sector of the United States. Temperatures in this image are shown at 5.5 km depth. (Adapted with permission from Southern Methodist University's Geothermal Laboratory)

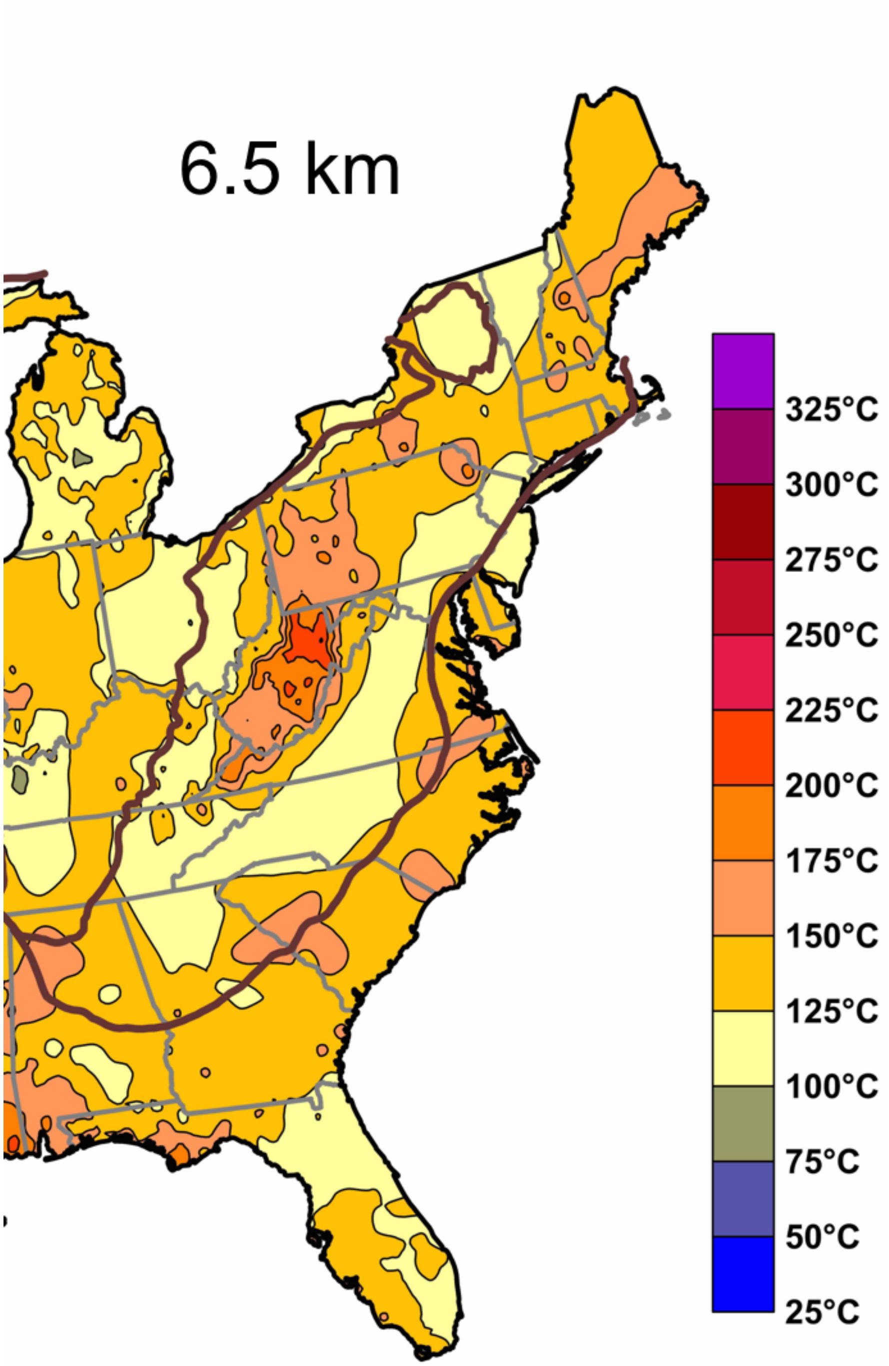

Animation 1, Image 4. Animation of temperatures at depth for the eastern sector of the United States. Temperatures in this image are shown at 6.5 km depth. (Adapted with permission from Southern Methodist University's Geothermal Laboratory)

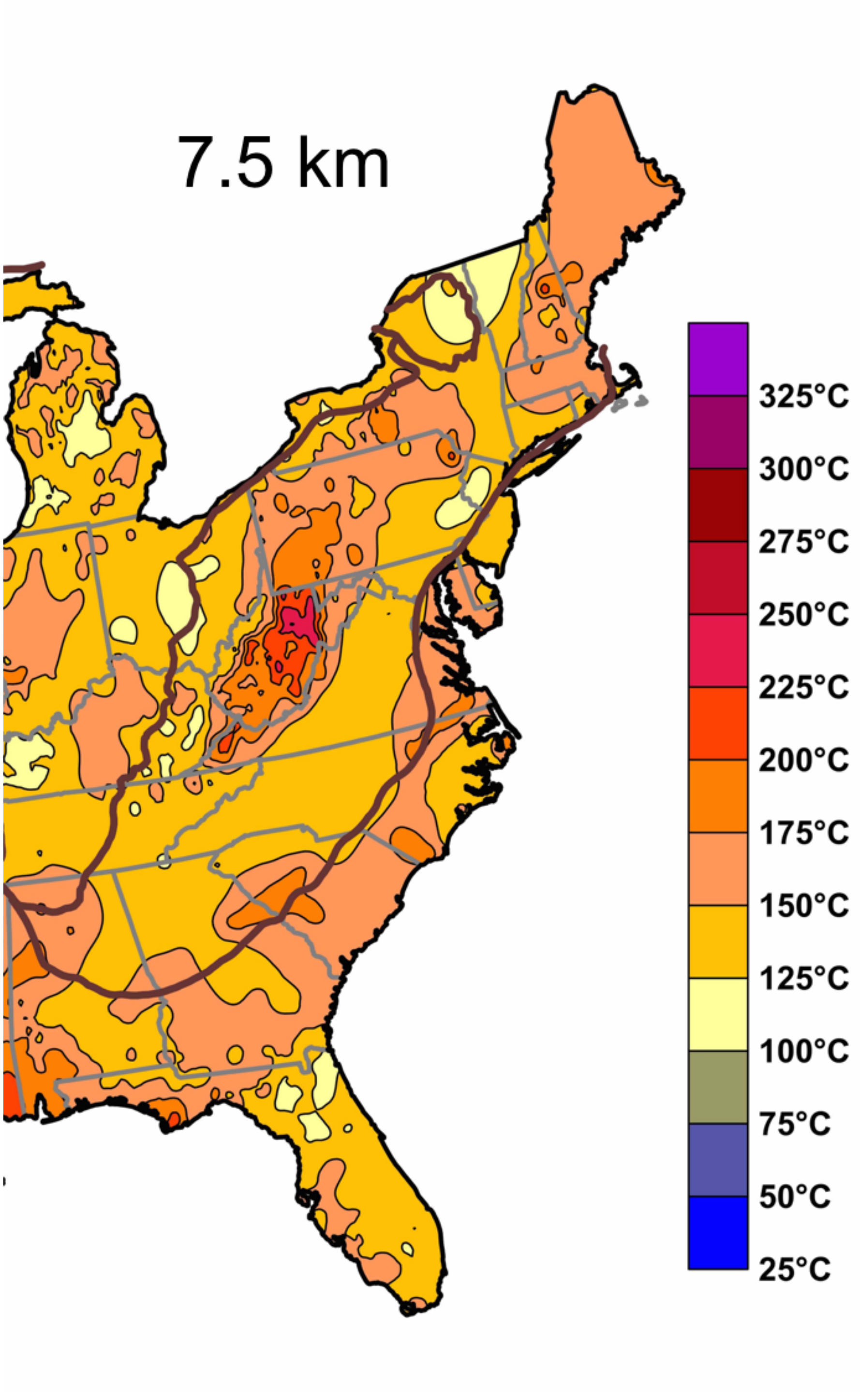

Animation 1, Image 5. Animation of temperatures at depth for the eastern sector of the United States. Temperatures in this image are shown at 7.5 km depth. (Adapted with permission from Southern Methodist University's Geothermal Laboratory)

APPENDIX B-2

Whiteman #1 Core Data: CoreLab File no. 52131-03-0120

SAMPLE NUMBER	START DEPTH	END DEPTH	INTERVAL THICKNESS	MAX PERMEABILITY (K,air)	MAX PERMEABILITY ERROR	90 DEG. PERMEABILITY (K,air)	90 DEG. PERM ERROR
	ft	ft	ft	md	md	md	md
1	9528.00-	9529	1	6.28	0.942	3.15	0.4725
2	9529.00-	9529.4	0.4	4.67	0.7005	4.08	0.612
3	9529.40-	9529.8	0.4	2.72	0.408	2.02	0.303
4	9529.80-	9530.1	0.3	10240	1024	540	54
5	9530.10-	9530.4	0.3	10240	1024	1350	135
6	9530.40-	9530.8	0.4	1970	197	159	7.95
7	9530.80-	9531.4	0.6	10240	1024	10240	1024
8	9531.40-	9531.8	0.4	10240	1024	10240	1024
9	9531.80-	9532.1	0.3	574	57.4	3.08	0.462
10	9532.10-	9532.8	0.7	2710	271	1800	180
11	9532.80-	9533.4	0.6	10240	1024	10240	1024
12	9533.40-	9534.4	1	12.7	0.635	2.05	0.3075
13	9534.50-	9535.4	0.9	1.77	0.2655	0.58	0.174
14	9535.40-	9536.4	1	0.99	0.297	0.46	0.138
15	9536.40-	9537.4	1	10240	1024	13.4	0.67
16	9537.40-	9539	1.6	6.18	0.927	1.72	0.258
17	9539.00-	9541.4	2.4	0.75	0.225	0.51	0.153
18	9541.40-	9543.7	2.3	17.1	0.855	11.5	0.575
19	9543.70-	9545.9	2.2	0.03	0.009	0.03	0.009
20	9545.90-	9548.1	2.2	9510	951	50	2.5
21	9548.10-	9550.7	2.6	140	7	79.3	3.965
22	9550.70-	9554.5	3.8	0.05	0.015	0.39	0.117
23	9554.50-	9557.9	3.4	0.07	0.021	0.07	0.021

Whiteman #1 core data, continued

SAMPLE NUMBER	POROSITY (helium)	POROSITY ERROR	CAPACITY (helium)	BULK DENSITY	GRAIN DENSITY	LITHOLOGY	FEATURES	
	%	%	í-ft	gm/cc	gm/cc		(sv=small vugs; mv= medium vugs; lv= large vugs; ppv = pinpoint vugs; fracs = fractures)	
1	4	0.5	4	2.76	2.87	dol	ppv sv	mv
2	4.5	0.5	1.8	2.73	2.85	dol	ppv sv	mv
3	6.5	0.5	2.6	2.68	2.86	dol	ppv sv	mv
4	10.7	0.5	3.21	2.54	2.84	dol	ppv sv	lv
5	15.1	0.5	4.53	2.43	2.86	dol	ppv sv	lv
6	8.5	0.5	3.4	2.61	2.86	dol	ppv sv	lv
7	10.1	0.5	6.06	2.58	2.87	dol	ppv sv	lv
8	11.8	0.5	4.72	2.52	2.86	dol	ppv sv	lv
9	10	0.5	3	2.57	2.86	dol	ppv sv	lv
10	9.2	0.5	6.44	2.6	2.86	dol	ppv sv	lv
11	26.9	0.5	16.14	2.1	2.87	dol	ppv sv	lv
12	11.3	0.5	11.3	2.54	2.86	dol	ppv sc	lv
13	5.5	0.5	4.95	2.69	2.85	dol	ppv sv	mv
14	6.3	0.5	6.3	2.68	2.85	dol	ppv sv	mv lv
15	9.7	0.5	9.7	2.56	2.83	dol	ppv sv	mv
16	1.1	0.5	1.76	2.82	2.85	dol	ppv sv	
17	1.1	0.5	2.64	2.82	2.85	dol	fracs	
18	1	0.5	2.3	2.82	2.85	dol	fracs	
19	0.5	0.5	1.1	2.84	2.85	dol	fracs	
20	3.2	0.5	7.04	2.72	2.81	dol	ppv sv	fracs
21	2.1	0.5	5.46	2.77	2.83	dol	ppv sv	fracs
22	0.5	0.5	1.9	2.83	2.84	dol	sty	
23	0.7	0.5	2.38	2.84	2.86	dol		

APPENDIX B-3

MatLab code for correcting NPHI logs due to the gas effect

```
% Correcting Neutron Logs with method from Bassiouni 1994
% Coded by Erin Camp erc85@cornell.edu

logs = load('Log_data_Combined.txt');
rhob = logs(:,4);
nphi = logs(:,3);

% trimming the dataset for outliers

rho_median = median(rhob);
rhob_mad = 1.482*median(abs(rhob-median(rhob)));

% Outlier bounds
rhob_ol_high = rho_median + 3*rhob_mad;
rhob_ol_low = rho_median - 3*rhob_mad;

% testing values in new matrix
new_logs = logs;

% removing outliers in for loop
for i = 1:length(new_logs)
    if (new_logs(i,4) > rhob_ol_high)||(new_logs(i,4) < rhob_ol_low)
        new_logs(i,:) = (NaN);
    end
end

%% Calculating DPHI from RhoB, RhoF, and RhoMa

rhof = 1.19; % assuming clean mud
rhomad = 2.85;
rhomal = 2.71;

%% Sorting by lithology
% creating more columns for lithology and dolomite-corrected NPHI
values
col = zeros(length(logs),1); % empty column
new_logs = [new_logs col col col col col];

% indexing limestone versus dolomite using PEFZ log and bulk density
for j = 1:length(new_logs)
    if new_logs(j,6) <= 3.14 % less than 3.14 PEFZ is dolomite
        new_logs(j,10) = 1;
%     elseif new_logs(j,4) >= -0.015*new_logs(j,3) + 2.69 %
limestone/dolomite cutoff
%         new_logs(j,10) = 1;
    else
        new_logs(j,10) = 2;
    end

end
```

```
%% Correcting neutron-density porosity and adjusting for gas effect

% Column 11 is: for dol, corrected dolomite apparent neutron
porosity, for
% limestone, original (limestone) apparent neutron porosity
% Column 12 is: calculated density porosity
% Column 13 is: calculated true porosity (accounting for gas effect)
% Column 14 is: permeability

for k = 1:length(new_logs)
    if new_logs(k,10)==1 % correcting dolomite neutron porosity,
leaving lime neutron porosity as is
        new_logs(k,11) = 0.0132*(new_logs(k,3)^2) +
0.3921*new_logs(k,3) - 1.4616 ; % dolomite equivalence curve from
Schlumberger charts
    else new_logs(k,11) = new_logs(k,3);
    end

    % calculating density porosity in column 12

    if new_logs(k,10)==1
        new_logs(k,12) = (rhomad - new_logs(k,4))/(rhomad - rhof);
    else
        new_logs(k,12) = (rhomal - new_logs(k,4))/(rhomal - rhof);
    end

    % calculating true porosity in column 13

    if abs(new_logs(k,12))>abs(new_logs(k,11)) % correcting for gas
effect where needed

            sxo1 = 1; % starting assuming Sxo = 1 and iterating down
towards zero
            sxo2 = 0;

            while abs(sxo1-sxo2) > 0.001 % while loop to iterate
until Sxo gets within 0.025

                new_logs(k,13) = 100*sqrt((new_logs(k,12)^2 +
new_logs(k,11)^2)/(2*(1+.12*(1-sxo1))^2));
                sxo2 = new_logs(k,11)/(new_logs(k,13)/100);
                sxo1 = ((sxo1-sxo2)/2)+sxo2;
            end

    elseif    new_logs(k,10)==1 % calculating porosity for dolomite,
with no gas effect
        new_logs(k,13) = 100*(((abs(rhomad - new_logs(k,4)))+
(abs(new_logs(k,11))/100))/rhomad);

    else % correcting porosity for limestone, with no gas effect
        new_logs(k,13) = 100*(((abs(rhomal - new_logs(k,4)))+
(abs(new_logs(k,11))/100))/rhomal);
```

```
    end

    new_logs(k,14) = 0.3941*new_logs(k,13).^2.8745;

end

%% printing data to csv

output = new_logs;
headers =
{'well','depth_ft','orig_poro','orig_dens','gamma','pefz','hdra','cal
','dphi','lith','neu_poro','dens_poro','true_poro','perm'};
csvwrite_with_headers('QB_log_data_modified_4-18-
16.csv',output,headers);

%% Creating Figure of raw data

dol_nphi = new_logs(find(new_logs(:,10)==1),11);
%dol_nphi_lithcorr = new_logs(find(new_logs(:,10)==1),11);
dol_rho = new_logs(find(new_logs(:,10)==1),4);
lim_nphi = new_logs(find(new_logs(:,10)==2),11);
lim_rho = new_logs(find(new_logs(:,10)==2),4);
dol_dphi = new_logs(find(new_logs(:,10)==1),12);
lim_dphi = new_logs(find(new_logs(:,10)==2),12);

x = linspace(0,35);

% equation for limestone porosity relationship is
y_lim = -0.015*x + 2.7;

% equation for dolomite porosity relationship is
y_dol = -0.013*x + 2.85;

% Figure of dolomite and limestone samples on NPHI v. RHO plot
(dolomite
% NOT corrected for lithology)
figure
plot(dol_nphi,dol_dphi,'o')
hold on
plot(lim_nphi,lim_dphi,'o')
hold on
% plot(x,y_lim)
% hold on
% plot(x,y_dol)
xlabel('CNL Apparent Neutron Porosity, p.u.','FontSize',20)
ylabel('Density Porosity','FontSize',20)
%title('Original NPHI v. RHO log data','FontSize',26)
% set(gca,'YDir','reverse')
addTopXAxis('exp', '(1.034+argu*.766)', 'xLabStr', 'CNL Apparent
Dolomite Porosity, p.u.')
legend({'Dolomite','Limestone','Limestone Curve','Dolomite
Curve'},'FontSize',18,'Location','northwest')
```

```
%% Histogram of true porosity values

binsporo = linspace(-2,2,50);
binsExpporo = 10.^binsporo;

figure
hist(new_logs(:,13),50)
grid on
% set(gca,'XScal','log')
set(get(gca,'child'),'FaceColor',[0.6 0.6 0.6],'EdgeColor','k');
axis([0 30 0 2500])
xlabel('Porosity, %','FontSize',18)
ylabel('Frequency','FontSize',18)
%title({'Well Log Derived Porosity in Black River Formation,'
,'Quackenbush Hill Field'},'FontSize',20)

%Histogram of permeability values

binsperm = linspace(-9,5,50);
binsExpperm = 10.^binsperm;

figure
hist(new_logs(:,14),binsExpperm)
set(gca,'XScal','log')
h = findobj(gca,'Type','line');
grid on
set(h,'Marker','none');
title({'Permeability in Black River Formation, Quackenbush Hill
Field','Empirical Core Relationship Applied to Well Log Porosity
Data'})
xlabel('Permeability, mD')
ylabel('Frequency')

%% Importing TVD values

depthdata = load('poroVdepth.csv');

tvd = depthdata(:,1);
tvdporo = depthdata(:,2);
tvdlith = depthdata(:,3);

tvdporodol = depthdata(find(tvdlith==1),2);
tvdporolim = depthdata(find(tvdlith==2),2);
tvddol = 0.3048*depthdata(find(tvdlith==1),1);
tvdlim = 0.3048*depthdata(find(tvdlith==2),1);

figure
plot(tvdporodol,tvddol,'o')
hold on
plot(tvdporolim,tvdlim,'o')
%title('Porosity with Depth in Quackenbush Hill Field')
xlabel('Porosity, %')
ylabel('Depth, m')
set(gca,'YDir','reverse')
legend({'Dolomite','Limestone'})
```